

Gas Phase Spectroscopy
and Kinetics of
Atmospheric Radicals

Thesis by
Leah G. Dodson

In Partial Fulfillment of the Requirements for
the degree of
Doctor of Philosophy

CALIFORNIA INSTITUTE OF TECHNOLOGY
Pasadena, California

2016
(Defended May 6, 2016)

© 2016

Leah G. Dodson
ORCID: 0000-0001-5960-056X

ACKNOWLEDGEMENTS

Something that cannot be overstated in this thesis is the fruitfulness of the collaborations we have undertaken. Many of the experiments were conducted with equipment designed, built, and cared for by members of the Combustion Research Facility (CRF) at Sandia National Laboratories. Inexplicably, these same individuals have spent countless hours discussing experiments with me and helping me to understand the data we obtained.

The Multiplexed Photoionization Mass Spectrometer, built by David Osborn and Craig Taatjes at the CRF, provided me with a whopping 170 GB of raw data (if you're reading this in the future, that was a lot of raw data in 2016...). Over the last 5 years, I spent 35 days, including countless graveyard shifts, at the ALS running experiments on their machine, confident that I had their full support. Members of their groups, including Rebecca Caravan, Arkke Eskola, Haifeng Huang, Krupa Ramasesha, Brandon Rotavera, Oliver Welz, and especially John Savee, sacrificed innumerable hours working with me. Sandia engineers Howard Johnsen, Kendrew Au, and Raybel Almeida always supported my tedious requests. Not to be outdone, the Lawrence Berkeley National Laboratory staff (especially Doug Taube and Bruce Rude) at the Advanced Light Source provided me with an amazing facility to accomplish all of this work. I'm not sure any of these people have healthy sleep schedules.

I spent an especially productive summer at the CRF in 2015 in the labs of David Osborn and Lenny Sheps. I don't know what possessed them to think it was a good idea to bring me into their groups, but it was a valuable experience for me. Lenny's time-resolved broadband cavity enhanced absorption spectrometer is an impressively designed machine that we used to tackle an especially difficult measurement.

I have also benefitted greatly from our collaboration with the nearby Jet Propulsion Laboratory. Stan Sander is someone you want in your corner when you're trying to understand a complex chemical reaction system of atmospheric radicals, as are all of his group members. Fred Grieman, of Pomona College, currently holds the record for having sat through the most talks given by me, and is a valuable source of advice on graduate school and beyond.

None of this would have been possible without the mentoring I received in the Okumura group—Mitchio, Kana Takematsu, Nathan Eddingsaas, Allan Nishimura, Matt Sprague, Dave Long, Luis Gomez, Aileen Hui, Damien Amedro and, of course, Thinh Bui provided me with examples of how to be a good scientist and, more importantly, a good member of our community. Members of the Caltech staff (Nora, Monica, Mike and Steve, Rick, Joe, and every person from Facilities who dealt with my inane demands during our move to Linde+Robinson) amazingly keep things running, always with an attitude of extreme kindness. My friends (Linhan, Elizabeth, Kate, and Kathryn) and family provided unwavering support throughout this entire process.

I was personally supported by two graduate research fellowships during the past five years—the U.S. Environmental Protection Agency (EPA) Science to Achieve Results Graduate

Fellowship supported me from 2011–2014 and Sandia National Laboratories (SNL) funded me as part of a Campus Executive Laboratory Directed Research and Development (LDRD) project from 2014–2016. Not only did these agencies cover my graduate stipend, but they importantly provided me with the necessary travel funds to make the aforementioned trips to the Bay Area. This thesis was developed under STAR Fellowship Assistance Agreement no. 91732501-0 awarded by the U.S. EPA and the LDRD project PO#1416776 awarded by SNL. It has not been formally reviewed by EPA or SNL. The views expressed in this thesis are solely those of Leah G. Dodson, and neither EPA nor SNL endorses any products or commercial services mentioned in this thesis. The research presented in this thesis was also supported by the National Science Foundation (CHE-0957490 and CHE-1413712) and the National Aeronautics and Space Administration's Upper Atmospheric Research Program (NNX12AI01G).

Thank you to everyone. It truly takes a village.

ABSTRACT

An important goal for atmospheric and combustion chemists is continued improvement in our understanding of the gas phase reactivity of free radical intermediates formed during hydrocarbon oxidation. The primary focus of this thesis was to measure gas phase kinetics of prototypical free radicals relevant to atmospheric and combustion chemistry, a goal that requires spectroscopy, quantitative product detection, and computational chemistry in order to address these complex chemical systems.

Near-infrared cavity ringdown spectroscopy was used to study the peroxy radicals (RO_2) formed from chlorine-initiated oxidation of isoprene and other unsaturated hydrocarbons. Isoprene is one of the most important hydrocarbons in the atmosphere; detection of RO_2 formed directly from isoprene oxidation will aid in understanding the initial steps of its fate in the atmosphere. As expected, the near-infrared chloro-isoprenyl peroxy radical spectrum has many features; each spectral feature corresponds to a different isomer and conformer, indicating that several RO_2 structures are formed. In small RO_2 , it was possible to identify the molecular structure of the absorber by comparing the experimental spectrum with the vibrationally-resolved electronic spectrum generated by computational chemistry. Identification of each feature then enabled preliminary isomer-specific kinetics measurements.

Photoionization mass spectrometry is another useful method for selective detection of radicals, with the added bonus of detecting many of the other species of interest, leading to a comprehensive understanding of the reaction mechanism. The yields of radical chain-propagating product channels of prototypical RO_2 reactions (self- and cross-reactions) are important in understanding radical chemistry in gas phase hydrocarbon oxidation. We obtained branching ratio information for reactions of acetyl peroxy radicals with HO_2 , with particular focus on OH-regenerating reactions. Along the way, we observed unexpected product formation from low-pressure reactions of acetyl radicals and oxygen. Using the same techniques, we also looked at the self-reaction of ethyl peroxy radicals, confirming past measurements of the radical-propagating channel for this reaction, and investigated

interesting product formation, like what may be the dialkyl peroxide. These studies were supported by measurements of VUV photoionization cross sections for several radical species. The utility of this instrumentation was also extended by the development of a low-temperature (200–300 K) flow reactor.

Finally, using time-resolved broadband cavity-enhanced absorption spectroscopy, we measured the rate coefficient of reactions of the smallest Criegee intermediate, CH_2OO with ozone. We observed that this reaction is rather fast, which could have significant implications for experimental ozonolysis studies that are carried out under high initial reactant concentrations.

PUBLISHED CONTENT AND CONTRIBUTIONS

Dodson, L. G. et al. (2015). “VUV photoionization cross sections of HO₂, H₂O₂, and H₂CO”. In: *Journal of Physical Chemistry A* 119(8), pp. 1279–1291. doi: 10.1021/jp508942a.

L.G.D. participated in the conception of the project and data collection, processed and analyzed the data, and participated in the writing of the manuscript.

TABLE OF CONTENTS

Acknowledgements	iii
Abstract	v
Published Content and Contributions	vii
Table of Contents	viii
List of Figures and Tables	xii
Chapter I: Introduction	1
Chapter II: Observation and assignment of the A–X electronic transition of chlorine-substituted hydrocarbon peroxy radicals	5
1 Introduction	5
2 Experimental	5
2.1 Near-infrared pulsed laser cavity ringdown spectrometer.....	6
2.2 Radical production.....	6
2.3 Spectrum	7
2.4 Quantum chemistry calculations	7
3 Results and Discussion	8
3.1 Peroxy radical spectra.....	9
3.2 Assignment of the chloro-ethyl peroxy radical spectrum.....	9
3.3 Assignment of the chloro-propyl peroxy radical spectrum	11
3.4 Assignment of the spectra of peroxy radicals with C4 backbones	12
4 Conclusions	13
5 References	14
6 Supporting Information.....	29
6.1 Adiabatic electronic 0–0 transition energy scaling.....	29
6.2 References.....	29
Chapter III: Observation and assignment of the A–X electronic transition of the peroxy radicals formed during chlorine-initiated oxidation of isoprene	44
1 Introduction	44
2 Experimental	44
2.1 Radical production.....	45
2.2 Experimental and theoretical spectrum.....	45
2.3 Peroxy radical kinetics.....	46
3 Results and Discussion	47
3.1 Peroxy radical spectrum and assignment	48
3.2 Peroxy radical kinetics.....	50
4 Conclusions	50
5 References	51
6 Supporting Information.....	65
Chapter IV: VUV photoionization cross sections of HO₂, H₂O₂, and H₂CO	70
1 Introduction	71

2 Experiment.....	73
2.1 Multiplexed Photoionization Mass Spectrometer	74
2.2 Photoionization cross section determination.....	76
2.3 Instrument response function.....	77
3 Results.....	78
3.1 Kinetics methodology	78
3.2 Single energy cross sections	81
3.3 Absolute photoionization spectra	83
3.4 Error analysis.....	84
4 Discussion.....	85
4.1 H ₂ CO	85
4.2 HO ₂	87
4.3 H ₂ O ₂	87
4.4 Validity of empirical estimates of cross sections	88
5 Conclusions	89
6 References.....	89
7 Supporting Information	111
7.1 Characterization of instrument effects using NO ₂ photolysis.....	111
7.2 Deconvolution of isobaric signals	113
7.3 Absolute photoionization cross section of methanol	114
7.4 Experiments 19–22	115
7.5 Highest occupied molecular orbitals of HO ₂ and H ₂ O ₂	115
7.6 Full kinetics model.....	116
7.6 Reference.....	116
Chapter V: Vacuum ultraviolet photoionization cross section of the hydroxyl radical.....	126
1 Introduction.....	126
2 Experiment.....	127
3 Results.....	131
3.1 Experiments.....	131
3.2 Kinetics modeling	131
3.3 Observed kinetics	132
3.5 Experimental cross section and spectrum	136
3.6 Error analysis.....	138
4 Discussion.....	140
5 Conclusions	141
6 References.....	141
7 Supporting Information	155
7.1 Determining the ozone concentration.....	155
7.2 The tabulated photoionization spectrum of OH	156
7.3 References	156
Chapter VI: Kinetics and branching fraction of the ethyl peroxy radical self-reaction measured using VUV photoionization mass spectrometry	159
1 Introduction.....	159

2	Experimental methods	161
2.1	Experimental conditions	162
2.2	Photoionization spectra	163
2.3	Kinetics model	164
3	Results	164
3.1	Photoionization spectra	164
3.2	$C_2H_5O_2 + HO_2$ cross-reaction.....	166
3.3	Prompt C_2H_4 and HO_2 formation	166
3.4	$C_2H_5O_2$ self-reaction rate constant	167
3.5	Branching fraction of the ethoxy channel	168
3.6	Dialkyl peroxide formation	169
3.7	Photoionization spectrum of C_2H_5OOH	170
4	Discussion	170
5	Conclusions	172
6	References	172
Chapter VII: Product yield studies of the reactions of acetyl radicals with O_2 and acetyl peroxy radicals with HO_2 using VUV photoionization mass spectrometry		186
1	Introduction	186
2	Experimental Methods.....	188
3	Results	188
3.1	Absolute photoionization cross section of CH_3O_2	189
3.2	Acetyl peroxy yield from $CH_3CO + O_2$	189
3.3	Co-product of OH	191
3.4	Ketene product channel	192
3.5	Reaction of $CH_3C(O)O_2$ with HO_2	192
4	Discussion	194
5	Conclusions	195
6	References	195
Chapter VIII: Design and performance of a temperature controlled flow reactor for low-temperature radical kinetics		211
1	Introduction	211
2	Low-temperature reactor design.....	212
2.1	Inner tube design.....	212
2.2	Outer tube design.....	213
2.3	Assembly of reactor.....	213
3	Low-temperature reactor performance.....	213
4	PID control	214
5	Low-temperature study of the HO_2 self-reaction.....	216
6	Discussion	219
7	References	219
Chapter IX: Experimental measurement of the rate coefficient for reaction of the simplest Criegee CH_2OO with ozone		239
1	Introduction	239
2	Experiment	241

3 Results.....	243
3.1 CH ₂ I ₂ + O(³ P) rate constant	243
3.2 CH ₂ OO + O ₃ rate constant.....	245
3.3 Time-dependent spectrum simulations.....	245
4 Discussion.....	250
5 References.....	250
6 Supporting Information	266
6.1 Igor procedure file for simulating 2D spectra for BB-CEAS	266
Appendix A: Changes made to the pulsed cavity ringdown apparatus after moving from Noyes to Linde+Robinson	269
1 Introduction.....	269
2 Relocated instruments	269
3 Single-wavelength kinetics	270
4 Lambda Physik dye laser installation	272
5 References.....	273
Appendix B: Predicting vibrationally-resolved A–X electronic and photoionization spectra using quantum chemical methods	279
1 Introduction.....	279
2 Calculation of electronically excited states	279
3 Identification of local minimum structures.....	280
4 Calculation of A–X adiabatic transitions.....	280
4.1 TD-DFT.....	281
4.2 EOMEE-CCSD	282
5 Simulation of vibrationally-resolved electronic spectra.....	282
6 Computing ionization energies and photoionization spectra	283
7 References.....	284
Appendix C: Matlab programs used in analyzing MPIMS data.....	297
1 Introduction.....	297
2 Modeling ALS data	297
2.1 createConvolvedModelEtO2.m	297
2.2 runKintecusEtO2.m.....	299
2.3 photolysis_calc.m.....	301
2.4 buildModel.m	302
2.5 convolveModel.m	303
2.6 convolvePrecursor.m.....	304
3 Fitting ALS data	304
3.1 fitALSEtO2.m	305
3.2 create_model.m	306

LIST OF FIGURES AND TABLES

Chapter II: Observation and assignment of the A–X electronic transition of chlorine-substituted hydrocarbon peroxy radicals**Figures**

1. Pulsed cavity ringdown instrument schematic.....18
2. Near-infrared cavity ringdown spectrum of the peroxy radicals formed from simple alkenes.....19
3. Near-infrared cavity ringdown spectrum of the peroxy radicals formed from alkenes with C4 backbones20
4. Geometries of the four unique conformers of the chloro-ethyl peroxy radical..... 21
5. Experimental spectrum of the A–X electronic transition of chloro-ethyl peroxy radical along with the computed Franck-Condon spectra of the four local minimum structures22
6. Geometries of the seven unique conformers of the 1-chloro propyl peroxy radical and the seven unique conformers of the 2-chloro propyl peroxy radical23
7. Experimental spectrum of the A–X electronic transition of chloro-propyl peroxy radical along with the computed Franck-Condon spectra of the 14 local minimum structures24

Tables

1. Origin frequencies for the chloro-ethyl peroxy radical25
2. Ground state degeneracies (g) and energy differences for conformers of chloro-ethyl and chloro-propyl peroxy radicals26
3. Comparison of X and A state bond lengths and adiabatic A–X electronic transitions calculated for the chloro-ethyl peroxy radical C_s conformer27
4. Origin frequencies for the chloro-propyl peroxy radical.....28
- S1. Comparison between the experimental and theoretical results for the ethyl peroxy radical30
- S2. Energies and Cartesian coordinates for equilibrium structures of chloro-ethyl peroxy radical conformers.....31
- S3. Unscaled UB3LYP/aug-cc-pVDZ harmonic frequencies for equilibrium structures of chloro-ethyl peroxy radical conformers.....34
- S4. Energies and Cartesian coordinates for equilibrium structures of the 1-chloro-propyl and 2-chloro-propyl peroxy radical conformers.....35
- S5. Unscaled UB3LYP/aug-cc-pVDZ harmonic frequencies for equilibrium structures of 1-chloro-propyl and 2-chloro-propyl peroxy radical conformers40

Chapter III: Observation and assignment of the A–X electronic transition of the peroxy radicals formed during chlorine-initiated oxidation of isoprene

Figures

1. Near-infrared cavity ringdown spectrum of the peroxy radicals formed from chlorine-initiated oxidation of isoprene..... 55
2. Structures of the six unique conformers of the chloro-isoprene peroxy radical 56
3. Structures of the three unsubstituted isoprene peroxy radicals formed from H-abstraction of isoprene 57
4. Comparison of the Franck-Condon spectra of the six chlorine-substituted isoprene peroxy radical isomers and the experimental spectrum..... 58
5. Comparison of the Franck-Condon spectra of the three unsubstituted isoprene peroxy radical isomers and the experimental spectrum 59
6. Experimental isoprene peroxy radical decays 60
7. Experimental isoprene peroxy radical decays with NO..... 61
8. First order decay rates of the peroxy radical absorption peaks as a function of NO..... 62

Tables

1. Ground state energy differences for conformers of chloro-substituted and unsubstituted peroxy radicals..... 63
2. The theoretical origins for the six chlorine-substituted and three unsubstituted isoprene peroxy radical conformers, along with the A state vibrations of the O–O stretch mode 64
- S1. Energies and Cartesian coordinates for equilibrium structures of chloro-isoprenyl peroxy radical conformers 65
- S2. Energies and Cartesian coordinates for equilibrium structures of unsubstituted isoprene peroxy radical conformers..... 68

Chapter IV: VUV photoionization cross sections of HO₂, H₂O₂, and H₂CO

Figures

1. Sample time-of-flight spectra 97
2. Typical raw H₂CO⁺, HO₂⁺, and H₂O₂⁺ signals versus time 98
3. Representative observed precursor depletions 99
4. Single energy kinetics traces for title molecules 100
5. Absolute photoionization spectrum of formaldehyde 101
6. Absolute photoionization spectrum of HO₂ 102
7. Absolute photoionization spectrum of H₂O₂ 103
- S1. NO₂ photolysis experiments to calibrate instrument effects..... 119
- S2. Absolute photoionization cross section of methanol 120
- S3. Single energy kinetics traces for title molecules, from the data set exhibiting a faster rise 121

S4. The HOMO and HOMO-1 for HO ₂ and H ₂ O ₂	122
---	-----

Tables

1. Single-energy experiments were conducted at 5 individual photon energies	104
2. A subset of the reactions used to simulate the concentration-dependent profiles.....	105
3. Photon energies and initial concentrations for all experiments.....	106
4. Photoionization cross sections for H ₂ CO, HO ₂ , and H ₂ O ₂	108
5. Absolute photoionization spectra for HO ₂ , H ₂ O ₂ , and H ₂ CO	109
S1. Minor reactions that were included in the full kinetics model used to fit data	123

Chapter V: Vacuum ultraviolet photoionization cross section of the hydroxyl radical

Figures

1. Observed O ₃ depletion.....	146
2. Observed OH decay.....	147
3. Observed O(³ P) decay	148
4. Absolute photoionization spectrum of OH	149
5. Absolute photoionization spectrum of O(³ P)	150
S1. Absolute photoionization spectrum of ozone	157

Tables

1. Conditions for each experiment	151
2. The reactions used to simulate the concentration-dependent profiles.....	152
3. Photoionization cross sections for OH.....	154
S1. Absolute photoionization spectrum of OH	158

Chapter VI: Kinetics and branching fraction of the ethyl peroxy radical self-reaction measured using VUV photoionization mass spectrometry

Figures

1. Absolute photoionization cross section of acetaldehyde, ethanol, ethylene, formaldehyde, chloroethane, and methyl hydroperoxide ...	175
2. Experimental data and kinetic fit of C ₂ H ₅ O ₂ + HO ₂ cross-reaction...	176
3. Experimental kinetic traces for C ₂ H ₄ and HO ₂ , formed from reaction of C ₂ H ₅ radicals and O ₂	177
4. Kinetics from the ethyl peroxy radical self-reaction	178
5. Ratio of acetaldehyde/ethanol in the ethyl peroxy radical self-reaction	179
6. Time-dependent ratio of CH ₃ CHO ÷ C ₂ H ₅ OH in the ethyl peroxy radical self-reaction.....	180
7. Fitted alkoxy yields as a function of % O ₂	181
8. Kinetics and spectroscopy at <i>m/z</i> 90	182

Tables

1. List of experimental parameters for the ethyl peroxy radical self-reaction	183
2. List of experimental parameters for the HO ₂ + C ₂ H ₅ O ₂ cross-reaction	184
3. Kinetics model for the C ₂ H ₅ O ₂ self-reaction.....	185
Chapter VII: Product yield studies of the reactions of acetyl radicals with O₂ and acetyl peroxy radicals with HO₂ using VUV photoionization mass spectrometry	

Figures

1. Potential energy surface of the reaction of acetyl radicals with O ₂ ...	198
2. Absolute photoionization spectra of the methyl peroxy radical and methyl hydroperoxide	199
3. Oxygen-dependent CH ₃ O ₂ formation from the acetyl peroxy radical self-reaction	200
4. Fitted values for the yield of acetyl peroxy radicals and OH radicals from reactions of CH ₃ C(O) with O ₂	201
5. Time-dependent traces of formaldehyde formed during CH ₃ C(O)O ₂ self-reaction experiment.....	202
6. Oxygen-dependent ketene (CH ₂ CO) formation from CH ₃ C(O)O ₂ self-reaction experiment	203
7. Experimental and simulated kinetics for the CH ₃ C(O)O ₂ + HO ₂ cross-reaction	204
8. Fitted rate coefficients for the acetic acid and radical channels	205

Tables

1. Literature results for the branching fractions of the three product channels of reaction of CH ₃ C(O)O ₂ with HO ₂	206
2. Kinetics model.....	207
3. Photoionization spectrum for CH ₃ O ₂ and CH ₃ OOH.....	209

Chapter VIII: Design and performance of a temperature controlled flow reactor for low-temperature radical kinetics

Figures

1. Conceptualization of cooled temperature-controlled flow reactor for low-temperature kinetics experiments.....	221
2. Drawing of the inner flow tube of the low-temperature reactor	222
3. Outer tube of temperature-controlled flow tube.....	223
4. Photograph of the pinhole region of the low-temperature flow tube.	224
5. Overall drawing of Okumura group temperature-controlled tube	225
6. Photograph of final assembled low-temperature flow reactor	226
7. Temperature stability of low-temperature flow reactor without active feedback.....	227
8. Temperature profile along the vertical axis of the cooled flow tube.	228
9. Photograph of PID-controlled heating of low-temperature tube	229

10. Schematic of PID controlled-heater	230
11. Temperature stability of PID-controlled reactor.....	231
12. Neutral and cation structures for one H ₂ O ₄ structure	232
13. The relative signal at <i>m/z</i> 66, with decreasing temperature.....	233
14. The photoionization spectrum of <i>m/z</i> 66.....	234
15. Room temperature HO ₂ + HO ₂ kinetics carried out in the temperature- controlled flow tube.....	235
16. HO ₂ + HO ₂ kinetics measured at -20 °C	236

Tables

1. Flow reactor temperatures achieved for various liquid nitrogen coolant flow rates.....	235
2. Temperature-dependent rate constants in the HO ₂ + HO ₂ reaction system	238

Chapter IX: Experimental measurement of the rate coefficient for reaction of the simplest Criegee CH₂OO with ozone

Figures

1. Kinetics traces for CH ₂ OO and IO formed from reaction of O(³ P) with CH ₂ I ₂	253
2. Dependence of CH ₂ OO and IO formation rates on [CH ₂ I ₂].....	254
3. Kinetics traces for CH ₂ OO formed from reaction of O(³ P) with CH ₂ I ₂	255
4. Ozone dependence of the CH ₂ OO decay rates	256
5. Absorption cross sections of relevant species present during experiments that absorb between 300–440 nm.....	257
6. Two-dimensional images showing the time-dependence of the spectrum during CH ₂ OO + CH ₂ OO experiments.....	258
7. One-dimensional images showing the experimental and modeled spectrum of the CH ₂ OO self-reaction	259
8. CH ₂ OO self-reaction kinetics traces for CH ₂ OO and IO formed during CH ₂ I ₂ photolysis in the presence of O ₂	260
9. The four simulated spectra of absorbers in the CH ₂ OO + O ₃ experiment	261
10. Two-dimensional plots of the (a) experimental and (b) simulated time- dependent spectra obtained during CH ₂ OO + O ₃ experiments	262
11. Experimental and simulated kinetics of CH ₂ OO and IO in CH ₂ OO + O ₃ experiments	263
12. Assessment of the perturbation to CH ₂ OO fits cause by absorption of other species like IO and CH ₂ I ₂	264

Tables

1. Kinetics model	265
-------------------------	-----

Appendix A: Changes made to the pulsed cavity ringdown apparatus after moving from Noyes to Linde+Robinson

Figures

1. Example of data collected for kinetics measurements that measured the decay of a spectral feature..... 274
2. Front panel of the kinetics acquisition Labview program..... 275
3. DAQ conversion program..... 276
4. Front panel of the Labview program that moves the dye laser grating 277
5. Labview Library File..... 278

Appendix B: Predicting vibrationally-resolved A–X electronic and photoionization spectra using quantum chemical methods**Figures**

1. Definition of α and β torsion angles in the chloro-ethyl peroxy radical 286
2. Chloro-ethyl peroxy radical ground state potential energy surface ... 287
3. Chloro-ethyl peroxy radical A state potential energy surface..... 288
4. Example Gaussian 09 input file for requesting a DFT-B3LYP/aug-cc-pVDZ ground state geometry optimization and frequency calculation 289
5. Example Gaussian 09 input file for requesting a TD-DFT-B3LYP/aug-cc-pVDZ excited state geometry optimization and frequency calculation 290
6. Example CFOUR input file for requesting a CCSD/aug-cc-pVDZ ground state geometry optimization 291
7. Example CFOUR input file for requesting an EOMEE-CCSD/aug-cc-pVDZ excited state geometry optimization..... 292
8. Example Gaussian 09 input file for requesting a Franck-Condon spectrum..... 293
9. A portion of the output of FCHT calculation 294
10. Optimized global minimum $C_2H_5OOC_2H_5$ neutral and cation structures 295

Tables

1. Comparison of ethyl peroxy radical past experiment and theory with results of methods described in this work..... 296

Chapter 1

INTRODUCTION

The atmosphere is a fascinating chemical reactor.¹⁻³ The vast majority of species in the atmosphere are chemically inert in the lower atmosphere (troposphere and stratosphere), yet the complexity of trace reactive species makes modeling atmospheric concentrations surprisingly complicated. Four processes control the concentrations of these species in Earth's atmosphere: emissions, chemistry, transport, and deposition. Box models incorporate these processes with various levels of complexity in order to model the atmospheric composition on a local or global scale.

In this thesis we present several experiments that were undertaken with the ultimate goal of providing a better understanding of several classes of chemical reactions that are important to atmospheric chemistry. We employed three experimental techniques: near-infrared pulsed cavity ringdown spectroscopy, multiplexed photoionization mass spectrometry, and time-resolved broadband cavity enhanced absorption spectroscopy. We supported these experiments computationally with numerical simulations for the complex chemical kinetics systems, as well as quantum chemical calculations for the spectroscopic studies.

Technique 1: Near-Infrared Pulsed Cavity Ringdown Spectroscopy

In Chapters 2 and 3, we present the near-infrared A–X electronic transition spectra of peroxy radicals formed during chlorine-initiated oxidation of unsaturated hydrocarbons. These experiments were carried out at Caltech using near-infrared pulsed cavity ringdown spectroscopy (this apparatus has been described in detail in previous theses).^{4,5} In Chapter 2, we measured the spectra for peroxy radicals from oxidation of small monounsaturated precursors—ethene, propene, 2-butene, 3-methyl-1-butene, and 2-methyl-3-buten-2-ol. We used electronic structure calculations to assign the spectra of the chloro-ethyl peroxy radical, identifying four unique rotational isomers whose distinct spectral features appear in the experimental spectrum. A similar study was made of the chloro-propyl peroxy radical. In

Chapter 3, we measured the spectrum for the peroxy radical mixture formed during chlorine-initiated oxidation of arguably the most important biogenic emission, isoprene, and investigated its spectrum using electronic structure theory.

Technique 2: Multiplexed Photoionization Mass Spectrometry

Chapters 4 through 8 all document experiments that were carried out as part of a large collaboration between Caltech, Sandia National Laboratories (SNL), Lawrence Berkeley National Laboratory (LBNL), and the NASA Jet Propulsion Laboratory. These experiments used synchrotron vacuum ultraviolet radiation from the Advanced Light Source at LBNL to selectively ionize species that were being created or destroyed in photochemical experiments. Using the sensitive time-resolved Multiplexed Photoionization Mass Spectrometer (MPIMS)⁶⁻⁸ created by SNL, we undertook several kinetics studies of interest to both atmospheric and combustion chemistry. In order to quantitatively detect the radical intermediates in hydrocarbon oxidation studies, we first measured the absolute photoionization cross sections of several species: HO₂, H₂O₂, and H₂CO (Chapter 4), and OH (Chapter 5). These species are central to atmospheric and combustion chemistry; measuring their absolute photoionization cross sections enables quantitative measurements of their gas phase number densities in a wide range of environments.

Chapters 6 and 7 address two important sets of chemical reactions. The first investigated the product branching for the ethyl peroxy radical self-reactions. This reaction is an important prototypical reaction used in large scale chemical kinetics box models as representative of all alkyl peroxy radical self-reactions. We sought to clear up a discrepancy in the literature regarding the products of this reaction. Chapter 7 looked at the acetyl peroxy radical reaction system as a whole – identifying the products of the reaction between acetyl radicals and oxygen molecules, as well as quantifying the yields of individual product channels in reactions between the acetyl peroxy radical and HO₂. As an intermediate in the isoprene oxidation mechanism, we wanted to address literature discrepancies regarding acetyl peroxy radicals and their penchant for recycling OH radicals in the atmosphere.

The final chapter of this section, Chapter 8, describes the construction of a low-temperature flow reactor that was incorporated into the existing MPIMS instrument for use in investigating temperature-dependent radical rate constants and products below room temperature. Details of the design, implementation, and testing of the low-temperature flow reactor are laid out here.

Technique 3: Time-Resolved Broadband Cavity-Enhanced Absorption Spectroscopy

The final chapter of this thesis, Chapter 9, describes a separate set of experiments carried out in collaboration with SNL,⁹⁻¹⁰ using the time-resolved broadband cavity-enhanced absorption spectrometer located in the Combustion Research Facility. This instrument is well-suited to detect the Criegee intermediate, a once-elusive species that forms in the atmosphere during ozone reactions with unsaturated hydrocarbons. In this chapter, we describe experiments that indicated that reaction of ozone with the smallest Criegee intermediate, CH₂OO is quite rapid, and that this reaction contributes to Criegee intermediate removal in environmental chamber studies where ozone concentrations are quite high.

References

1. Finlayson-Pitts, B. J.; Pitts, J., James N., *Chemistry of the Upper and Lower Atmosphere*. Academic Press: San Diego, California, 2000.
2. Seinfeld, J. H.; Pandis, S. N., *Atmospheric Chemistry and Physics: From Air Pollution to Climate Change*. Wiley: New York, 2006.
3. Jacob, D. J., *Introduction to Atmospheric Chemistry*. Princeton University Press: Princeton, NJ, 1999.
4. Deev, A. Cavity Ringdown Spectroscopy of Atmospherically Important Radicals. Dissertation (Ph.D.), California Institute of Technology, 2005. <http://resolver.caltech.edu/CaltechETD:etd-03172005-154741>
5. Takematsu, K. Cavity Ringdown Spectroscopy of the Nitrate and Peroxy Radicals. Dissertation (Ph.D.), California Institute of Technology, 2011. <http://resolver.caltech.edu/CaltechTHESIS:06012011-114553466>
6. Osborn, D. L.; Zou, P.; Johnsen, H.; Hayden, C. C.; Taatjes, C. A.; Knyazev, V. D.; North, S. W.; Peterka, D. S.; Ahmed, M.; Leone, S. R., The Multiplexed Chemical Kinetic Photoionization Mass Spectrometer: A New Approach to Isomer-Resolved Chemical Kinetics. *Rev. Sci. Instrum.* **2008**, *79*, 104103.

7. Taatjes, C. A.; Hansen, N.; Osborn, D. L.; Kohse-Hoinghaus, K.; Cool, T. A.; Westmoreland, P. R., "Imaging" Combustion Chemistry via Multiplexed Synchrotron-Photoionization Mass Spectrometry. *Phys. Chem. Chem. Phys.* **2008**, *10*, 20-34.

8. Dodson, L. G.; Shen, L.; Savee, J. D.; Eddingsaas, N. C.; Welz, O.; Taatjes, C. A.; Osborn, D. L.; Sander, S. P.; Okumura, M., VUV Photoionization Cross Sections of HO₂, H₂O₂, and H₂CO. *J. Phys. Chem. A* **2015**, *119*, 1279-1291.

9. Sheps, L., Absolute Ultraviolet Absorption Spectrum of a Criegee Intermediate CH₂OO. *J. Phys. Chem. Lett.* **2013**, *4*, 4201-4205.

10. Sheps, L.; Chandler, D. W., *Time-Resolved Broadband Cavity-Enhanced Absorption Spectroscopy for Chemical Kinetics*. SAND2013-2664, Sandia National Laboratories, Livermore, CA, 2013.

*Chapter 2***OBSERVATION AND ASSIGNMENT OF THE A–X ELECTRONIC TRANSITION OF CHLORINE-SUBSTITUTED HYDROCARBON PEROXY RADICALS****Abstract**

Presented here are the origin and excited state vibrations of the A–X electronic transitions in the near-infrared for the peroxy radicals formed from chlorine-initiated oxidation of alkenes in the presence of oxygen. Using pulsed cavity-ringdown spectroscopy, we directly observed the origin frequencies around 7300 cm^{-1} , and the C–O–O bend and O–O stretch vibrations of the excited state $300\text{--}400$ and 1000 cm^{-1} , respectively, shifted from the origin. Using quantum chemistry, we predicted the ground and excited state conformations of the chloro-ethyl peroxy radical and chloro-propyl peroxy radical and assign the spectra.

1 Introduction

Oxidation of hydrocarbons in the atmosphere leads to formation of peroxy radical intermediates, which play a central role in atmospheric chemistry.¹ When a free radical attacks a hydrocarbon, the new carbon-centered radical is susceptible to association with O₂. In the case of alkenyl hydrocarbons, the initial free radical can add to the double bond and the final O₂ addition occurs on the β position. The resulting β -substituted peroxy radicals can have different reactivity and spectroscopy than their unsubstituted analogs.² In this work, we investigate the effect of a chlorine atom β to the peroxy moiety on the spectroscopy of hydrocarbons with C₂–C₄ backbones.

Biogenic emissions of volatile organic compounds result in high concentrations of unsaturated hydrocarbons in remote regions.³ There are also industrial sources of alkenes.⁴ Industrial emissions follow daily cycles due to industrial plant schedules. Oceans emit C₂–C₄ unsaturated hydrocarbons.⁵ Specific sources of ethene include emissions from vegetation, soil, and oceans, as well as industrial sources.⁴⁻⁵ 2-methyl-3-buten-2-ol (MBO-232) is an oxygenated volatile organic compound emitted by vegetation. Concentration has been found

6

to be comparable or higher than that of isoprene and monoterpenes over some forests. Concentrations follow a diurnal cycle, suggesting reactivity with oxidants (most likely OH).⁶⁻

7

Peroxy radicals have a strong A–X electronic transition in the ultraviolet that has long been used as a spectroscopic tool for kineticists who wish to quantify the fate of peroxy radicals in the atmosphere.⁸⁻¹¹ More recently, sensitive detection by cavity-enhanced spectroscopies has enabled investigations of the weak A–X electronic transition,¹²⁻²² leading to selective kinetics measurements.²³⁻²⁴

In order to assign the structured spectra of peroxy radicals in the near-infrared, we used quantum chemistry calculations on the substituted C2 and C3 peroxy radicals studied in this work.

2 Experimental

The A–X spectrum of the chloro-ethyl peroxy radical was measured experimentally using a near-infrared pulsed laser cavity ringdown spectrometer. The spectral features are identified using theoretical vibrationally-resolved adiabatic excitation spectra for the predicted rotational conformers.

2.1 Near-infrared pulsed laser cavity ringdown spectrometer

The near-infrared pulsed laser cavity ringdown spectrometer has been described elsewhere.²⁵⁻²⁶ Tunable visible light (575–655 nm) was generated from a dye laser (Lambda Physik) pumped by an Nd:YAG laser (Continuum). The laser dyes used were DCM, Rhodamine 640, and Rhodamine B. The dye laser output was collimated and passed through a 3-pass steel tube filled with hydrogen gas (>200 Psi). The desired near-infrared probe light (7000–9000 cm^{-1}) was generated by selecting the second order Stimulated Raman scattering of the tunable visible laser by the hydrogen gas.

The probe light was focused into a 50-cm long stainless-steel optical cavity through high reflectivity mirrors. Three sets of mirrors were used: Layertec 1390 nm, $R = 99.95\%$, LGR 1330 nm, $R = 99.99\%$, and LGR 1200 nm, $R = 99.999\%$. The cell is designed so that the gas

sample for interrogation flows through the center of the optical cavity. Purge gas (N_2) protects the cavity mirrors and constricts the sample gases to this region. The pulsed output of an excimer laser (Lambda Physik) was shaped by a cylindrical lens and entered the stainless-steel cell through quartz windows coated with a fluoropolymer (DuPont AF 400S2-100-1) before it intersected the reactant gases perpendicular to their flow to initiate radical formation. The timing between the excimer photolysis laser and the near-infrared probe laser was controlled by a digital delay generator.

The near-infrared probe laser was scanned to obtain the peroxy radical spectrum. The absorption at each wavelength was determined by measuring the ringdown decay time in the presence and absence of radical chemistry. An average ringdown decay time was computed from 30 laser pulses.

2.2 Radical production

The desired peroxy radicals were generated by chlorine-initiated oxidation of alkene precursors in the presence of oxygen. In general, a chlorine atom adds to the double bond in an alkene to form a chloro-substituted alkyl radical. O_2 adds to the chloro-alkyl radical, forming the chloro-substituted peroxy radical, which can be stabilized by collisions with the bath gas (N_2). Chlorine atoms were formed from the 351 nm photolysis of Cl_2 gas. The hydrocarbon precursor was diluted in N_2 and either supplied from pre-mixed gas cylinders or from a temperature-controlled bubbler. Experiments were conducted at room temperature with the following initial conditions $[\text{alkene}] = 1 \times 10^{16} \text{ cm}^{-3}$, $[\text{O}_2] = 4 \times 10^{17} \text{ cm}^{-3}$, $[\text{Cl}_2] = 3.5 \times 10^{16} \text{ cm}^{-3}$, and $[\text{N}_2] = 1.8 \times 10^{18} \text{ cm}^{-3}$. Each excimer laser pulse generated approximately 5×10^{14} chlorine atoms cm^{-3} .

2.3 Spectrum

To account for day-to-day fluctuations in the excimer photolysis laser power, we measured the spectrum of the ethyl peroxy radical each day. We scaled our data to the literature spectrum.^{14,16-17} Different spectral regions were collected using combinations of laser dyes and ringdown mirrors, so each region was scaled to the reported ethyl peroxy radical bands in that region. The spectral components were merged into one spectrum.

2.4 Quantum chemistry calculations

Chemical structures for the peroxy radicals formed from chlorine-initiated oxidation of ethene and propene were generated using quantum chemistry. First, we identified candidate structures through a relaxed minimum energy scan at B3LYP/6-31+G(d,p) of the X state across the two primary dihedral angles: α (C–C–O–O) and β (Cl–C–C–O). Conformers are labeled by the dihedral angles (T for a *trans* dihedral angle and G for a *gauche* dihedral angle). Local minima with ground state energies $< 3kT$ were further optimized using the G2 compound method. The A state potential energy surface (at TD-B3LYP/6-31+G(d,p)) did not differ significantly from the X state. The two major dihedral angles of the local minima generally varied less than 5% between the two states. For the chloro-propyl peroxy radical, a third dihedral angle (Cl–C–C–C) was considered in differentiating structures. Calculations were not attempted on the peroxy radicals with C4 backbones.

For the chloro-ethyl peroxy radical, we used the equation of motion excitation energy (EOMEE) method to obtain the A state energetics. We optimized the A state local minimum structures using EOMEE-CCSD/aug-cc-pVDZ calculations. The adiabatic 0–0 transition of each conformer was calculated compared to a reoptimization of the X state local minima at CCSD/aug-cc-pVDZ. The same electronic transition energies were computed for a reference molecule to obtain a scaling factor for use in obtaining the final origin transition energies for comparison with experiment (see Supporting Information).

Ground and excited state vibrations were calculated for each conformer at B3LYP/aug-cc-pVDZ. Using these frequencies, the Franck-Condon overlap was calculated for the origin transition and excitation to vibrational levels in the excited state. Vibrational frequencies were scaled by 0.970.²⁷ The origin intensities were scaled to 1, and each conformer was weighted by its Boltzmann factor (using the G2 method).

Density functional theory and G2 calculations were carried out using the Gaussian 09 computational chemistry program.²⁸ Coupled-cluster calculations were carried out using CFOUR, a quantum chemical program package.²⁹

3 Results and Discussion

Chlorine substitution of a β hydrogen atom on an alkyl peroxy radical leads to higher-energy electronic transitions as well as increasing the complexity of the system by increasing the number of structural isomers.

3.1 Peroxy radical spectra

Figure 2 shows the cavity ringdown spectra for the peroxy radicals formed upon chlorine-initiated oxidation of ethene and propene. Both spectra have the strongest absorption between 7300 and 7400 cm^{-1} ; the most intense peak in the chloro-ethyl peroxy radical is centered at 7353 cm^{-1} (50 cm^{-1} FWHM) and that of the chloro-propyl peroxy radical is centered at 7388 cm^{-1} (35 cm^{-1} FWHM). These features likely correspond to the A–X origin transition for the most-abundant peroxy radical conformer formed from the two hydrocarbons. Several other bands appear in the origin region, which we assigned using quantum chemistry (described below). The origin transition of these chlorine-substituted peroxy radicals is red-shifted compared to that of the fully-saturated ethyl peroxy radical (the strongest peak appears at 7596 cm^{-1})^{14,16-17} and that of the fully-saturated propyl peroxy radical (peaking at 7567 cm^{-1})^{13,21}. Typical peroxy radicals have absorptions corresponding to the C–O–O bend vibration and O–O stretch vibration of the \tilde{A} state, appearing above the origin transition around 500 cm^{-1} and 950 cm^{-1} , respectively.¹⁵ Both spectra in Figure 3 have strong features near 8400 cm^{-1} , likely belonging to the O–O stretch mode and weak intensity near 7800 cm^{-1} from the C–O–O bend. Figure 3 shows the cavity ringdown spectra for three peroxy radicals formed from a C4 backbone. The origin region of each spectrum, from about 7000–7750 cm^{-1} shows multiple overlapping peaks. Intensity drops around 8000 cm^{-1} before rising again in the O–O stretch region above 8000 cm^{-1} .

3.2 Assignment of the chloro-ethyl peroxy radical spectrum

The observed bands in the chloro-ethyl peroxy radical spectrum were assigned using quantum chemistry predictions of the A–X vibrationally-resolved spectrum. These computations were complicated by the presence of the three peroxy radical conformers with C_1 symmetries. In fact, the only conformer (TT) with C_s symmetry is not the global minimum, but actually has an X state energy greater than the other three conformers

considered here (+346 cm^{-1} compared to GT, at G2 level). Tarczay et al. faced a similar problem when assigning the peroxy radical spectra for 1- and 2-propyl peroxy radicals.¹³ We used similar methods in calculating electronic spectra; however, we chose to use the EOMEE, rather than the EOMIP method, which we discuss later.

3.2.a Origin Transitions

In the origin region of the experimental spectrum, we observed four distinct bands. The spectrum was fit as the sum of four Gaussian functions (listed in Table 1), each with a FWHM of 50 cm^{-1} . The difference in energy between the lowest energy transition and the highest energy transition is 240 cm^{-1} . Each band likely corresponds to a different chloro-ethyl peroxy radical conformer. To assign these bands, we identified four candidate structures from our ground state potential energy surface search (listed in Table 2, shown in Figure 4, equilibrium structures can be found in the Supporting Information). The conformer with the lowest X state energy was the GT conformer, with a CCOO dihedral angle of 73° and a ClCCO dihedral angle of 178°. The other three conformers have ground state energies within $2kT$ of the GT conformer. Table 2 lists the energy differences of the ground states for each conformer, relative to that of the GT conformer.

The A–X adiabatic electronic transitions calculated for the four conformers are listed in Table 1. These values are calculated using the EOMEE-CCSD method using a scaling factor determined from reference calculations on the ethyl peroxy radical. We scale the adiabatic electronic transition energy by the average scale factor needed to align the two calculated unsubstituted ethyl peroxy radical conformers with the experimentally-observed origin transitions.^{14,16-17} The scaling factor was very close to unity (0.956). The electronic transition energy for the global minimum chloro-ethyl peroxy radical GT conformer is the closest in energy to the most prominent peak in the experimental spectrum, falling only 9 cm^{-1} to the blue of the peak center. This is in good agreement with our assignment of the GT conformer as the global minimum structure.

In order to assess our choice of the EOMEE method for modeling excited states, we compared the performance of the method with high-level calculations on the chloro-ethyl

peroxy radical conformer with C_s symmetry. Again, we stress that this conformer is not the global minimum, but can be computed quite accurately for comparison. Specifically, we want to test the ability of the EOMEE method in predicting the structure of the conformer in the A state. Following the approach laid out by Tarczay et al.¹³ we investigated the A–X transitions and O–O bond lengths for the chloro-ethyl peroxy radical with C_s symmetry with different levels of theory by taking advantage of the symmetry differences between the A and X states in the C_s conformer. Table 3 demonstrates the method-dependence of several key results. The O–O bond length is an important metric in this analysis since the electronic excitation of X state peroxy radicals to the first excited A state involves orbitals localized on the O–O bond and a lengthening is usually observed in the distance between the two O atoms upon excitation.¹⁵ As seen by Tarczay et al., we calculate X state O–O bond lengths < 1.35 Å for all methods. For the A state, as the level of correlation increases, the A state O–O bond length converges to a value < 1.40 Å, with predicted A–X excitation energies becoming closer to the origin transitions observed in experiments. The EOMIP method used by Tarczay et al. significantly underestimates the O–O bond length for the A state. However, in this work, EOMEE calculations predict an A state O–O bond length for C_s chloro-ethyl peroxy radicals of 1.406 Å, in much better agreement with expected values. We are therefore confident in our use of EOMEE calculations to predict the A–X spectrum of the C_1 chloro-ethyl peroxy radicals studied in this work.

3.2.b Vibrational Structure

The A–X spectra of peroxy radicals typically exhibit excitations to vibrationally-excited electronic states—specifically exciting C–O–O bend and O–O stretch modes of the excited state which appear 500 and 950 cm^{-1} shifted from the origin.¹⁵ Using DFT and TD-DFT optimized geometries, we computed the vibrational harmonic frequencies of the X and A states at B3LYP/aug-cc-pVDZ (listed in the Supporting Information). The A state C–O–O bend and O–O stretch frequencies are listed in Table 1, scaled by 0.970.²⁷ For the chloro-ethyl peroxy radical, the C–O–O bend vibrations are lower in energy (with A state frequencies closer to 300–400 cm^{-1}) for all conformers than the corresponding vibration in alkyl peroxy radicals. The O–O stretch vibrations are slightly higher-energy (A state

frequencies of 1000 cm^{-1}) than those of alkyl peroxy radicals. This is the same trend observed by Zalyubovsky et al. in their investigation of the fluorinated peroxy radical, CF_3O_2 .¹² They computed CF_3O_2 A state C–O–O bend and O–O stretch frequencies of 256 and 1048 cm^{-1} , respectively.

The simulated Franck-Condon spectra are shown in Figure 5. The overlap integral for each origin transition was assumed to be equal, and then each spectrum was scaled by the Boltzmann populations of the four conformers, as determined from the X state G2 energies. The peaks observed in the experimental spectrum between 7700 and 8000 cm^{-1} are assigned to excitations directly to the C–O–O bend vibration of the A state. The C–O–O bend of the GT and GG conformers contribute the most intensity in this region. The O–O stretch modes of all four conformers contribute to several peaks above 8000 cm^{-1} , with some intensity contributed by several other active modes. The Franck-Condon spectra also help us to assign the small feature centered at 7592 cm^{-1} . This is not the origin transition of an unidentified conformer—it is excitation of the GT conformer directly to the ClCCO backbone rock, which is active due to significant changes in the GT backbone structure.

The position of the O–O stretch modes does not align as well with the most intense peaks of the O–O region. Previous work by the Miller group (see e.g. Rupper et al.¹⁴) observed similar trends, often scaling the O–O stretch modes by a slightly smaller scale factor (0.84 compared to the expected 0.97) to account for large anharmonicities in the O–O stretch vibration.

3.3 Assignment of the chloro-propyl peroxy spectrum

The origin region of the chloro-propyl peroxy radical spectrum can be fit with the sum of ten Gaussian functions (Figure 2). These bands likely each correspond to the origin transitions of different isomers and conformers. Two structural isomers form from chlorine-initiated oxidation of propene, since the chlorine atom can either add to the terminal carbon atom or the secondary carbon. We generated the potential energy surface for the X and A states of both 1-chloro propyl peroxy radical and 2-chloro propyl peroxy radical. We investigated only those conformers with ground state energies within $< 3 k_B T$ ($\sim 600\text{ cm}^{-1}$) of the global minimum conformation for each of the two structural isomers. We investigated 7 conformers

of 1-chloro propyl peroxy and 7 conformers of 2-chloro propyl peroxy, shown in Figure 6. The ground state energy differences for the two structural isomers are reported in Table 2. The global minimum 1-chloro propyl peroxy radical conformer (GTG) is more stable than the 2-chloro propyl peroxy minimum conformer (GTG) by 307 cm^{-1} . The allylic peroxy radical, formed by an addition-elimination reaction rather than addition of the chlorine atom has been studied previously.²² Very few (13%) of the peroxy radicals from reaction of chlorine with propene will form the allylic peroxy radical.³⁰ Lee and Rowland demonstrated more favorable addition to the terminal carbon atom in chlorine atom reactions with propene (with a ratio of terminal:central of 6:1).³¹ Competition between isomerization of the chlorine adduct and O_2 addition further weights the contribution to the spectrum in favor of the 1-chloro propyl peroxy radical.

Table 4 lists the center frequencies of each peak in the experimental spectrum, along with calculated A–X electronic transitions for the 14 chloro propyl peroxy radical conformers. Figure 7 presents the experimental spectrum, along with the theoretical spectrum generated taking into account Franck-Condon factors for both the 1-chloro and 2-chloro propyl peroxy radicals. Origin transitions were normalized and then weighted by the partition functions computed using the G2 method. 2-chloro propyl peroxy transitions were further weighted by $1/6^{\text{th}}$, to account for the initial partitioning of the Cl-addition. The most intense peak in the experimental spectrum appears at 7387 cm^{-1} ; this agrees well with the global minimum 1-chloro propyl peroxy radical conformer (GTG), which is computed to have an adiabatic A–X electronic transition energy of 7382 cm^{-1} . Several other peaks appear in the origin region—most of which can be assigned to other 1-chloro propyl peroxy radical conformers. However, we note that the peaks appearing to the blue of most intense peak likely do not belong to the 1-chloro propyl peroxy radical, but appear to have origin transitions closer to that expected for the global minimum 2-chloro propyl peroxy radical conformer (GTG).

3.4 Assignment of the spectra of peroxy radicals with C4 backbones

We did not attempt to calculate the structures of the peroxy radicals formed from chlorine-initiated oxidation of 2-butene, 3-methyl-1-butene, or 2-methyl-3-buten-2-ol (MBO-232) because the number of possible conformers and isomers becomes prohibitively large with

these molecules. We note, however, that the peroxy radicals formed from these three alkenes (shown in Figure 3) share the same characteristics as those for the C1 and C2 peroxy radicals studied in this work. The origin region is crowded with several overlapping peaks between 7000–7750 cm^{-1} . Intensity decreases around 8000 cm^{-1} , with evidence for some structure that likely corresponds to excitation of C–O–O bending modes in the excited state. Then, above 8000 cm^{-1} , intensity rises again in the region typically assigned to excitation of the O–O stretch.

In 2-butene, we observe three distinct peaks in the origin region, centered at 7365, 7479, and 7594 cm^{-1} . This pattern is repeated in the O–O stretch region, with three peaks appearing at 8275, 8401, and 8532 cm^{-1} . The three O–O vibrations probably correspond to the same conformer or isomer as the three absorbers in the origin region.

The origin region of 3-methyl-1-butene has several overlapping features, but the most notable is the sharp, intense feature centered at 7533 cm^{-1} . This spectral feature is reminiscent of the sharp features observed in the origin region of allylic peroxy radical. Hydrogen abstraction of the hydrogen atom on the C3 carbon atom would lead to a stable tertiary radical site, which could ultimately form the allylic peroxy radical.

The spectrum of MBO-232 is highly congested, leading to absorption throughout the entire spectral region covered in this experiment.

4 Conclusions

The chlorine-substituted peroxy radicals studied in this work have characteristic spectra in the near-infrared. The appearance of several bands in the origin region of each spectrum indicated the presence of multiple conformers and isomers that form upon chlorine-initiated oxidation of alkenes. Much like previous work on fluorine-substituted peroxy radicals, we observed a red-shift in the position of the A–X electronic transition upon β -substitution of the peroxy radical with an electron-withdrawing halogen—however, not to the extent of the more-electrophilic fluorine atom.¹²

5 References

1. Wallington, T. J.; Nielsen, O. J., Peroxy Radicals and the Atmosphere. In *Peroxy Radicals*, Alfassi, Z. B., Ed. John Wiley & Sons Ltd: West Sussex, England, 1997.
2. Orlando, J. J.; Tyndall, G. S., Laboratory Studies of Organic Peroxy Radical Chemistry: An Overview with Emphasis on Recent Issues of Atmospheric Significance. *Chem. Soc. Rev.* **2012**, *41*, 6294-6317.
3. Finlayson-Pitts, B. J.; Pitts, J., James N., *Chemistry of the Upper and Lower Atmosphere*. Academic Press: San Diego, California, 2000.
4. Johansson, J. K. E.; Mellqvist, J.; Samuelsson, J.; Offerle, B.; Lefer, B.; Rappenglück, B.; Flynn, J.; Yarwood, G., Emission Measurements of Alkenes, Alkanes, SO₂, and NO₂ from Stationary Sources in Southeast Texas Over a 5 Year Period Using SOF and Mobile DOAS. *J. Geophys. Res.: Atmos.* **2014**, *119*, 1973-1991.
5. Kesselmeier, J.; Staudt, M., Biogenic Volatile Organic Compounds (VOC): An Overview on Emission, Physiology and Ecology. *J. Atmos. Chem.* **1999**, *33*, 23-88.
6. Goldan, P. D.; Kuster, W. C.; Fehsenfeld, F. C.; Montzka, S. A., The Observation of a C5 Alcohol Emission in a North American Pine Forest. *Geophys. Res. Lett.* **1993**, *20*, 1039-1042.
7. Schade, G. W.; Goldstein, A. H., Fluxes of Oxygenated Volatile Organic Compounds from a Ponderosa Pine Plantation. *J. Geophys. Res.: Atmos.* **2001**, *106*, 3111-3123.
8. Lightfoot, P. D.; Cox, R. A.; Crowley, J. N.; Destriau, M.; Hayman, G. D.; Jenkin, M. E.; Moortgat, G. K.; Zabel, F., Organic Peroxy Radicals: Kinetics, Spectroscopy and Tropospheric Chemistry. *Atmos. Environ., Part A* **1992**, *26*, 1805-1961.
9. Wallington, T. J.; Dagaut, P.; Kurylo, M. J., UV Absorption Cross Sections and Reaction Kinetics and Mechanisms for Peroxy Radicals in the Gas Phase. *Chem. Rev.* **1992**, *92*, 667-710.
10. Nielsen, O. J.; Wallington, T. J., Ultraviolet Absorption Spectra of Peroxy Radicals in the Gas Phase. In *Peroxy Radicals*, Alfassi, Z. B., Ed. John Wiley & Sons Ltd.: New York, NY, 1997; pp 69-80.
11. Miller, T. A., Spectroscopic Probing and Diagnostics of the Geometric Structure of the Alkoxy and Alkyl Peroxy Radical Intermediates. *Mol. Phys.* **2006**, *104*, 2581-2593.
12. Zalyubovsky, S. J.; Wang, D.; Miller, T. A., Observation of the $\tilde{A}-\tilde{X}$ electronic transition of the CF₃O₂ radical. *Chem. Phys. Lett.* **2001**, *335*, 298-304.
13. Tarczay, G.; Zalyubovsky, S. J.; Miller, T. A., Conformational analysis of the 1- and 2-propyl peroxy radicals. *Chem. Phys. Lett.* **2005**, *406*, 81-89.
14. Rupper, P.; Sharp, E. N.; Tarczay, G.; Miller, T. A., Investigation of Ethyl Peroxy Radical Conformers via Cavity Ringdown Spectroscopy of the $\tilde{A}-\tilde{X}$ Electronic Transition. *J. Phys. Chem. A* **2007**, *111*, 832-840.
15. Sharp, E. N.; Rupper, P.; Miller, T. A., The Structure and Spectra of Organic Peroxy Radicals. *Phys. Chem. Chem. Phys.* **2008**, *10*, 3955-3981.

16. Just, G. M. P.; Rupper, P.; Miller, T. A.; Meerts, W. L., High-resolution Cavity Ringdown Spectroscopy of the Jet-cooled Ethyl Peroxy Radical $C_2H_5O_2$. *J. Chem. Phys.* **2009**, *131*, 184303.
17. Melnik, D.; Chhantyal-Pun, R.; Miller, T. A., Measurements of the Absolute Absorption Cross Sections of the $\tilde{A} \leftarrow \tilde{X}$ Transition in Organic Peroxy Radicals by Dual-Wavelength Cavity Ring-Down Spectroscopy. *J. Phys. Chem. A* **2010**, *114*, 11583-11594.
18. Sprague, M. K.; Garland, E. R.; Mollner, A. K.; Bloss, C.; Bean, B. D.; Weichman, M. L.; Mertens, L. A.; Okumura, M.; Sander, S. P., Kinetics of *n*-Butoxy and 2-Pentoxy Isomerization and Detection of Primary Products by Infrared Cavity Ringdown Spectroscopy. *J. Phys. Chem. A* **2012**, *116*, 6327-6340.
19. Sprague, M. K.; Mertens, L. A.; Widgren, H. N.; Okumura, M.; Sander, S. P.; McCoy, A. B., Cavity Ringdown Spectroscopy of the Hydroxy-Methyl-Peroxy Radical. *J. Phys. Chem. A* **2013**, *117*, 10006-10017.
20. Kline, N. D.; Miller, T. A., Observation of the Electronic Transition of C_6 - C_{10} Peroxy Radicals. *Chem. Phys. Lett.* **2014**, *601*, 149-154.
21. Zalyubovsky, S. J.; Glover, B. G.; Miller, T. A.; Hayes, C.; Merle, J. K.; Hadad, C. M., Observation of the $\tilde{A} \leftarrow \tilde{X}$ Electronic Transition of the 1- $C_3H_7O_2$ and 2- $C_3H_7O_2$ Radicals Using Cavity Ringdown Spectroscopy. *J. Phys. Chem. A* **2005**, *109*, 1308-1315.
22. Thomas, P. S.; Miller, T. A., Cavity Ringdown Spectroscopy of the NIR Electronic Transition of Allyl Peroxy Radical ($H_2C=CH-CH_2OO\cdot$). *Chem. Phys. Lett.* **2010**, *491*, 123-131.
23. Atkinson, D. B.; Spillman, J. L., Alkyl Peroxy Radical Kinetics Measured Using Near-infrared CW-Cavity Ring-down Spectroscopy. *J. Phys. Chem. A* **2002**, *106*, 8891-8902.
24. Melnik, D.; Miller, T. A., Kinetic Measurements of the $C_2H_5O_2$ Radical Using Time-resolved Cavity Ring-down Spectroscopy with a Continuous Source. *J. Chem. Phys.* **2013**, *139*, 094201.
25. Deev, A.; Sommar, J.; Okumura, M., Cavity Ringdown Spectrum of the Forbidden $\tilde{A}^2E'' \leftarrow \tilde{X}^2A'_2$ Transition of NO_3 : Evidence for Static Jahn-Teller Distortion in the \tilde{A} State. *J. Chem. Phys.* **2005**, *122*, 224305.
26. Takematsu, K.; Eddingsaas, N. C.; Robichaud, D. J.; Okumura, M., Spectroscopic Studies of the Jahn-Teller Effect in the \tilde{A}^2E'' State of the Nitrate Radical NO_3 . *Chem. Phys. Lett.* **2013**, *555*, 57-63.
27. Johnson III, R. D., NIST Computational Chemistry Comparison and Benchmark Database. NIST Standard Reference Database Number 101, Release 17b, September 2015.
28. Frisch, M. J.; Trucks, G. W.; Schlegel, H. B.; Scuseria, G. E.; Robb, M. A.; Cheeseman, J. R.; Scalmani, G.; Barone, V.; Mennucci, B.; Petersson, G. A., et al. *Gaussian 09*, Revision E.01; Gaussian, Inc.: Wallingford CT, 2009.
29. Stanton, J. F.; Gauss, J.; Harding, M. E.; Szalay, P. G. *CFOUR*, with contributions from Auer, A. A.; Bartlett, R. J.; Benedikt, U.; Berger, C.; Bernholdt, D. E.; Bomble, Y. J.; Cheng, L.; Christiansen, O.; Heckert, M.; Heun, O., et al. and the integral packages MOLECULE (Almlöf, J. and Taylor, P. R.), PROPS (Taylor, P. R.), ABACUS (Helgaker, T.; Jensen, H. J. Aa.; Jørgensen, P. and Olsen, J.), and ECP routines A. V. Mitin, A. V. and van Wüllen, C.

30. Ezell, M. J.; Wang, W.; Ezell, A. A.; Soskin, G.; Finlayson-Pitts, B. J., Kinetics of Reactions of Chlorine Atoms with a Series of Alkenes at 1 atm and 298 K: Structure and Reactivity. *Phys. Chem. Chem. Phys.* **2002**, *4*, 5813-5820.

31. Lee, F. S. C.; Rowland, F. S., Thermal Chlorine-38 Reactions with Propene. *J. Phys. Chem.* **1977**, *81*, 1222-1229.

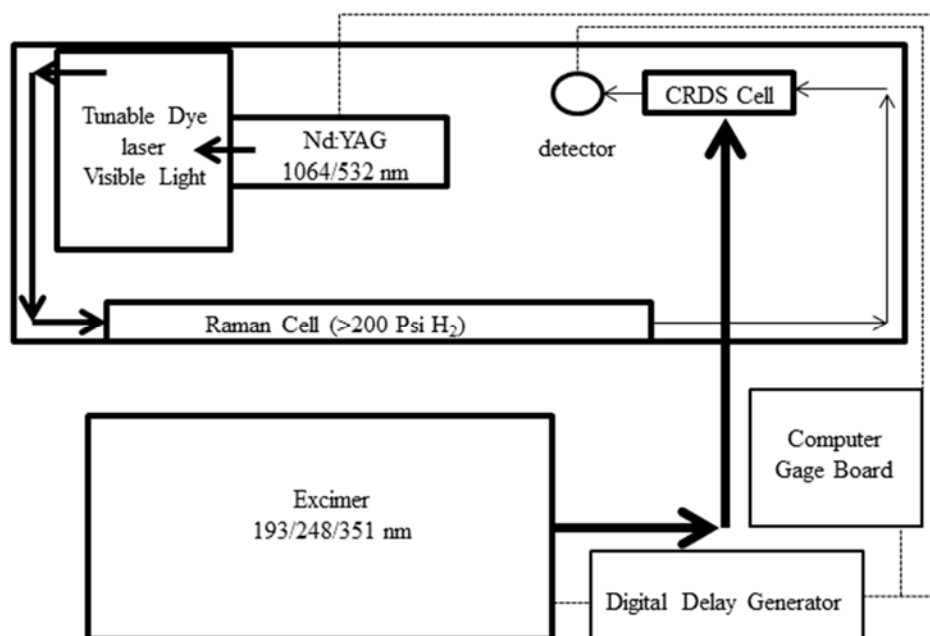


Figure 1. Pulsed cavity ringdown instrument schematic.

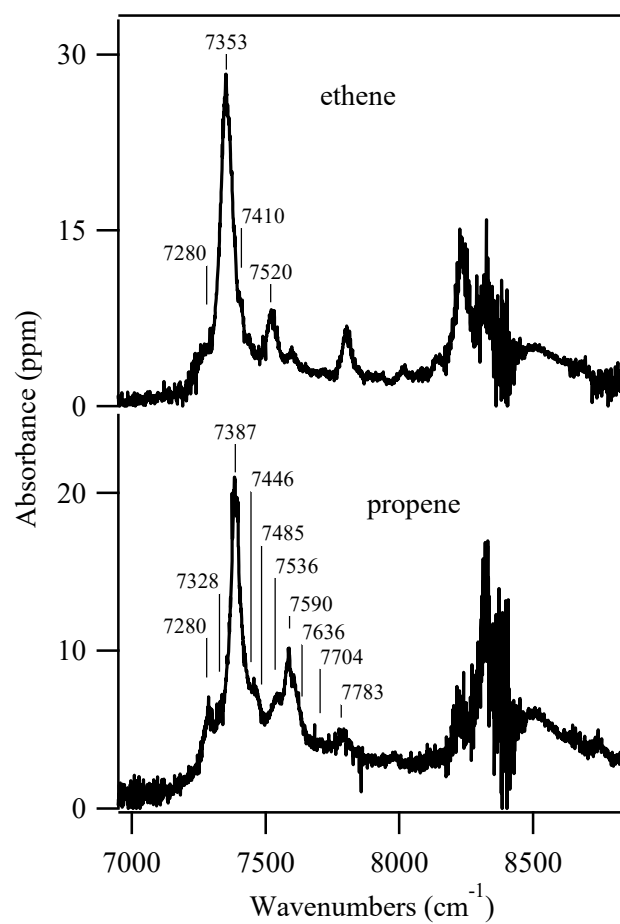


Figure 2. Near-infrared cavity ringdown spectrum of the peroxy radicals formed from simple alkenes. The top panel shows the experimental spectrum collected during chlorine-initiated oxidation of ethene. The bottom panel shows the experimental spectrum collected during chlorine-initiated oxidation of propene. The origin regions have been fit as a sum of Gaussian functions.

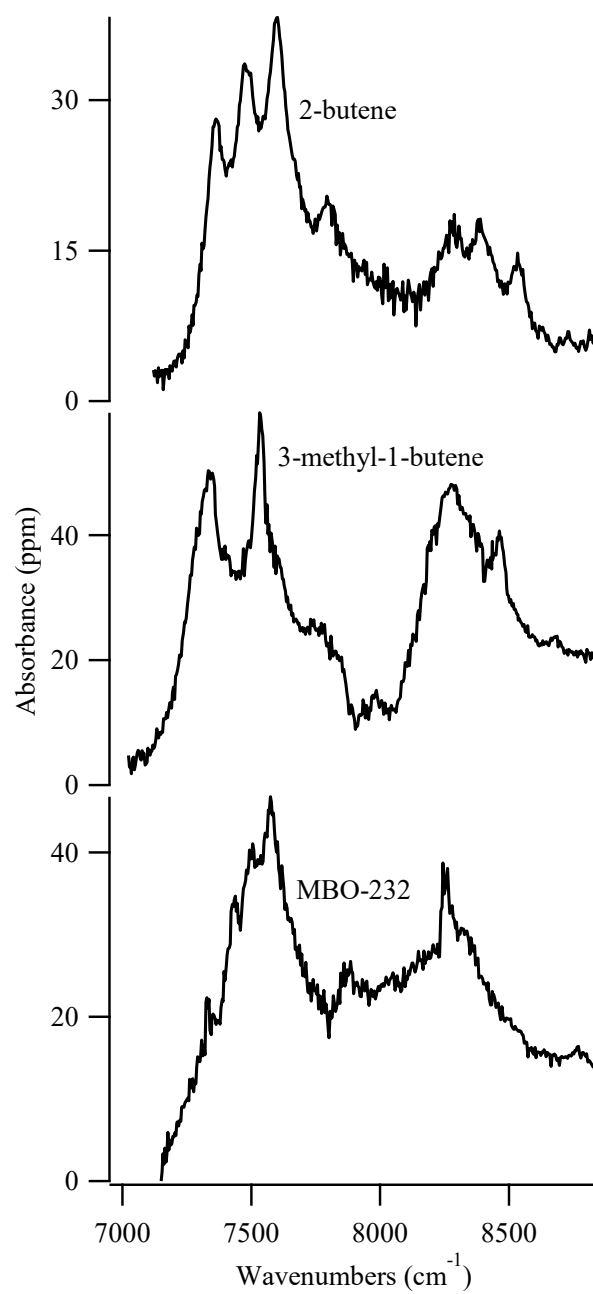


Figure 3. Near-infrared cavity ringdown spectrum of the peroxy radicals formed from alkenes with C4 backbones. The panels show the peroxy radicals formed by chlorine-initiated oxidation of (top) 2-butene, (middle) 3-methyl-1-butene, (bottom) MBO-232.

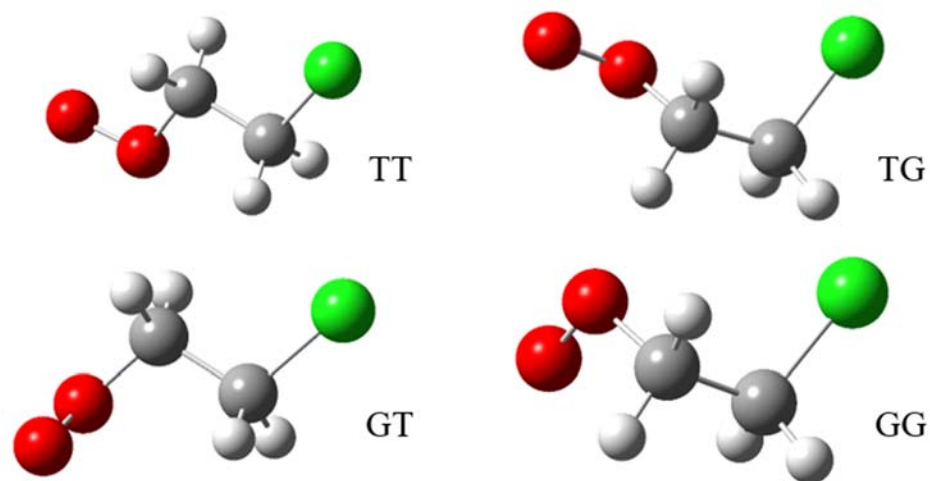


Figure 4. Geometries of the four unique conformers of the chloroethyl peroxy radical. The labels indicate the C-C-O-O and Cl-C-C-O dihedral angles, respectively, as *trans* (T) or *gauche* (G).

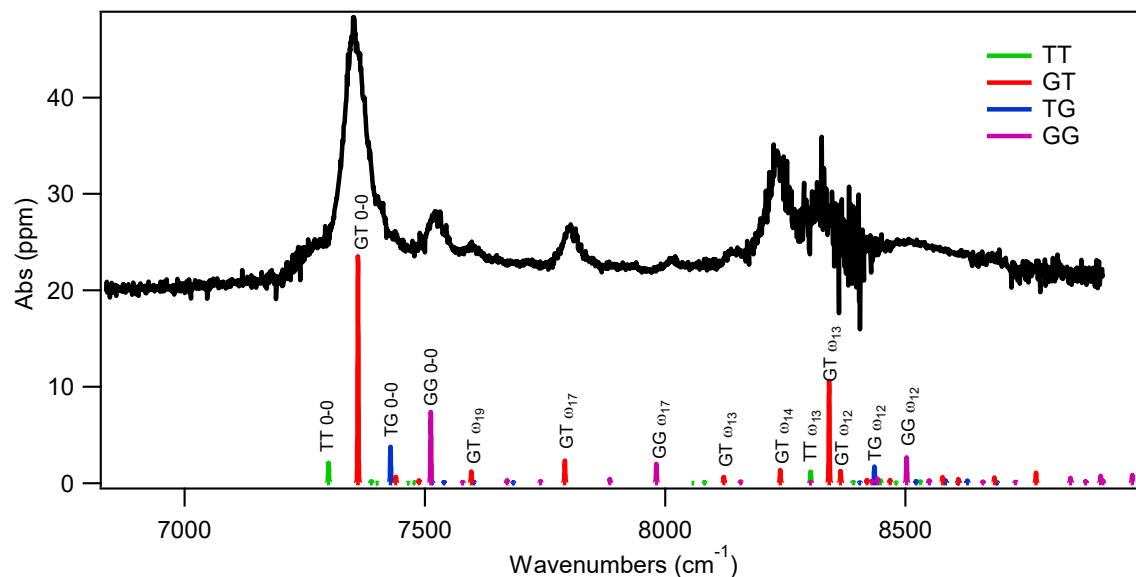


Figure 5. Experimental spectrum of the A–X electronic transition of chloro-ethyl peroxy radical (offset in the y-direction by 20 ppm) along with the computed Franck-Condon spectra of the four local minimum structures. The origin transitions were set to the values obtained at EOMEE-CCSD/aug-cc-pVDZ. The Franck-Condon spectrum was simulated from normal modes computed at TD-B3LYP/aug-cc-pVDZ, with frequencies scaled by 0.970. Intensities were weighted by Boltzmann factors computed using the G2 method.

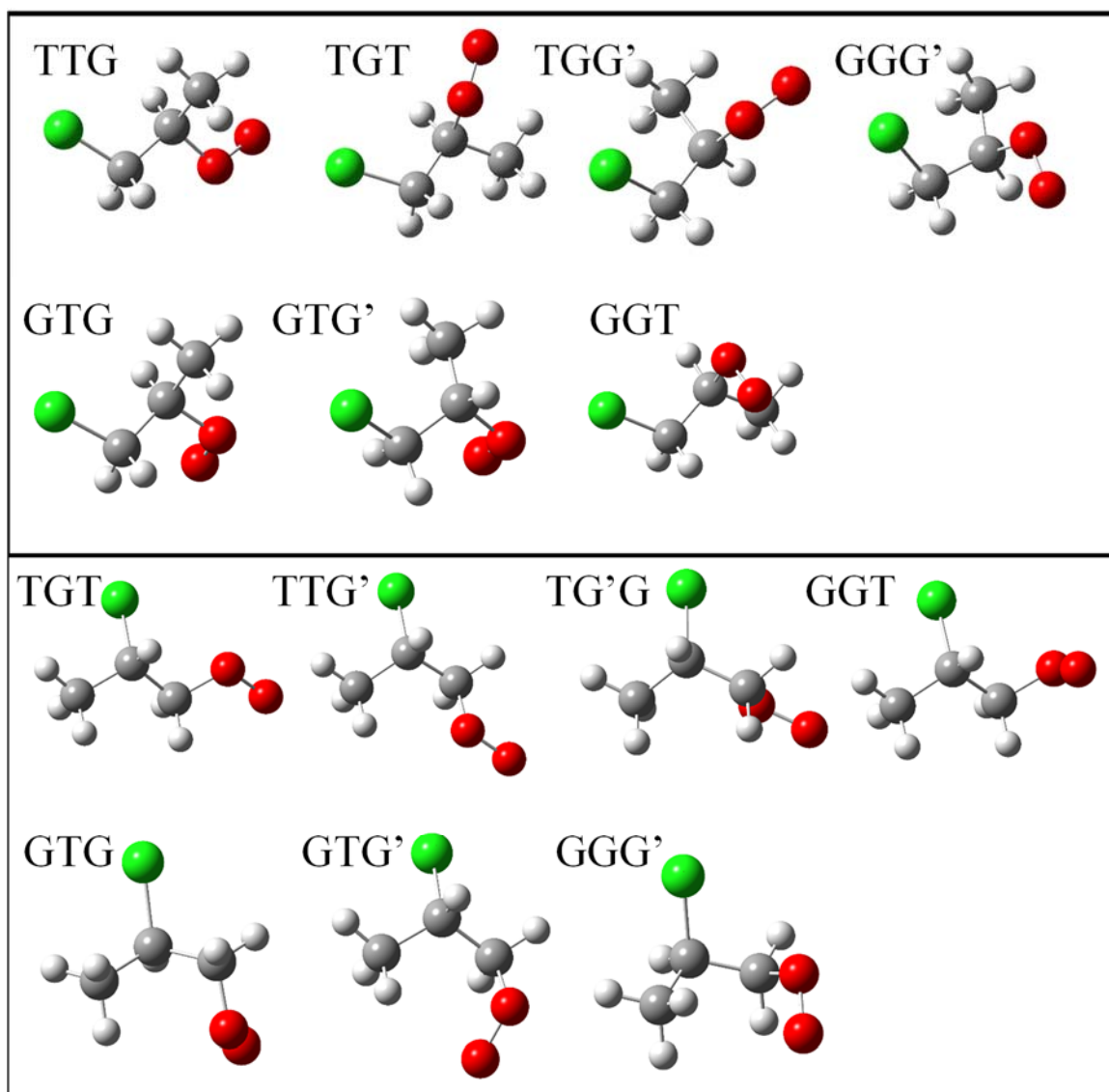


Figure 6. Geometries of the seven unique conformers of the 1-chloro propyl peroxy radical (top) and the seven unique conformers of the 2-chloro propyl peroxy radical (bottom). The labels indicate the C–O–O, Cl–C–O, and Cl–C–C–C dihedral angles, respectively, as *trans* (T) or *gauche* (G).

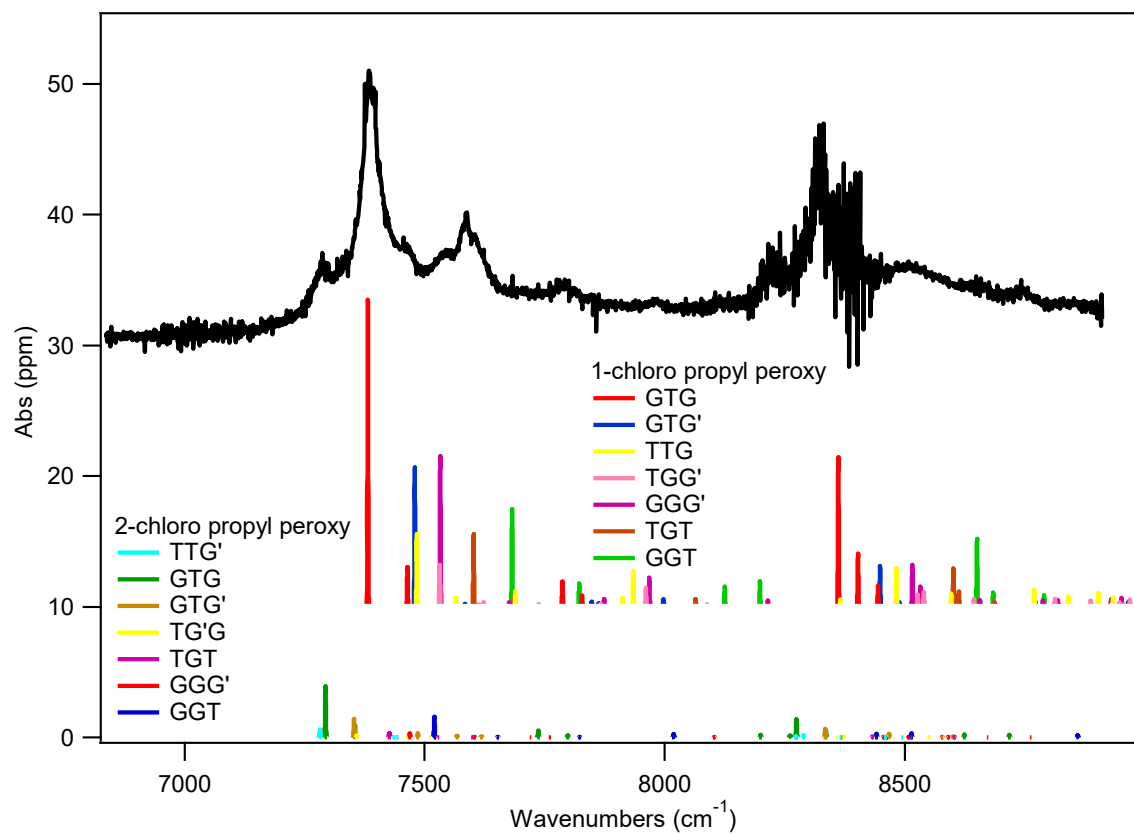


Figure 7. Experimental spectrum of the A–X electronic transition of chloro-propyl peroxy radical (offset in the y-direction by 30 ppm) along with the computed Franck-Condon spectra of the 14 local minimum structures (spectra for the 1-chloro propyl peroxy radical conformers are offset in the y-direction by 10 ppm). The origin transitions were set to the values obtained at TD-B3LYP/aug-cc-pVDZ. The Franck-Condon spectrum was simulated from normal modes computed at TD-B3LYP/aug-cc-pVDZ, with frequencies scaled by 0.970. Intensities were weighted by Boltzmann factors computed using the G2 method, with additional weighting of the 2-chloro propyl peroxy radical spectrum by $1/6^{\text{th}}$ to account for preferred addition of the chlorine atom to the primary carbon.

Table 1. Origin frequencies for the chloro-ethyl peroxy radical. Experimental origins for all peaks with centers $< 7550 \text{ cm}^{-1}$ are listed. The theoretical origins are listed for the four conformers, along with the A state vibrations of the C–O–O bend and O–O stretch modes. Energies and vibrations are given in cm^{-1} .

	experimental origin ^a		theoretical origin ^b	bend ^c	stretch ^c
A	7280	TT	7229	379	1003
B	7353	GT	7362	430	980
C	7410	TG	7390	298	1007
D	7520	GG	7542	373	990

^aThe origin region was fit with the sum of four Gaussian functions, each with FWHM = 50 cm^{-1} . Reported here are the center frequencies.

^bThe origin for each conformer was computed as the adiabatic energy difference between the ground state energies of the X and A states, using EOM-EE/CCSD/aug-cc-pVDZ. The adiabatic energy difference was corrected by comparison to the same calculations for the ethyl peroxy radical, as described in the text.

^cThe vibrational frequencies for the A state of each conformer were calculated using TD-DFT B3LYP/aug-cc-pVDZ. Vibrations were scaled by 0.970.²⁶

Table 2. Ground state degeneracies (g) and energy differences for conformers of chloro-ethyl and chloro-propyl peroxy radicals. Energy differences are given in cm^{-1} and include zero-point energy corrections unless otherwise noted.^a

chloro-ethyl peroxy radical				
Conformer	g	B3LYP/aug-cc-pVDZ	CCSD/aug-cc-pVDZ ^a	G2
TT	1	253	355	346
GT	2	0	0	0
TG	2	214	377	322
GG	1	73	96	91
1-chloro propyl peroxy radical				
Conformer	g	B3LYP/aug-cc-pVDZ	G2	
GTG	2	0	0	
GTG'	2	282	164	
TTG	2	268	298	
TGG'	2	425	414	
GGG'	2	197	148	
TGT	2	233	299	
GGT	2	327	237	
2-chloro propyl peroxy				
Conformer	g	B3LYP/aug-cc-pVDZ	G2	
TTG'	2	214	386	
GTG	2	0	0	
GTG'	2	187	207	
TG'G	2	555	645	
TGT	2	379	508	
GGG'	2	591	522	
GGT	2	211	187	

^aCCSD energies are not corrected for zero point energies.

Table 3. Comparison of X and A state bond lengths (in Å) and adiabatic A–X electronic transitions (cm^{-1}) calculated for the chloro-ethyl peroxy radical C_s conformer. Energies were not corrected for zero-point energies for ease in comparison, as CCSD frequency calculations were too computationally-expensive.

	HF	B3LYP	MP2	CCSD	TD- B3LYP	EOM- CCSD
${}^2A''$ $d_{\text{O-O}}$	1.301	1.323	1.315	1.335	1.313	1.325
${}^2A'$ $d_{\text{O-O}}$	1.362	1.390	1.393	1.412	1.373	1.406
E (A–X)	4593	7486	6846	6894	8894	7558
Scaled E (A–X)					7304	7229

Table 4. Origin frequencies for the chloro-propyl peroxy radical. Experimental origins for all peaks with centers $<7800\text{ cm}^{-1}$ are listed. The theoretical origins are listed for the 1-chloro and 2-chloro propyl peroxy conformers. Energies are given in cm^{-1} .

	experimental origin ^a	1-chloro propyl peroxy conformer	1-chloro propyl peroxy origin	2-chloro propyl peroxy conformer	2-chloro propyl peroxy origin
A	7280	GTG	7382	TTG'	7282
B	7328	GTG'	7480	GTG	7294
C	7387	TTG	7484	GTG'	7353
D	7446	TGG'	7531	TG'G	7359
E	7485	GGG'	7533	TGT	7427
F	7536	TGT	7602	GGG'	7469
G	7590	GGT	7682	GGT	7520
H	7636				
I	7704				
J	7783				

^aThe origin region was fit with the sum of ten Gaussian functions, each with $\text{FWHM} = 35\text{ cm}^{-1}$. Reported here are the center frequencies.

^bThe origin for each conformer was computed as the adiabatic energy difference between the ground state energies of the X and A states, using TD-DFT B3LYP/aug-cc-pVDZ. The adiabatic energy difference was corrected by comparison to the same calculations for the ethyl peroxy radical, as described in the text.

6 Supporting Information

6.1 Adiabatic electronic 0–0 transition energy scaling

Quantum chemistry calculations of the 0–0 electronic transition using TD-DFT or EOMEE overestimate the energy of the origin transition. To account for this, a correction scaling factor is computed at each level of theory and basis set by calculating the same transition for a reference molecule.¹ In this work, we used the ethyl peroxy radical as the reference molecule because its experimental spectrum has been reported, along with computations of its electronic structure.^{2–4} This molecule serves as a good test to calculations of a molecule with both C_s and C_1 conformations. Table S1 compares the results reported by Rupper et al. on the ethyl peroxy radical. In general, the results reported by Rupper et al. agree well with those computed in this work. The TD-DFT work finds the T conformer as the local minimum, in contradiction to both CCSD calculations. EOMEE-CCSD calculations report A state O–O bond lengths closer to the expected $> 1.4 \text{ \AA}$ value. The scale factor (the conformer-specific theoretical transition divided by the conformer-specific experimentally-observed transition) for the A–X adiabatic excitation energy is reported in the final row of Table S1 for each computation. The EOMEE-CCSD calculations achieve the scale factor closest to unity, and also report very similar conformer-specific scale factors. The average of these two values was used to scale the adiabatic transition energies reported in the text.

6.2 References

1. Sprague, M. K.; Mertens, L. A.; Widgren, H. N.; Okumura, M.; Sander, S. P.; McCoy, A. B., Cavity Ringdown Spectroscopy of the Hydroxy-Methyl-Peroxy Radical. *J. Phys. Chem. A* **2013**, *117*, 10006-10017.
2. Rupper, P.; Sharp, E. N.; Tarczay, G.; Miller, T. A., Investigation of Ethyl Peroxy Radical Conformers via Cavity Ringdown Spectroscopy of the $\tilde{A}-\tilde{X}$ Electronic Transition. *J. Phys. Chem. A* **2007**, *111*, 832-840.
3. Just, G. M. P.; Rupper, P.; Miller, T. A.; Meerts, W. L., High-resolution Cavity Ringdown Spectroscopy of the Jet-cooled Ethyl Peroxy Radical $C_2H_5O_2$. *J. Chem. Phys.* **2009**, *131*, 184303.
4. Melnik, D.; Chhantyal-Pun, R.; Miller, T. A., Measurements of the Absolute Absorption Cross Sections of the $\tilde{A}-\tilde{X}$ Transition in Organic Peroxy Radicals by Dual-Wavelength Cavity Ringdown Spectroscopy. *J. Phys. Chem. A* **2010**, *114*, 11583-11594.
5. Johnson III, R. D., NIST Computational Chemistry Comparison and Benchmark Database. NIST Standard Reference Database Number 101, Release 17b, September 2015.

Table S1. Comparison between the experimental and theoretical results for the ethyl peroxy radical, reported by Rupper et al. and the theoretical values used in this work as a reference molecule. Energies and vibrational frequencies are given in cm^{-1} , bond lengths are given in Å. TD-DFT vibrational frequencies are unscaled. TD-DFT and EOMEE-CCSD calculations used the aug-cc-pVDZ basis set.

	Experiment ^a		EOMIP-CCSD ^a		TD-DFT		EOMEE-CCSD	
	T	G	T	G	T	G	T	G
0^0_0	7362	7592	7938	8059	8736	8922	7690	7944
$\Delta 0^0_0$ (G-T)	230		121		186		254	
A C–O–O bend	512	457	436	463	427	456		
A O–O stretch	945	915	948	951	1029	1022		
X do-o			1.322	1.324	1.316	1.317	1.324	1.325
A do-o			1.379	1.380	1.377	1.377	1.406	1.407
X C–C–O–O angle			180	60	180	75	180	72
A C–C–O–O angle					180	68	180	68
Ground state energy difference (T – G)			81		–26		26	
0^0_0 scale factor (experiment \div theory)			0.927	0.842	0.843	0.851	0.957	0.956

^aTaken from Rupper et al.²

Table S2. Energies (Hartrees) and Cartesian coordinates (Å) for equilibrium structures of chloro-ethyl peroxy radical conformers. TD-DFT energies are ZPVE-corrected but EOMEE energies are not.

TD-DFT

TT (UB3LYP/aug-cc-pVDZ)						
X: E = -689.1233017				A: E = -689.0840254		
C	0.679381	0.582909	0.000011	0.685602	0.582128	0.000037
H	1.306669	0.563153	0.896508	1.309767	0.563332	0.898100
H	1.306638	0.563120	-0.896506	1.309829	0.563327	-0.897981
C	-0.335198	-0.546386	0.000049	-0.323888	-0.554264	0.000007
H	-0.961847	-0.542172	0.899340	-0.952274	-0.537748	0.901037
H	-0.961938	-0.542153	-0.899176	-0.952299	-0.537681	-0.901003
O	0.440205	-1.787566	-0.000008	0.478906	-1.762836	-0.000052
Cl	-0.206051	2.163735	-0.000014	-0.215487	2.152728	-0.000010
O	-0.346675	-2.843005	-0.000027	-0.381660	-2.839013	0.000021
GT (UB3LYP/aug-cc-pVDZ)						
X: E = -689.1244559				A: E = -689.0848507		
C	0.420486	0.403460	0.389890	0.410588	0.394945	0.404890
H	0.054261	0.142746	1.386939	0.038062	0.151160	1.403584
H	1.514801	0.402287	0.372695	1.504372	0.380069	0.394788
C	-0.154788	-0.529551	-0.663472	-0.164242	-0.530449	-0.660044
H	-1.249798	-0.542057	-0.648059	-1.262519	-0.518863	-0.662729
H	0.219269	-0.293284	-1.666156	0.211560	-0.277991	-1.657773
O	0.315504	-1.888953	-0.410048	0.300386	-1.888414	-0.469112
Cl	-0.120932	2.097655	0.037792	-0.113695	2.092647	0.035914
O	-0.325113	-2.437708	0.604250	-0.304979	-2.423629	0.649427
TG (UB3LYP/aug-cc-pVDZ)						
X: E = -689.1234803				A: E = -689.0835113		
C	0.252464	0.721648	0.917443	0.258641	0.710427	0.908003
H	-0.182454	1.207209	1.797209	-0.182315	1.171706	1.798164
H	1.340052	0.659372	1.030084	1.346110	0.651312	1.017819
C	-0.359421	-0.647221	0.738944	-0.346357	-0.661724	0.715776
H	-0.283775	-1.222695	1.672872	-0.246065	-1.240126	1.649093
H	-1.401588	-0.608629	0.402317	-1.403516	-0.608159	0.419435
O	0.412257	-1.363705	-0.271474	0.407429	-1.322815	-0.322921
Cl	-0.071176	1.809610	-0.497821	-0.077366	1.824181	-0.481032
O	-0.114821	-2.541944	-0.525757	-0.116516	-2.586939	-0.483283
GG (UB3LYP/aug-cc-pVDZ)						
X: E = -689.1241211				A: E = -689.083701		

C	0.590899	0.481099	0.685978	0.586952	0.486400	0.685462
H	0.819415	0.956250	1.646138	0.790358	0.952144	1.656632
H	1.512306	0.121147	0.217858	1.523036	0.148678	0.231046
C	-0.380635	-0.658347	0.898765	-0.387634	-0.662175	0.874372
H	0.007186	-1.342470	1.665809	-0.018116	-1.334824	1.665567
H	-1.384513	-0.307905	1.164024	-1.392068	-0.306917	1.130844
O	-0.583026	-1.443835	-0.314570	-0.610763	-1.433350	-0.322545
Cl	-0.092887	1.772261	-0.390385	-0.084788	1.783023	-0.387985
O	0.503413	-2.117661	-0.631148	0.528547	-2.156128	-0.608375

EOMEE-CCSD

TT (CCSD/aug-cc-pVDZ)						
X: E = -688.0667863				A: E = -688.0323484		
C	0.686675	0.588061	-0.000008	0.693179	0.589046	0.000055
H	1.315193	0.566852	0.899715	1.319120	0.572468	0.901054
H	1.315151	0.566861	-0.899761	1.319225	0.572412	-0.900870
C	-0.326292	-0.548342	0.000026	-0.306149	-0.560642	0.000035
H	-0.954299	-0.537799	0.902108	-0.936967	-0.538630	0.903345
H	-0.954345	-0.537823	-0.902025	-0.937056	-0.538545	-0.903210
O	0.452282	-1.780971	0.000016	0.505459	-1.755950	-0.000075
Cl	-0.212125	2.150879	-0.000004	-0.225460	2.140149	-0.000022
O	-0.362016	-2.826698	-0.000025	-0.412170	-2.821631	0.000015
GT (CCSD/aug-cc-pVDZ)						
X: E = -688.0684057				A: E = -688.0333353		
C	0.419315	0.395859	0.392694	0.440186	0.392231	0.383075
H	0.047487	0.127745	1.389181	0.121607	0.141345	1.402278
H	1.517032	0.385742	0.377048	1.535344	0.381938	0.314977
C	-0.157180	-0.530077	-0.670895	-0.181212	-0.538407	-0.655726
H	-1.255772	-0.530258	-0.658944	-1.282072	-0.520870	-0.606743
H	0.220245	-0.279276	-1.672474	0.144103	-0.270527	-1.670782
O	0.303898	-1.890159	-0.430758	0.295362	-1.890453	-0.495627
Cl	-0.117636	2.081099	0.037884	-0.117967	2.075231	0.040153
O	-0.316646	-2.394507	0.629553	-0.303784	-2.376266	0.684823
TG (CCSD/aug-cc-pVDZ)						
X: E = -688.0666844				A: E = -688.0314811		
C	0.251749	0.729975	0.925292	0.249569	0.718411	0.917163
H	-0.196682	1.218421	1.800828	-0.211638	1.180139	1.800633
H	1.341787	0.671501	1.047590	1.338849	0.665831	1.044627
C	-0.352667	-0.648706	0.744633	-0.339229	-0.665147	0.711761

H	-0.258530	-1.235340	1.672641	-0.240184	-1.249642	1.644351
H	-1.402932	-0.606445	0.423583	-1.398291	-0.611594	0.410043
O	0.410953	-1.332278	-0.287944	0.432093	-1.294492	-0.327617
Cl	-0.073666	1.784412	-0.501943	-0.079961	1.803002	-0.484438
O	-0.114179	-2.526565	-0.515951	-0.131024	-2.574927	-0.477101
GG (CCSD/aug-cc-pVDZ)						
X: E = -688.0679662				A: E = -688.032039		
C	0.593678	0.480955	0.703212	0.589789	0.480110	0.698640
H	0.802989	0.968271	1.665569	0.781959	0.952975	1.672392
H	1.526024	0.119429	0.251359	1.534461	0.140410	0.255229
C	-0.380288	-0.664709	0.909257	-0.390352	-0.671980	0.878409
H	0.010233	-1.365092	1.664017	-0.015104	-1.364717	1.653531
H	-1.380898	-0.307531	1.191475	-1.387426	-0.306959	1.162712
O	-0.594378	-1.416575	-0.318028	-0.638694	-1.404081	-0.332970
Cl	-0.095348	1.735365	-0.395726	-0.085138	1.749142	-0.388928
O	0.517156	-2.060144	-0.646957	0.555799	-2.096657	-0.616328

Table S3. Unscaled UB3LYP/aug-cc-pVDZ harmonic frequencies (cm^{-1}) for equilibrium structures of chloro-ethyl peroxy radical conformers. The analysis described in the paper used a scale factor of 0.970 on all modes.⁵ O–O stretch modes are highlighted in bold.

Harmonic Frequencies (UB3LYP/aug-cc-pVDZ)								
	TT		GT		TG		GG	
	X	A	X	A	X	A	X	A
ω_{21}	51	92	91	81	56	90	72	69
ω_{20}	101	104	102	131	119	115	139	164
ω_{19}	176	171	240	243	259	263	252	236
ω_{18}	328	338	323	303	349	307	419	384
ω_{17}	490	391	532	444	527	477	540	484
ω_{16}	752	754	754	748	664	671	663	665
ω_{15}	783	806	788	785	794	810	802	815
ω_{14}	937	944	897	906	956	972	942	946
ω_{13}	1030	1034	1044	1011	1000	1007	968	958
ω_{12}	1088	1044	1060	1035	1068	1038	1078	1021
ω_{11}	1164	1070	1149	1061	1178	1074	1152	1069
ω_{10}	1191	1184	1221	1192	1202	1191	1207	1193
ω_9	1259	1259	1254	1254	1237	1237	1256	1254
ω_8	1272	1269	1291	1288	1301	1301	1303	1308
ω_7	1366	1369	1360	1365	1368	1373	1368	1372
ω_6	1471	1470	1460	1463	1441	1437	1438	1437
ω_5	1474	1497	1467	1468	1453	1477	1444	1442
ω_4	3082	3053	3090	3070	3058	3022	3067	3031
ω_3	3100	3105	3102	3106	3094	3086	3096	3091
ω_2	3145	3111	3156	3144	3135	3097	3145	3135
ω_1	3171	3176	3179	3179	3159	3162	3165	3163

Table S4. Energies (Hartrees) and Cartesian coordinates (Å) for equilibrium structures of the 1-chloro-propyl and 2-chloro-propyl peroxy radical conformers. Reported energies include zero-point energy corrections.

1-chloro-propyl peroxy radical conformers						
GTG (UB3LYP/aug-cc-pVDZ)						
X: E = -728.4197689				A: E = -728.380051245		
C	0.519562	0.464014	0.524516	0.555510	0.469311	0.490551
H	0.394932	0.201001	1.578256	0.499063	0.209042	1.550356
H	1.581849	0.497000	0.260068	1.600263	0.521254	0.167896
C	-0.246904	-0.517472	-0.357129	-0.239338	-0.524852	-0.357768
H	-1.315177	-0.488270	-0.111929	-1.308617	-0.459740	-0.112606
O	0.219664	-1.871640	0.013532	0.212868	-1.873098	-0.004465
Cl	-0.133596	2.145494	0.320188	-0.142330	2.139257	0.321915
O	-0.252221	-2.252954	1.181973	-0.257628	-2.212166	1.244243
C	0.005601	-0.386598	-1.846603	-0.008850	-0.413893	-1.853628
H	-0.568917	-1.138559	-2.400841	-0.633306	-1.135048	-2.393047
H	-0.303125	0.609919	-2.184127	-0.269602	0.598908	-2.184094
H	1.072464	-0.517398	-2.073366	1.045943	-0.603059	-2.094216
GTG' (UB3LYP/aug-cc-pVDZ)						
X: E = -728.4185934				A: E = -728.378349371		
C	0.184403	0.497317	0.704727	0.194019	0.501255	0.710280
H	-0.303978	0.446845	1.682230	-0.290198	0.448620	1.688896
H	1.253582	0.291262	0.804626	1.266202	0.304845	0.807823
C	-0.482447	-0.461500	-0.279680	-0.478903	-0.462115	-0.269299
H	-1.534132	-0.179337	-0.415498	-1.527447	-0.168659	-0.405024
O	-0.615057	-1.768359	0.403558	-0.645394	-1.750689	0.409462
Cl	0.018488	2.209846	0.124805	0.020573	2.211725	0.123263
O	0.554423	-2.303072	0.691447	0.573015	-2.336492	0.673970
C	0.224918	-0.628847	-1.611920	0.220078	-0.623742	-1.610204
H	-0.322150	-1.336530	-2.246894	-0.306571	-1.366912	-2.220287
H	0.270364	0.339196	-2.125484	0.216287	0.336202	-2.141052
H	1.245858	-0.999189	-1.459468	1.259854	-0.948353	-1.477935
TTG (UB3LYP/aug-cc-pVDZ)						
X: E = -728.4184967				A: E = -728.37822947		
C	0.473279	0.683339	0.655529	0.454931	0.689062	0.671737
H	0.263155	0.615866	1.726938	0.217592	0.635824	1.737425
H	1.554716	0.722202	0.487554	1.539388	0.714590	0.523917
C	-0.174422	-0.475547	-0.096129	-0.184437	-0.477611	-0.079102
H	-1.261847	-0.462639	0.045462	-1.277239	-0.431793	0.032534
O	0.312460	-1.667317	0.635750	0.279771	-1.630157	0.704844
Cl	-0.209171	2.263768	0.085224	-0.204612	2.262760	0.060128

O	-0.417560	-2.729804	0.375446	-0.394695	-2.759043	0.303147
C	0.198046	-0.593978	-1.562315	0.221816	-0.606206	-1.538342
H	-0.261518	-1.492711	-1.989347	-0.250085	-1.484019	-1.993696
H	-0.167625	0.283316	-2.109899	-0.097653	0.287945	-2.088153
H	1.288422	-0.656007	-1.681591	1.311935	-0.707332	-1.623898

TGG' (UB3LYP/aug-cc-pVDZ)

X: E = -728.4178846				A: E = -728.377362729		
C	0.972459	0.793261	-0.115193	0.974050	0.804501	-0.066220
H	1.670014	1.213547	0.616828	1.619192	1.215745	0.717505
H	1.451197	0.749037	-1.098296	1.509219	0.785760	-1.019779
C	0.544303	-0.594186	0.332064	0.545475	-0.598864	0.331330
H	1.458091	-1.198753	0.435363	1.475381	-1.180340	0.456148
O	-0.182824	-1.184468	-0.807961	-0.130882	-1.139215	-0.845373
Cl	-0.398250	1.976077	-0.264390	-0.404076	1.967961	-0.267088
O	-0.271298	-2.491942	-0.698161	-0.286054	-2.497327	-0.697472
C	-0.297352	-0.674950	1.593138	-0.321179	-0.704809	1.577484
H	-0.526083	-1.723433	1.814365	-0.532032	-1.755147	1.807254
H	0.265067	-0.253306	2.437689	0.211391	-0.261177	2.430612
H	-1.231516	-0.113870	1.477601	-1.268448	-0.172815	1.435945

GGG' (UB3LYP/aug-cc-pVDZ)

X: E = -728.4189127				A: E = -728.378383669		
C	-0.931264	0.533355	0.234189	-0.927730	0.535587	0.242851
H	-1.790161	0.973952	-0.283500	-1.785180	0.969666	-0.283916
H	-1.216672	0.242441	1.249137	-1.217162	0.263179	1.261545
C	-0.439937	-0.682603	-0.534588	-0.433100	-0.688691	-0.522470
H	-1.293136	-1.372863	-0.613124	-1.295518	-1.371521	-0.612355
O	0.574464	-1.409248	0.254035	0.597294	-1.402039	0.219938
Cl	0.312250	1.848127	0.394666	0.312430	1.850655	0.395924
O	0.061449	-1.933709	1.345133	0.051184	-1.952256	1.356729
C	0.187328	-0.424451	-1.891612	0.171345	-0.419901	-1.889750
H	0.449267	-1.373593	-2.374283	0.396478	-1.365615	-2.395378
H	-0.530194	0.106018	-2.531691	-0.549651	0.143318	-2.497480
H	1.088585	0.191739	-1.797141	1.088813	0.172228	-1.800249

TGT (UB3LYP/aug-cc-pVDZ)

X: E = -728.418771				A: E = -728.377868402		
C	0.816767	0.761156	0.328215	0.790061	0.768236	0.338431
H	0.833666	0.711085	1.422400	0.792554	0.715784	1.432242
H	1.809807	1.031484	-0.043923	1.789961	1.027961	-0.023614
C	0.383370	-0.565204	-0.266511	0.368220	-0.561751	-0.261700
H	0.077045	-0.452434	-1.312941	0.086226	-0.431174	-1.316045
O	-0.830034	-0.959410	0.471661	-0.840980	-0.931945	0.467401

Cl	-0.296524	2.121048	-0.121194	-0.303101	2.135217	-0.127215
O	-1.499006	-1.897879	-0.160375	-1.448848	-1.993094	-0.161113
C	1.440683	-1.650001	-0.106966	1.449202	-1.627908	-0.104760
H	1.034662	-2.608385	-0.450546	1.073745	-2.600156	-0.442733
H	2.322175	-1.407009	-0.715527	2.324463	-1.362847	-0.714022
H	1.750943	-1.749947	0.942118	1.759492	-1.719414	0.944697
GGT (UB3LYP/aug-cc-pVDZ)						
X: E = -728.4184484				A: E = -728.377114836		
C	0.606199	0.542781	0.567123	0.604716	0.564948	0.565691
H	0.064455	0.321347	1.491514	0.090282	0.352629	1.507760
H	1.662788	0.727795	0.784827	1.665872	0.758276	0.755417
C	0.472702	-0.606938	-0.415007	0.460789	-0.595109	-0.413724
H	0.753457	-0.287051	-1.425745	0.737342	-0.268350	-1.423622
O	-0.950691	-0.962617	-0.602064	-0.939156	-0.941208	-0.617126
Cl	-0.067148	2.094653	-0.091274	-0.094094	2.106111	-0.081742
O	-1.516178	-1.351900	0.519362	-1.493955	-1.465593	0.528135
C	1.258325	-1.839024	0.016150	1.283210	-1.811215	0.006576
H	1.079738	-2.662200	-0.686418	1.063800	-2.654076	-0.659075
H	2.332842	-1.612593	0.018389	2.353375	-1.575547	-0.067940
H	0.959836	-2.161166	1.021106	1.061522	-2.114148	1.037734

2-chloro-propyl peroxy radical conformers						
TTG' (UB3LYP/aug-cc-pVDZ)						
X: E = -728.4171807				A: E = -728.3779995		
C	-0.522051	-0.297925	0.373571	-0.522156	-0.305506	0.377673
H	-0.488287	-0.308510	1.468742	-0.490853	-0.320202	1.472243
C	0.651065	0.508475	-0.168592	0.660103	0.498492	-0.155650
H	0.669088	0.525860	-1.264988	0.648562	0.551533	-1.253645
H	0.670078	1.528702	0.229421	0.684849	1.507910	0.274595
O	1.869938	-0.164715	0.288031	1.845648	-0.224396	0.273343
Cl	-2.031326	0.657863	-0.038940	-2.014380	0.673586	-0.039588
O	2.948632	0.444999	-0.156089	2.946275	0.485795	-0.151742
C	-0.620813	-1.707990	-0.183355	-0.633123	-1.709166	-0.190148
H	0.286546	-2.267356	0.084607	0.264911	-2.280495	0.082025
H	-1.489129	-2.229168	0.235960	-1.512498	-2.220682	0.218132
H	-0.713517	-1.690840	-1.277035	-0.714856	-1.683145	-1.284406
GTG (UB3LYP/aug-cc-pVDZ)						
X: E = -728.4182976				A: E = -728.3790545		
C	-0.360376	-0.238557	0.282105	-0.351152	-0.239550	0.289323

H	-0.083071	-0.066704	1.327463	-0.105372	-0.109427	1.348315
C	0.609111	0.519481	-0.620392	0.593286	0.598577	-0.573921
H	0.384833	0.358471	-1.681706	0.341900	0.515704	-1.637698
H	0.636669	1.587331	-0.382678	0.590938	1.652927	-0.268626
O	1.961902	-0.008145	-0.450959	1.950979	0.093393	-0.522622
Cl	-1.990407	0.578105	0.082611	-2.006434	0.529500	0.095394
O	2.503193	0.411017	0.676640	2.475969	0.315425	0.732659
C	-0.472414	-1.721861	-0.024761	-0.397437	-1.709152	-0.084876
H	0.511276	-2.194735	0.104697	0.603820	-2.141825	0.045237
H	-1.182311	-2.203659	0.657389	-1.100913	-2.249980	0.558605
H	-0.809160	-1.885842	-1.056710	-0.704768	-1.838703	-1.130977

GTG' (UB3LYP/aug-cc-pVDZ)

	X: E = -728.4174563			A: E = -728.3778926		
C	-0.194197	0.430212	0.418689	-0.192056	0.412671	0.422710
H	-0.104334	0.445878	1.510676	-0.091636	0.424153	1.513328
C	0.825542	-0.548665	-0.160791	0.849871	-0.536853	-0.168717
H	0.748360	-0.632746	-1.249864	0.800555	-0.571354	-1.265325
H	1.843502	-0.281306	0.143580	1.859878	-0.253255	0.145368
O	0.607484	-1.877664	0.406905	0.715680	-1.884863	0.357147
Cl	0.352200	2.100806	-0.117395	0.330190	2.095809	-0.113887
O	-0.171380	-2.623832	-0.352143	-0.266715	-2.572444	-0.321867
C	-1.630154	0.186456	-0.009622	-1.627296	0.154090	0.004312
H	-1.948172	-0.810929	0.323299	-1.930209	-0.841702	0.354345
H	-2.294055	0.933243	0.441434	-2.296229	0.903057	0.444445
H	-1.728663	0.236110	-1.101165	-1.730422	0.189349	-1.088165

TG'G (UB3LYP/aug-cc-pVDZ)

	X: E = -728.4157262			A: E = -728.3761310		
C	-0.683347	-0.483551	0.529662	-0.670843	-0.472522	0.530782
H	-1.161522	-0.667916	1.499313	-1.125494	-0.647428	1.513884
C	0.754316	-0.089257	0.815354	0.767681	-0.059112	0.796178
H	0.824482	0.845268	1.382696	0.820557	0.890612	1.345390
H	1.268377	-0.897162	1.355156	1.273824	-0.852883	1.370162
O	1.461252	0.102485	-0.445930	1.436842	0.089298	-0.474772
Cl	-1.597070	0.951146	-0.159982	-1.617603	0.935982	-0.161512
O	2.722663	0.414965	-0.238553	2.748340	0.421203	-0.220043
C	-0.840803	-1.692129	-0.383447	-0.825137	-1.696108	-0.360160
H	-0.314088	-2.551978	0.057119	-0.272249	-2.539311	0.079915
H	-1.899652	-1.951977	-0.492510	-1.881476	-1.975545	-0.443052
H	-0.419720	-1.495708	-1.375627	-0.427582	-1.504696	-1.362875

TGT (UB3LYP/aug-cc-pVDZ)

	X: E = -728.4165804			A: E = -728.3766212		
--	---------------------	--	--	---------------------	--	--

C	-0.660568	-0.437030	0.365467	-0.647912	-0.434391	0.369664
H	-0.558289	-0.405322	1.456264	-0.546800	-0.396621	1.459752
C	0.698456	-0.662744	-0.265979	0.720500	-0.631516	-0.257911
H	1.039252	-1.691832	-0.084909	1.073284	-1.656387	-0.059233
H	0.703162	-0.446313	-1.340588	0.700703	-0.444159	-1.341134
O	1.662908	0.223262	0.376305	1.629536	0.295762	0.371896
Cl	-1.281584	1.227116	-0.088652	-1.320226	1.203798	-0.094566
O	2.856131	0.097151	-0.163888	2.881333	0.080995	-0.162859
C	-1.668932	-1.497172	-0.057406	-1.619428	-1.528510	-0.054660
H	-1.333050	-2.486890	0.285717	-1.256674	-2.505596	0.296560
H	-2.648431	-1.290264	0.387805	-2.607209	-1.347639	0.383585
H	-1.781764	-1.521983	-1.149033	-1.725374	-1.561722	-1.146769
GGG' (UB3LYP/aug-cc-pVDZ)						
X: E = -728.4156627				A: E = -728.3754745		
C	-0.529498	-0.429440	0.603360	-0.520403	-0.418984	0.611550
H	-1.011807	-0.655767	1.562998	-1.013181	-0.620906	1.572831
C	0.665637	0.461932	0.916993	0.668580	0.480567	0.929242
H	0.343875	1.415542	1.350416	0.334020	1.430540	1.360077
H	1.359912	-0.058515	1.588780	1.339526	-0.025948	1.640969
O	1.417365	0.826404	-0.275106	1.444711	0.902062	-0.214267
Cl	-1.791135	0.533724	-0.320451	-1.767167	0.526342	-0.345093
O	2.395901	-0.025293	-0.515602	2.303702	-0.103461	-0.603729
C	-0.202096	-1.711810	-0.145653	-0.194584	-1.722585	-0.100394
H	0.526299	-2.298079	0.432835	0.533622	-2.291889	0.496692
H	-1.109471	-2.311348	-0.280367	-1.099573	-2.330387	-0.214608
H	0.230100	-1.498110	-1.129534	0.238556	-1.532010	-1.087805
GGT (UB3LYP/aug-cc-pVDZ)						
X: E = -728.4174071				A: E = -728.3769442		
C	-0.471797	-0.437033	0.284719	-0.470398	-0.434042	0.292029
H	-0.078199	-0.384534	1.305366	-0.094843	-0.378453	1.318928
C	0.687219	-0.598515	-0.683417	0.697655	-0.578567	-0.677042
H	1.121070	-1.602697	-0.587984	1.120006	-1.593604	-0.602938
H	0.387222	-0.401762	-1.719265	0.388902	-0.381569	-1.710230
O	1.759486	0.354320	-0.427163	1.754980	0.374976	-0.461301
Cl	-1.281067	1.184906	0.006244	-1.300122	1.174117	0.013724
O	2.398984	0.060016	0.686605	2.412217	0.056405	0.708728
C	-1.494285	-1.555836	0.144664	-1.473606	-1.568363	0.133141
H	-1.023095	-2.520073	0.386295	-0.991584	-2.527544	0.374108
H	-2.330082	-1.396572	0.835179	-2.321339	-1.427917	0.812985
H	-1.893370	-1.604147	-0.877071	-1.858547	-1.616120	-0.894347

Table S5. Unscaled UB3LYP/aug-cc-pVDZ harmonic frequencies (cm^{-1}) for equilibrium structures of 1-chloro-propyl and 2-chloro-propyl peroxy radical conformers. The analysis described in the paper used a scale factor of 0.970 on all modes.⁵

1-chloro-propyl peroxy radical								
Harmonic Frequencies (UB3LYP/aug-cc-pVDZ)								
	GTG		GTG'		TTG		TGG'	
	X	A	X	A	X	A	X	A
ω_{30}	87	85	82	85	65	79	77	85
ω_{29}	106	120	103	108	89	84	93	95
ω_{28}	194	199	201	202	186	183	194	199
ω_{27}	216	217	215	216	217	211	219	212
ω_{26}	272	256	291	261	298	282	317	279
ω_{25}	373	374	357	380	340	333	337	346
ω_{24}	420	417	388	395	440	442	465	443
ω_{23}	532	459	602	534	523	465	590	574
ω_{22}	752	745	764	754	747	752	690	692
ω_{21}	813	813	791	793	829	814	801	797
ω_{20}	867	867	870	868	867	873	876	867
ω_{19}	905	914	915	906	907	909	919	926
ω_{18}	1052	1010	1041	998	1052	1029	1041	1026
ω_{17}	1078	1052	1075	1040	1071	1044	1068	1039
ω_{16}	1151	1074	1142	1071	1147	1072	1145	1070
ω_{15}	1194	1152	1154	1146	1194	1147	1194	1147
ω_{14}	1219	1217	1226	1218	1223	1218	1225	1218
ω_{13}	1262	1261	1267	1262	1264	1262	1297	1296
ω_{12}	1321	1324	1353	1332	1324	1325	1319	1320
ω_{11}	1365	1370	1363	1360	1366	1374	1347	1357
ω_{10}	1401	1398	1393	1396	1391	1398	1392	1397
ω_9	1455	1456	1459	1455	1458	1457	1443	1438
ω_8	1465	1463	1465	1464	1466	1463	1462	1459
ω_7	1476	1478	1479	1475	1478	1476	1474	1473
ω_6	3049	3050	3054	3053	3047	3049	3051	3016
ω_5	3093	3073	3099	3098	3093	3066	3057	3049
ω_4	3104	3102	3104	3105	3101	3100	3096	3096

ω_3	3128	3129	3135	3133	3128	3128	3127	3126
ω_2	3139	3143	3139	3139	3141	3140	3149	3148
ω_1	3173	3177	3176	3175	3165	3173	3160	3165
	GGG'		TGT		GGT			
	X	A	X	A	X	A		
ω_{30}	73	67	76	88	75	70		
ω_{29}	126	148	105	99	135	144		
ω_{28}	193	198	199	183	195	194		
ω_{27}	210	209	219	230	217	219		
ω_{26}	295	261	289	260	294	256		
ω_{25}	345	352	348	343	339	339		
ω_{24}	519	449	444	443	439	456		
ω_{23}	556	564	534	476	591	532		
ω_{22}	696	703	741	743	733	743		
ω_{21}	797	797	774	780	777	782		
ω_{20}	874	879	894	886	887	881		
ω_{19}	905	907	919	923	917	908		
ω_{18}	1025	1013	1045	1030	1029	998		
ω_{17}	1072	1030	1093	1041	1106	1032		
ω_{16}	1162	1077	1128	1099	1127	1103		
ω_{15}	1203	1158	1195	1129	1157	1129		
ω_{14}	1211	1210	1224	1210	1215	1206		
ω_{13}	1289	1293	1267	1271	1269	1267		
ω_{12}	1319	1325	1325	1333	1346	1337		
ω_{11}	1347	1355	1354	1359	1369	1355		
ω_{10}	1401	1396	1387	1390	1389	1392		
ω_9	1441	1439	1443	1439	1438	1439		
ω_8	1460	1457	1462	1459	1461	1461		
ω_7	1473	1474	1472	1471	1474	1470		
ω_6	3053	3017	3043	3043	3049	3048		
ω_5	3059	3054	3091	3067	3098	3093		
ω_4	3097	3092	3104	3093	3106	3104		
ω_3	3128	3131	3120	3117	3126	3124		

ω_2	3145	3150	3137	3139	3137	3137		
ω_1	3166	3163	3159	3160	3168	3163		

2-chloro-propyl peroxy radical
Harmonic Frequencies (UB3LYP/aug-cc-pVDZ)

	TTG'		GTG		GTG'		TG'G	
	X	A	X	A	X	A	X	A
ω_{30}	45	79	74	63	68	63	46	79
ω_{29}	109	111	103	127	96	137	112	107
ω_{28}	169	166	226	233	223	221	183	186
ω_{27}	243	239	243	233	243	255	238	241
ω_{26}	286	286	286	279	299	294	316	295
ω_{25}	356	351	359	341	357	319	341	345
ω_{24}	393	372	418	421	410	405	422	369
ω_{23}	499	446	530	457	524	444	590	581
ω_{22}	691	690	694	689	686	680	624	629
ω_{21}	890	898	878	885	866	864	892	882
ω_{20}	923	932	887	889	907	909	920	929
ω_{19}	930	941	940	934	935	924	935	953
ω_{18}	1031	1021	1020	1011	1019	1011	1027	1031
ω_{17}	1121	1038	1129	1020	1123	1024	1107	1044
ω_{16}	1151	1135	1145	1131	1146	1134	1134	1114
ω_{15}	1192	1151	1169	1147	1175	1149	1199	1142
ω_{14}	1213	1214	1239	1227	1233	1219	1224	1228
ω_{13}	1251	1249	1272	1262	1272	1266	1262	1259
ω_{12}	1336	1341	1336	1342	1337	1343	1342	1332
ω_{11}	1377	1373	1367	1371	1367	1372	1363	1367
ω_{10}	1397	1398	1397	1395	1400	1398	1400	1401
ω_9	1461	1460	1455	1456	1453	1453	1452	1458
ω_8	1463	1467	1461	1461	1459	1461	1463	1470
ω_7	1478	1495	1474	1473	1472	1473	1475	1483
ω_6	3043	3045	3043	3045	3047	3045	3041	3020
ω_5	3079	3050	3087	3072	3089	3070	3059	3042
ω_4	3104	3107	3110	3110	3106	3110	3097	3092
ω_3	3120	3117	3124	3125	3124	3126	3120	3095
ω_2	3137	3127	3137	3136	3137	3133	3136	3120
ω_1	3152	3138	3164	3147	3165	3152	3149	3149

TGT		GGG'		GGT	
X	A	X	A	X	A

ω_{30}	54	84	64	54	70	62
ω_{29}	112	106	104	139	114	136
ω_{28}	176	178	217	211	205	203
ω_{27}	235	232	255	259	234	229
ω_{26}	300	284	315	301	316	312
ω_{25}	356	345	335	336	391	361
ω_{24}	437	439	496	393	412	404
ω_{23}	506	450	574	579	573	513
ω_{22}	625	629	649	653	616	620
ω_{21}	907	905	838	836	871	878
ω_{20}	931	938	917	924	919	914
ω_{19}	954	969	940	929	948	949
ω_{18}	1037	1037	1031	1017	1047	1024
ω_{17}	1104	1051	1095	1024	1099	1041
ω_{16}	1154	1102	1137	1102	1145	1098
ω_{15}	1197	1147	1175	1143	1165	1143
ω_{14}	1204	1213	1246	1243	1246	1234
ω_{13}	1281	1284	1285	1281	1295	1292
ω_{12}	1304	1304	1326	1332	1300	1305
ω_{11}	1385	1383	1363	1367	1377	1380
ω_{10}	1397	1396	1403	1402	1396	1396
ω_9	1452	1461	1441	1441	1443	1441
ω_8	1462	1471	1457	1460	1460	1460
ω_7	1474	1478	1475	1471	1473	1473
ω_6	3038	3022	3046	3036	3038	3030
ω_5	3059	3040	3072	3041	3068	3038
ω_4	3101	3084	3089	3074	3106	3103
ω_3	3114	3106	3122	3116	3121	3119
ω_2	3133	3122	3146	3137	3138	3134
ω_1	3141	3141	3147	3152	3145	3140

OBSERVATION AND ASSIGNMENT OF THE A–X ELECTRONIC TRANSITION OF THE PEROXY RADICALS FORMED DURING CHLORINE-INITIATED OXIDATION OF ISOPRENE

1 Introduction

Biogenic emissions of volatile organic compounds result in high concentrations of unsaturated hydrocarbons in remote regions.¹ Isoprene (2-methyl-1,3-butadiene) has the highest emission rates into the atmosphere of all non-methane hydrocarbons; its branched structure, containing two double bonds, gives it rich photochemistry in the atmosphere.²⁻⁷ Oxidation of isoprene is usually dominated by reaction with OH radicals; however, there is increasing interest in chlorine atoms as an oxidant, as more sources of atmospheric chlorine are identified in or near remote regions.⁸⁻¹¹

Peroxy radicals have a strong A–X electronic transition in the ultraviolet that has long been used as a spectroscopic tool for kineticists who wish to quantify the fate of peroxy radicals in the atmosphere.¹²⁻¹⁵ More recently, sensitive detection by cavity-enhanced spectroscopies has enabled investigations of the weak A–X electronic transition,¹⁶⁻²⁶ leading to selective kinetics measurements.²⁷⁻²⁸

In this study, we measured the experimental spectrum of the peroxy radical mixture formed from reactions of Cl atoms with isoprene in the presence of oxygen. Experiments were carried out at 70 Torr at room temperature. The resulting spectrum contains several prominent features in the A–X origin region. Based on prior work (Chapter 2), we recognized this as a signature of multiple isomers and conformers that are formed and can interconvert. In order to assign the structured spectra of peroxy radicals in the near-infrared, we undertook preliminary quantum chemistry calculations on the peroxy radicals that are predicted to form during chlorine-initiated oxidation of isoprene. This included six different structural isomers—defined by the position of the chlorine and peroxy substituents—as well as the

allylic peroxy radical formed when the chlorine atom abstracts a hydrogen atom from isoprene.

At the same time, we made preliminary measurements of the isoprene peroxy radical decay kinetics under our experimental conditions. We investigated the conformer dependence on the decay rates with and without NO by measuring the time-dependent disappearance of two absorption features.

2 Experimental

The A–X spectrum of the peroxy radical mixture formed during chlorine-initiated oxidation of isoprene was measured experimentally using the same near-infrared pulsed laser cavity ringdown spectrometer described in Chapter 2 and elsewhere.²⁹⁻³⁰ Preliminary quantum chemical calculations were undertaken to assign the spectrum to the peroxy radicals formed when Cl atoms add to the double bonds, as well as the allylic peroxy radical that forms upon H-abstraction.

2.1 Radical production

Peroxy radicals were generated here in the same manner as the experiments described in Chapter 2. Chlorine gas was photodissociated using an excimer laser pulse (351 nm); the formed chlorine atoms attacked the isoprene molecule, either adding to one of the four positions on the double bonds, or abstracting a hydrogen atom. The carbon-centered radical then reacted with oxygen to form the detected peroxy radicals. We flowed isoprene into the reactor through a mass flow meter; the isoprene was from a homemade premixed stainless steel cylinder filled with 5% isoprene vapor and balance N₂. These experiments were carried out at room temperature under the following conditions: [isoprene] = 6×10^{14} cm⁻³, [O₂] = 4×10^{17} cm⁻³, [Cl₂] = 3.6×10^{16} cm⁻³, and [N₂] = 1.8×10^{18} cm⁻³. Each excimer laser pulse generated approximately 5×10^{14} chlorine atoms cm⁻³. We kept the isoprene concentration low (compared to the alkene concentrations used in Chapter 2) to prohibit isoprene polymerization. At higher isoprene concentrations, a black film began to collect on the coated quartz photolysis windows after several minutes of the excimer laser firing, even in the absence of Cl₂ or O₂. Although isoprene does not absorb 351 nm light very strongly, we

believe that some heating may be occurring that might induce polymerization when high concentrations of isoprene are present. At concentrations below 10^{15} cm^{-3} , the experiment could be run continually for several days before the windows became too dirty to continue.

2.2 Experimental and theoretical spectrum

The peroxy radical spectrum from 7000 cm^{-1} to 9000 cm^{-1} was collected as described in Chapter 2. We measured the ethyl peroxy radical spectrum on the same day that we carried out each segment of the isoprene spectrum and pieced everything together by using the ethyl peroxy radical reference spectrum.^{18,20-21}

To assign the peroxy radical spectrum formed during oxidation of isoprene, we carried out electronic structure calculations on the chlorine-substituted isoprene peroxy radicals and the allylic peroxy radical that is formed during H-abstraction. Due to the complexity of isoprene oxidation, we have not undertaken to identify all possible energetically-accessible isomers and conformers. We took the same approach as Dibble,³¹ who computed the adiabatic A–X excitation energies for ten OH-isoprene peroxy radical isomers using time-dependent density functional theory and a range of basis sets, but instead of performing an exhaustive potential energy search to identify starting points for ground state structures, he obtained optimized structures from previous work.³² Similarly, we looked to past ground state calculations to provide us with starting points for structures, rather than performing full potential energy surfaces searches like we have done in the past. In the case of chlorine, the Cl atom can add to any one of four positions on the double bonds in the molecule;³³ O₂ addition to the Cl-isoprene adduct can further form six unique isomers. Lei et al. investigated the ground state structures of these isomers, including about 5–6 rotational isomers for each of the 6 structural isomers.³⁴ They reported the minimum energy structure for each of the unique structural isomers (optimized at B3LYP/6-31G(d,p)) and we have adopted these structures as starting points for our calculations.

Unlike oxidation by OH, oxidation by Cl atoms is less-selective, leading to 13–18% of the reactions undergoing methyl-hydrogen abstraction. Braña and Sordo optimized the structure

of the allyl radical formed by an addition-elimination hydrogen abstraction process by the chlorine atom.³⁵ We investigated the resulting unsubstituted peroxy radicals.

Ground and excited state vibrations were calculated for each conformer at B3LYP/aug-cc-pVDZ. Using these frequencies, the Franck-Condon overlap was calculated for the origin transition and excitation to vibrational levels in the excited state. Vibrational frequencies were scaled by 0.970.³⁶ The most intense peak in each spectrum was scaled to 1.

Density functional theory calculations were carried out using the Gaussian 09 computational chemistry program.³⁷

2.3 Peroxy radical kinetics

With the assumption that different spectral features in the origin region correspond to different peroxy radical isomers or conformers, we measured the decay kinetics of two different peroxy radical structures. To measure decay kinetics, we moved the laser to one of two spectral features (7453 and 7652 cm^{-1}). Then we collected 60 ringdowns (30 with the photolysis laser on, 30 with the photolysis laser off), varying the delay time between the photolysis laser and the near-infrared probe laser. We collected ringdowns at 100 different delay times, randomly, between 0 and 10 ms (for the RO_2 self-reaction) and between 0–0.3 ms (with added NO). To assess the dependence of the $\text{RO}_2 + \text{NO}$ reaction rate on the identity of the peroxy radical, we varied the NO concentration. Kinetics decays were fit to a simple second-order integrated rate law, in the case of the self-reaction, and a pseudo-first order integrated rate law, for reactions with NO. Although the decays in the presence of NO were fast, use of the simultaneous kinetics and ringdown (SKaR)³⁸ technique did not significantly improve the fits, and was not used to analyze this data. Bimolecular rate coefficients for the self-reaction are reported in $\text{cm}^3 \text{ molecule}^{-1} \text{ s}^{-1}$ by assuming that the initial number of isoprene peroxy radicals formed was the same as the measured concentration of ethyl peroxy radicals during calibration experiments.

3 Results and Discussion

3.1 Peroxy radical spectrum and assignment

Figure 1 shows the cavity ringdown spectra for the peroxy radicals formed upon chlorine-initiated oxidation of isoprene. There is broad absorption through most of the near-infrared region between 7000–9000 cm^{-1} ; but there are several distinct features that appear at 7444, 7646, 7728, 7873, and 8019 cm^{-1} . These features likely correspond to the A–X origin transition of several distinct isomeric structures. There is also significant absorbance in the region around 8500 cm^{-1} , probably appearing from an excitation to the A state with one quanta of excitation in the O–O stretch mode.¹⁹ The feature observed at 7646 cm^{-1} is very sharp, not unlike the spectral features observed by Thomas and Miller in their investigation of the C3 allylic peroxy radical.²⁶ There are several possible allylic peroxy radicals that are expected to form during chlorine-initiated oxidation of isoprene. In fact, the only isomers that are not allylic peroxy radicals are isomers B and C. The observed bands in the peroxy radical spectrum were assigned using quantum chemistry predictions of the A–X vibrationally-resolved spectrum. The computed structures all have C_1 symmetries, leading us to use the techniques discussed in Chapter 2 to compute the electronically excited states. We used time-dependent density functional theory as the only method for these calculations because of the computational expense in performing equation of motion calculations.

3.1.a Ground State Energies

Chlorine-substituted peroxy radicals. In order to identify the absorbers present in the spectrum, we performed density functional theory calculations on the six isomers identified by Lei et al.³² (shown in Figure 2). Lei et al. optimized the geometries for all six isomers at using B3LYP and the 6-31G(d,p) basis set; then, using those structures computed the energy differences with both MP2 and CCSD(T) methods. Table 1 lists the ground state energy differences (relative to the energy of the A conformer, in cm^{-1}) reported by Lei et al., using CCSD(T)/6-31G(d,p) calculations. The A conformer was found to be the lowest-energy structure. Only two of the other five isomers were found to have energies within $< 3k_B T$ ($\sim 600 \text{ cm}^{-1}$) of the global minimum, suggesting that we should not expect all isomers to appear in our room temperature experiments.

Starting with the structures reported by Lei et al., we performed ground state geometry optimization calculations using B3LYP and two different basis sets: the basis set used by Lei et al. for their geometry optimizations (6-31G(d,p)) and one including more correlation (aug-cc-pVDZ). The zero-point energy corrected ground state energy differences are listed in Table 1, relative to the energy of isomer A. These two sets of calculations identify the F isomer, not the A isomer as the minimum energy structure, appearing almost 900 cm^{-1} lower in energy than the A isomer. This discrepancy may be due to the fact that we did not perform an exhaustive search for the minimum energy structures with these basis sets. The geometries calculated here do not differ significantly from those reported by Lei et al.

Unsubstituted isoprene peroxy radicals. Additionally, we considered the possible formation of unsubstituted peroxy radicals, formed during chlorine-initiated abstraction of an allylic hydrogen atom on isoprene. To our knowledge, no prior calculations have been carried out on the peroxy radical formed from the allylic radical formed during the chlorine atom addition-elimination process. We started with the global minimum allylic radical computed by Braña and Sordo, and using intuition, added the O_2 group to the C5 carbon atom, forming an allylic peroxy radical. We investigated this structure, scanning over two major dihedral angles (O–O–C5–C2) and (O–C5–C2–C3), finding three local minimum structures, shown in Figure 3. Table 1 lists their ground state energy differences, relative to Isomer G, the minimum structure for the unsubstituted peroxy radicals.

3.2.b A–X Electronic Transition

The A–X adiabatic electronic transitions calculated for the six chlorine-substituted isoprene peroxy radical isomers and three unsubstituted isoprene peroxy radicals are listed in Table 2. These values are calculated using the TD-DFT method using a scaling factor as discussed in Chapter 2. We scaled the adiabatic electronic transition energy by the average scale factor needed to align the two calculated unsubstituted ethyl peroxy radical conformers with the experimentally-observed origin transitions.^{18,20-21} The scaling factor was 0.847. The electronic transition energy for the A conformer (identified by Lei et al. as the global minimum structure) is closest in energy to a prominent peak in the experimental spectrum

(at 7444 cm^{-1}). The A–X electronic transition for the A conformer was calculated to be 7431 cm^{-1} , within 15 cm^{-1} of that experimental peak.

3.2.c Vibrational Structure

The A–X spectra of peroxy radicals typically exhibit excitations to vibrationally-excited electronic states—specifically exciting C–O–O bend and O–O stretch modes of the excited state which appear 500 and 950 cm^{-1} shifted from the origin.¹⁹ Using DFT and TD-DFT optimized geometries, we computed the vibrational harmonic frequencies of the X and A states at B3LYP/aug-cc-pVDZ (listed in the Supporting Information). The A state O–O stretch frequencies are listed in Table 1, scaled by 0.970 .³⁶ The O–O stretch vibrations are slightly higher-energy (A state frequencies of 1000 cm^{-1}) than those of alkyl peroxy radicals. This is the same trend noted in Chapter 2 and observed for fluorinated peroxy radicals by Zalyubovsky et al.¹⁶

The simulated Franck-Condon spectra for all six isomers with chlorine substitutions are shown in Figure 3. The same spectra for the three unsubstituted peroxy radicals are shown in Figure 4. The most intense peak in each spectrum was normalized to 1. Isomers A, C, E, and G all have Franck-Condon spectra reminiscent of the spectra presented in Chapter 2, with a very intense 0-0 excitation, followed by less-intense peaks, primarily favoring excitation of the O–O stretch modes. Isomer F similarly has a strong 0–0 overlap integral, but has reasonably strong excitations of several low-frequency modes. Both isomers B and D have surprisingly strong excitations to low-frequency A state torsional modes, with intensities exceeding that of the origin transition. Without improved ground state energy optimizations and higher-level frequency calculations, it is impossible to know whether these features are real.

3.2 Peroxy radical kinetics

We measured the decay of two different features in the peroxy radical spectrum, presumably coming from distinct isomers or conformers. Figure 4 compares the decays of the two features, caused by peroxy radical self- and cross-reactions. Since the peroxy radicals are formed as a mixture of several different species, this decay rate represents the weighted

average of all peroxy radicals, including self-reactions, reactions with other peroxy radicals, and reaction with HO₂. The measured rate coefficient for the weighted self- and cross-reactions at 7453 cm⁻¹ ($(1.27 \pm 0.04) \times 10^{-12}$ cm³ s⁻¹) was slower than the decay at 7652 cm⁻¹ ($(8.4 \pm 1.5) \times 10^{-12}$ cm³ s⁻¹). Since we expect the reactions of primary allylic peroxy radicals to be significantly faster than a tertiary allylic peroxy radical (the A chlorine-substituted isomer), it makes sense that the peak we tentatively assigned to the unsubstituted allylic peroxy radical has a faster decay rate.³⁹

Figure 7 shows the NO-dependent decays for the reaction of peroxy radicals with NO, measured at 7453 cm⁻¹. We collected similar data for the peak at 7652 cm⁻¹. NO concentrations ranged from 5×10^{14} – 5×10^{15} cm⁻³. We fit each decay trace to an exponential function and plotted these decays as a function of NO for both peaks (Figure 8). The two peaks have the same fitted RO₂ + NO rate constant— $(5.3 \pm 0.09) \times 10^{-12}$ cm³ s⁻¹ for 7453 cm⁻¹ and $(5 \pm 2) \times 10^{-12}$ cm³ s⁻¹ at 7652 cm⁻¹. Past work on the reaction of chlorine-substituted isoprene-derived peroxy radicals with NO found a bulk reaction rate constant of $(11.5 \pm 1.1) \times 10^{-12}$ cm³ s⁻¹, measured from a mixture of all chlorine-substituted isomers and conformers.⁴⁰ In their work, Patchen et al. calculated the isomer-specific rate constant for these reactions, finding that the chloro-isoprenyl peroxy radical reaction with NO has an isomer-dependence, with one of the isomers (isomer C) having a significantly faster computed rate.

4 Conclusions

In this chapter, we report the near-infrared spectrum of the peroxy radicals formed during chlorine-initiated oxidation of isoprene. We assign the congested spectrum to absorption of multiple peroxy radicals, including chlorine-substituted isoprene peroxy radicals as well as the unsubstituted allylic peroxy radicals formed from addition-elimination by the chlorine atom, rather than addition. We measured the isomer-dependent decay rates of the peroxy radical self-/cross-reactions and reported an isomer-independent rate coefficient for reaction with NO.

5 References

1. Finlayson-Pitts, B. J.; Pitts, J., James N., *Chemistry of the Upper and Lower Atmosphere*. Academic Press: San Diego, California, 2000.
2. Rasmussen, R. A.; Khalil, M. A. K., Isoprene over the Amazon Basin. *J. Geophys. Res.: Atmos.* **1988**, *93*, 1417-1421.
3. Trainer, M.; Williams, E. J.; Parrish, D. D.; Buhr, M. P.; Allwine, E. J.; Westberg, H. H.; Fehsenfeld, F. C.; Liu, S. C., Models and Observations of the Impact of Natural Hydrocarbons on Rural Ozone. *Nature* **1987**, *329*, 705-707.
4. Jacob, D. J.; Wofsy, S. C., Photochemistry of Biogenic Emissions Over the Amazon Forest. *J. Geophys. Res.: Atmos.* **1988**, *93*, 1477-1486.
5. Blake, N. J.; Penkett, S. A.; Clemmshaw, K. C.; Anwyl, P.; Lightman, P.; Marsh, A. R. W.; Butcher, G., Estimates of Atmospheric Hydroxyl Radical Concentrations from the Observed Decay of Many Reactive Hydrocarbons in Well-defined Urban Plumes. *J. Geophys. Res.: Atmos.* **1993**, *98*, 2851-2864.
6. Moore, R. M.; Oram, D. E.; Penkett, S. A., Production of Isoprene by Marine Phytoplankton Cultures. *Geophys. Res. Lett.* **1994**, *21*, 2507-2510.
7. Ratte, M.; Bujok, O.; Spitzzy, A.; Rudolph, J., Photochemical Alkene Formation in Seawater from Dissolved Organic Carbon: Results from Laboratory Experiments. *J. Geophys. Res.: Atmos.* **1998**, *103*, 5707-5717.
8. Tanaka, P. L.; Oldfield, S.; Neece, J. D.; Mullins, C. B.; Allen, D. T., Anthropogenic Sources of Chlorine and Ozone Formation in Urban Atmospheres. *Environ. Sci. Technol.* **2000**, *34*, 4470-4473.
9. Knipping, E. M.; Lakin, M. J.; Foster, K. L.; Jungwirth, P.; Tobias, D. J.; Gerber, R. B.; Dabdub, D.; Finlayson-Pitts, B. J., Experiments and Simulations of Ion-Enhanced Interfacial Chemistry on Aqueous NaCl Aerosols. *Science* **2000**, *288*, 301-306.
10. Singh, H. B.; Thakur, A. N.; Chen, Y. E.; Kanakidou, M., Tetrachloroethylene as an Indicator of Low Cl Atom Concentrations in the Troposphere. *Geophys. Res. Lett.* **1996**, *23*, 1529-1532.
11. Spicer, C. W.; Chapman, E. G.; Finlayson-Pitts, B. J.; Plastridge, R. A.; Hubbe, J. M.; Fast, J. D.; Berkowitz, C. M., Unexpectedly High Concentrations of Molecular Chlorine in Coastal Air. *Nature* **1998**, *394*, 353-356.
12. Lightfoot, P. D.; Cox, R. A.; Crowley, J. N.; Destriau, M.; Hayman, G. D.; Jenkin, M. E.; Moortgat, G. K.; Zabel, F., Organic Peroxy Radicals: Kinetics, Spectroscopy and Tropospheric Chemistry. *Atmos. Environ., Part A* **1992**, *26*, 1805-1961.
13. Wallington, T. J.; Dagaut, P.; Kurylo, M. J., UV Absorption Cross Sections and Reaction Kinetics and Mechanisms for Peroxy Radicals in the Gas Phase. *Chem. Rev.* **1992**, *92*, 667-710.
14. Nielsen, O. J.; Wallington, T. J., Ultraviolet Absorption Spectra of Peroxy Radicals in the Gas Phase. In *Peroxy Radicals*, Alfassi, Z. B., Ed. John Wiley & Sons Ltd.: New York, NY, 1997; pp 69-80.

15. Miller, T. A., Spectroscopic Probing and Diagnostics of the Geometric Structure of the Alkoxy and Alkyl Peroxy Radical Intermediates. *Mol. Phys.* **2006**, *104*, 2581-2593.
16. Zalyubovsky, S. J.; Wang, D.; Miller, T. A., Observation of the $\tilde{A}-\tilde{X}$ electronic transition of the CF_3O_2 radical. *Chem. Phys. Lett.* **2001**, *335*, 298-304.
17. Tarczay, G.; Zalyubovsky, S. J.; Miller, T. A., Conformational analysis of the 1- and 2-propyl peroxy radicals. *Chem. Phys. Lett.* **2005**, *406*, 81-89.
18. Rupper, P.; Sharp, E. N.; Tarczay, G.; Miller, T. A., Investigation of Ethyl Peroxy Radical Conformers via Cavity Ringdown Spectroscopy of the $\tilde{A}-\tilde{X}$ Electronic Transition. *J. Phys. Chem. A* **2007**, *111*, 832-840.
19. Sharp, E. N.; Rupper, P.; Miller, T. A., The Structure and Spectra of Organic Peroxy Radicals. *Phys. Chem. Chem. Phys.* **2008**, *10*, 3955-3981.
20. Just, G. M. P.; Rupper, P.; Miller, T. A.; Meerts, W. L., High-resolution Cavity Ringdown Spectroscopy of the Jet-cooled Ethyl Peroxy Radical $\text{C}_2\text{H}_5\text{O}_2$. *J. Chem. Phys.* **2009**, *131*, 184303.
21. Melnik, D.; Chhantyal-Pun, R.; Miller, T. A., Measurements of the Absolute Absorption Cross Sections of the $\tilde{A}-\tilde{X}$ Transition in Organic Peroxy Radicals by Dual-Wavelength Cavity Ring-Down Spectroscopy. *J. Phys. Chem. A* **2010**, *114*, 11583-11594.
22. Sprague, M. K.; Garland, E. R.; Mollner, A. K.; Bloss, C.; Bean, B. D.; Weichman, M. L.; Mertens, L. A.; Okumura, M.; Sander, S. P., Kinetics of *n*-Butoxy and 2-Pentoxy Isomerization and Detection of Primary Products by Infrared Cavity Ringdown Spectroscopy. *J. Phys. Chem. A* **2012**, *116*, 6327-6340.
23. Sprague, M. K.; Mertens, L. A.; Widgren, H. N.; Okumura, M.; Sander, S. P.; McCoy, A. B., Cavity Ringdown Spectroscopy of the Hydroxy-Methyl-Peroxy Radical. *J. Phys. Chem. A* **2013**, *117*, 10006-10017.
24. Kline, N. D.; Miller, T. A., Observation of the Electronic Transition of C_6-C_{10} Peroxy Radicals. *Chem. Phys. Lett.* **2014**, *601*, 149-154.
25. Zalyubovsky, S. J.; Glover, B. G.; Miller, T. A.; Hayes, C.; Merle, J. K.; Hadad, C. M., Observation of the $\tilde{A}-\tilde{X}$ Electronic Transition of the 1- $\text{C}_3\text{H}_7\text{O}_2$ and 2- $\text{C}_3\text{H}_7\text{O}_2$ Radicals Using Cavity Ringdown Spectroscopy. *J. Phys. Chem. A* **2005**, *109*, 1308-1315.
26. Thomas, P. S.; Miller, T. A., Cavity Ringdown Spectroscopy of the NIR Electronic Transition of Allyl Peroxy Radical ($\text{H}_2\text{C}=\text{CH}-\text{CH}_2\text{OO}\cdot$). *Chem. Phys. Lett.* **2010**, *491*, 123-131.
27. Atkinson, D. B.; Spillman, J. L., Alkyl Peroxy Radical Kinetics Measured Using Near-infrared CW-Cavity Ring-down Spectroscopy. *J. Phys. Chem. A* **2002**, *106*, 8891-8902.
28. Melnik, D.; Miller, T. A., Kinetic Measurements of the $\text{C}_2\text{H}_5\text{O}_2$ Radical Using Time-resolved Cavity Ring-down Spectroscopy with a Continuous Source. *J. Chem. Phys.* **2013**, *139*, 094201.
29. Deev, A.; Sommar, J.; Okumura, M., Cavity Ringdown Spectrum of the Forbidden $\tilde{A}^2E''\leftarrow\tilde{X}^2A'_2$ Transition of NO_3 : Evidence for Static Jahn-Teller Distortion in the \tilde{A} State. *J. Chem. Phys.* **2005**, *122*, 224305.

30. Takematsu, K.; Eddingsaas, N. C.; Robichaud, D. J.; Okumura, M., Spectroscopic Studies of the Jahn-Teller Effect in the \tilde{A}^2E'' State of the Nitrate Radical NO₃. *Chem. Phys. Lett.* **2013**, *555*, 57-63.
31. Dibble, T. S., Computations on the $\tilde{A}-\tilde{X}$ Transition of Isoprene-OH-O₂ Peroxy Radicals. *J. Comput. Chem.* **2005**, *26*, 836-845.
32. Lei, W.; Zhang, R.; McGivern, W. S.; Derecskei-Kovacs, A.; North, S. W., Theoretical Study of OH-O₂-Isoprene Peroxy Radicals. *J. Phys. Chem. A* **2001**, *105*, 471-477.
33. Lei, W.; Zhang, R., Chlorine Atom Addition Reaction to Isoprene: A Theoretical Study. *J. Chem. Phys.* **2000**, *113*, 153-157.
34. Lei, W.; Zhang, R.; Molina, L. T.; Molina, M. J., Theoretical Study of Chloroalkenylperoxy Radicals. *J. Phys. Chem. A* **2002**, *106*, 6415-6420.
35. Braña, P.; Sordo, J. A., Mechanistic Aspects of the Abstraction of an Allylic Hydrogen in the Chlorine Atom Reaction with 2-Methyl-1,3-Butadiene (Isoprene). *J. Am. Chem. Soc.* **2001**, *123*, 10348-10353.
36. Johnson III, R. D., NIST Computational Chemistry Comparison and Benchmark Database. NIST Standard Reference Database Number 101, Release 17b, September 2015.
37. Frisch, M. J.; Trucks, G. W.; Schlegel, H. B.; Scuseria, G. E.; Robb, M. A.; Cheeseman, J. R.; Scalmani, G.; Barone, V.; Mennucci, B.; Petersson, G. A., et al. *Gaussian 09*, Revision E.01; Gaussian, Inc.: Wallingford CT, 2009.
38. Brown, S. S.; Ravishankara, A. R.; Stark, H., Simultaneous Kinetics and Ring-down: Rate Coefficients from Single Cavity Loss Temporal Profiles. *J. Phys. Chem. A* **2000**, *104*, 7044-7052.
39. Jenkin, M. E.; Hayman, G. D., Kinetics of Reactions of Primary, Secondary and Tertiary β -Hydroxy Peroxyl Radicals. *J. Chem. Soc., Faraday Trans.* **1995**, *91*, 1911-1922.
40. Patchen, A. K.; Pennino, M. J.; Elrod, M. J., Overall Rate Constant Measurements of the Reaction of Chloroalkylperoxy Radicals with Nitric Oxide. *J. Phys. Chem. A* **2005**, *109*, 5865-5871.

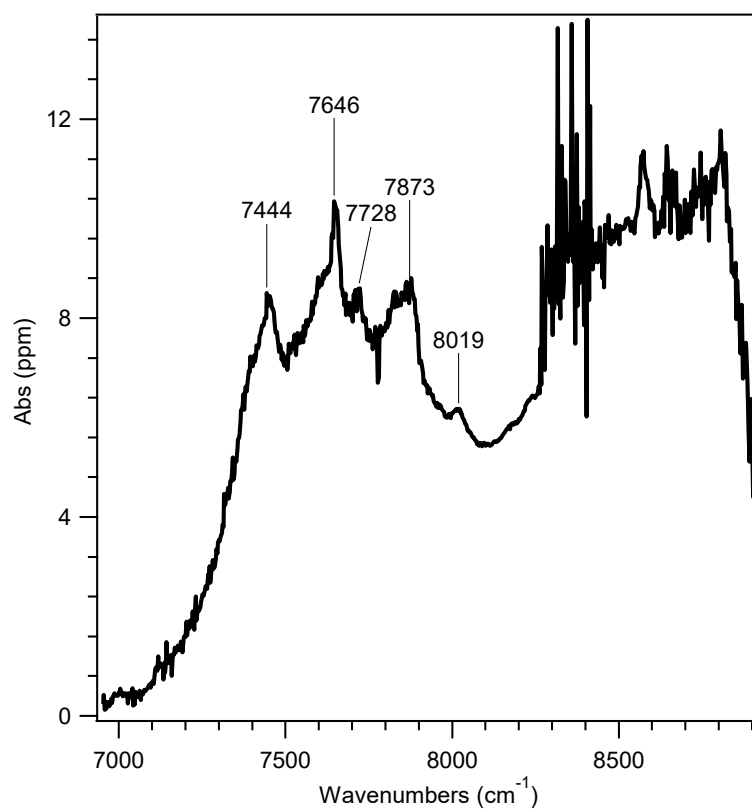


Figure 1. Near-infrared cavity ringdown spectrum of the peroxy radicals formed from chlorine-initiated oxidation of isoprene, simple alkenes. Some of the prominent peaks have been arbitrarily selected and tagged with their transition frequencies.

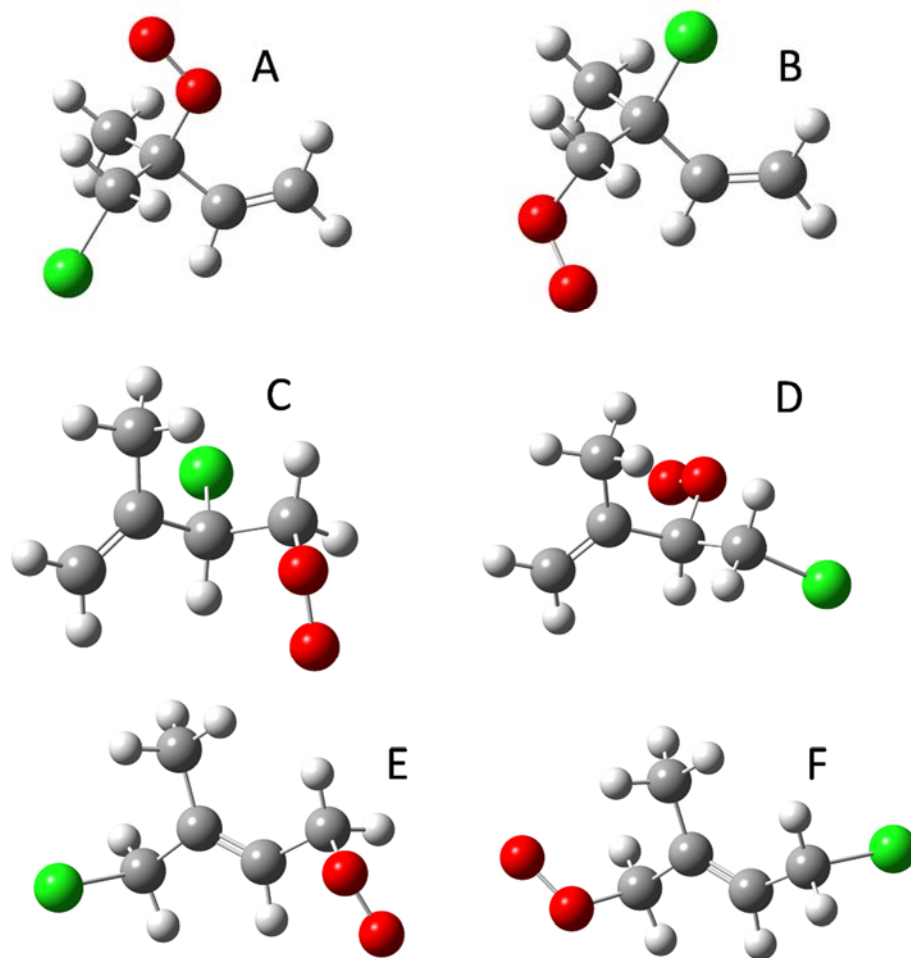


Figure 2. Structures of the six unique conformers of the chloro-isoprene peroxy radical.

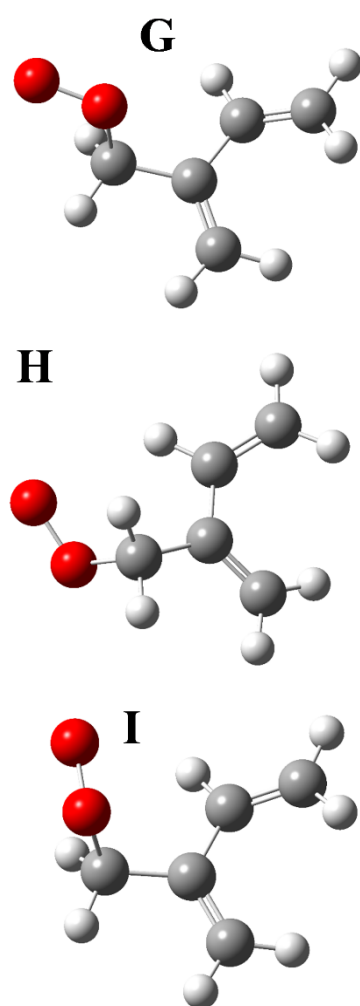


Figure 3. Structures of the three unsubstituted isoprene peroxy radicals formed from H-abstraction of isoprene.

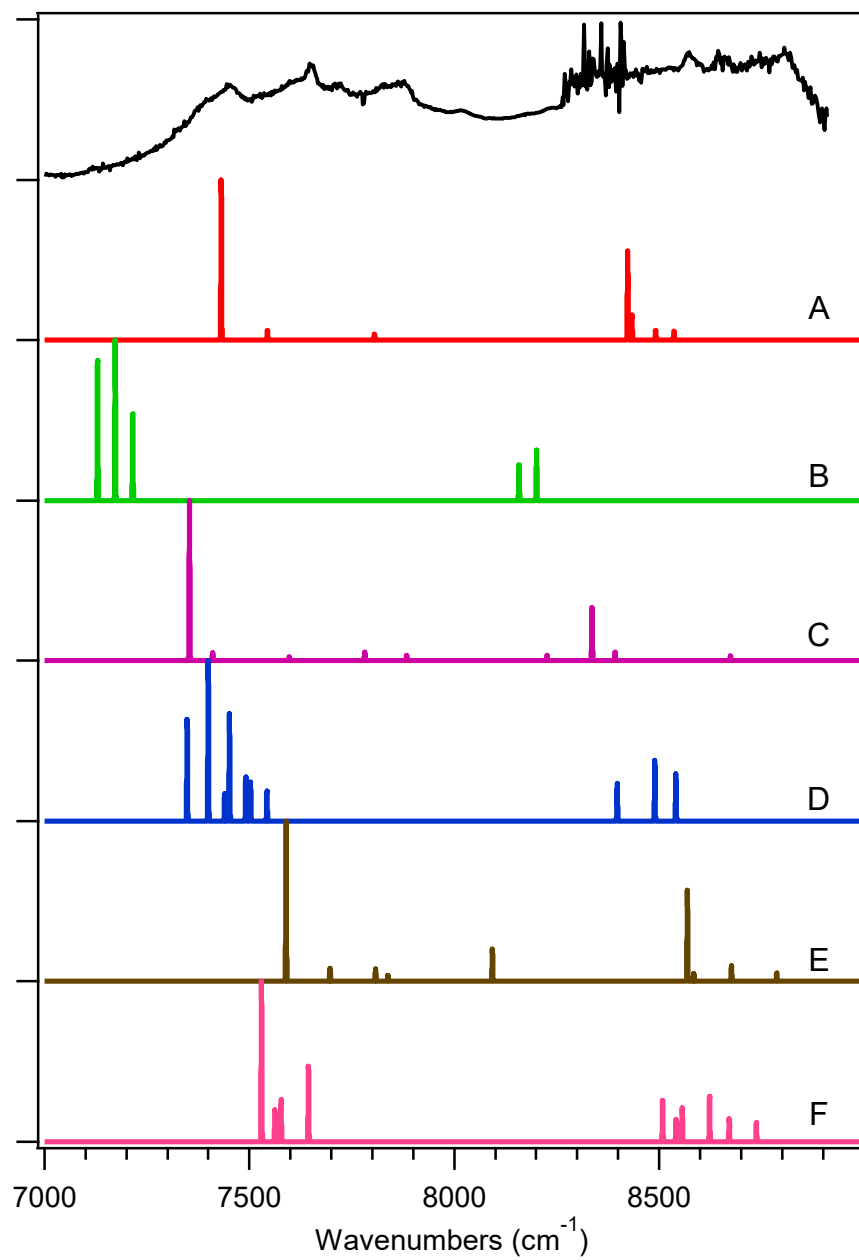


Figure 4. Comparison of the Franck-Condon spectra of the six chlorine-substituted isoprene peroxy radical isomers and the experimental spectrum of the peroxy radicals formed during chlorine-initiated oxidation of isoprene.

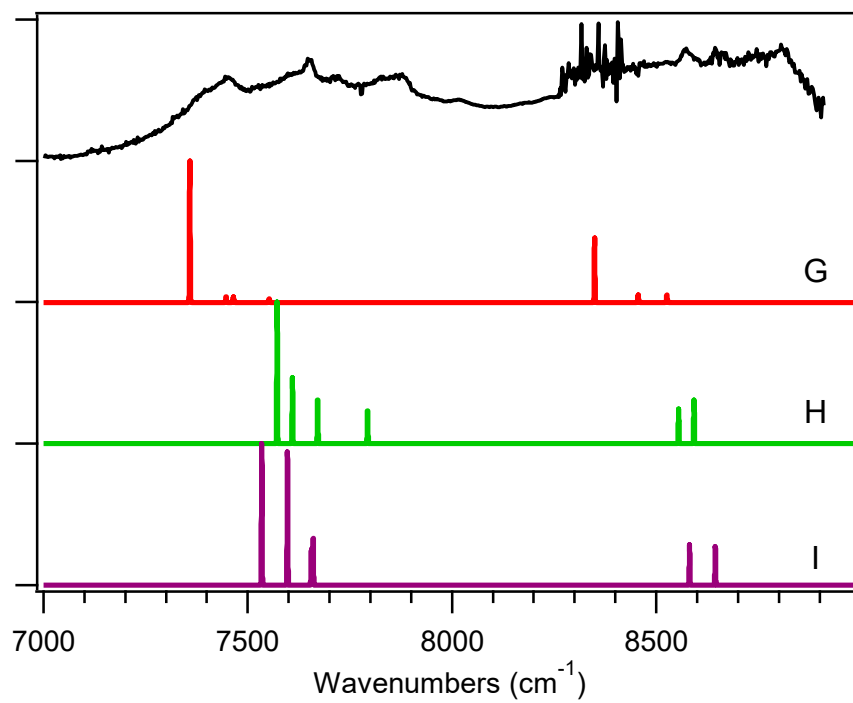


Figure 5. Comparison of the Franck-Condon spectra of the three unsubstituted isoprene peroxy radical isomers and the experimental spectrum of the peroxy radicals formed during chlorine-initiated oxidation of isoprene.

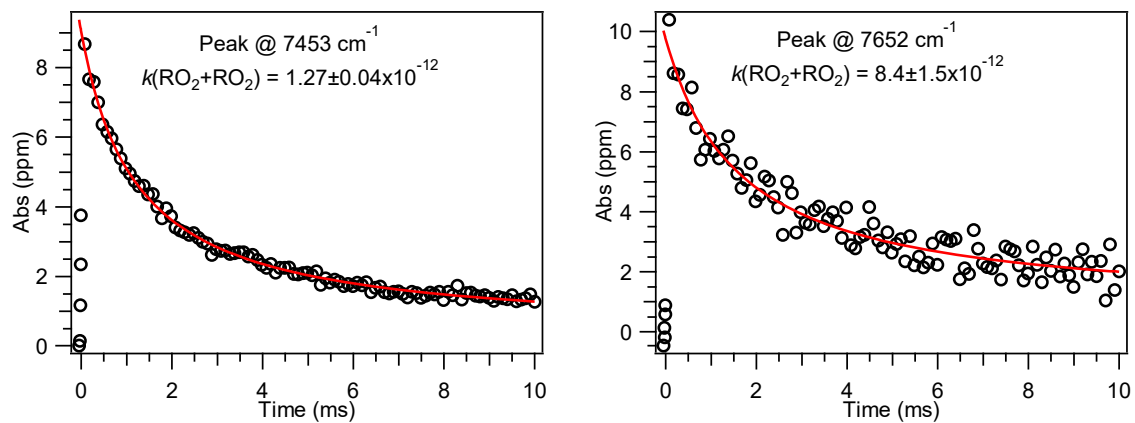


Figure 6. Experimental isoprene peroxy radical decays measured for two absorption features, measured at 7453 and 7652 cm⁻¹. Each decay has been fit to a bimolecular decay, with the decay rates reported in cm³ s⁻¹.

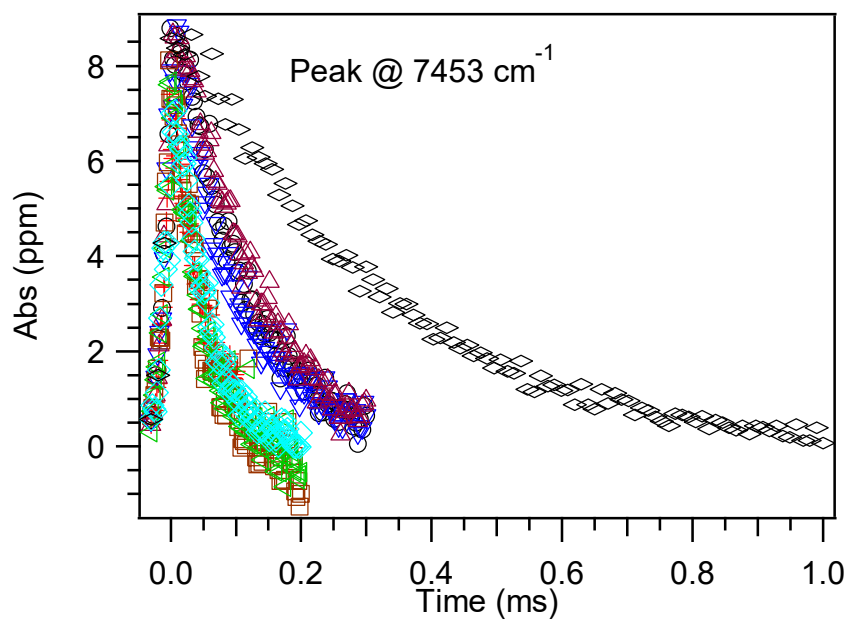


Figure 7. Experimental isoprene peroxy radical decays with NO measured for the absorption feature at 7453 cm⁻¹.

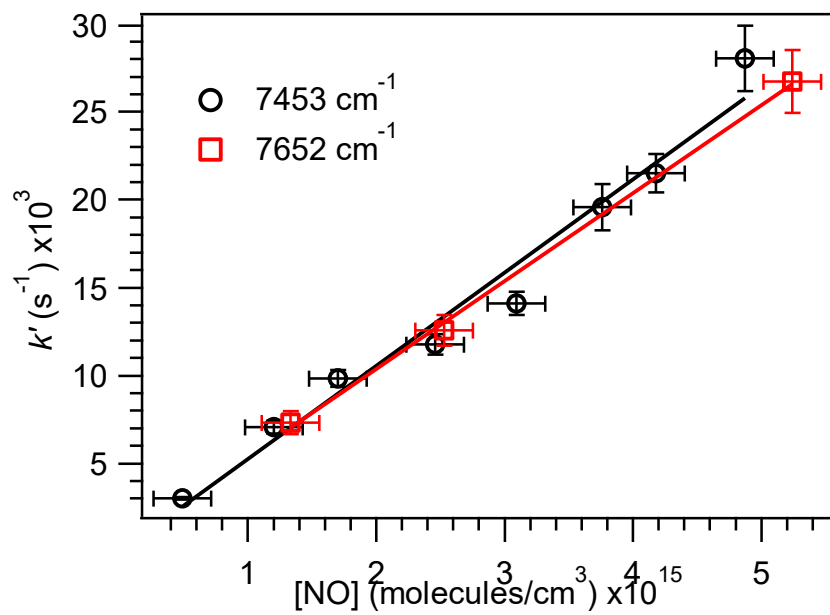


Figure 8. First order decay rates of the peroxy radical absorption peaks as a function of NO. The black circles show the decays at 7453 cm^{-1} and the red squares show the decays at 7652 cm^{-1} .

Table 1. Ground state energy differences for conformers of chloro-isoprenyl and unsubstituted peroxy radicals. Energy differences (relative to the global minimum structure for the two types of peroxy radicals) are given in cm^{-1} and include zero-point energy corrections.

chloro-isoprenyl peroxy radical			
Conformer	CCSD(T)/6-31G(d) ^a	B3LYP/6-31G(d,p)	B3LYP/aug-cc-pVDZ
A	0	0	0
B	700	740	510
C	310	380	-490
D	520	-290	-400
E	880	-670	-810
F	780	-850	-890
unsubstituted isoprenyl peroxy radical			
Conformer	B3LYP/aug-cc-pVDZ		
G	0		
H	49		
I	46		

^aEnergies taken from Lei et al., calculated at CCSD(T)/6-31G(d) for structures with geometries optimized at B3LYP/6-31G(d,p).

Table 2. The theoretical origins for the six chlorine-substituted and three unsubstituted isoprene peroxy radical conformers, along with the A state vibrations of the O–O stretch mode. Energies and vibrations are given in cm^{-1} .

chloro-isoprenyl peroxy radical		
	theoretical origin ^a	stretch ^b
A	7431	992
B	7129	986
C	7354	983
D	7348	998
E	7589	980
F	7530	979
unsubstituted peroxy radical		
	theoretical origin ^a	stretch ^b
G	7358	991
H	7572	983
I	7534	984

^aThe origin for each conformer was computed as the adiabatic energy difference between the ground state energies of the X and A states, using TD-DFT/B3LYP/aug-cc-pVDZ. The adiabatic energy difference was corrected by comparison to the same calculations for the ethyl peroxy radical, as described in the text.

^bThe vibrational frequencies for the A state of each conformer were calculated using TD-DFT B3LYP/aug-cc-pVDZ. Vibrations were scaled by 0.970.³⁶

6 Supporting Information

Table S1. Energies (Hartrees) and Cartesian coordinates (Å) for equilibrium structures of chloro-isoprenyl peroxy radical conformers. Energies are ZPVE-corrected.

Conformer A (UB3LYP/aug-cc-pVDZ)						
	X: E = -805.7859101			A: E = -805.74592746		
C	0.523425	-1.628626	0.266000	0.529254	-1.608550	0.261928
H	0.264838	-2.169763	1.183607	0.340472	-2.127339	1.208164
H	1.609245	-1.653612	0.121297	1.604018	-1.637423	0.043550
H	0.039830	-2.125357	-0.582522	-0.005921	-2.127278	-0.540972
C	0.025639	-0.187914	0.362544	0.024970	-0.166765	0.365706
C	0.496036	0.705176	-0.801651	0.467146	0.730967	-0.810113
H	1.587453	0.694912	-0.859815	1.558197	0.766922	-0.869170
H	0.128805	1.726891	-0.670224	0.060483	1.738024	-0.688002
C	-1.467430	-0.120910	0.564649	-1.467483	-0.118860	0.575732
H	-2.040007	-0.433410	-0.310964	-2.038085	-0.416658	-0.306298
C	-2.105297	0.257223	1.675044	-2.097914	0.231639	1.697821
H	-1.581811	0.578573	2.573895	-1.561199	0.534284	2.595994
H	-3.194567	0.254670	1.708102	-3.186617	0.224215	1.743581
Cl	-0.121317	0.129396	-2.409030	-0.120399	0.113318	-2.415813
O	0.619599	0.453299	1.575458	0.600504	0.482281	1.560380
O	1.932198	0.393910	1.598369	1.966946	0.356254	1.606562
Isomer B (UB3LYP/aug-cc-pVDZ)						
	X: E = -805.7835862			A: E = -805.74522681		
C	0.866319	-1.643435	0.305694	0.936495	-1.611827	0.201627
H	0.516237	-2.226125	1.164829	0.587283	-2.280960	0.996048
H	1.957595	-1.545772	0.359352	2.019093	-1.469678	0.304807
H	0.605392	-2.183167	-0.614652	0.734679	-2.080332	-0.770697
C	0.195180	-0.266795	0.293855	0.201803	-0.273258	0.273670
C	0.754855	0.630183	-0.831732	0.750578	0.739142	-0.760185
H	1.842970	0.723190	-0.739130	1.824946	0.892295	-0.611843
H	0.269280	1.609460	-0.851536	0.217943	1.696068	-0.695085
C	-1.305290	-0.395827	0.201991	-1.290153	-0.455745	0.141825
H	-1.627621	-0.887513	-0.719890	-1.561272	-1.055744	-0.730118
C	-2.224648	-0.005800	1.085943	-2.254797	0.028227	0.928106
H	-1.961101	0.488649	2.019428	-2.039647	0.623067	1.814402
H	-3.282292	-0.177218	0.887903	-3.300737	-0.174163	0.699458
O	0.544729	0.003630	-2.134081	0.689591	0.252480	-2.121196
O	-0.537270	0.455876	-2.738673	-0.602674	0.275952	-2.599804
Cl	0.700081	0.624265	1.831837	0.632871	0.533103	1.885340
Isomer C (UB3LYP/aug-cc-pVDZ)						

X: E = -805.7881353				A: E = -805.748568099		
C	1.949516	0.667271	1.156179	1.973403	0.611182	1.146040
H	1.664797	0.311930	2.146660	1.682281	0.288649	2.145844
H	2.973290	1.021414	1.034651	3.009008	0.923431	1.010533
C	1.085927	0.664873	0.131243	1.103901	0.616540	0.126434
C	1.454281	1.143389	-1.249588	1.480642	1.046586	-1.267897
H	2.453492	1.593813	-1.248213	2.495782	1.459712	-1.283076
H	1.463245	0.313475	-1.972546	1.454640	0.198151	-1.968279
H	0.735959	1.890810	-1.614854	0.788558	1.811271	-1.648120
C	-0.310164	0.149142	0.361061	-0.308600	0.160524	0.374621
C	-0.791826	-0.926423	-0.612599	-0.842333	-0.902492	-0.590639
H	-0.734794	-0.596753	-1.655159	-0.803940	-0.565465	-1.631356
H	-1.805937	-1.255305	-0.365919	-1.870732	-1.185780	-0.332908
O	0.084330	-2.092268	-0.548344	-0.008166	-2.084856	-0.595352
O	-0.134396	-2.797570	0.544354	-0.164831	-2.758885	0.596981
Cl	-1.544426	1.521499	0.211985	-1.493492	1.576533	0.209083
H	-0.420667	-0.215666	1.385795	-0.424336	-0.175154	1.408558

Isomer D (UB3LYP/aug-cc-pVDZ)

X: E = -805.7877429				A: E = -805.748206715		
C	0.468915	0.201724	-1.535013	0.549959	0.128337	-1.490307
C	-0.077796	0.278141	-0.126226	-0.038007	0.307217	-0.100642
C	0.893559	-0.244357	0.921673	0.787427	-0.400216	0.968680
H	1.875742	0.216102	0.778985	1.836930	-0.114614	0.852161
H	0.981515	-1.334166	0.878251	0.680957	-1.486632	0.900065
Cl	0.359029	0.166305	2.605946	0.297706	0.070587	2.648638
O	-1.283309	-0.577474	-0.009675	-1.364317	-0.290130	0.005993
O	-2.350445	0.013668	-0.496567	-2.237910	0.383851	-0.815829
H	-0.403629	1.295500	0.111804	-0.127417	1.374639	0.143349
C	0.898169	-1.150229	-2.046668	0.473001	-1.244133	-2.104817
H	1.751110	-1.549476	-1.476493	0.990876	-1.996289	-1.490571
H	0.080654	-1.880189	-1.958039	-0.573791	-1.566265	-2.191074
H	1.196275	-1.089573	-3.099692	0.926569	-1.247624	-3.102778
C	0.541213	1.320542	-2.267475	1.113785	1.180366	-2.096998
H	0.935397	1.307962	-3.284032	1.579665	1.088462	-3.078249
H	0.205116	2.282173	-1.879684	1.126039	2.169151	-1.636565

Isomer E (UB3LYP/aug-cc-pVDZ)

X: E = -805.7895906				A: E = -805.748755714		
C	0.903607	-1.675984	0.181886	0.900353	-1.671163	0.193773
H	1.485831	-1.371488	1.055009	1.467697	-1.369999	1.077790
H	1.503052	-2.329953	-0.461865	1.511822	-2.320035	-0.443827
C	0.353105	-0.498329	-0.571422	0.358122	-0.490918	-0.561217
C	0.568279	0.732413	-0.072097	0.558237	0.738457	-0.051345

H	1.097655	0.833249	0.878485	1.063359	0.830935	0.912626
C	-0.354781	-0.818496	-1.861191	-0.325840	-0.806364	-1.865344
H	0.345243	-1.277470	-2.577153	0.397285	-1.218492	-2.586992
H	-1.154322	-1.550191	-1.681745	-1.097500	-1.572686	-1.710962
H	-0.796666	0.062080	-2.337635	-0.799037	0.067422	-2.324325
C	0.162751	2.034119	-0.682999	0.163039	2.037721	-0.678924
H	1.023192	2.683427	-0.889763	1.035177	2.666207	-0.915549
H	-0.458279	1.930710	-1.578108	-0.449787	1.923642	-1.577770
Cl	-0.435949	-2.759650	0.827915	-0.445760	-2.763095	0.813035
O	-0.694797	2.787777	0.252468	-0.711166	2.822770	0.194841
O	0.015756	3.373641	1.191675	0.026846	3.317134	1.245881
Isomer F (UB3LYP/aug-cc-pVDZ)						
X: E = -805.7899716				A: E = -805.749458802		
C	0.555017	-1.648953	0.780138	0.610777	-1.651585	0.791704
H	0.544292	-1.389751	1.844856	0.626508	-1.368290	1.849286
H	1.535536	-2.039611	0.481220	1.601727	-2.025934	0.494321
C	0.092566	-0.505461	-0.083571	0.136671	-0.524466	-0.086365
C	-0.340491	0.616427	0.522384	-0.331519	0.586984	0.514128
H	-0.334953	0.654684	1.614394	-0.351109	0.621481	1.606226
C	0.176158	-0.736655	-1.567881	0.256362	-0.742122	-1.569668
H	1.213648	-0.962925	-1.856759	1.289868	-1.017726	-1.828827
H	-0.425383	-1.609839	-1.858555	-0.382656	-1.580858	-1.882888
H	-0.160924	0.124910	-2.152327	-0.013832	0.142102	-2.155751
C	-0.835336	1.853344	-0.142803	-0.840810	1.814038	-0.157779
H	-1.782202	2.191589	0.291021	-1.801376	2.131944	0.261105
H	-0.937667	1.763995	-1.225876	-0.924341	1.723510	-1.242431
Cl	0.331545	3.251991	0.138256	0.291959	3.237031	0.142848
O	-0.382556	-2.783536	0.675335	-0.300480	-2.804202	0.806197
O	-0.014455	-3.652602	-0.242577	-0.199143	-3.514905	-0.366394

Table S2. Energies (Hartrees) and Cartesian coordinates (Å) for equilibrium structures of unsubstituted isoprene peroxy radical conformers. Energies are ZPVE-corrected.

Isomer G (UB3LYP/aug-cc-pVDZ)						
	X: E = -344.9498007			A: E = -344.910209124		
C	-1.299008	-0.424785	0.728803	1.296485	-0.417359	-0.727110
C	-0.600488	-0.181907	-0.549543	0.593275	-0.174199	0.546833
C	-2.367535	0.250480	1.175457	2.382326	0.242820	-1.154859
H	-0.872980	-1.209412	1.361672	0.859273	-1.184772	-1.372556
C	-1.220574	0.219070	-1.673514	1.204802	0.211261	1.680782
H	-2.795792	1.085313	0.619181	2.820527	1.062755	-0.584388
H	-2.834368	-0.001809	2.127069	2.853936	-0.007193	-2.104726
H	-2.301782	0.347814	-1.712839	2.287937	0.316384	1.734266
H	-0.663731	0.411199	-2.590529	0.639656	0.412037	2.590603
C	0.874993	-0.468544	-0.568247	-0.885280	-0.451761	0.555813
H	1.323195	-0.306701	-1.555204	-1.338267	-0.263345	1.538342
H	1.111291	-1.479321	-0.208991	-1.101151	-1.483636	0.235017
O	1.538310	0.460827	0.365479	-1.491397	0.447296	-0.422469
O	2.800421	0.137553	0.544758	-2.830048	0.138103	-0.508195
Isomer H (UB3LYP/aug-cc-pVDZ)						
	X: E = -344.9491899			A: E = -344.908450401		
C	1.060232	-0.055047	-0.827685	1.080657	-0.050572	-0.796937
C	0.531345	0.068177	0.546350	0.481148	0.045790	0.550098
C	2.345895	0.088130	-1.180547	2.377759	0.133047	-1.082079
H	0.318706	-0.251165	-1.606714	0.383512	-0.270789	-1.610502
C	1.211630	-0.301359	1.645759	1.099134	-0.385398	1.664346
H	3.121140	0.338053	-0.454649	3.104928	0.403006	-0.314723
H	2.658523	-0.026047	-2.218196	2.747890	0.032836	-2.102198
H	2.206733	-0.740278	1.580309	2.079506	-0.859324	1.625229
H	0.787528	-0.181722	2.642771	0.635924	-0.285424	2.646330
C	-0.868001	0.616001	0.679752	-0.893226	0.659836	0.655653
H	-1.034369	1.526459	0.092908	-0.980840	1.600497	0.093365
H	-1.143014	0.767652	1.729909	-1.177308	0.825941	1.700192
O	-1.845990	-0.371398	0.182632	-1.965076	-0.227429	0.188477
O	-2.229242	-0.119647	-1.051146	-1.993229	-0.255440	-1.186500
Isomer I (UB3LYP/aug-cc-pVDZ)						
	X: E = -344.9493719			A: E = -344.90883353		
C	-0.756572	-0.445593	-1.044094	-0.663602	-0.479176	-1.089846
C	0.609243	-0.184185	-0.547487	0.637694	-0.176597	-0.464327
C	-1.365850	0.235374	-2.025314	-1.216265	0.198416	-2.107384
H	-1.306732	-1.241515	-0.535360	-1.217429	-1.318130	-0.658104
C	1.625093	0.206287	-1.338149	1.693338	0.308155	-1.143196
H	-0.891193	1.084356	-2.519116	-0.737630	1.076810	-2.542249

H	-2.372739	-0.026446	-2.349228	-2.180996	-0.095007	-2.519904
H	1.499814	0.312942	-2.415176	1.652861	0.476426	-2.219056
H	2.615204	0.411817	-0.930910	2.634318	0.535890	-0.641987
C	0.857262	-0.430742	0.918672	0.785171	-0.508776	0.998387
H	1.906039	-0.258443	1.185820	1.817995	-0.389829	1.341950
H	0.532575	-1.428906	1.238261	0.436396	-1.529998	1.219314
O	0.111690	0.527023	1.751603	0.064878	0.400794	1.886767
O	-1.086444	0.080396	2.066390	-1.292819	0.248169	1.720511

**VUV PHOTOIONIZATION CROSS SECTIONS OF HO₂, H₂O₂,
AND H₂CO**

This chapter was published as

Dodson, L. G. et al. (2015). “VUV photoionization cross sections of HO₂, H₂O₂, and H₂CO”. In: *Journal of Physical Chemistry A* 119(8), pp. 1279–1291. doi: 10.1021/jp508942a.

Abstract

The absolute vacuum ultraviolet (VUV) photoionization spectra of the hydroperoxyl radical (HO_2), hydrogen peroxide (H_2O_2), and formaldehyde (H_2CO) have been measured from their first ionization thresholds to 12.008 eV. HO_2 , H_2O_2 , and H_2CO were generated from the oxidation of methanol initiated by pulsed-laser-photolysis of Cl_2 in a low pressure slow flow reactor. Reactants, intermediates, and products were detected by time-resolved multiplexed synchrotron photoionization mass spectrometry. Absolute concentrations were obtained from the time-dependent photoion signals by modeling the kinetics of the methanol oxidation chemistry. Photoionization cross sections were determined at several photon energies relative to the cross section of methanol, which was in turn determined relative to that of propene. These measurements were used to place relative photoionization spectra of HO_2 , H_2O_2 , and H_2CO on an absolute scale, resulting in absolute photoionization spectra.

1 Introduction

Synchrotron photoionization mass spectrometry has seen increasing use in the study of gas phase free radical reactions.¹ Photoionization provides a nearly universal method for the detection of small molecules with high sensitivity. Bayes pioneered the use of photoionization mass spectrometric detection of gas phase free radicals in flow tubes,² and this technique has become an important tool for time-resolved kinetics studies in combustion and atmospheric chemistry as well as astrochemistry.³⁻⁹ While earlier studies used quadrupole mass filters, which allowed the detection of ions with a single mass-to-charge ratio (m/z) at a time, the introduction of pulsed-extraction time-of-flight mass spectrometers gave a multiplex advantage, since one could measure the evolution of the full mass spectrum in real time.^{6,8} Dynamics experiments have further exploited the additional multiplexing that comes from imaging the ion kinetic energy distributions.¹⁰⁻¹¹

Recently, Osborn, Taatjes, and co-workers developed a Multiplexed Photoionization Mass Spectrometer (MPIMS), a significant advance in this technique, by using tunable vacuum ultraviolet (VUV) radiation from a synchrotron as the photoionization light source, coupled to either a double-focusing sector mass spectrometer or an orthogonal acceleration time-of-flight (OA-TOF) mass spectrometer.¹²⁻¹³ This approach exploits the high photon flux, wide

tunability, and spectral resolution of modern synchrotron VUV light sources by enabling one to obtain complete, well-resolved photoionization spectra (photoion signal vs. photon energy) at each mass and kinetic reaction time. Isomers of a given sum formula can be resolved by their unique photoionization spectra,¹² and the multiplexing advantage allows measurement of isomer-specific chemical kinetics.¹⁴⁻¹⁵

Accurate photoionization cross sections are necessary in MPIMS chemical kinetics studies to quantify the concentrations of reactants, intermediates, and products. The photoionization cross section of a stable molecule can be measured by ionizing a binary mixture of that molecule and a reference standard. From the ratio of the ion signals of these two species, their known concentrations, and the absolute photoionization cross section of the reference standard, the unknown molecule's cross section may be placed on an absolute basis.¹⁶⁻¹⁷ This method requires that the molar ratio of the two compounds in the binary mixture does not vary with time – a requirement not easily satisfied when one of the two species is reactive. Moreover, even measuring cross sections of stable molecules can present a challenge if they have low vapor pressures, are prone to polymerization, or cannot be supplied as pure samples.

Measurements of photoionization cross sections for polyatomic free radicals and other transient intermediates are challenging due to the difficulty in producing these species with detectable and quantifiable concentrations. As a consequence, photoionization cross sections for free radicals are commonly measured relative to a reference compound that is formed simultaneously with the target free radical in specific molar ratios. There is a growing body of studies that measure cross sections for free radical species important to the chemical kinetics of combustion and the atmosphere.¹⁸⁻³²

To provide an example of the complex techniques that have been employed to measure free radical photoionization cross sections, we consider three different approaches applied to the methyl radical. The first method for measuring the CH_3 cross section is to form radicals by photodissociation of a suitable precursor generating stoichiometric photofragments. Taatjes et al.¹⁸ followed this approach by photolyzing CH_3I and determined the CH_3 cross section

relative to the known cross section of I from the yields of the momentum-matched photofragments. In the same study, Taatjes et al.¹⁸ also used photolysis to generate methyl radicals with a known quantum yield from a precursor molecule (acetone or methyl vinyl ketone); however, in this time-dependent method using a flow-reactor setup, the observed depletion of the precursor, whose photoionization cross section is known, was used to quantify the initial CH₃ number density. The initial radical signal, as determined from the radical decay kinetics, was used to obtain the photoionization cross section of CH₃ relative to the cross section of the precursor. Gans et al.¹⁹ used a similar approach, employing pyrolysis of CH₃I and CH₃NO₂, to measure the CH₃ cross section. The third approach to measuring the CH₃ cross section used a detailed kinetics model to predict the decay of CH₃ in the presence of NO₂.²⁰ Simulated CH₃ and NO time profiles (NO forms from reaction of CH₃ and NO₂) were used to provide a quantitative relationship between the CH₃ and NO signals, yielding a methyl radical cross section relative to the known NO cross section. Given the complexity of these efforts to measure the CH₃ photoionization cross section, there is remarkable agreement amongst the results. These three techniques have been used to obtain absolute photoionization cross sections for a variety of free radicals.²¹⁻³²

In this work, we measured absolute photoionization spectra for three important species relevant to hydrocarbon oxidation, namely the hydroperoxyl radical (HO₂), hydrogen peroxide (H₂O₂), and formaldehyde (H₂CO). These species were formed in a flow reactor through a set of reactions initiated by Cl₂ photolysis in a methanol/O₂/Cl₂/He gas mixture. We measured absolute precursor depletions and used detailed chemical kinetics modeling to quantify the concentrations of all relevant species. We measured the photoionization cross sections relative to that of the methanol precursor, which in turn was determined relative to the known absolute cross section of a standard, propene.

2 Experiment

The MPIMS instrument has been described in detail in previous publications.¹²⁻¹³ The key features will be summarized in the following sections.

Briefly, we used MPIMS to probe the products resulting from laser flash photolysis of $\text{Cl}_2/\text{CH}_3\text{OH}/\text{O}_2/\text{He}$ mixtures in a slow flow reactor. An excimer laser propagated along the reactor axis, collinear with the gas flow, generating $\sim 10^{13} \text{ cm}^{-3}$ radicals at room temperature and 2.5–8 Torr total pressure. Products were sampled and detected using the MPIMS apparatus coupled to tunable VUV radiation from the Chemical Dynamics Beamline of the Advanced Light Source (ALS) at Lawrence Berkeley National Laboratory.

2.1 Multiplexed Photoionization Mass Spectrometer

The slow flow reactor was a 62 cm long, 1.05 cm inner diameter quartz tube with the inner wall coated with a fluoropolymer solution – either DuPont AF 400S2-100-1 (Experiments 1–18, 23) or Cytonix FluoroPel™ PFC 1102V-FS (Experiments 19–22) – to minimize wall reactions. Helium (Matheson Tri-Gas, 99.9999%), Cl_2 (Matheson Tri-Gas, 5.2% Cl_2 in He), O_2 (Matheson Tri-Gas, 99.998%), and CH_3OH (manometrically prepared mixture of 4.667% methanol (Sigma-Aldrich, 99.93%, purified by three freeze-pump-thaw cycles) with balance of He) were introduced into the reactor using calibrated mass flow controllers (MKS Instruments), with a total flow of 200 ± 1.2 sccm, unless otherwise noted. The total pressure was maintained at 2.50 ± 0.01 – 8.00 ± 0.04 Torr (measured with a capacitance manometer (MKS Baratron)) by throttling a Roots pump in the exhaust line.

Typical starting mole fractions of reagent gases were 30–60% O_2 , 0.3–0.6% Cl_2 , and 0.1–0.2% CH_3OH with balance of He. Approximately 1% of the Cl_2 was photolyzed by the unfocused excimer pulse (Coherent COMPex Pro 110 XeF, 351 nm, 15 ns, 4 Hz) at typical laser fluences of $28 \text{ mJ cm}^{-2} \text{ pulse}^{-1}$, leading to initial radical concentrations on the order of $\sim 10^{13} \text{ cm}^{-3}$. In separate experiments we measured the absolute photoionization spectrum of methanol relative to propene (Matheson Tri-Gas, 1.00% in Ar) (see Supporting Information).

The reactive mixture was sampled through a pinhole in the side wall of the reactor tube, expanded into the source chamber and passed through a skimmer (1.5 mm diameter) to form a nearly effusive molecular beam in a first differential chamber (pressure $\sim 10^{-6}$ Torr). The beam was intersected ~ 2.4 cm from the pinhole by quasi-continuous (500 MHz repetition rate) synchrotron undulator-generated VUV radiation.^{13,33-34} Formed cations were

accelerated and collimated into the acceleration region of a 50 kHz pulsed OA-TOF mass spectrometer and detected by a time-sensitive micro-channel plate detector. The resolution of the OA-TOF mass spectrometer ($m/\Delta m$) was ~ 1000 for these experiments. The time-of-flight spectrum was accumulated in a single-start, multiple-stop time-to-digital converter. We recorded full mass spectra every 20 μs , from 20 ms before the photolysis laser pulse to 130 ms after the pulse, providing information about the kinetics in the flow tube at all detected m/z ratios. Typically, we averaged 2,400–10,000 laser shots for two-dimensional kinetics experiments (ion counts vs. kinetic time and m/z). Time dependencies of individual species were obtained by integrating over the corresponding mass peaks at each time interval. We detected each species (HO_2 , H_2O_2 , H_2CO , CH_3OH , and Cl_2) at its parent m/z , with no dissociative ionization expected near its respective threshold energy.³⁵⁻³⁸ Table 1 summarizes the neutral species detected, the m/z of the observed ion, and the photon energies used. Cl_2 and HO_2 were only detected at 11.40 and 11.45 eV due to their high ionization thresholds.

The VUV radiation first passed through a gas filter (30 Torr Ar) to remove higher harmonics.³³ We observed no evidence of ionization by higher harmonic photons presumably leaking through the gas filter. This observation is confirmed by the absence of He ions, dissociation products (e.g. HCO^+ from H_2CO^+), and ion signals below the literature IE for measured spectra. The VUV photons were then dispersed using a 3 m monochromator. Typically, monochromator slit widths of 50–100 microns led to a photon rate of $\sim 10^{13}$ photons s^{-1} with an energy bandwidth of better than $\Delta E(\text{FWHM}) = 9$ meV. The exit slit of the monochromator was sometimes further narrowed as needed to reduce the photon flux and prevent saturation of the ion detector.

To record photoionization spectra, we scanned the energy of the ionizing photons from the synchrotron source from 10.508–12.008 eV in steps of 0.025 eV, generating three-dimensional data (i.e. ion signal as a function of m/z , kinetic time, and photoionization energy). Photoionization spectra were normalized to the photon flux measured at each photon energy with an SXUV100 photodiode placed after the photoionization volume. We daily

calibrated the photon energy axis by measurement of the $8s \leftarrow 5p$ Xe atomic resonance, observing day-to-day changes less than 10 meV.

2.2 Photoionization cross section determination

The absolute photoionization cross section of a target species (“ i ”) can be obtained relative to a reference species (“ ref ”) using gas mixtures with known concentrations of both species.³⁹ The time- and energy-dependent signal S of a species i is equal to the product of an energy-dependent scale factor $C(E)$ which includes all instrument-specific, non-mass-dependent parameters including collection efficiency and photon flux, a mass-dependent discrimination factor α_i specific to the experimental apparatus, the energy-dependent photoionization cross section $\sigma_i(E)$ and the time-dependent concentration $[N_i](t)$.

$$S_i(E, t) = C(E) \alpha_i \sigma_i(E) [N_i](t) \quad (E1)$$

The mass discrimination factor, $\alpha_i = m_i^{0.643 \pm 0.086}$, was determined empirically for this instrument.³⁰

The scale factor C is a constant for a given set of experimental conditions (number of shots, ion optics settings, VUV intensity). It can be determined experimentally by measuring the ion counts for a reference species for which $[N_{ref}](t)$ and $\sigma_{ref}(E)$ are already known. When counting two independent photoions from a single multiplexed experiment, the unknown species’ cross section can be determined relative to the reference species from the value of C determined from the reference compound. The time-dependent concentrations of the unknown species i , $[N_i](t)$, come from the kinetics model. The absolute cross section of i , $\sigma_i(E)$ which must be consistent at all times t , is obtained by fitting the observed ion signal $S_i(E, t)$ to the modeled $[N_i](t)$ over a time interval for which the kinetic model is valid.

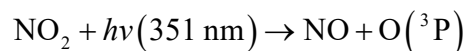
In some cases, two species were present with the same nominal m/z . At the two masses where this presented a problem ($m/z = 33$ and 34), the mass resolution of the OA-TOF spectrometer was sufficient to partially resolve the two peaks. Figure 1(a) demonstrates the fits achieved when only one species is present (H_2CO) whereas the following two panels demonstrate the extraction technique used to separate (b) HO_2 from $^{13}\text{CH}_3\text{OH}$ and (c) H_2O_2 from $\text{CH}_3^{18}\text{OH}$. Details of the separation approach are given in the Supporting Information.

2.3 Instrument response function

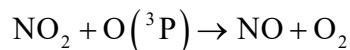
As detailed elsewhere, there is a finite instrument response function (IRF) arising from sampling a Maxwell-Boltzmann distribution of velocities in the flow cell.⁴⁰ Measurement of the time dependence of photochemically-generated species revealed that there was a slower-than-expected IRF and a slight gradient in the photolysis yield along the axis of the reactor. We characterized these effects by performing additional experiments using NO_2 photolysis in which the NO product was formed instantaneously.

The first instrumental effect is a temporal IRF caused by the transport of gas from the reactor to the ionization region and to the ion transit time from the ionization region to the extraction region.⁴⁰ These effects broaden the time-dependence observed in the ion signal. The second effect is a variation in the excimer laser fluence along the axial dimension of the flow reactor. The latter effect is primarily ascribed to divergence of the laser beam. This gradient in photolysis energy results in comparatively higher radical concentrations at the top of the flow tube than at the pinhole. This spatial gradient of radical concentration, which is established immediately following the excimer laser pulse at $t = 0$, is observed as an increase in the $t = 0$ radical concentrations as the gas flows down the tube towards the sampling pinhole.

We characterized these two effects by performing a calibration experiment with NO_2 photolysis,



followed by rapid O(³P) removal by the subsequent reaction with NO₂ ($k_{298\text{K}} = 1.04 \times 10^{-11} \text{ cm}^3 \text{ molecule}^{-1} \text{ s}^{-1}$)⁴¹⁻⁴³:



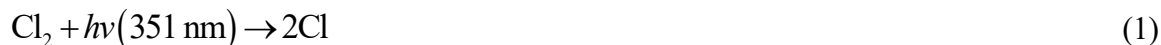
Photolysis of NO₂ occurs on the sub-picosecond time scale and reaction of NO₂ with O atoms occurs on the 0.1 ms time scale at $[\text{NO}_2] = 1.9 \times 10^{15} \text{ cm}^{-3}$. Thus, NO₂ depletion and NO product formation are essentially instantaneous compared to the time binning (0.2 ms bin size) used in the present experiments. The time traces for both species should appear as step functions that promptly reach a constant value. However, the IRF will broaden the transition times of both signals, while the photolysis gradient will result in a slight increase in NO and decrease in NO₂ signal at longer times.

The instrument responses measured for the NO₂ photolysis system were convolved with the simulated kinetic profiles for the Cl₂/CH₃OH/O₂ system. Further details on these experiments are given in the Supporting Information.

3 Results

3.1 Kinetics methodology

Flash photolysis of Cl₂/CH₃OH/O₂/He mixtures is a straightforward technique for generating HO₂ radicals, H₂O₂, and H₂CO, as it has a relatively simple chemistry.^{41,44-57} 351 nm photolysis of Cl₂ generates Cl atoms essentially instantaneously



The Cl atoms exclusively abstract a methyl hydrogen from methanol to form CH₂OH:



CH₂OH subsequently reacts with O₂ to form HO₂ and H₂CO:



Under our conditions, HO₂ reacts primarily via self-reaction:



Neglecting secondary reactions for the moment (see below), reactions (1)–(4) quantitatively link the molar consumption of CH₃OH and Cl₂ with the molar production of HO₂, H₂O₂, and H₂CO.

Figure 2 shows typical time-dependent ion counts of HO₂⁺ (triangles), H₂O₂⁺ (pluses), and H₂CO⁺ (circles). Dwell times were 0.02 ms and binned to 0.2 ms. We collected signal in the 20 ms before the excimer fired to establish a baseline for each *m/z* and then collected signal until 130 ms after the excimer pulse to follow the time-dependent concentration. The excimer fires at *t* = 0. All products were fully removed from the reaction region before beginning the next cycle.

To fit the observed kinetics, we employed a comprehensive model that also includes forty reactions listed in Table S1 of the Supplement (using the Kintecus software package).⁵⁸ Table 2 shows the most important reactions. The majority of the rate coefficients were taken directly from the NASA Panel for Data Evaluation of Chemical Kinetics and Photochemical Data.⁴¹

Table 3 lists initial reactant concentrations for all experiments. These concentrations were used to simulate the time-dependent concentrations of Cl₂, methanol, HO₂, H₂O₂, and H₂CO.

In order to predict absolute product concentrations from our model, we needed to determine absolute initial Cl atom concentrations. Cl atoms could not be observed directly, both because they could not be ionized at the highest photon energy used and because the short expected lifetime (~1 ms) of the Cl atoms is on the same order as the IRF. Instead, we used two independent methods to determine the initial Cl atom concentration. First, we measured

the fraction of Cl_2 photolyzed from the depletion of its ion signal, measured for $^{35}\text{Cl}_2^+$, $^{37}\text{Cl}^{35}\text{Cl}^+$, and/or $^{37}\text{Cl}_2^+$. Although the adiabatic ionization energy (AIE) of $\text{Cl}_2 = 11.481$ eV,³⁷ enough signal could be observed to measure Cl_2 depletions at 11.40 and 11.45 eV. We therefore determined the Cl atom concentration from the photolysis fraction and the known Cl_2 concentration, as determined by the mass flows. In the second method, we modeled the observed time dependence of the methanol signal. Most of the CH_3OH depletion was due to the nearly instantaneous $\text{Cl} + \text{CH}_3\text{OH}$ reaction after photolysis, with some additional chemistry from chain chlorination and trace OH radicals. Cl_2 depletion was determined only at photon energies ≥ 11.40 eV, but CH_3OH was detected in all experiments.

Figure 3 shows examples of observed Cl_2 and CH_3OH depletions. The depletions were small ($0.79 \pm 0.04\%$ for $^{35}\text{Cl}^{37}\text{Cl}^+$ and $2.82 \pm 0.06\%$ for CH_3OH^+) but were statistically significant when averaged over the 200 points from -20 to 20 ms. The Cl atom concentrations derived from these two *in-situ* measurements were in good agreement with each other and agreed well with depletions of 0.90% Cl_2 and 3.6% CH_3OH estimated using the measured laser fluence ($28 \text{ mJ cm}^{-2} \text{ pulse}^{-1}$).

Table 3 lists the Cl atom concentration for each experiment. As discussed in the Supporting Information, the Cl atom concentration formed from photolysis had a slight negative gradient from the top to the bottom of the flow tube. The reported value is the mean $[\text{Cl}]_{t=0}$ derived from the Cl_2 or methanol depletions in the first 20 ms after photolysis. The measured depletion was consistent in all experiments and ranged from $0.72 \pm 0.04\%$ to $0.81 \pm 0.05\%$. Chlorine atom concentrations ranged from $0.3\text{--}3.4 \times 10^{13} \text{ cm}^{-3}$. The uncertainty in the Cl concentration in a typical experiment was $\approx 6\%$.

H_2CO was expected to form rapidly after the reaction of Cl with methanol and reach its maximum concentration in the first 0.2 ms. After the initial rise, H_2CO should not undergo further reaction, and its concentration should remain constant at the maximum value until it is pumped out.

We determined the final H₂CO concentration from the Cl atom concentration as derived above. From reactions (2) and (3), each Cl atom results in the formation of one H₂CO molecule. However, the final modeled H₂CO concentration was ~6% lower than the initial Cl atom concentration due to secondary reactions of Cl. In particular, reaction (5) consumes one Cl atom and reaction (6) consumes one Cl atom and one H₂CO molecule.



OH reacts with methanol leading to additional CH₂OH radicals; however, the OH densities produced by reaction (5) were sufficiently low that they had < 0.2% effect on the title molecule yields. H₂CO could potentially form an adduct with HO₂, but this reaction was unimportant under our low-pressure conditions:



To first order, one HO₂ radical should be formed for each Cl atom; however, secondary chemistry, primarily HO₂ + Cl (reaction (5)) resulted in a slightly lower maximum value. The expected maximum concentration of HO₂ was slightly higher than H₂CO because reaction (6) results in the effective loss of two H₂CO molecules, forming one HCO radical which contributes to a net gain of one HO₂ radical by reaction (8).



In the absence of additional chemistry, H₂O₂ should form at half the rate of HO₂ decay.

3.2 Single energy cross sections

We determined absolute photoionization cross sections for HO₂, H₂O₂, and H₂CO at a subset of photon energies using methanol as the photoionization reference. Initial radical concentrations were determined from the measured depletion of radical precursors with

known concentrations (i.e., Cl₂ and CH₃OH). Time-dependent concentrations of HO₂, H₂O₂, and H₂CO were determined from the kinetics model.

3.2.a Observed Kinetics

We collected photoion signals of Cl₂, CH₃OH, HO₂, H₂O₂, and H₂CO from -20 to 60 ms relative to the excimer laser pulse. Figure 4 shows typical time traces for H₂CO, HO₂, and H₂O₂ for a representative experiment (Experiment 6, see Table 3) at 11.45 eV where all species of interest were observed (including CH₃OH and Cl₂).

Figure 4(a) shows a representative H₂CO⁺ time-dependent signal. As expected, the signal rises promptly and then levels off. However, in the first few ms after photolysis the observed H₂CO⁺ signal rises slightly slower than predicted by the kinetics model alone, and also has a slow rise at long times (10–60 ms). We can largely correct for these deviations by using the IRF and photolysis gradients reported in the Supporting Information.

Figure 4(b) shows a representative time-dependent signal of HO₂⁺. HO₂ rises rapidly through reactions (2) and (3), similar to H₂CO. The signal then decays, primarily due to self-reaction (4), with a half-life of ~20 ms. A small additional contribution to the HO₂ decay is discernable at long times, which we assign to wall reactions as described below.

The rise of H₂O₂⁺ (Figure 4(c)) reflects the decay of HO₂ at times < 20 ms, but levels off at longer times, in contradiction with the kinetics model. We can explain this reduced yield by a combination of HO₂ and H₂O₂ wall losses as described in the following section.

3.2.b Wall Loss

We observed loss of HO₂ and H₂O₂ at longer times ($t > 20$ ms) that could not be explained by gas phase reactions or pump out. We assigned these losses to heterogeneous loss at the walls of the flow tube.

In the low-pressure slow flow reactor all species within the flow tube collided with the walls of the reactor many times before exiting the pinhole. It is well known that both HO₂ and H₂O₂ are lost to wall reactions in similar flow reactors.⁵⁹⁻⁶³ We coated the walls with

fluoropolymer to reduce wall reactions. In the absence of coatings, we observed that a significant fraction of the products remained in the flow cell, even after complete pump out was expected ($t > 100$ ms). With coatings, this problem was eliminated. However, we still observed that HO₂ disappeared at a rate slightly faster than predicted by our model, while the H₂O₂ appearance rate and total yield were lower than predicted. These losses varied from coating to coating.

We found that the measured time-dependent signals and modeled species concentrations show significantly improved agreement by invoking typical wall loss rates for HO₂ and H₂O₂ of 5–12 s⁻¹ and 5–15 s⁻¹, respectively. These rates were significantly slower than the chemical rates and had a small, though not insignificant, impact on the final concentrations and cross sections.

3.2.c Photoionization Cross Sections

We conducted twenty-two experiments (Table 3) to measure absolute photoionization cross sections of HO₂, H₂O₂, and H₂CO at five discrete photon energies: 10.90, 11.00, 11.20, 11.40, and 11.45 eV. We measured the photoionization cross section (Table 4) of a pure methanol sample relative to propene at each of these photon energies (see Supporting Information).

In each single energy experiment, we obtained the absolute cross section for HO₂, H₂O₂, and H₂CO by solving for the optimal values of the wall loss rates to obtain the best fit to the time-dependent concentrations. The final cross sections, obtained from averaging several individual determinations, are given in Table 4.

3.3 Absolute photoionization spectra

We collected relative photoionization spectra for HO₂, H₂O₂, and H₂CO from 10.508–12.008 eV at 0.025 eV steps (100 micron slit widths, corresponding to 9 meV FWHM), averaging 300 repetitions for each step, and data was integrated over 0–60 ms (Table 3, Experiment 23). We placed the relative photoionization spectra on an absolute basis by fitting each spectrum to the absolute cross sections measured at all discrete photon energies. Table 5 reports the resulting absolute photoionization spectrum for each species; these spectra are

also shown in Figures 5–7. The photoionization spectrum collected for the $m/z = 32$ peak contains only contributions from CH_3OH , making it an acceptable reference compound with no interfering isobaric species at all photon energies used here (Supporting Information). As seen in Figure S2, normalization to the photon flux did not fully remove interference from Ar absorption resonances (at 11.62 and 11.83 eV⁶⁴) in the VUV harmonic filter. The interferences caused by the Ar filter are especially apparent in the H_2CO spectrum and are noted on the figures with blue asterisks. Spectra for HO_2 and H_2O_2 were obtained using the isobaric signal separation method described above. We note that these spectra are free from contamination by the corresponding isobaric methanol isotopologue, which would grow in quickly at about 10.8 eV (Figure S2); this validates our separation and extraction procedure.

3.4 Error analysis

Several sources of error contribute to the overall uncertainty in the reported single energy cross section measurements. The uncertainty primarily stems from error in: 1) absolute methanol cross section, 2) modeled concentrations of HO_2 , H_2O_2 , and H_2CO , and 3) random noise in the data.

The HO_2 , H_2O_2 , and H_2CO absolute cross sections were measured relative to the cross section of CH_3OH , which in turn was measured relative to propene, using the methodology reported in Welz et al.⁶⁵ (see Supporting Information). We propagated the 20% systematic uncertainty in the reference cross section of methanol⁶⁵⁻⁶⁶ as part of the systematic error in the HO_2 , H_2O_2 , and H_2CO absolute cross section values.

The error in rate constants used in the kinetics model (Table 2, 1σ error bars) is propagated through the model to determine the time-dependent standard deviation of concentrations of CH_3OH , HO_2 , H_2O_2 , and H_2CO . For each experiment listed in Table 3, uncertainties were estimated by running 100 simulations with Monte Carlo sampling of the rate constant uncertainties. Typical concentration uncertainties introduced by the kinetic model were: CH_3OH 0.1%, HO_2 8%, H_2O_2 12%, and H_2CO 2%, and were determined mostly by uncertainties in the $\text{HO}_2 + \text{HO}_2$ rate constant.

We repeated several experiments at each photon energy. The cross sections $\sigma_i(E)$ at each photon energy were averaged, and the random experimental error was estimated from the standard deviation of the mean.

The total error reported for each single energy ionization cross section in Table 4 was determined for each species i by summing all errors in quadrature. The dominant source of the error in the absolute cross sections of CH₃OH, HO₂, H₂O₂, and H₂CO reported in Table 4 is the uncertainty in the cross section of the reference compound propene. The uncertainty in the ratio of these cross sections relative to the absolute cross section of methanol is actually quite low; therefore, our estimates of the cross sections could be improved by a more precise determination of the methanol cross section.

4 Discussion

4.1 H₂CO

Formaldehyde has been the subject of many VUV studies due to its fundamental importance, as well as its central role in astrochemistry (it was the first organic molecule discovered in the interstellar medium),⁶⁷ combustion, and atmospheric science.^{36,68-84} The first band (AIE = 10.889 eV)³⁶, which arises from the removal of an electron from the nonbonding 2b₂ oxygen lone pair orbital, consists of a strong origin band followed by a low-intensity vibrational progression.

Two studies have reported the relative photoionization spectrum of H₂CO in the ionization onset region at high resolution.^{73,75} These spectra have a sharp onset at threshold yielding an AIE = 10.88 eV, consistent with the photoelectron results. Two studies reported low resolution absolute VUV photoionization cross sections in this region.^{81,83} Cooper et al.⁸¹ determined the absolute H₂CO photoionization cross section using dipole (e,e + ion) coincidence spectroscopy. In these experiments, they first measured absolute total absorption oscillator strengths from electron scattering experiments, and then derived partial differential photoionization oscillator strengths from the coincident mass spectrometry measurements. The energy resolution was 1 eV FWHM. The cross sections obtained after deconvolving for

the resolution (triangles) is shown in Figure 5(a). Theoretical work reproduces the Cooper absolute photoionization spectrum from 18–100 eV, but tends to overestimate the threshold region cross section at energies lower than 18 eV.^{82,84}

Fitzpatrick et al.⁸³ measured the photoionization cross section of formaldehyde relative to that of the vinyl radical (C_2H_3) in a molecular beam experiment on the 193 nm photodissociation of epichlorohydrin. They assigned formaldehyde and vinyl radicals as products in a 1:1 ratio from the unimolecular decomposition of the C_3H_5O intermediate. The experiments were conducted under collisionless conditions using photofragment translational spectroscopy to resolve the velocity and angular distributions of the products. The products were photoionized by VUV radiation generated on the 21A1 U9/Chemical Dynamics Beamline at the National Synchrotron Radiation Research Center in Hsinchu, Taiwan. The spectral resolution ($\Delta E/E$) was 0.4 eV at 11.27 eV. FitzPatrick et al. scaled their vinyl spectrum to match a preliminary absolute spectrum from unpublished data by Taatjes ($\sigma_{\text{vinyl}}(10.43 \text{ eV}) = 12.0 \text{ Mb}$) (while noting some difference from prior work by Robinson et al.²³) and determined a photoionization cross section of 4.23 Mb for formaldehyde at 11.27 eV. However, Savee et al. recently reported an absolute photoionization spectrum of C_2H_3 measured with the present MPIMS apparatus (the final analysis of the preliminary cross section reported by Taatjes) that has a significantly lower cross section ($\sigma_{\text{vinyl}}(10.424 \text{ eV}) = 8.3 \text{ Mb}$), suggesting an even smaller cross section for formaldehyde in the work of FitzPatrick et al.³¹ In Figure 5(a), we show their cross sections reevaluated using Savee's new vinyl cross section and corrected for their spectral resolution (squares).

In Figure 5(a) we compare our experimental H_2CO absolute photoionization spectrum with that of Cooper et al. and FitzPatrick et al. We are in reasonable agreement with the measurements by Cooper et al, but our measurements are a factor of 2 larger than those by FitzPatrick et al.

As seen in Figure 5(b), the energy dependence of our spectrum in the threshold region (below 11.2 eV) matches the higher resolution relative spectra of Mentall et al.⁷³ (resolution 0.5 Å (0.5 meV at 11 eV)) and Guyon et al.⁷⁵ (resolution halfwidth 0.83 Å (0.9 meV at 11 eV)).

All three spectra are similar in the threshold region, although our lower-resolution spectrum does not capture resonances in the 10.9 eV region. Above ~ 11.2 eV, the spectrum of Guyon et al. is independent of energy, whereas our spectrum increases slowly with photon energy. This discrepancy might be due to different strategies to normalize ion signal to the photon flux.

4.2 HO₂

The HO₂ first ionization potential corresponds to removal of an electron from the antibonding combination of the oxygen $2p\pi$ orbitals in the neutral $^2A''$ to form the $^3A''$ cation. There have been several previous studies of the ionization of the HO₂ radical.^{38,85-87} Early electron ionization studies⁸⁵⁻⁸⁶ determined the adiabatic ionization potential to be 11.53 eV. In 1981, Dyke et al.⁸⁷ reported the low resolution photoelectron spectrum of HO₂ and assigned a progression of 1560 cm^{-1} to ν_2 , the O-O stretch mode in HO₂⁺. Litorja and Ruscic measured the relative photoionization spectrum of HO₂ from 100–111 nm (12.4–11.2 eV) at high resolution (step sizes of 0.02 nm) (shown in Figure 6, scaled to match the absolute cross sections measured here).³⁸ Because the spectrum exhibited a sharp rise at threshold, they could determine the AIE of HO₂ with high precision: AIE = 11.352 ± 0.007 eV. There is very good agreement in the shape of our spectrum and that of Litorja and Ruscic, including the positions of the $\nu' = 0$ and 1 steps in the underlying staircase structure caused by the O-O stretch vibrational progression.

Prior to this study, there were no reports of the absolute photoionization cross section of HO₂. One study measured the HO₂ photoionization cross section relative to the photoionization cross section of the methyl peroxy radical, CH₃O₂, at two photon energies (the Ar resonance lines 11.62 and 11.83 eV), and estimated the HO₂ cross section to be about 5 times lower.⁸⁸ Although the relative photoionization spectrum of CH₃O₂ has been reported,¹⁴ there are no absolute cross sections for CH₃O₂ (and therefore HO₂) with which to compare our results.

4.3 H₂O₂

There have been a number of photoelectron and photoionization studies of H₂O₂. The AIE is well-established (10.631 ± 0.007 eV).³⁸ The first broad band in the photoelectron spectrum

corresponds to removal of an electron from the antisymmetric combinations of oxygen nonbonding orbitals, which have some anti-bonding character. The dihedral angle significantly increases upon ionization from 120° in the neutral to *trans* planar (180° , C_{2h}) in the cation.⁸⁹⁻⁹² Litorja and Ruscic³⁸ reported the only relative photoionization spectrum of H_2O_2 (shown in Figure 7, scaled arbitrarily to match our spectrum). The very gradual rise after threshold is consistent with an extended Franck-Condon envelope resulting from a large geometry change between the neutral and cation.

The relative photoionization spectrum of H_2O_2 reported here is in good agreement with past work by Litorja and Ruscic (see Figure 7). There have been no reports of the photoionization cross section of H_2O_2 in the VUV with which to compare our absolute cross sections.

4.4 Validity of empirical estimates of cross sections

Bobeldijk et al. developed a semi-empirical model for estimating the photoionization cross section for closed shell molecules like H_2CO .⁹³ The calculated value for H_2CO at 11.8 eV using this model is 13 Mb. Our experimental spectrum above 11.6 eV is noisy, because there are resonances in the spectrum of the Ar gas filter, but the mean cross section from 11.6–12 eV is 14.9 Mb (Table 5) and agrees reasonably with the model. Note that the Bobeldijk et al.⁹³ method does not provide a means to estimate either the HO_2 or the H_2O_2 cross sections.

Because HO_2 and H_2O_2 exhibit very similar HOMOs (see Supporting Information) they might serve as a novel test of Xu and Pratt's method²⁸ for estimating photoionization cross sections for free radicals. In short, this model suggests that the cross section for photoionization from the HOMO of a free radical can be estimated by using the cross section for photoionization from an orbital of similar shape on a corresponding closed-shell species. This method also requires scaling the estimated cross section value by the orbital occupancies. A proper comparison should be performed after the Franck-Condon envelope associated with each molecular orbital, although this is not possible in the threshold region of H_2O_2 due to overlapping transitions to multiple electronic states. However, it is qualitatively clear that the near-threshold photoionization cross section of HO_2 is roughly

half that of H₂O₂, as expected from the single vs. double occupancy of the HOMOs in these two molecules.

5 Conclusions

We report absolute VUV photoionization cross sections for HO₂, H₂O₂, and H₂CO derived from measurements relative to the photoionization cross section of methanol. The key to this approach has been to obtain concentrations of all species from detailed kinetics modeling of all primary and secondary reactions occurring in the chlorine-initiated oxidation of methanol. Initial radical concentrations were derived from accurate measurements of precursor depletion. The current results are a significant improvement over previous measurements of the absolute cross section of H₂CO, which were recorded at much lower resolution. These represent the first measurements of the HO₂ and H₂O₂ absolute cross sections.

The largest source of error stems from the 20% uncertainty in determining cross sections relative to propene.⁶⁵⁻⁶⁶ The precision of the HO₂, H₂O₂, and H₂CO cross sections relative to that of CH₃OH is much higher, hence the absolute cross sections could be improved by better measurements of propene or CH₃OH.

With our measurement of the HO₂ photoionization spectrum, it may be possible to infer the absolute cross section of CH₃O₂ based on the relative relationship provided by Imamura and Washida.⁸⁸ If the HO₂ cross section at 11.62 and 11.83 eV is approximately 5 times lower than that of CH₃O₂, then the estimated CH₃O₂ cross sections at these energies would be 15.2 and 22.5 Mb, respectively.

HO₂, H₂O₂, and H₂CO are important in a number of oxidation processes. The cross sections measured here will aid in quantifying concentrations of these species in photoionization mass spectrometry studies of combustion and atmospheric chemistry reactions.

6 References

1. Sablier, M.; Fujii, T., Mass Spectrometry of Free Radicals. *Chem. Rev.* **2002**, *102*, 2855-2924.
2. Jones, I. T. N.; Bayes, K. D., Detection of Steady-State Free-Radical Concentrations by Photoionization. *J. Am. Chem. Soc.* **1972**, *94*, 6869-6871.

3. Slagle, I. R.; Yamada, F.; Gutman, D., Kinetics of Free Radicals Produced by Infrared Multiphoton-Induced Decompositions. 1. Reactions of Allyl Radicals with Nitrogen Dioxide and Bromine. *J. Am. Chem. Soc.* **1981**, *103*, 149-153.
4. Slagle, I. R.; Gutman, D., Kinetics of Polyatomic Free Radicals Produced by Laser Photolysis. 5. Study of the Equilibrium Methyl + Oxygen \rightleftharpoons CH₃O₂ Between 421 and 538 °C. *J. Am. Chem. Soc.* **1985**, *107*, 5342-5347.
5. Timonen, R. S.; Ratajczak, E.; Gutman, D.; Wagner, A. F., The Addition and Dissociation Reaction Atomic Hydrogen + Carbon Monoxide \rightleftharpoons Oxomethyl. 2. Experimental Studies and Comparison with Theory. *J. Phys. Chem.* **1987**, *91*, 5325-5332.
6. Fockenberg, C.; Bernstein, H. J.; Hall, G. E.; Muckerman, J. T.; Preses, J. M.; Sears, T. J.; Weston, R. E., Repetitively Sampled Time-of-Flight Mass Spectrometry for Gas-Phase Kinetics Studies. *Rev. Sci. Instrum.* **1999**, *70*, 3259-3264.
7. Eskola, A. J.; Timonen, R. S., Kinetics of the Reactions of Vinyl Radicals with Molecular Oxygen and Chlorine at Temperatures 200-362 K. *Phys. Chem. Chem. Phys.* **2003**, *5*, 2557-2561.
8. Blitz, M. A.; Goddard, A.; Ingham, T.; Pilling, M. J., Time-of-Flight Mass Spectrometry for Time-Resolved Measurements. *Rev. Sci. Instrum.* **2007**, *78*, 034103.
9. Baeza-Romero, M. T.; Blitz, M. A.; Goddard, A.; Seakins, P. W., Time-of-Flight Mass Spectrometry for Time-Resolved Measurements: Some Developments and Applications. *Int. J. Chem. Kin.* **2012**, *44*, 532-545.
10. Eppink, A. T. J. B.; Parker, D. H., Velocity Map Imaging of Ions and Electrons Using Electrostatic Lenses: Application in Photoelectron and Photofragment Ion Imaging of Molecular Oxygen. *Rev. Sci. Instrum.* **1997**, *68*, 3477-3484.
11. Brouard, M.; Campbell, E. K.; Johnsen, A. J.; Vallance, C.; Yuen, W. H.; Nomerotski, A., Velocity Map Imaging in Time of Flight Mass Spectrometry. *Rev. Sci. Instrum.* **2008**, *79*, 123115.
12. Osborn, D. L.; Zou, P.; Johnsen, H.; Hayden, C. C.; Taatjes, C. A.; Knyazev, V. D.; North, S. W.; Peterka, D. S.; Ahmed, M.; Leone, S. R., The Multiplexed Chemical Kinetic Photoionization Mass Spectrometer: A New Approach to Isomer-Resolved Chemical Kinetics. *Rev. Sci. Instrum.* **2008**, *79*, 104103.
13. Taatjes, C. A.; Hansen, N.; Osborn, D. L.; Kohse-Hoinghaus, K.; Cool, T. A.; Westmoreland, P. R., "Imaging" Combustion Chemistry via Multiplexed Synchrotron-Photoionization Mass Spectrometry. *Phys. Chem. Chem. Phys.* **2008**, *10*, 20-34.
14. Meloni, G.; Zou, P.; Klippenstein, S. J.; Ahmed, M.; Leone, S. R.; Taatjes, C. A.; Osborn, D. L., Energy-Resolved Photoionization of Alkylperoxy Radicals and the Stability of Their Cations. *J. Am. Chem. Soc.* **2006**, *128*, 13559-13567.
15. Welz, O.; Savee, J. D.; Osborn, D. L.; Vasu, S. S.; Percival, C. J.; Shallcross, D. E.; Taatjes, C. A., Direct Kinetic Measurements of Criegee Intermediate (CH₂OO) Formed by Reaction of CH₂I with O₂. *Science* **2012**, *335*, 204-207.

16. Yang, B.; Wang, J.; Cool, T. A.; Hansen, N.; Skeen, S.; Osborn, D. L., Absolute Photoionization Cross-Sections of Some Combustion Intermediates. *Int. J. Mass Spectrom.* **2012**, *309*, 118-128.
17. Xie, M.; Zhou, Z.; Wang, Z.; Chen, D.; Qi, F., Determination of Absolute Photoionization Cross-Sections of Oxygenated Hydrocarbons. *Int. J. Mass Spectrom.* **2010**, *293*, 28-33.
18. Taatjes, C. A.; Osborn, D. L.; Selby, T. M.; Meloni, G.; Fan, H.; Pratt, S. T., Absolute Photoionization Cross-Section of the Methyl Radical. *J. Phys. Chem. A* **2008**, *112*, 9336-9343.
19. Gans, B.; Mendes, L. A. V.; Boyé-Péronne, S.; Douin, S.; Garcia, G.; Soldi-Lose, H.; de Miranda, B. K. C.; Alcaraz, C.; Carrasco, N.; Pernot, P., et al., Determination of the Absolute Photoionization Cross Sections of CH₃ and I Produced from a Pyrolysis Source, by Combined Synchrotron and Vacuum Ultraviolet Laser Studies. *J. Phys. Chem. A* **2010**, *114*, 3237-3246.
20. Loison, J.-C., Absolute Photoionization Cross Section of the Methyl Radical. *J. Phys. Chem. A* **2010**, *114*, 6515-6520.
21. Flesch, R.; Schurmann, M. C.; Plenge, J.; Hunnekuhl, M.; Meiss, H.; Bischof, M.; Ruhl, E., Absolute Photoionization Cross Sections of the Primary Photofragments of Chlorine Dioxide and Dichlorine Monoxide. *Phys. Chem. Chem. Phys.* **1999**, *1*, 5423-5428.
22. Flesch, R.; Plenge, J.; Köhl, S.; Klusmann, M.; Rühl, E., Photoionization of the Primary Photoproducts of A(²Π)-Excited ClO. *J. Chem. Phys.* **2002**, *117*, 9663-9670.
23. Robinson, J. C.; Sveum, N. E.; Neumark, D. M., Determination of Absolute Photoionization Cross Sections for Vinyl and Propargyl Radicals. *J. Chem. Phys.* **2003**, *119*, 5311-5314.
24. Robinson, J. C.; Sveum, N. E.; Neumark, D. M., Determination of Absolute Photoionization Cross Sections for Isomers of C₃H₅: Allyl and 2-Propenyl Radicals. *Chem. Phys. Lett.* **2004**, *383*, 601-605.
25. Sveum, N. E.; Goncher, S. J.; Neumark, D. M., Determination of Absolute Photoionization Cross Sections of the Phenyl Radical. *Phys. Chem. Chem. Phys.* **2006**, *8*, 592-598.
26. FitzPatrick, B. L.; Maienschein-Cline, M.; Butler, L. J.; Lee, S. H.; Lin, J. J., Determining the Partial Photoionization Cross-Sections of Ethyl Radicals. *J. Phys. Chem. A* **2007**, *111*, 12417-12422.
27. Shubert, V. A.; Pratt, S. T., Photodissociation of Acetaldehyde and the Absolute Photoionization Cross Section of HCO. *J. Phys. Chem. A* **2010**, *114*, 11238-11243.
28. Xu, H.; Pratt, S. T., Photoionization Cross Section of the Propargyl Radical and Some General Ideas for Estimating Radical Cross Sections. *J. Phys. Chem. A* **2012**, *117*, 9331-9342.
29. Xu, H.; Pratt, S. T., Photodissociation of Anisole and Absolute Photoionization Cross-Section of the Phenoxy Radical. *J. Phys. Chem. A* **2013**, *117*, 12075-12081.
30. Savee, J. D.; Soorkia, S.; Welz, O.; Selby, T. M.; Taatjes, C. A.; Osborn, D. L., Absolute Photoionization Cross-Section of the Propargyl Radical. *J. Chem. Phys.* **2012**, *136*, 134307-10.

31. Savee, J. D.; Lockyear, J. F.; Borkar, S.; Eskola, A. J.; Welz, O.; Taatjes, C. A.; Osborn, D. L., Note: Absolute Photoionization Cross-Section of the Vinyl Radical. *J. Chem. Phys.* **2013**, *139*, 056101.
32. Gans, B.; Garcia, G. A.; Boyé-Péronne, S.; Loison, J.-C.; Douin, S.; Gaie-Levrel, F.; Gauyacq, D., Absolute Photoionization Cross Section of the Ethyl Radical in the Range 8–11.5 eV: Synchrotron and Vacuum Ultraviolet Laser Measurements. *J. Phys. Chem. A* **2011**, *115*, 5387-5396.
33. Heimann, P. A.; Koike, M.; Hsu, C. W.; Blank, D.; Yang, X. M.; Suits, A. G.; Lee, Y. T.; Evans, M.; Ng, C. Y.; Flaim, C., et al., Performance of the Vacuum Ultraviolet High-Resolution and High-Flux Beamline for Chemical Dynamics Studies at the Advanced Light Source. *Rev. Sci. Instrum.* **1997**, *68*, 1945-1951.
34. Leone, S. R.; Ahmed, M.; Wilson, K. R., Chemical Dynamics, Molecular Energetics, and Kinetics at the Synchrotron. *Phys. Chem. Chem. Phys.* **2010**, *12*, 6564-6578.
35. Macneil, K. A. G.; Dixon, R. N., High-Resolution Photoelectron Spectroscopy of Methanol and its Deuterated Derivatives: Internal Rotation in the Ground Ionic State. *J. Electron Spectrosc. Relat. Phenom.* **1977**, *11*, 315-331.
36. Niu, B.; Shirley, D. A.; Bai, Y., High Resolution Photoelectron Spectroscopy and Femtosecond Intramolecular Dynamics of H_2CO^+ and D_2CO^+ . *J. Chem. Phys.* **1993**, *98*, 4377-4390.
37. Yench, A. J.; Hopkirk, A.; Hiraya, A.; Donovan, R. J.; Goode, J. G.; Maier, R. R. J.; King, G. C.; Kvaran, A., Threshold Photoelectron Spectroscopy of Cl_2 and Br_2 up to 35 eV. *J. Phys. Chem.* **1995**, *99*, 7231-7241.
38. Litorja, M.; Ruscic, B., A Photoionization Study of the Hydroperoxyl Radical, HO_2 , and Hydrogen Peroxide, H_2O_2 . *J. Electron Spectrosc. Relat. Phenom.* **1998**, *97*, 131-146.
39. Cool, T. A.; McIlroy, A.; Qi, F.; Westmoreland, P. R.; Poisson, L.; Peterka, D. S.; Ahmed, M., Photoionization Mass Spectrometer for Studies of Flame Chemistry with a Synchrotron Light Source. *Rev. Sci. Instrum.* **2005**, *76*, 094102-7.
40. Taatjes, C. A., How does the Molecular Velocity Distribution Affect Kinetics Measurements by Time-Resolved Mass Spectrometry? *Int. J. Chem. Kin.* **2007**, *39*, 565-570.
41. Sander, S. P.; Abbatt, J.; Barker, J. R.; Burkholder, J. B.; Friedl, R. R.; Golden, D. M.; Huie, R. E.; Kolb, C. E.; Kurylo, M. J.; Moortgat, G. K., et al., Chemical Kinetics and Photochemical Data for Use in Atmospheric Studies, Evaluation Number 17. *JPL Publication 10-6* **2011**.
42. Estupiñán, E. G.; Nicovich, J. M.; Wine, P. H., A Temperature-Dependent Kinetics Study of the Important Stratospheric Reaction $\text{O}(^3\text{P}) + \text{NO}_2 \rightarrow \text{O}_2 + \text{NO}$. *J. Phys. Chem. A* **2001**, *105*, 9697-9703.
43. Gierczak, T.; Burkholder, J. B.; Ravishankara, A. R., Temperature Dependent Rate Coefficient for the Reaction $\text{O}(^3\text{P}) + \text{NO}_2 \rightarrow \text{NO} + \text{O}_2$. *J. Phys. Chem. A* **1999**, *103*, 877-883.
44. Atkinson, R.; Baulch, D. L.; Cox, R. A.; Crowley, J. N.; Hampson, R. F.; Hynes, R. G.; Jenkin, M. E.; Rossi, M. J.; Troe, J., Evaluated Kinetic and Photochemical Data for Atmospheric

- Chemistry: Volume II - Gas Phase Reactions of Organic Species. *Atmos. Chem. Phys.* **2006**, *6*, 3625-4055.
45. Sander, S. P.; Peterson, M.; Watson, R. T.; Patrick, R., Kinetics Studies of the Hydrogen Dioxide + Hydrogen Dioxide and Deuterium Dioxide + Deuterium Dioxide Reactions at 298 K. *J. Phys. Chem.* **1982**, *86*, 1236-1240.
46. Thrush, B. A.; Tyndall, G. S., The Rate of Reaction Between HO₂ Radicals at Low Pressures. *Chem. Phys. Lett.* **1982**, *92*, 232-235.
47. Thrush, B. A.; Tyndall, G. S., Reactions of HO₂ Studied by Flash Photolysis with Diode-Laser Spectroscopy. *J. Chem. Soc., Faraday Trans. 2* **1982**, *78*, 1469-1475.
48. Simonaitis, R.; Heicklen, J., A Kinetic Study of the Perhydroxyl + Perhydroxyl Reaction. *J. Phys. Chem.* **1982**, *86*, 3416-3418.
49. Kircher, C. C.; Sander, S. P., Kinetics and Mechanism of Hydroperoxo and Hydroperoxo-d Disproportionations. *J. Phys. Chem.* **1984**, *88*, 2082-2091.
50. Sander, S. P., Low-Pressure Study of the Perhydroxyl (HO₂) + Perhydroxyl (HO₂) Reaction at 298 K. *J. Phys. Chem.* **1984**, *88*, 6018-6021.
51. Takacs, G. A.; Howard, C. J., Room-Temperature Rate Constant for the Hydroperoxo + Hydroperoxo Reaction at Low Pressures. *J. Phys. Chem.* **1984**, *88*, 2110-2116.
52. Kurylo, M. J.; Ouellette, P. A.; Laufer, A. H., Measurements of the Pressure Dependence of the Hydroperoxy (HO₂) Radical Self-Disproportionation Reaction at 298 K. *J. Phys. Chem.* **1986**, *90*, 437-440.
53. Takacs, G. A.; Howard, C. J., Temperature Dependence of the Reaction Hydroperoxo (HO₂) + Hydroperoxo at Low Pressures. *J. Phys. Chem.* **1986**, *90*, 687-690.
54. Lightfoot, P. D.; Veyret, B.; Lesclaux, R., The Rate Constant for the HO₂+HO₂ Reaction at Elevated Temperatures. *Chem. Phys. Lett.* **1988**, *150*, 120-126.
55. Maricq, M. M.; Szente, J. J., A Kinetic Study of the Reaction between Ethylperoxy Radicals and HO₂. *J. Phys. Chem.* **1994**, *98*, 2078-2082.
56. Christensen, L. E.; Okumura, M.; Sander, S. P.; Salawitch, R. J.; Toon, G. C.; Sen, B.; Blavier, J. F.; Jucks, K. W., Kinetics of HO₂ + HO₂ → H₂O₂ + O₂: Implications for Stratospheric H₂O₂. *Geophys. Res. Lett.* **2002**, *29*, 13-1-13-4.
57. Christensen, L. E.; Okumura, M.; Hansen, J. C.; Sander, S. P.; Francisco, J. S., Experimental and ab Initio Study of the HO₂·CH₃OH Complex: Thermodynamics and Kinetics of Formation. *J. Phys. Chem. A* **2006**, *110*, 6948-6959.
58. Ianni, J. C., A comparison of the Bader-Deuflhard and the Cash-Karp Runge-Kutta integrators for the GRI-MECH 3.0 model based on the chemical kinetics code Kintecus. In *Computational Fluid and Solid Mechanics 2003*, Bathe, K. J., Ed. Elsevier Science Ltd: Oxford, 2003; pp 1368-1372.

59. Gershenzon, Y. M.; Grigorieva, V. M.; Ivanov, A. V.; Remorov, R. G., O₃ and OH Sensitivity to Heterogeneous Sinks of HO_x and CH₃O₂ on Aerosol Particles. *Faraday Discuss.* **1995**, *100*, 83-100.
60. Loukhovitskaya, E.; Bedjanian, Y.; Morozov, I.; Le Bras, G., Laboratory Study of the Interaction of HO₂ Radicals with the NaCl, NaBr, MgCl₂·6H₂O and Sea Salt Surfaces. *Phys. Chem. Chem. Phys.* **2009**, *11*, 7896-7905.
61. Pradhan, M.; Kalberer, M.; Griffiths, P. T.; Braban, C. F.; Pope, F. D.; Cox, R. A.; Lambert, R. M., Uptake of Gaseous Hydrogen Peroxide by Submicrometer Titanium Dioxide Aerosol as a Function of Relative Humidity. *Environ. Sci. Technol.* **2010**, *44*, 1360-1365.
62. Pradhan, M.; Kyriakou, G.; Archibald, A. T.; Papageorgiou, A. C.; Kalberer, M.; Lambert, R. M., Heterogeneous Uptake of Gaseous Hydrogen Peroxide by Gobi and Saharan Dust Aerosols: a Potential Missing Sink for H₂O₂ in the Troposphere. *Atmos. Chem. Phys.* **2010**, *10*, 7127-7136.
63. Zhao, Y.; Chen, Z.; Shen, X.; Zhang, X., Kinetics and Mechanisms of Heterogeneous Reaction of Gaseous Hydrogen Peroxide on Mineral Oxide Particles. *Environ. Sci. Technol.* **2011**, *45*, 3317-3324.
64. Minnhagen, L., Spectrum and the Energy Levels of Neutral Argon, Ar I. *J. Opt. Soc. Am.* **1973**, *63*, 1185-1198.
65. Welz, O.; Zador, J.; Savee, J. D.; Ng, M. Y.; Meloni, G.; Fernandes, R. X.; Sheps, L.; Simmons, B. A.; Lee, T. S.; Osborn, D. L., et al., Low-Temperature Combustion Chemistry of Biofuels: Pathways in the Initial Low-Temperature (550 K-750 K) Oxidation Chemistry of Isopentanol. *Phys. Chem. Chem. Phys.* **2012**, *14*, 3112-3127.
66. Cool, T. A.; Wang, J.; Nakajima, K.; Taatjes, C. A.; McLlroy, A., Photoionization Cross Sections for Reaction Intermediates in Hydrocarbon Combustion. *Int. J. Mass Spectrom.* **2005**, *247*, 18-27.
67. Snyder, L. E.; Buhl, D.; Zuckerman, B.; Palmer, P., Microwave Detection of Interstellar Formaldehyde. *Phys. Rev. Lett.* **1969**, *22*, 679-681.
68. Baker, A. D.; Baker, C.; Brundle, C. R.; Turner, D. W., The Electronic Structures of Methane, Ethane, Ethylene and Formaldehyde Studied by High-Resolution Molecular Photoelectron Spectroscopy. *Int. J. Mass Spectrom. Ion Phys.* **1968**, *1*, 285-301.
69. Matthews, C. S.; Warneck, P., Heats of Formation of CHO⁺ and C₃H₃⁺ by Photoionization. *J. Chem. Phys.* **1969**, *51*, 854-855.
70. Gentieu, E. P.; Mentall, J. E., Formaldehyde Absorption Coefficients in the Vacuum Ultraviolet (650 to 1850 Angstroms). *Science* **1970**, *169*, 681-683.
71. Turner, D. W.; Baker, C.; Baker, A. D.; Brundle, C. R., *Molecular Photoelectron Spectroscopy*. Wiley Interscience: London, 1970.
72. Warneck, P., Photoionisation von Methanol und Formaldehyd. *Z. Naturforsch.* **1971**, *26a*, 2047-2057.

73. Mentall, J. E.; Gentieu, E. P.; Krauss, M.; Neumann, D., Photoionization and Absorption Spectrum of Formaldehyde in the Vacuum Ultraviolet. *J. Chem. Phys.* **1971**, *55*, 5471-5479.
74. Moule, D. C.; Walsh, A. D., Ultraviolet Spectra and Excited States of Formaldehyde. *Chem. Rev.* **1975**, *75*, 67-84.
75. Guyon, P. M.; Chupka, W. A.; Berkowitz, J., Photoionization Mass Spectrometric Study of Formaldehyde H₂CO, HDCO and D₂CO. *J. Chem. Phys.* **1976**, *64*, 1419-1436.
76. Hernandez, R.; Masclet, P.; Mouvier, G., Spectroscopie de Photoelectrons d'Aldehydes et de Cetonnes Aliphatiques. *J. Electron Spectrosc. Relat. Phenom.* **1977**, *10*, 333-347.
77. von Niessen, W.; Bieri, G.; Åsbrink, L., 30.4-nm He (II) Photoelectron Spectra of Organic Molecules: Part III. Oxo-Compounds (C, H, O). *J. Electron Spectrosc. Relat. Phenom.* **1980**, *21*, 175-191.
78. Kimura, K.; Katsumata, S.; Achiba, Y.; Yamazaki, T.; Iwata, S., *Handbook of He I Photoelectron Spectra*. Halsted Press: New York, 1981.
79. Traeger, J. C., Heat of Formation for the Formyl Cation by Photoionization Mass Spectrometry. *Int. J. Mass Spectrom. Ion Processes* **1985**, *66*, 271-282.
80. Holland, D. M. P., A Photoelectron Spectroscopy Study of the Four Outermost Valence Orbitals of Formaldehyde. *Chem. Phys.* **1989**, *133*, 453-460.
81. Cooper, G.; Anderson, J. E.; Brion, C. E., Absolute Photoabsorption and Photoionization of Formaldehyde in the VUV and Soft X-ray Regions (3-200 eV). *Chem. Phys.* **1996**, *209*, 61-77.
82. Cacelli, I.; Moccia, R.; Montuoro, R., Calculation of the Differential Photoionization Cross-Section of Formaldehyde. *Chem. Phys. Lett.* **2001**, *347*, 261-267.
83. FitzPatrick, B. L.; Alligood, B. W.; Butler, L. J.; Lee, S.-H.; Lin, J. J.-M., Primary Photodissociation Pathways of Epichlorohydrin and Analysis of the C-C Bond Fission channels from an O(³P) + Allyl Radical Intermediate. *J. Chem. Phys.* **2010**, *133*, 094306.
84. Ruberti, M.; Yun, R.; Gokhberg, K.; Kopelke, S.; Cederbaum, L. S.; Tarantelli, F.; Averbukh, V., Total Molecular Photoionization Cross-Sections by Algebraic Diagrammatic Construction-Stieltjes-Lanczos method: Benchmark Calculations. *J. Chem. Phys.* **2013**, *139*, 144107.
85. Foner, S. N.; Hudson, R. L., Ionization Potential of the Free HO₂ Radical and the H – O₂ Bond Dissociation Energy. *J. Chem. Phys.* **1955**, *23*, 1364-1365.
86. Foner, S. N.; Hudson, R. L., Mass Spectrometry of the HO₂ Free Radical. *J. Chem. Phys.* **1962**, *36*, 2681-2688.
87. Dyke, J. M.; Jonathan, N. B. H.; Morris, A.; Winter, M. J., Vacuum Ultraviolet Photo-Electron Spectroscopy of Transient Species Part 13. Observation of the X³A" state of HO₂⁺. *Mol. Phys.* **1981**, *44*, 1059-1066.
88. Imamura, T.; Washida, N., Measurements of Rate Constants for HO₂+NO and NH₂+NO Reactions by Time-Resolved Photoionization Mass Spectrometry. *Laser Chem.* **1995**, *16*, 43-51.

89. Osafune, K.; Kimura, K., Photoelectron Spectroscopic Study of Hydrogen Peroxide. *Chem. Phys. Lett.* **1974**, *25*, 47-50.
90. Brown, R. S., A Photoelectron Investigation of the Peroxide Bond. *Can. J. Chem.* **1975**, *53*, 3439-3447.
91. Ashmore, F. S.; Burgess, A. R., Study of Some Medium Size Alcohols and Hydroperoxides by Photoelectron Spectroscopy. *J. Chem. Soc., Faraday Trans. 2* **1977**, *73*, 1247-1261.
92. Takeshita, K.; Mukherjee, P. K., Theoretical Study on the First Broad Band of the Photoelectron Spectrum of H₂O₂ with Inclusion of the Vibrational Structure. *Chem. Phys. Lett.* **1989**, *160*, 193-199.
93. Bobeldijk, M.; van der Zande, W. J.; Kistemaker, P. G., Simple Models for the Calculation of Photoionization and Electron Impact Ionization Cross Sections of Polyatomic Molecules. *Chem. Phys.* **1994**, *179*, 125-130.
94. Tyndall, G. S.; Orlando, J. J.; Kegley-Owen, C. S.; Wallington, T. J.; Hurley, M. D., Rate Coefficients for the Reactions of Chlorine Atoms with Methanol and Acetaldehyde. *Int. J. Chem. Kin.* **1999**, *31*, 776-784.

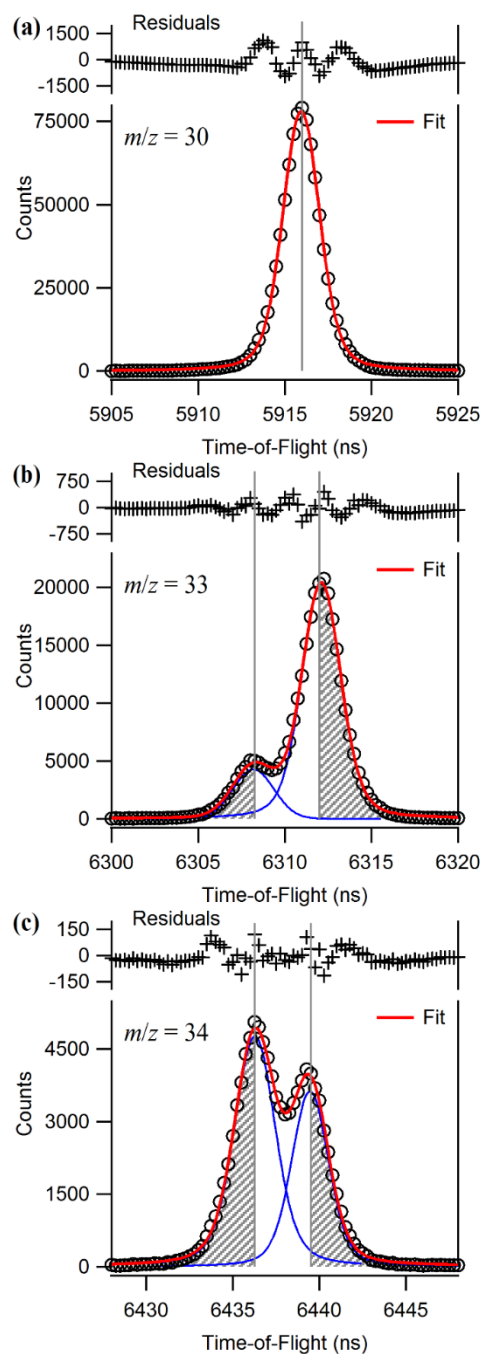


Figure 1. Sample time-of-flight spectra: (a) $m/z = 30$, containing a contribution from only one species, H_2CO^+ , which is fit with a Voigt distribution. (b) $m/z = 33$, containing contributions from HO_2^+ and $^{13}\text{CH}_3\text{OH}^+$ and (c) $m/z = 34$, contains H_2O_2^+ and $\text{CH}_3^{18}\text{OH}^+$. Thus, $m/z = 33$ and 34 were fit with a linear combination of two Voigt distributions. Data is taken from Experiment 23 (see Table 3). The gray hashed areas in (b) and (c) indicate the regions that were integrated and renormalized to produce the final unencumbered data sets. (See Supporting Information)

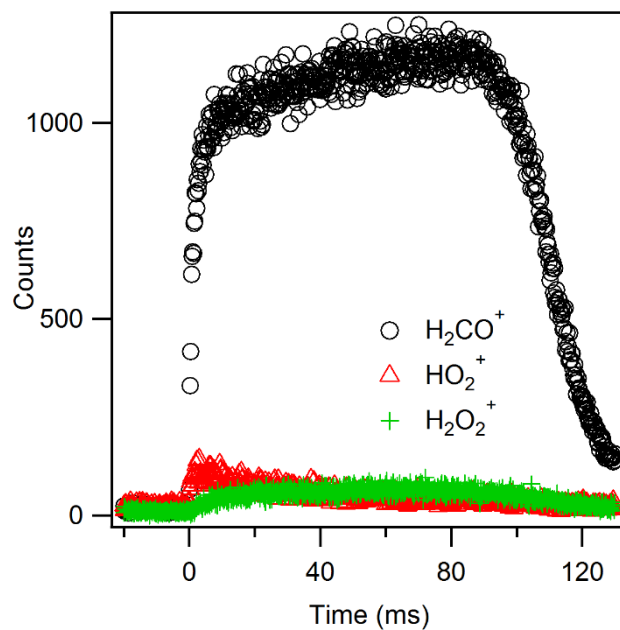


Figure 2. Typical raw H_2CO^+ (black circles), HO_2^+ (red triangles), and H_2O_2^+ (green pluses) signals versus time, collected at a photon energy of 11.45 eV. The H_2CO signal is larger due to its higher cross section at 11.45 eV than HO_2 and H_2O_2 , resulting in an order of magnitude more counts, even though H_2CO and HO_2 have comparable number densities. The data are taken from Experiment 6 (see Table 3).

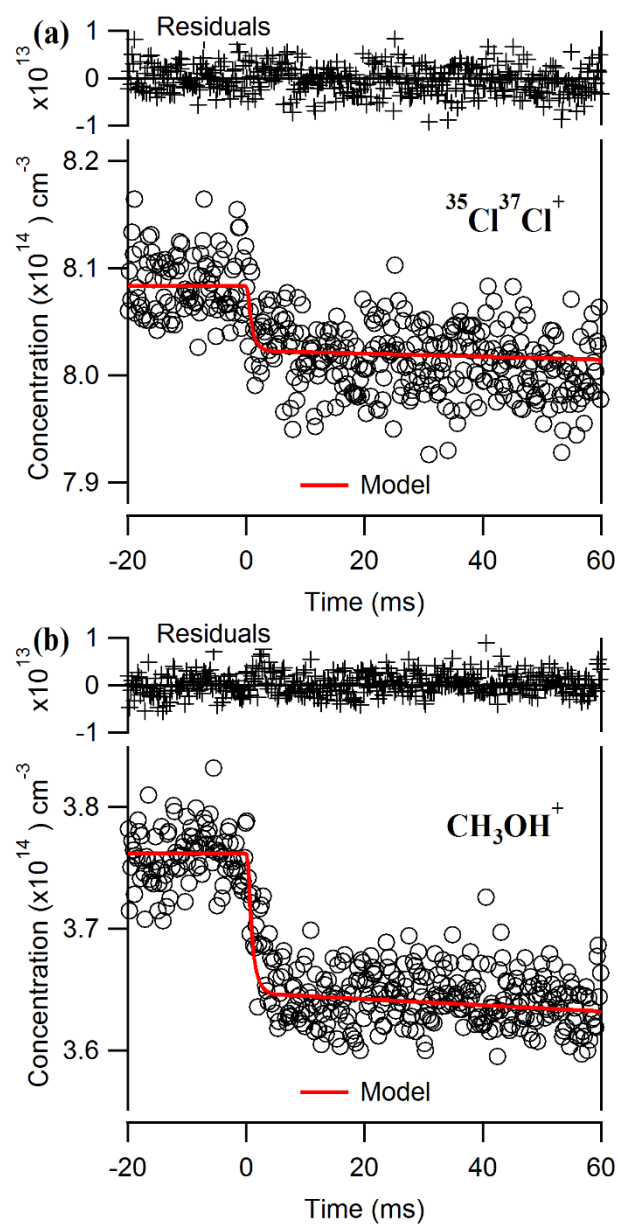


Figure 3. Representative observed precursor depletions for constraining radical concentrations: (a) Cl₂, detected at $m/z = 72$ (³⁵Cl³⁷Cl⁺) and (b) methanol, detected at $m/z = 32$ (CH₃OH⁺). Model depletion fit (red line) to the data (fitting window -20 to 20 ms). The kinetics model includes the IRF and the photolysis gradient. The experimental data are taken from Experiment 6 at 11.45 eV (see Table 3).

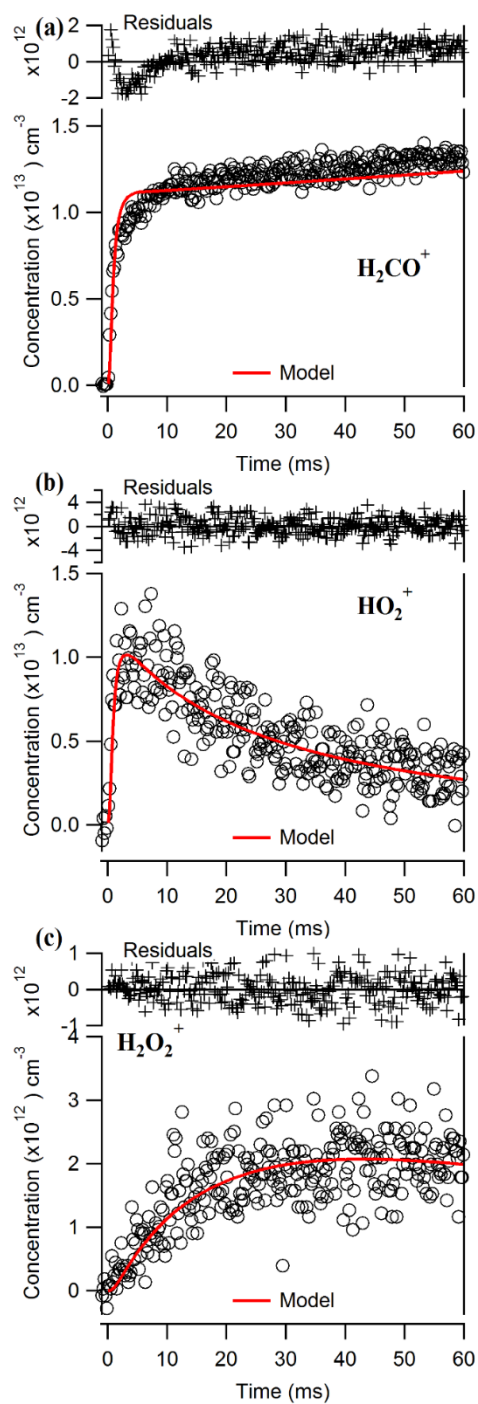


Figure 4. Single energy kinetics traces for title molecules. Data are scaled to the model as part of the cross section determination process. Representative time-dependent traces of (a) H_2CO^+ , (b) HO_2^+ , and (c) H_2O_2^+ at 11.45 eV. These data are from Experiment 6 (see Table 3). Modeled kinetics (red line), convolved with the IRF and including a photolysis gradient and first order wall losses of HO_2 and H_2O_2 (9.8 and 12.0 s^{-1} , respectively).

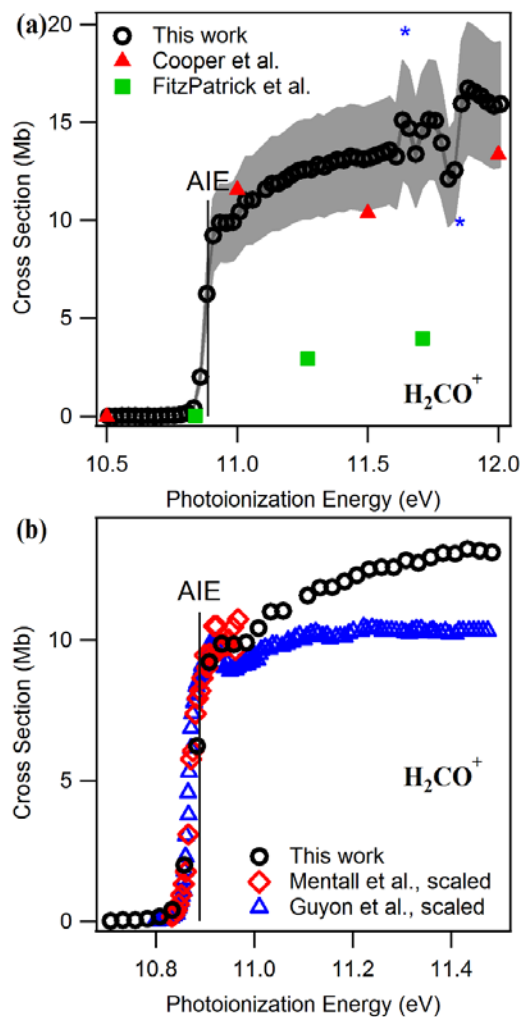


Figure 5. Absolute photoionization spectrum of formaldehyde. (a) Energy-dependent scan in this work, scaled to match the absolute photoionization cross sections determined in single point experiments. The dark gray shading indicates the systematic error from the 2% error in $[\text{H}_2\text{CO}]$ propagated from the kinetics model. The light gray shading is the total systematic error, including both the error in the kinetics model and the error in the reference methanol cross section. Data taken from Cooper et al.⁸¹ have been deconvolved to match our energy resolution and are plotted here (triangles). Data taken from FitzPatrick et al.⁸³ have been corrected with the new C_2H_3 measurement, have been deconvolved to match our energy resolution, and are plotted here (squares). Interferences caused by Ar resonances are indicated by asterisks. Panel (b) compares the experimental rise at threshold with literature high-resolution relative H_2CO spectra. Data (diamonds) were taken from Mentall et al., and scaled to match experiment.⁷³ Also shown is data (triangles) taken from Guyon et al. and scaled to match experiment.⁷⁵ The AIE is indicated for reference.³⁶

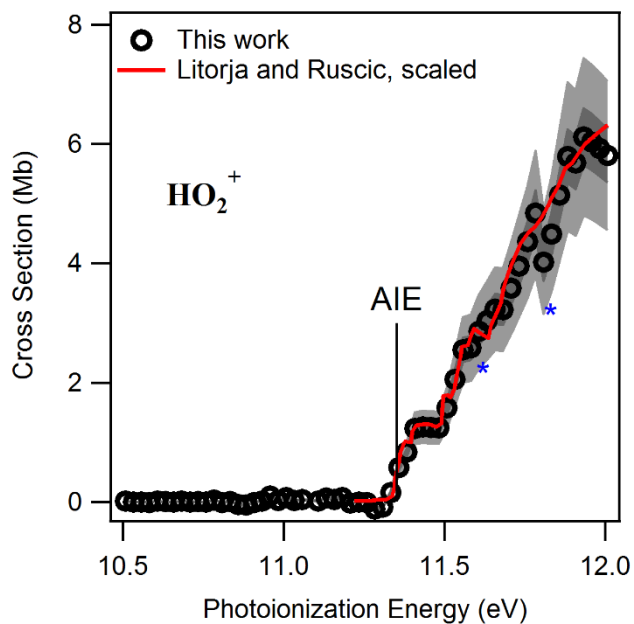


Figure 6. Absolute photoionization spectrum of HO_2 . Energy-dependent scan in this work, scaled to match the absolute photoionization cross sections determined in single point experiments. The dark gray shading indicates the systematic error from the 8% error $[\text{HO}_2]$ from the kinetics model. The light gray shading is the total systematic error, including both the error in the kinetics model and the error in the reference cross section. The red line is taken from Litorja and Ruscic, arbitrarily scaled to compare the shape with this study.³⁸ The AIE is indicated for reference.³⁸ Interferences caused by Ar resonances are indicated by asterisks.

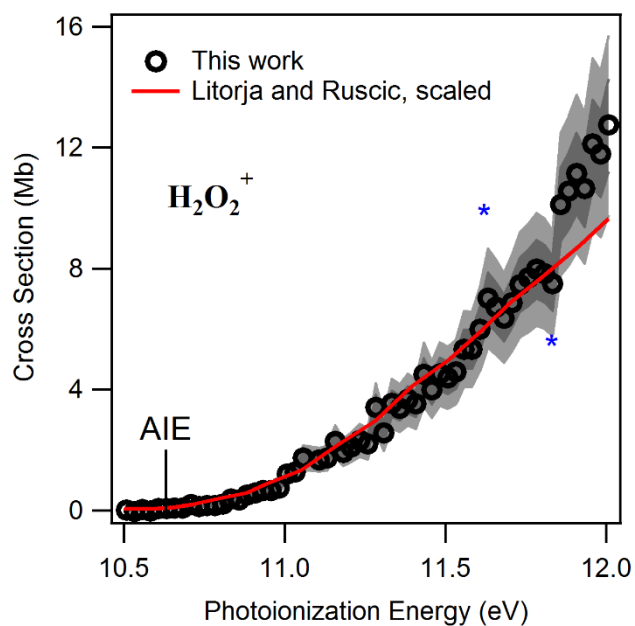


Figure 7. Absolute photoionization spectrum of H_2O_2 . Energy-dependent scan in this work, scaled to match the absolute photoionization cross sections determined in single point experiments. The dark gray shading indicates the systematic error from the 12% error $[\text{H}_2\text{O}_2]$ from the kinetics model. The light gray shading is the total systematic error, including both the error in the kinetics model and the error in the reference cross section. The red line is taken from Litorja and Ruscic, arbitrarily scaled to compare the shape with this study.³⁸ The AIE is indicated for reference.³⁸ Interferences caused by Ar resonances are indicated by asterisks.

Table 1. Single-energy experiments were conducted at 5 individual photon energies (each with an energy resolution of ~ 9 meV). Below are the photon energies at which each species was detected. The m/z as well as the AIE for each species monitored in the kinetics experiments are listed below. All species were detected at their parent ion m/z .

species	m/z	AIE (eV)	photon energies used (eV)
H₂CO	30.011	10.889 ^a	10.90, 11.00, 11.20, 11.40, 11.45
CH₃OH	32.026	10.846 ^b	10.90, 11.00, 11.20, 11.40, 11.45
HO₂	32.998	11.352 ^c	11.40, 11.45
¹³CH₃OH	33.030		10.90, 11.00, 11.20, 11.40, 11.45
H₂O₂	34.005	10.631 ^c	10.90, 11.00, 11.20, 11.40, 11.45
CH₃¹⁸OH	34.030		10.90, 11.00, 11.20, 11.40, 11.45
Cl₂	69.938	11.481 ^d	11.40, 11.45
³⁵Cl³⁷Cl	71.935		11.40, 11.45
³⁷Cl₂	73.932		11.40, 11.45

^aNiu et al.³⁶ ^bMacneil and Dixon.³⁵ ^cLitorja and Ruscic.³⁸ ^dYencha et al.³⁷

Table 2. A subset of the reactions used to simulate the concentration-dependent profiles for CH₃OH, HO₂, H₂O₂, and H₂CO are listed below. Rate coefficients for eleven of the key reactions are listed here; the remaining 29 reactions are given in Table S1. Pressure-dependent rate constants are for 8 Torr. All rate constants are taken from the NASA Data Evaluation⁴¹ unless otherwise noted.

	$k_{298\text{K}}$ (cm ³ molecule ⁻¹ s ⁻¹)
(1) Cl ₂ $\xrightarrow{h\nu}$ 2Cl	-
(2) CH ₃ OH + Cl → CH ₂ OH + HCl	5.5 ^{+1.1} _{-0.9} × 10 ⁻¹¹
(3) CH ₂ OH + O ₂ → HO ₂ + H ₂ CO	9.1 ^{+2.7} _{-2.1} × 10 ⁻¹²
(4) HO ₂ + HO ₂ → H ₂ O ₂ + O ₂	1.4 ± 0.2 × 10 ⁻¹²
(5) HO ₂ + Cl → HCl + O ₂	3.5 ^{+0.7} _{-0.6} × 10 ⁻¹¹
→ OH + ClO	1.0 ^{+0.4} _{-0.3} × 10 ⁻¹¹
(6) ^a Cl + H ₂ CO → HCO + HCl	7.2 ^{+1.1} _{-0.9} × 10 ⁻¹¹
(7) ^a HO ₂ + H ₂ CO $\xrightarrow{\text{M}}$ HOCH ₂ O ₂	7.9 ^{+7.9} _{-3.9} × 10 ⁻¹⁴
HOCH ₂ O ₂ $\xrightarrow{\text{M}}$ HO ₂ + H ₂ CO	1.5 ^{+1.5} _{-0.8} × 10 ² (s ⁻¹)
(8) HCO + O ₂ → HO ₂ + CO	5.2 ^{+2.1} _{-1.5} × 10 ⁻¹²
(9) ^b CH ₂ OH + Cl ₂ → ClCH ₂ OH + Cl	2.9 ± 0.3 × 10 ⁻¹¹
(10) HO ₂ + ClO → HOCl + O ₂	6.9 ^{+1.4} _{-1.1} × 10 ⁻¹²
(11) CH ₃ OH + OH → CH ₂ OH + H ₂ O	7.7 ^{+0.8} _{-0.7} × 10 ⁻¹³
→ CH ₃ O + H ₂ O	1.4 ± 0.1 × 10 ⁻¹³

^aTaken from IUPAC.⁴⁴ ^bTaken from Tyndall et al. 1999.⁹⁴

Table 3. Photon energies and initial concentrations for all experiments. Twenty-two single-energy experiments were conducted to determine absolute energy-dependent photoionization cross sections at five photon energies (given in Table 4). Also listed are the experimental conditions used in photon energy scans used to obtain the full photoionization spectra (given in Table 5). All experiments were performed at 298 K. Experiments were performed at 8 Torr and 200 sccm total flow rate unless otherwise noted. The Cl atom concentrations listed here were measured as the average observed depletion in the Cl₂ and/or methanol signals from -20 to 20 ms.

experiment	photon energy (eV)	[CH ₃ OH] ($\times 10^{14}$) (cm ⁻³)	[O ₂] ($\times 10^{16}$) cm ⁻³	[Cl ₂] ($\times 10^{14}$) cm ⁻³	[Cl] ($\times 10^{13}$) cm ⁻³
1	11.45	3.75	7.80	8.09	1.22 ± 0.07
2	10.90	3.75	7.80	8.09	1.22 ± 0.07
3	11.00	3.75	7.80	8.09	1.22 ± 0.07
4	11.20	3.75	7.80	8.09	1.22 ± 0.07
5	11.40	3.75	7.80	8.09	1.22 ± 0.07
6	11.45	3.76	15.6	8.08	1.22 ± 0.07
7 ^a	11.45	1.21	2.45	2.53	0.38 ± 0.02
8	11.45	3.77	7.80	8.09	1.22 ± 0.07
9	11.45	3.76	7.80	16.20	2.4 ± 0.1
10	11.45	3.77	7.80	8.09	1.17 ± 0.07
11	11.45	3.76	7.80	2.04	0.30 ± 0.02
12 ^b	11.45	1.94	3.90	3.99	0.57 ± 0.03
13 ^b	11.45	1.94	7.78	3.98	0.57 ± 0.03
14 ^b	10.90	1.94	7.78	3.98	0.57 ± 0.03
15 ^b	11.40	1.94	7.78	3.98	0.57 ± 0.03
16 ^b	11.20	1.94	7.78	3.98	0.57 ± 0.03
17 ^c	11.45	3.63	7.78	8.09	1.32 ± 0.08
18 ^c	11.45	3.63	7.78	8.09	1.32 ± 0.08

19	11.45	3.24	7.78	7.78	1.7 ± 0.1
20	10.90	3.24	7.78	7.78	1.7 ± 0.1
21	11.45	3.24	7.78	15.60	3.4 ± 0.2
22	10.90	3.24	7.78	15.60	3.4 ± 0.2
Photon energy scan	10.508 – 12.008	3.52	7.78	8.09	1.32 ± 0.08

^aExperiment conducted at 2.5 Torr. ^bExperiment conducted at 4 Torr. ^cExperiment conducted with 400 sccm total flow rate.

Table 4. Photoionization cross sections for H₂CO, HO₂, and H₂O₂, determined from single energy experiments. Reported here are the average values at each energy. The uncertainty includes all systematic and random errors discussed in the text. Also reported are the CH₃OH cross sections, measured relative to propene (see Supporting Information), that were used as the reference cross sections in each single energy experiment.

photon energy (eV)	CH₃OH (Mb)	HO₂ (Mb)	H₂O₂ (Mb)	H₂CO (Mb)
10.90	2.3 ± 0.5	-	0.40 ± 0.12	7.3 ± 1.5
11.00	4.4 ± 0.9	-	0.93 ± 0.22	9.6 ± 1.9
11.20	7.5 ± 1.5	-	1.8 ± 0.4	12.4 ± 2.5
11.40	10.2 ± 2.0	1.1 ± 0.3	3.6 ± 0.9	14.1 ± 2.9
11.45	10.7 ± 2.1	1.3 ± 0.3	4.6 ± 1.2	14.0 ± 3.0

Table 5. Absolute photoionization spectra for HO₂, H₂O₂, and H₂CO, obtained in the present work. A relative spectrum was scaled to absolute measurements as outlined in the text. Overall uncertainties are: HO₂, 21%; H₂O₂, 23%; H₂CO, 20%, encompassing the systematic errors described in the text. The data point at 11.083 eV has been removed (see Supporting Information).

photon energy (eV)	HO₂ (Mb)	H₂O₂ (Mb)	H₂CO (Mb)
10.508	0.014	0.013	-0.003
10.533	0.000	-0.029	0.000
10.558	0.000	0.026	0.001
10.583	-0.004	-0.014	0.001
10.608	0.014	0.065	0.003
10.633	0.004	0.063	-0.009
10.658	0.000	0.075	0.003
10.683	0.013	0.087	-0.002
10.708	0.000	0.194	0.010
10.733	0.004	0.135	0.033
10.758	0.002	0.163	0.039
10.783	0.030	0.167	0.079
10.808	-0.005	0.221	0.164
10.833	0.006	0.382	0.403
10.858	-0.040	0.351	1.999
10.883	-0.047	0.514	6.242
10.908	-0.011	0.579	9.221
10.933	0.021	0.667	9.874
10.958	0.100	0.672	9.853
10.983	0.022	0.752	9.912
11.008	0.077	1.213	10.429
11.033	0.024	1.282	11.010
11.058	0.042	1.760	11.040
11.108	0.016	1.694	11.593
11.133	0.071	1.751	11.877
11.158	0.044	2.309	11.886
11.183	0.077	1.937	12.081
11.208	-0.014	2.114	12.319
11.233	0.003	2.338	12.524
11.258	-0.004	2.219	12.593
11.283	-0.119	3.446	12.594
11.308	-0.084	2.598	12.845
11.333	0.160	3.572	12.742
11.358	0.579	3.415	12.949

11.383	0.836	3.707	13.101
11.408	1.235	3.554	13.082
11.433	1.258	4.545	13.241
11.458	1.253	4.028	13.193
11.483	1.246	4.558	13.129
11.508	1.574	4.437	13.190
11.533	2.059	4.627	13.322
11.558	2.552	5.393	13.438
11.583	2.582	5.385	13.574
11.608	2.858	6.056	13.241
11.633	3.039	7.086	15.110
11.658	3.234	6.790	14.705
11.683	3.226	6.430	13.373
11.708	3.584	6.936	14.585
11.733	3.951	7.546	15.137
11.758	4.363	7.772	15.088
11.783	4.843	8.055	13.966
11.808	4.018	7.912	12.132
11.833	4.494	7.583	12.564
11.858	5.146	10.227	15.955
11.883	5.795	10.667	16.730
11.908	5.685	11.255	16.562
11.933	6.123	10.756	16.336
11.958	6.033	12.249	16.045
11.983	5.923	11.906	15.842
12.008	5.806	12.877	15.927

7 Supporting Information

7.1 Characterization of instrument effects using NO₂ photolysis

Experiments measuring the instrument response function (IRF) used a certified mix of NO₂ in He (Matheson Tri-Gas, 1.00% NO₂ with 0.5% O₂ as a stabilizing agent in He). We conducted NO₂ photolysis experiments at 8 Torr and 10.0 eV photon energy. The NO⁺ and NO₂⁺ signals are shown in Figure S1. Following photolysis at $t = 0$, we observed a small depletion in the NO₂⁺ and a fast rise in the NO⁺ signal. The measured depletion of NO₂ (from both photolytic and kinetic reactions) was $4.6 \pm 0.5\%$ determined by fitting the data over the time range from -20 to 20 ms. At later times, a further slight increase in the NO⁺ signal and a corresponding decrease in NO₂⁺ persisted, which we attributed to the gradient in excimer photolysis energy mentioned earlier. The modeled kinetics (with no modifications) for NO and NO₂ are shown in Figure S1(a) and (b) as green dashed lines.

7.1.a Instrument Response Function

The IRF arises from the velocity distribution of the sampled molecule beam and the finite transit time. Taatjes derived a functional form for the response function $h(t)$ for this instrument based on work by Moore and Carr by assuming effusive sampling.¹⁻² A Maxwell-Boltzmann velocity spread and finite transit time lead to the following expression for the temporal instrument response function:

$$h(t) \propto \frac{\exp\left(\frac{A}{(t-t_0)^2}\right)}{(t-t_0)^4} \quad (\text{SE1})$$

where A and t_0 are fitted constants. Our experiments were carried out at 8 Torr total pressure in He bath gas. The mean free path of the gas molecules in the flow tube was 10–40 μm , while the diameter of the sampling pinhole was 650 μm . The flow through the nozzle was intermediate between molecular and viscous, and we used equation (SE1) empirically.

We determined the IRF from the observed rise of the initial NO formation, shown in Figure S1. The kinetics model predicts that NO rises in the first 0.1 ms to 50% of its final value,

whereas the actual 50% rise time is 1 ms. Using MATLAB, we fit the NO^+ rise to the kinetics model curve convolved with the IRF³⁻⁴ described in Equation (SE1) and determined the values for A and t_0 to be -1.2 ms^2 and -0.49 ms , respectively. The instrument response is slower than in previous studies,³⁻⁴ and varied run-to-run (see below for an example of the data from an independent run from the data shown in the main text).

Alternatively to fitting the rise in the NO signal, we could obtain the IRF by fitting the depletion in the NO_2^+ signal (Figure S1(b)), but the inferior signal-to-noise makes the latter option a poor choice.

7.2.a Photolysis Gradient

After the initial rise in NO that occurs promptly after photolysis (1 ms 50% rise time, including IRF), the NO is expected to remain constant. Instead, we observe an additional increase in the NO signal of approximately 12% from 10 to 60 ms, as seen in Figure S1(c). Over the same time interval, a linear fit to the NO_2 data (Figure S1(d)) shows a slow depletion of $\sim 0.4\%$ on top of the initial 4.60% depletion due to photolysis. This long-time depletion corresponds to a comparable increase in NO.

We estimated the photolysis gradient from a linear regression of the NO^+ data from 15 to 60 ms. The initial yield of NO was determined using the window from 3–15 ms wherein the NO data are not impacted by the IRF. The slope obtained from the NO rise was $0.23\% \text{ ms}^{-1}$.

The IRF and photolysis gradient found for NO and NO_2 are used to define the IRF and photolysis gradient of all other experiments performed here. All time traces were convolved with the IRF to take into account the broadening effects of the instrument. Treatment of the photolysis gradient required a more detailed procedure.

The existence of a photolysis gradient implies that the chemical conditions (i.e. the radical concentrations) vary along the length of the flow tube. If we divide the flow tube into 3.66 mm sections that correspond to 1 ms time windows at our flow velocity of 3.66 mm ms^{-1} , we can map out the effect of changing the initial radical concentration along the length of the

flow tube. The radical concentrations measured at (e.g.) 10 ms would correspond to the time evolution of the gas packet initiated 36.6 mm upstream.

The photolysis gradient was incorporated into the kinetic model for NO₂ photolysis by varying the initial radical concentration and simulating the kinetics model in 1 ms steps. Each 1 ms step was combined into one model, which was convolved with the IRF. The red solid lines in Figures S1(c) and S1(d) demonstrate the effect of increasing the initial radical concentration at longer times on the NO and NO₂ modeled kinetics, respectively. Compared to the convolved model without a photolysis gradient (red dashed lines in Figures S1(c) and S1(d)), modeling the kinetics with a photolysis gradient captures both the positive slope in the NO and the negative slope in the NO₂. The negative slope derived from the NO₂ kinetics is in good agreement with the NO linear fit.

7.2 Deconvolution of isobaric signals

We derived the lineshape from the time-of-flight profile for a nominal m/z with only one species present. For example, H₂CO⁺, $m/z = 30.011$ is shown in Figure 1(a) (in the text). The lineshape was best described by a Voigt function (with residuals of < 3%); a single Gaussian function gave poorer fits, significantly underpredicting the wings.

Blended peaks were then fit as a sum of two Voigt functions. Figure 1(b) (in the text) shows the fit of the $m/z = 33$ peak, which contains contributions from HO₂⁺ (at $m/z = 32.998$) and ¹³CH₃OH⁺ (at $m/z = 33.030$). Figure 1(c) (in the text) shows fit of the $m/z = 34$ peak, which has contributions from H₂O₂⁺ (at $m/z = 34.005$) and CH₃¹⁸OH⁺ (at $m/z = 34.030$).

We used the fits to identify areas in the time-of-flight distribution that are nearly pure contributions from a single species. For the two nominal m/z peaks in question ($m/z = 33$ and 34), we found that we could take half of each Voigt profile. For example, at $m/z = 33$ (Figure 1(b)), the left half (gray hashed area, lower m/z) of the HO₂⁺ and right half (gray hashed area, higher m/z) of the ¹³CH₃OH⁺ peaks were used. The same procedure was used to separate the H₂O₂⁺ ion signal from CH₃¹⁸OH⁺ at $m/z = 34$. Kinetic traces for a given species were obtained

by summing over the hashed areas (and renormalizing for peak area) at each kinetic time interval.

7.3 Absolute photoionization cross section of methanol

The absolute methanol photoionization spectrum was measured relative to the propene spectrum following the procedure outlined in Welz et al.,⁵ and compared to previous reports. The photoionization spectrum of propene is well-known⁶ and has been used previously as a reference compound for determining photoionization cross sections.^{5,7-8}

Experiments were conducted by introducing propene (2 sccm of 1.00% propene in He) and methanol (1 sccm of 4.667% methanol in He) into the flow tube. Propene was Matheson Tri-Gas, 1.00% in Ar. The total flow was 300 sccm at 4 Torr (balance He). The photon energy was scanned from 10.5–11.5 eV in 0.025 eV increments. We averaged 15 mass spectra for each photon energy. For each photon energy, we measured the integrated intensities of the parent m/z peaks of propene and methanol, summed over 0–60 ms. We then determined the absolute cross sections of methanol $\sigma_{\text{CH}_3\text{OH}}(E)$ from the ratio of the peak areas using:

$$\sigma_{\text{CH}_3\text{OH}}(E) = \left(\frac{S_{\text{CH}_3\text{OH}}(E)}{S_{\text{C}_3\text{H}_6}(E)} \right) \cdot \left(\frac{[\text{C}_3\text{H}_6]}{[\text{CH}_3\text{OH}]} \right) \cdot \left(\frac{\alpha_{\text{C}_3\text{H}_6}}{\alpha_{\text{CH}_3\text{OH}}} \right) \cdot \sigma_{\text{C}_3\text{H}_6}(E) \quad (\text{SE2})$$

The absolute photoionization spectrum of methanol is shown in Figure S2. Both the shape and absolute cross sections of the methanol spectrum agree well with the spectrum recorded by Cool, et al., which was also measured relative to propene.⁸⁻⁹ They assigned a 20% systematic uncertainty in methanol cross sections due to the uncertainty in the cross section of propene.⁵ The same 20% systematic uncertainty also applies to our results. We measured the methanol spectrum several times; the scatter in the methanol cross section measurements results in typical cross section errors of ~5%, likely caused by uncertainties in the manometric preparation of the methanol tanks as well as uncertainties in delivery of the sample to the reaction tube. The CH₃OH cross sections reported in the text (Table 4) reflect the average of several measurements, with total error of ~21%.

Also shown in Figure S2 is the spectrum collected at $m/z = 32$ during the spectrum collection in the $\text{Cl}_2/\text{CH}_3\text{OH}/\text{O}_2$ photolysis experiment (scaled to match the CH_3OH spectrum collected above). The methanol spectrum collected during photolysis experiments matches the reference spectrum very well, indicating that observed kinetics depletions at $m/z = 32$ are free of contamination. Also notable is the sharp dip in signal at 11.083 eV in the spectrum obtained during kinetics experiments, which is apparently caused by imperfect normalization to the photon flux. As a consequence, we have removed this data point from the spectra reported in the paper.

7.4 Experiments 19–22

The photolysis gradient and instrument response function are dependent upon the alignment of the excimer beam as it travels down the flow tube. Experiments 19–22 were conducted using a different excimer alignment. This alignment resulted in a faster rise time. Figures S3(a), S3(b), S3(c) show the kinetic traces for HO_2 , H_2O_2 , and H_2CO for this data set. The A and t_0 values for this data set were -0.1 ms^2 and -0.1 ms , respectively. The HO_2 , H_2O_2 , and H_2CO cross sections obtained with this data set are consistent with the cross sections obtained from Experiments 1–18 and have been included in the final evaluation.

7.5 Highest occupied molecular orbitals of HO_2 and H_2O_2

The HOMO and HOMO-1 of HO_2 and H_2O_2 were investigated at the HF/6-311G level using the Gaussian09¹⁰ suite of programs (UHF/6-311G used for HO_2). The resulting molecular orbitals are shown in Figure S4. With this approach the HOMO of HO_2 is predicted to be the singly occupied $2a''$ orbital and the HOMO-1 being the doubly occupied $7a'$ orbital, from which electrons can be removed via photoionization to yield the $^1A'$ and $^3A''$ cations of HO_2 , respectively. Both ionization processes are expected to contribute to the photoionization cross section over the range of photoionization energies used in the present study. The HOMO and HOMO-1 of H_2O_2 are predicted to be the doubly occupied $4b$ and $5a$ orbitals; removal of an electron forms the 2B and 2A cations of H_2O_2 , respectively. The 2A cation state is not expected to be accessed until photoionization energies of $\sim 12.6 \text{ eV}$, in slight excess of the range explored in the present work.¹¹

Multiple overlapping vibronic states in the near-threshold photoionization of HO₂ and H₂O₂ and highly non-diagonal Franck-Condon factors for the ionization process make it impossible to quantitatively apply the model of Xu and Pratt for estimating photoionization cross sections of free radicals.¹² However, from Figure S4 it is clear that both the HOMO and HOMO-1 of both HO₂ and H₂O₂ are qualitatively similar. As discussed in the main text, the observation of near-threshold photoionization cross-sections that differ by a factor of ~2 is consistent with anticipated orbital occupancy effects predicted by the model for the case where the measured cross-section is dominated by ionization from the singly occupied HOMO of HO₂ or the double occupied HOMO of H₂O₂.

7.6 Full kinetics model

Table S1 shows all minor reactions that were included in the full kinetics model. These reactions, along with the major reactions listed in Table 2 in the text, were used in the Kintecus¹³ kinetics modeling program used to fit the data. These reactions played a minor role in the chemistry, but were included mainly to capture any chemistry that could result in radical recycling.

7.7 References

1. Taatjes, C. A., How does the Molecular Velocity Distribution Affect Kinetics Measurements by Time-Resolved Mass Spectrometry? *Int. J. Chem. Kin.* **2007**, *39*, 565-570.
2. Moore, S. B.; Carr Jr, R. W., Molecular Velocity Distribution Effects in Kinetic Studies by Time-Resolved Mass Spectrometry. *Int. J. Mass Spectrom. Ion Phys.* **1977**, *24*, 161-171.
3. Welz, O.; Savee, J. D.; Osborn, D. L.; Vasu, S. S.; Percival, C. J.; Shallcross, D. E.; Taatjes, C. A., Direct Kinetic Measurements of Criegee Intermediate (CH₂OO) Formed by Reaction of CH₂I with O₂. *Science* **2012**, *335*, 204-207.
4. Savee, J. D.; Welz, O.; Taatjes, C. A.; Osborn, D. L., New Mechanistic Insights to the O(³P) + Propene Reaction from Multiplexed Photoionization Mass Spectrometry. *Phys. Chem. Chem. Phys.* **2012**, *14*, 10410-10423.
5. Welz, O.; Zador, J.; Savee, J. D.; Ng, M. Y.; Meloni, G.; Fernandes, R. X.; Sheps, L.; Simmons, B. A.; Lee, T. S.; Osborn, D. L., et al., Low-Temperature Combustion Chemistry of Biofuels: Pathways in the Initial Low-Temperature (550 K-750 K) Oxidation Chemistry of Isopentanol. *Phys. Chem. Chem. Phys.* **2012**, *14*, 3112-3127.
6. Person, J. C.; Nicole, P. P., Isotope Effects in the Photoionization Yields and the Absorption Cross Sections for Acetylene, Propyne, and Propene. *J. Chem. Phys.* **1970**, *53*, 1767-1774.

7. Cool, T. A.; McIlroy, A.; Qi, F.; Westmoreland, P. R.; Poisson, L.; Peterka, D. S.; Ahmed, M., Photoionization Mass Spectrometer for Studies of Flame Chemistry with a Synchrotron Light Source. *Rev. Sci. Instrum.* **2005**, *76*, 094102-7.
8. Cool, T. A.; Wang, J.; Nakajima, K.; Taatjes, C. A.; McIlroy, A., Photoionization Cross Sections for Reaction Intermediates in Hydrocarbon Combustion. *Int. J. Mass Spectrom.* **2005**, *247*, 18-27.
9. Cool, T. A.; Nakajima, K.; Mostefaoui, T. A.; Qi, F.; McIlroy, A.; Westmoreland, P. R.; Law, M. E.; Poisson, L.; Peterka, D. S.; Ahmed, M., Selective Detection of Isomers with Photoionization Mass Spectrometry for Studies of Hydrocarbon Flame Chemistry. *J. Chem. Phys.* **2003**, *119*, 8356-8365.
10. Frisch, M. J.; Trucks, G. W.; Schlegel, H. B.; Scuseria, G. E.; Robb, M. A.; Cheeseman, J. R.; Scalmani, G.; Barone, V.; Mennucci, B.; Petersson, G. A., et al. *Gaussian 09*, Gaussian, Inc.: Wallingford, CT, USA, 2009.
11. Chevdonnet, C.; Cardy, H.; Dargelos, A., Ab Initio CI Calculations on the PE and VUV Spectra of Hydrogen Peroxide. *Chem. Phys.* **1986**, *102*, 55-61.
12. Xu, H.; Pratt, S. T., Photoionization Cross Section of the Propargyl Radical and Some General Ideas for Estimating Radical Cross Sections. *J. Phys. Chem. A* **2012**, *117*, 9331-9342.
13. Ianni, J. C., A comparison of the Bader-Deuflhard and the Cash-Karp Runge-Kutta integrators for the GRI-MECH 3.0 model based on the chemical kinetics code Kintecus. In *Computational Fluid and Solid Mechanics 2003*, Bathe, K. J., Ed. Elsevier Science Ltd: Oxford, 2003; pp 1368-1372.
14. Sander, S. P.; Abbatt, J.; Barker, J. R.; Burkholder, J. B.; Friedl, R. R.; Golden, D. M.; Huie, R. E.; Kolb, C. E.; Kurylo, M. J.; Moortgat, G. K., et al., Chemical Kinetics and Photochemical Data for Use in Atmospheric Studies, Evaluation Number 17. *JPL Publication 10-6* **2011**.
15. Atkinson, R.; Baulch, D. L.; Cox, R. A.; Crowley, J. N.; Hampson, R. F.; Hynes, R. G.; Jenkin, M. E.; Rossi, M. J.; Troe, J., Evaluated Kinetic and Photochemical Data for Atmospheric Chemistry: Volume II - Gas Phase Reactions of Organic Species. *Atmos. Chem. Phys.* **2006**, *6*, 3625-4055.
16. Veyret, B.; Rayez, J. C.; Lesclaux, R., Mechanism of the Photooxidation of Formaldehyde Studied by Flash Photolysis of Formaldehyde-Oxygen-Nitric Oxide Mixtures. *J. Phys. Chem.* **1982**, *86*, 3424-3430.
17. Atkinson, R.; Baulch, D. L.; Cox, R. A.; Crowley, J. N.; Hampson, R. F.; Hynes, R. G.; Jenkin, M. E.; Rossi, M. J.; Troe, J., Evaluated Kinetic and Photochemical Data for Atmospheric Chemistry: Volume III - Gas Phase Reactions of Inorganic Halogens. *Atmos. Chem. Phys.* **2007**, *7*, 981-1191.
18. Tyndall, G. S.; Orlando, J. J.; Kegley-Owen, C. S.; Wallington, T. J.; Hurley, M. D., Rate Coefficients for the Reactions of Chlorine Atoms with Methanol and Acetaldehyde. *Int. J. Chem. Kin.* **1999**, *31*, 776-784.

19. Biggs, P.; Canosa-Mas, C. E.; Fracheboud, J.-M.; Shallcross, D. E.; Wayne, R. P., Kinetics of the Reaction of F Atoms with CH₃ONO and CH₃O, and the Reaction of CH₃O with a Number of Hydrocarbons. *J. Chem. Soc., Faraday Trans.* **1997**, *93*, 2481-2486.

20. Tsang, W.; Hampson, R. F., Chemical Kinetic Data Base for Combustion Chemistry. Part I. Methane and Related Compounds. *J. Phys. Chem. Ref. Data* **1986**, *15*, 1087-1279.

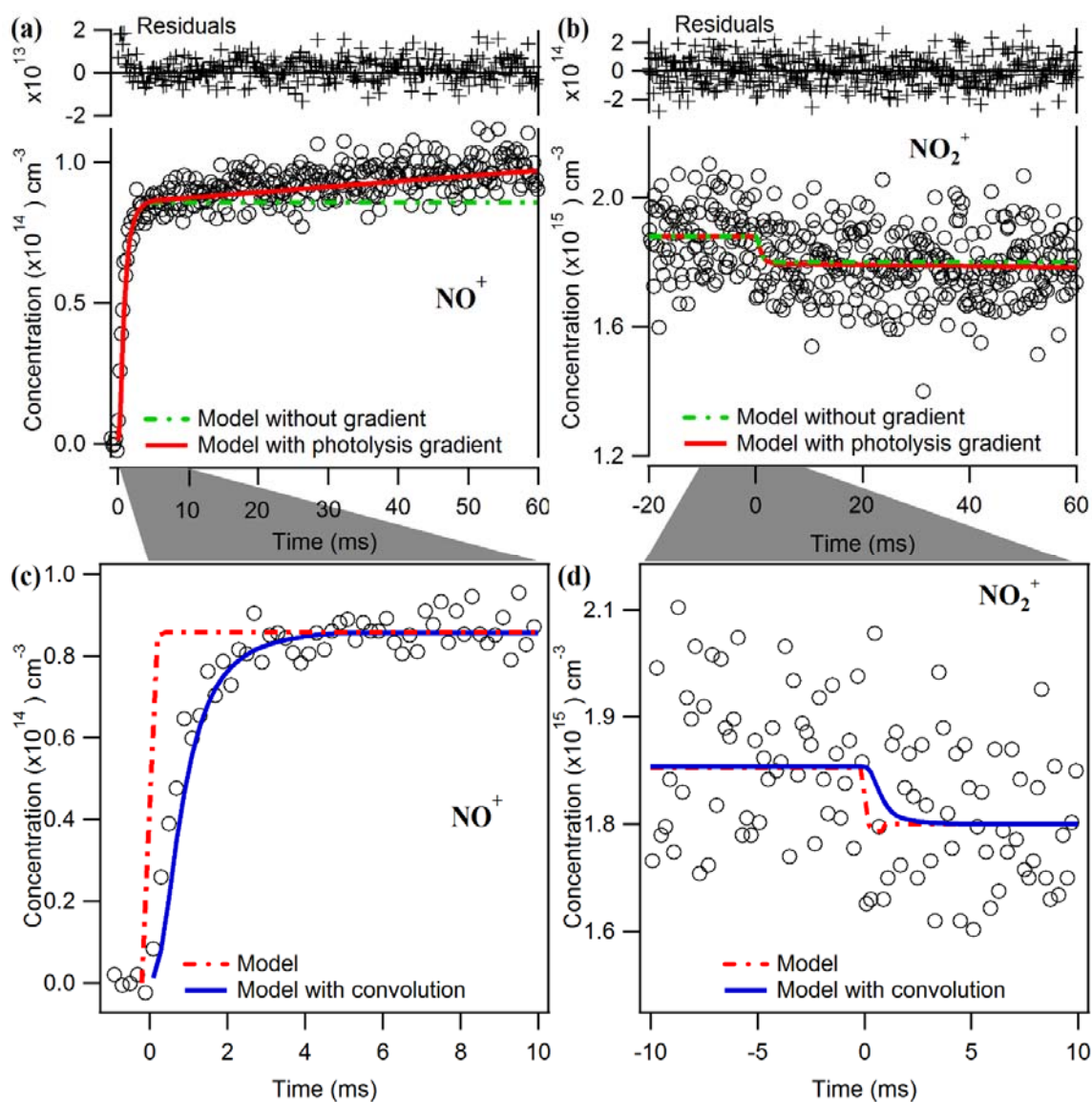


Figure S1. NO_2 photolysis experiments to calibrate instrument effects. Data were scaled to the modeled concentrations as described in the text. (a) Time-dependent NO^+ ion signal at $m/z = 30$, demonstrating the slow rise in NO^+ signal from the photolysis gradient. Unadjusted model (green dash-dot line); Model including photolysis gradient (red solid line). (b) Time-dependent NO_2^+ ion signal at $m/z = 46$, also showing the small change in precursor depletion due to the photolysis gradient. Unadjusted model (green dash-dot line); Model including photolysis gradient (red solid line). (c) NO^+ ion signal zoomed in to early times (0 – 10 ms). Unmodified model (red dash-dot line); Model including linear photolysis gradient, convolved with IRF (blue solid line). (d) NO_2^+ ion signal zoomed in to early times (-10 – 10 ms). Unmodified model (red dash-dot line); Model including linear photolysis gradient, convolved with IRF (blue solid line).

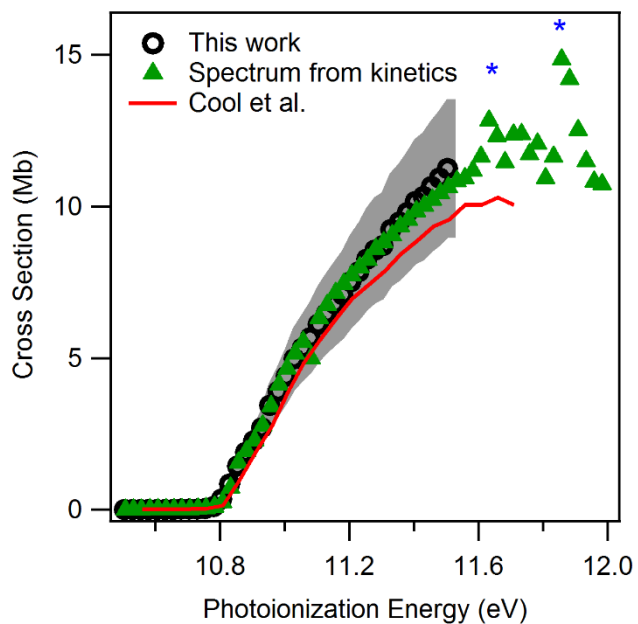


Figure S2. Absolute photoionization cross section of methanol. Literature methanol photoionization spectrum, taken from Cool et al. (red line).⁵ Our measured absolute cross section obtained here is shown, the gray shading demonstrates the 20% error associated with referencing the CH₃OH ion signal to the literature propene spectrum. Also shown is the $m/\tilde{\nu} = 32$ spectrum (triangles) obtained during kinetics experiments described in the paper (scaled relative to our measured reference methanol spectrum). Interferences caused by Ar resonances are indicated by asterisks.

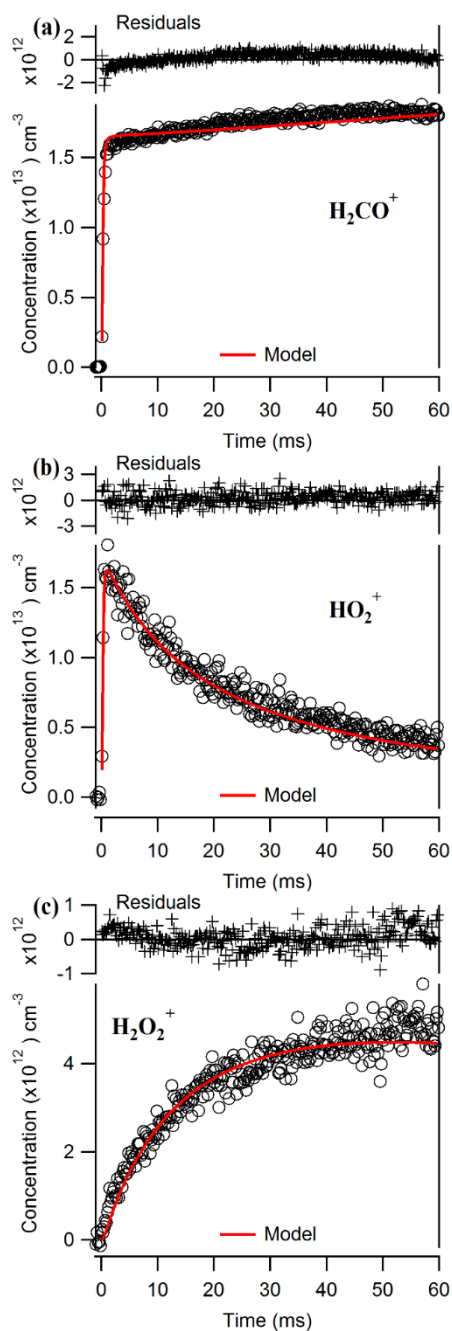


Figure S3. Single energy kinetics traces for title molecules, from the data set exhibiting a faster rise, indicating a faster IRF. Data are scaled to the model as part of the cross section determination process. Representative time-dependent traces of (a) H_2CO^+ , (b) HO_2^+ , and (c) H_2O_2^+ at 11.45 eV. These data are from Experiment 19 (see Table 3 in the text). The red line is the modeled kinetics of each corresponding trace, convolved with the IRF and including a photolysis gradient and first order wall losses of HO_2 and H_2O_2 (6.6 and 6.9 s⁻¹, respectively).

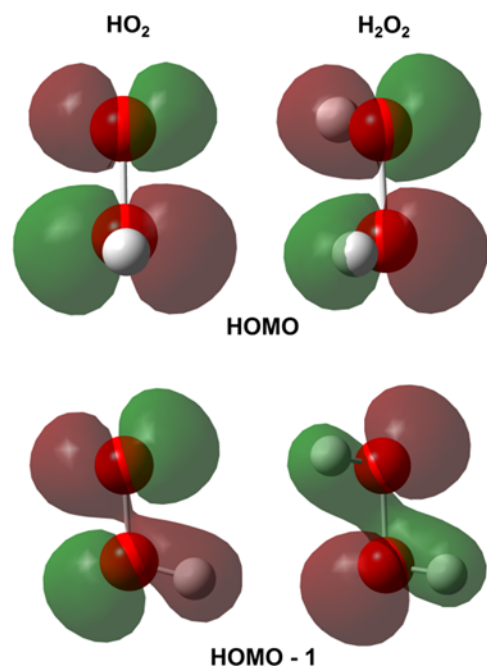


Figure S4. The HOMO and HOMO-1 for HO₂ and H₂O₂ generated using HF/6-311G.

Table S1. Minor reactions that were included in the full kinetics model used to fit data. This table does not include all of the major reactions that were listed in Table 2 in the text. The summation of these two tables represents the full kinetics model. Pressure-dependent rate constants are for 8 Torr. All rate constants are taken from the NASA Data Evaluation¹⁴ unless otherwise noted.

	$k_{298\text{K}}$ (cm^3 $\text{molecule}^{-1} \text{s}^{-1}$)
Hydroxy methyl peroxy reactions	
(12) ^a $\text{HOCH}_2\text{O}_2 + \text{HOCH}_2\text{O}_2 \rightarrow \text{HC(O)OH} + \text{HOCH}_2\text{OH} + \text{O}_2$	7.0×10^{-13}
$\text{HOCH}_2\text{O}_2 + \text{HOCH}_2\text{O}_2 \rightarrow \text{HOCH}_2\text{O} + \text{HOCH}_2\text{O} + \text{O}_2$	5.5×10^{-12}
(13) ^a $\text{HOCH}_2\text{O}_2 + \text{HO}_2 \rightarrow \text{HOCH}_2\text{OOH} + \text{O}_2$	7.2×10^{-12}
$\text{HOCH}_2\text{O}_2 + \text{HO}_2 \rightarrow \text{HC(O)OH} + \text{H}_2\text{O} + \text{O}_2$	4.8×10^{-12}
(14) ^b $\text{HOCH}_2\text{O} + \text{O}_2 \rightarrow \text{HC(O)OH} + \text{HO}_2$	3.5×10^{-14}
HO₂ reactions	
(15) $\text{H} + \text{O}_2 \xrightarrow{\text{M}} \text{HO}_2$	1.1×10^{-14}
(16) $\text{HO}_2 + \text{OH} \rightarrow \text{H}_2\text{O} + \text{O}_2$	1.1×10^{-10}
(17) ^c $\text{HO}_2 + \text{ClO} \rightarrow \text{HOCl} + \text{O}_2$	6.9×10^{-12}
OH reactions	
(18) $\text{OH} + \text{OH} \xrightarrow{\text{M}} \text{H}_2\text{O}_2$	1.6×10^{-13}
(19) $\text{OH} + \text{OH} \rightarrow \text{H}_2\text{O} + \text{O}$	1.8×10^{-12}
(20) $\text{OH} + \text{H}_2\text{O}_2 \rightarrow \text{HO}_2 + \text{H}_2\text{O}$	1.8×10^{-12}
(21) $\text{OH} + \text{H}_2\text{CO} \rightarrow \text{HCO} + \text{H}_2\text{O}$	8.5×10^{-12}
(22) $\text{OH} + \text{HCl} \rightarrow \text{H}_2\text{O} + \text{Cl}$	7.8×10^{-13}
(23) ^c $\text{OH} + \text{ClO} \rightarrow \text{HO}_2 + \text{Cl}$	1.9×10^{-11}
$\rightarrow \text{HCl} + \text{O}_2$	1.2×10^{-12}

(24)	$\text{OH} + \text{HOCl} \rightarrow \text{H}_2\text{O} + \text{ClO}$	5.0×10^{-13}
(25) ^c	$\text{OH} + \text{Cl}_2 \rightarrow \text{HOCl} + \text{Cl}$	6.5×10^{-14}
(26) ^c	$\text{OH} + \text{OCIO} \rightarrow \text{HOCl} + \text{O}_2$	1.1×10^{-11}
Cl reactions		
(30) ^d	$\text{Cl} + \text{CH}_2\text{OH} \rightarrow \text{HCl} + \text{H}_2\text{CO}$	3.0×10^{-10}
(31)	$\text{Cl} + \text{H}_2\text{O}_2 \rightarrow \text{HCl} + \text{HO}_2$	4.1×10^{-13}
(32)	$\text{Cl} + \text{O}_2 \xrightarrow{\text{M}} \text{ClO}_2$	5.7×10^{-16}
	$\text{ClO}_2 \xrightarrow{\text{M}} \text{Cl} + \text{O}_2$	$2.0 \times 10^5 (\text{s}^{-1})$
(33)	$\text{Cl} + \text{ClO}_2 \rightarrow \text{Cl}_2 + \text{O}_2$	2.3×10^{-10}
	$\rightarrow 2\text{ClO}$	1.2×10^{-11}
(34)	$\text{ClO} + \text{ClO} \rightarrow \text{Cl}_2 + \text{O}_2$	4.8×10^{-15}
	$\rightarrow \text{ClO}_2 + \text{Cl}$	8.0×10^{-15}
	$\rightarrow \text{OCIO} + \text{Cl}$	3.5×10^{-15}
(35) ^c	$\text{ClO} + \text{ClO} \xrightarrow{\text{M}} \text{Cl}_2\text{O}_2$	2.3×10^{-15}
	$\text{Cl}_2\text{O}_2 \xrightarrow{\text{M}} \text{ClO} + \text{ClO}$	$2.7 \times 10^{-1} (\text{s}^{-1})$
(36) ^c	$\text{ClO} + \text{OCIO} \xrightarrow{\text{M}} \text{Cl}_2\text{O}_3$	9.6×10^{-15}
	$\text{Cl}_2\text{O}_3 \xrightarrow{\text{M}} \text{ClO} + \text{OCIO}$	$6.4 \times 10^1 (\text{s}^{-1})$
(37)	$\text{Cl} + \text{OCIO} \rightarrow \text{ClO} + \text{ClO}$	5.8×10^{-11}
(38)	$\text{Cl} + \text{HOCl} \rightarrow \text{Cl}_2 + \text{OH}$	2.2×10^{-12}
(39)	$\text{Cl} + \text{Cl}_2\text{O}_2 \rightarrow \text{Cl}_2 + \text{ClO}_2$	1.0×10^{-10}
(40)	$\text{Cl} + \text{Cl} \xrightarrow{\text{M}} \text{Cl}_2$	1.4×10^{-14}

Methoxy reactions

^aTaken from IUPAC (Volume II).¹⁵ ^bTaken from Veyret et al.¹⁶ ^cTaken from IUPAC (Volume III).¹⁷ ^dTaken from Tyndall et al.¹⁸ ^eTaken from Biggs et al.¹⁹ ^fTaken from Tsang and Hampson.²⁰

VACUUM ULTRAVIOLET PHOTOIONIZATION CROSS SECTION OF THE HYDROXYL RADICAL

1 Introduction

The hydroxyl (OH) radical has been the subject of many photoionization studies due to its importance in atmospheric¹⁻³ and combustion⁴ oxidation processes, and its presence in the interstellar medium.⁵ There have been several OH oxidation studies performed recently using vacuum ultraviolet (VUV) energies to detect hydrocarbon precursors and products.^{6,7} However, the OH radical was not observed in these experiments. In our efforts to quantitatively characterize oxidation processes relevant to the atmosphere and combustion environments using photoionization mass spectrometry, we found it necessary to develop methods to quantitatively produce and detect the radical intermediates that control key chemical reactions. However, absolute VUV photoionization cross sections exist for very few radicals, so they must be measured to fully utilize kinetics experiments. We recently described methodology to successfully measure the absolute photoionization spectrum of the hydroperoxyl radical (HO₂).⁸

Outside of the world of reaction kinetics, much work has been done to characterize OH ionization. Several photoelectron studies,⁹⁻¹³ photoabsorption¹⁴ and relative photoionization spectra¹⁵⁻¹⁷ have characterized the OH cation. Photoionization of OH ($X^2\Pi$) in the threshold region removes an electron from the valence ($2p\pi$) molecular orbital to form the ground electronic state of OH⁺ ($X^3\Sigma^-$). The adiabatic ionization energy of OH is 13.0170 ± 0.0002 eV.⁹ High-resolution relative photoionization spectra have been presented in two separate works.^{15,16} In both experimental spectra, the photoionization spectrum increases rapidly to a peak at threshold, then OH photoionization spectrum decreases to a plateau and remains constant before reaching an intense structure that was ascribed to a rotationally-resolved member of the Rydberg series converging to the $a^1\Delta$ excited state appearing centered at 13.55 eV. The high energy resolution relative photoionization spectra reported in both studies are

in very good agreement in terms of the shape and position of the various observed spectroscopic features. Yet, to our knowledge, no absolute photoionization cross section measurements exist for the OH radical.

The increasingly widespread use of tunable VUV radiation from synchrotrons supports the need to obtain quantitative photoionization cross sections for free radical intermediates. VUV mass spectrometric detection of gas phase free radicals was introduced by Bayes in 1972,¹⁸ and has since become an important tool for time-resolved gas phase kinetics investigations.¹⁹⁻²⁶ The multiplexed photoionization mass spectrometer (MPIMS) couples the tunability of synchrotron light sources with the detection sensitivity of mass spectrometry and the time resolution of pulsed-laser-photolysis kinetics experiments in order to tackle questions of importance in gas phase chemistry.^{27,28}

In this chapter, we combined photoionization spectroscopy with chemical kinetics to perform time-resolved photoionization experiments that generate OH from the $O(^1D) + H_2O$ reaction. We obtained absolute photoionization cross sections for the OH radical at two photon energies by measuring the ion signal of OH relative to a known standard, either $O(^3P)$ or Xe. The concentration of OH was quantified by modeling the time-dependent kinetics of OH, O_3 , and $O(^3P)$, and estimating the initial absolute concentration of $O(^1D)$.

2 Experiment

The Multiplexed Photoionization Mass Spectrometer has been described in detail in previous publications.^{27,28} The experiments conducted here are similar to our prior work.⁸

Initial concentrations of approximately 10^{12} cm^{-3} OH radicals were produced in a slow flow reactor by flash photolysis of $O_3/H_2O/O_2$ mixtures with added xenon (photoionization calibration standard) highly diluted in helium at 8 Torr and room temperature. UV radiation at 248 nm from a KrF excimer laser propagating along the axis of the flow cell photodissociated O_3 to initiate reactions. Time-resolved measurements were made by sampling the reaction mixture after expansion from a small orifice in the side of the reactor tube. Neutral species in the jet were ionized by tunable VUV synchrotron radiation, and the

ions were detected with orthogonal acceleration time-of-flight (OA-TOF) mass spectrometry. Experiments were performed using tunable synchrotron VUV light generated at the Chemical Dynamics Beamline of the Advanced Light Source, Lawrence Berkeley National Laboratory. Radicals were detected, along with reactants and co-products, at their parent ions.

The reactor comprised a 1.05 cm inner diameter, 62 cm long quartz tube coated with an amorphous fluoroplastic resin, DuPont AF 400S2-100-1. Gases were introduced upstream of the 600 μm diameter sampling orifice. Helium (Matheson Tri-Gas, 99.9999%) was introduced into the reactor using a calibrated mass flow controller (MKS Instruments). A saturated stream of water vapor was introduced through a calibrated mass flow controller by flowing He through a fritted bubbler of distilled, purified water immersed in a temperature-controlled bath. Ozone was generated from pure oxygen (Matheson Tri-Gas, 99.998%) by a commercial corona discharge ozone generator (OzoneLab Instruments). The combined O_3/O_2 flow was measured with a variable rotameter (King Instruments Company 45 sccm full scale, error $\pm 4\%$ full scale). The ozone concentration was measured on the input line before the rotameter using an ozone monitor (2B Technologies Model 202). The m/z 48 ozone ion signal was linear with the expected ozone concentration in the cell, although the ozone mixing ratio delivered to the monitor exceeded the rated range by as much as a factor of 5. The ion signal also agreed with the signal computed from the absolute photoionization cross section reported in the literature,²⁹ leading us to conclude that the ozone monitor measurement was reasonably accurate (see supplementary material)³⁰. A cylinder of xenon diluted in He ($0.974 \pm 0.001\%$) was prepared, and a small flow (0.5 ± 0.2 sccm) was added to the flow reactor as a photoionization reference gas. The total flow of all gases through the reactor was 200 ± 5 sccm. The total pressure was maintained at 8.00 ± 0.04 Torr (measured with a capacitance manometer (MKS Baratron) with a butterfly valve leading to a Roots pump).

Typical starting mole fractions of reagent gases were 1% O_2 , 1% H_2O , 100 ppm O_3 , and 20 ppm Xe (photoionization cross section reference gas) with the balance composed of He. The

O₃ was photolyzed by an unfocused excimer laser pulse (Coherent COMPex Pro 110 KrF, 248 nm, 15 ns, 4 Hz) at two laser fluences of 18 or 12 mJ cm⁻² pulse⁻¹ (the lower fluence was obtained by inserting a wire mesh filter). Time-resolved radical concentrations were measured by recording complete OA-TOF mass spectra at 50 kHz. We summed every 10 spectra to obtain a mass spectrum every 0.2 ms. With each laser shot, we acquired a two-dimensional data set (ion counts as a function of mass-to-charge ratio (m/z) and reaction time relative to the excimer laser pulse). We averaged data from 2,000–5,000 laser shots for the kinetics experiments. To record the photoionization spectrum, we scanned the photon energy over the range 12.513–14.213 eV in steps of 0.05 eV (spectral resolution of $\Delta E(\text{FWHM}) = 8$ meV), averaging 50 laser shots at each photon energy. Such scans generated three-dimensional data-sets (i.e. ion counts as a function of m/z , reaction time, and photoionization energy).

Several instrument effects were treated as described previously.⁸ The mass-dependent sensitivity of the OA-TOF to the ion signal was measured empirically, which was necessary to compare the ion signal of the target species with that of the reference compounds (O(³P) and Xe) in order to obtain photoionization cross sections.³¹ Additionally, in order to compare the time-dependent ion signals with a quantitative kinetics model, we needed to incorporate the finite instrument time-response function caused by Maxwell-Boltzmann sampling in the experiment,^{32,33} and the small gradient in the photolysis yield along the flow axis, into our kinetics model. In this work, we measured the instrument response function and photolysis gradient under conditions with the lower photolysis laser fluence (12 mJ cm⁻² pulse⁻¹). These conditions created less radical recycling, which enabled a clearer measurement of the latter two instrument effects. Finally, background ion counts from the strong H₂O⁺ signal had to be subtracted from both OH and O(³P) signals. Background signals were identified by their existence before the excimer laser fired ($t < 0$ ms).

Observed ion signals were first background-subtracted to remove background ion counts that occurred due to high concentrations of water in the reactor. We computed an average pre-photolysis ion signal at each mass from -19 to -1 ms for each set of experiments, and then

subtracted this average from each time-dependent ion signal. These background signals are small—but significant—and by performing a simple background subtraction, we assumed that the neutral species yielding these ions were time independent after the photolysis laser fires. On average, these background signals were on the order of 1% of the peak ion counts for OH and 6% of the peak ion counts for O(³P).

We measured the photoionization cross section of OH at two photon energies—13.436 and 14.193 eV—relative to two different reference compounds—xenon and O(³P). First, we conducted experiments with a photon energy (14.193 eV) above the ionization energy of O(³P) (the ionization energy of O(³P) is 13.6181 eV)³⁴ in order to obtain a photoionization cross section for OH relative to the known photoionization cross section of O(³P). The OH and O(³P) time-dependent concentrations were simulated from a detailed analysis of the reaction kinetics and an estimate of the initial O(¹D) concentration formed from the photolysis of ozone. By relating the time-dependent ion signals to the simulated concentrations, we determined the photoionization cross section of OH at 14.193 eV relative to that of O(³P). At the same time, we measured the photoion signal for the added xenon calibration gas and used its literature photoionization cross section to quantify its concentration in these experiments. Although the absolute gas flow of the xenon standard into the reactor has a large uncertainty (0.5 sccm ±40%) derived from the mass flow controller's specification, the precision of this flow was much higher. Xenon ion signals were constant across all experiments to ±1%. Therefore, the average xenon concentration, measured at 14.193 eV relative to the quantitative O(³P) signal, was used as the absolute photoionization standard for experiments at 13.436 eV, a photon energy below the ionization energy of O(³P). At 13.436 eV, we again used the modeled OH kinetics and the OH ion signal to obtain the photoionization cross section of OH, this time relative to the average xenon concentration and the well-known xenon cross section. The photoionization spectrum of OH was obtained by recording the relative photoionization spectrum from 12.513 to 14.213 eV and scaling to the absolute OH photoionization cross sections measured at these two energies.

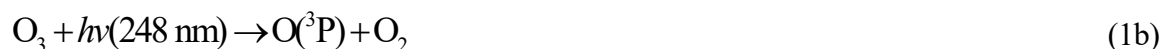
3 Results

3.1 Experiments

Sixteen experiments were conducted, varying conditions such as initial O₃ or H₂O concentration, excimer laser fluence, or the VUV photon energy. Table I lists the VUV photon energy, initial reactant conditions, and estimated O(¹D) concentrations for each experiment. Eight experiments were performed at a photon energy of 13.436 eV, and five experiments at a photon energy of 14.193 eV. Lower radical concentrations were achieved with a laser attenuator in three experiments (13 through 15). In experiment 16, the VUV photon energy was scanned to obtain the relative photoionization spectrum. The O₂ and He concentrations were determined from the mass flows and total pressure. The concentration of H₂O was computed from the mass flows and the vapor pressure of water, given the measured bath temperature and bubbler pressure. The initial concentration of ozone was determined from the mass flows and the external ozone monitor measurement of the O₃/He mixture immediately after the ozonizer (see supplementary material)³⁰. We detected photoionization signals of OH, O₃, and O(³P) at their parent *m/z* ratios.

3.2 Kinetics modeling

Photolysis of O₃ at 248 nm generated oxygen atoms promptly by direct photodissociation



Reaction (1a) is 90±9 % of the total yield for reaction (1).⁴¹⁻⁴³ The O(¹D) atoms reacted with H₂O to form two OH radicals in < 0.2 ms,



However, a significant fraction of the O(¹D) atoms underwent a competing process—collisional quenching, primarily by O₂:

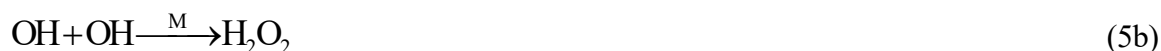


Approximately 5–40% are quenched through reaction (3), depending on conditions.

Under our conditions, OH primarily reacted with O(³P) at early times ($t < 5$ ms) until O(³P) was depleted.



At longer times, the OH self-reaction becomes the dominant removal mechanism.



Reaction (4) regenerates OH radicals since the H atoms react quickly with O₃.



Reaction (6) effectively slows the observed OH decay rate so long as O(³P) atoms were available to create H atoms in reaction (4). Reactions (3) through (6) largely determine the time-dependence of the OH concentrations.

We modeled the reaction kinetics using a numerical program (Kintecus⁴⁴). The full kinetics model is listed in Table II. All of the rate coefficients were obtained from the NASA Panel for Data Evaluation of Chemical Kinetics and Photochemical Data.⁴³ In addition to reactions (1) through (6) listed here, we included 12 other reactions in the model, but these had a minor effect on the kinetics of the relevant species. For example, reaction of OH with O₃ was not fast enough to affect the time-dependent nature of either species on our timescale. The time-dependent concentrations modeled for OH, O₃, and O(³P) were convolved with the instrument response function, as discussed previously.⁸

OH radicals are known to undergo reactions on the inner surface of a reactor. This wall loss must be empirically determined, as it depends on the specific nature of the wall substrate and any coatings.

3.3 Observed kinetics

Examples of the time-dependent O₃, OH, and O(³P) signals are shown in Figures 1–3. Photolysis led to an instantaneous depletion of typically 10–20% in O₃. The ozone signal continued to drop as secondary chemistry (reaction (6)) removed additional O₃. OH radicals formed rapidly after the reaction of the photolysis product O(¹D) with H₂O, reaching peak concentrations of approximately $0.2\text{--}1.5 \times 10^{13} \text{ cm}^{-3}$ in the first 0.5 ms. O(³P) atoms, formed from photolysis of O₃ (reaction (1b)) or quenching by O₂ (reaction (3)) were also present in relatively high concentrations ($0.2\text{--}4 \times 10^{12} \text{ cm}^{-3}$) at early times.

3.3.a Ozone Photolysis

Figure 1(a) shows the observed O₃ signal measured at m/z 48 during Experiment 4 (Table I). The instantaneous depletion from photolysis was $23.3 \pm 0.3\%$ (indicated by the dashed black line in Figure 1(b)), in good agreement with the O₃ depletion of 24% estimated from the measured laser fluence, O₃ concentration, and the O₃ absorption cross section ($1.08 \times 10^{-17} \text{ cm}^2$) at 248 nm.⁴³ As seen in Figure 1(b), subsequent removal of O₃ occurs through reaction with H atoms (reaction (6)) at early times and reaction with remaining OH later. The model slightly overpredicts the initial loss and underpredicts the loss rate at longer times ($t > 10$ ms).

3.3.b O(¹D) Atoms

In order to model $[\text{OH}](t)$, we needed to determine the absolute O(¹D) atom concentrations. O(¹D) atoms could not be observed directly because their expected lifetime ($\sim 1 \mu\text{s}$) was much shorter than the instrument temporal resolution. Instead, we estimated the initial O(¹D) atom concentrations from the measured O₃ concentration, observed fractional depletion of O₃ caused by photolysis, and known O(¹D) quantum yield (reaction (1a)).

Table II lists the measured $[O(^1D)]_0$ atom concentration for each experiment, measured from the initial O_3 depletion. The measured depletion was consistent for experiments with the same laser settings (Experiments 1–12) and ranged from 21.0 ± 0.1 % to 23.8 ± 0.2 % (experiments using an attenuator to achieve lower radical concentrations (experiments 13–15) had smaller, self-consistent depletions around 14%). $O(^1D)$ atom concentrations ranged from $1\text{--}13 \times 10^{12} \text{ cm}^{-3}$.

3.3.c OH Radicals

OH radicals were formed from reaction of photolytically-generated $O(^1D)$ atoms with H_2O . Figure 2 shows the time-dependent behavior of the OH^+ signal from Experiment 4 (13.436 eV). There is a sharp rise in OH upon O_3 photolysis reaching a peak at $t < 1$ ms, followed by a decay that approaches baseline after 60 ms. The modeled OH time profile shown in Figure 2 (red dashed line) agrees reasonably with the observed trace with two notable differences.

First, the observed OH decay appears to have two components, with a fast component with ~ 2 ms lifetime that is not present in the kinetics model (the lifetime of OH with respect to $O(^3P)$, reaction (3), at the maximum $O(^3P)$ concentration is 8 ms). We attribute this feature to the decay of vibrationally-excited OH radicals formed in the flow tube from reaction (2). Experiments on isotopically-labeled $H_2^{18}O$ revealed that two OH radicals are formed from reaction (2); the heavier OH radical product is formed cold, with nearly all of its population in $OH(v=0)$.⁴⁵⁻⁵⁰ At the same time, a significant fraction of the lighter OH radical is in $OH(v=1)$ (29%) and $OH(v \geq 2)$ (30%).⁵⁰ In our experiments, we did not isotopically label the water, meaning that all OH products would appear at the same mass regardless of their vibrational states. Vibrationally-excited OH radicals would exhibit a different dependence on photoionization energy than $OH(v=0)$, as well as dissimilar kinetics. $OH(v \geq 1)$ would primarily decay to form ground state OH via vibrational quenching with all the other collision partners (e.g., the lifetime of $OH(v=1)$ with respect to collisional deactivation⁵¹ by O_2 is 1.5–11 ms for the range of $[O_2]$ used here). However, the spectroscopic evidence to assign this fast component in the OH decay to $OH(v \geq 1)$ is inconclusive.

The other difference between model and observation is in the second component of the decay, which should be equal to the modeled OH decay if the model is complete. The measured lifetime is about 16 ms—slightly longer than the modeled lifetime of about 13 ms. Similar to our observations of the HO₂ radical,⁸ it is expected that some of the OH radicals are removed through heterogeneous interactions with the wall of the flow tube. Under this assumption, we conducted several experiments where we varied the initial conditions of the reaction system (in particular, varying the initial OH radical density over a range 0.2–1.5×10¹³ OH radicals cm⁻³) and independently fit the model to these data to quantify the OH wall loss rate. The average heterogeneous wall loss rate across all experiments was 28±6 s⁻¹. The random error in this measurement was quite small, but the reported uncertainty in this wall loss rate is on the order of 20% due to the uncertainty in the kinetics simulation.

Figure 2 (green line) shows the modeled decay of OH when incorporating a fitted wall loss rate. We did not attempt to fit the sharp spike in signal at early times (the component assumed to be from OH(*v*=1)), but used the model with the added wall loss term in our determination of the photoionization cross section of OH. The OH wall loss rate described above is not large, and is of a similar magnitude as the HO₂ wall loss rate we measured previously,⁸ but it significantly perturbs the kinetics and must be included in order to obtain an OH cross section.

The model including OH wall loss predicts slightly less depletion of O₃ at long times (Fig. 1b, green line) than the model without OH wall loss (red dashed line). Modeling of the secondary depletion of O₃ plays only a minor role in constraining [OH](*t*), so discrepancies between the modeled and observed O₃ traces do not have a large effect on the reported OH cross section.

3.3.d O(³P) Atoms

O(³P) atoms, formed from initial photolysis and rapid collisional deactivation of O(¹D) were also observed during these experiments. The O(³P) signal rises quickly, and then decays rapidly primarily due to reaction with OH. Figure 3 shows the measured O(³P) signal, scaled relative to the kinetics model for Experiment 11 (14.193 eV). The agreement between the

observed and modeled $[O(^3P)](t)$ is good; both show $O(^3P)$ decay on the order of 4 ms. Due to the rapid reaction of $O(^3P)$ atoms with OH, heterogeneous decay of $O(^3P)$ on the reactor walls makes a negligible contribution to $O(^3P)$ loss.

3.4 Experimental cross section and spectrum

3.4.a Cross Section

We measured the absolute photoionization cross section for OH at two VUV photon energies. Xenon and $O(^3P)$ were used as the absolute photoionization reference compounds at 13.436 and 14.193 eV, respectively. The xenon absolute cross section at 13.436 eV was evaluated by Samson and Stolte (65.3 ± 1 Mb).⁵² The absolute photoionization cross section of $O(^3P)$ was measured by Angel and Samson at 14.25 eV (3.1 ± 0.3 Mb),⁵³ and we use this value for our analysis at 14.193 eV because the $O(^3P)$ spectrum is flat in this region.

The OH cross section ($\sigma_{OH}(E)$) was measured relative to the reference molecule cross section ($\sigma_{ref}(E)$) using equation (I).

$$\sigma_{OH}(E) = \sigma_{ref}(E) \times \frac{\alpha_{ref} \times f_{ref}}{\alpha_{OH} \times f_{OH,17}} \times \frac{\left\langle \frac{S_{OH}(E)}{N_{OH}} \right\rangle_t}{\left\langle \frac{S_{ref}(E)}{N_{ref}} \right\rangle_t} \quad (I)$$

where α_i is the mass discrimination factor and f_i is the isotopic abundance of each molecule. The mass discrimination factor, $\alpha_i = (m_i)^n$, was described by Savee et al.³¹, where m_i is the mass-to-charge ratio for the ion and n is a factor that defines the mass-dependence of the ion sampling efficiency (in this work, we found $n = 1.0$). We compute the average OH cross section for each experiment by summing over the ratio of the background-subtracted time-dependent OH signal ($S_{OH}(E,t)$) and the simulated OH reaction profile ($N_{OH}(t)$) from 5 to 40 ms and dividing that sum by the number of time bins (a), as shown in equation (II):

$$\left\langle \frac{S_{\text{OH}}(E)}{N_{\text{OH}}} \right\rangle_t = \frac{1}{a} \sum_{t=5 \text{ ms}}^{40 \text{ ms}} \frac{S_{\text{OH}}(E,t)}{N_{\text{OH}}(t)} \quad (\text{II})$$

This value placed on an absolute scale when it is divided by the average of the same ratio for the reference species:

$$\left\langle \frac{S_{\text{ref}}(E)}{N_{\text{ref}}} \right\rangle_t = \frac{1}{b} \sum \frac{S_{\text{ref}}(E,t)}{N_{\text{ref}}(t)} \quad (\text{III})$$

In equation (III), the limits of the summation depend on the reference compound; b is defined as the number of time bins in the summation. At 14.193 eV, O(³P) served as the reference atom, and we averaged the background-subtracted O(³P) signal ($S_{\text{ref}}(E,t)$), divided by the simulated O(³P) kinetics ($N_{\text{ref}}(t)$) from 1–10 ms in order to determine the OH cross section at 14.193 eV and to measure the xenon concentration in the reactor. At 13.436 eV, xenon served as the reference atom. The reference xenon signal was not background subtracted because it added as a time-independent, chemically-inert reference. We averaged the ratio of the signal and the measured xenon concentration from –20 to 130 ms. We used this procedure to obtain the absolute cross section for OH independently for each experiment listed in Table II. The average cross section is reported for the two photon energies in Table III.

3.4.b Spectrum

The OH absolute photoionization cross sections measured at the two photon energies were used to place a relative photoionization spectrum on an absolute ordinate. The relative spectrum was collected by scanning the synchrotron photon energy from 12.513–14.213 eV at 0.05 eV steps using the reaction conditions listed in Table I (Experiment 16). The data, shown in Figure 4, was integrated over 0–60 ms, with the background ion signal measured from –19 to –1 ms subtracted. This relative signal was normalized to the VUV photon flux, measured at each energy using a photodiode (SXUV100), and was scaled to the absolute cross section measurements reported in Table III. The absolute photoionization spectrum of OH is reported as tabulated data in the supplementary materials.³⁰

We also obtained the absolute VUV photoionization spectrum of $O(^3P)$ in the same experiment. The black open circles in Figure 5 are the photoionization spectrum measured in this work, scaled by the literature absolute photoionization cross section of $O(^3P)$ at 14.25 eV (3.1 Mb)⁵³. Since the $O(^3P)$ atoms are present at much lower concentrations and are more transient than OH radicals, the integrated ion count of $O(^3P)$ at each VUV energy is significantly smaller, leading to a poorer signal to noise as compared to the OH signal.

3.5 Experimental error analysis

In this section, we define the sources of error that contribute to the uncertainty in the reported OH photoionization cross sections. There are two main sources of error in modeling the time dependence of the species present in our experiments: uncertainty in the rate constants in the kinetics model and uncertainty in the initial number of radicals formed. Uncertainty in initial $[H_2O]$, $[O_2]$, temperature, and pressure have a negligible effect on the OH concentration.

Uncertainty in the literature rate constants in the kinetics model propagates to the modeled concentrations. The largest source of uncertainty for OH is the 25% uncertainty in the room temperature OH self-reaction rate constant, and the largest uncertainty for $O(^3P)$ is the 15% uncertainty in the $O(^3P) + OH$ rate constant. To understand the uncertainty in our kinetics model, we varied all rate constants in Table I using Monte Carlo sampling ($N = 1000$) from a normal distribution of the standard deviations of the rate constants listed in the JPL evaluation, finding the standard deviation of the time-dependent OH concentration in the fitting window to be about 12% and for $O(^3P)$ about 29%.

Uncertainty in the initial $[O(^1D)]$ formed during photolysis also contributes to uncertainty in modeled concentrations. Three parameters must be known to find the initial $[O(^1D)]$: the initial O_3 concentration, the fraction of O_3 photodissociated, and the $O(^1D)$ quantum yield. The first parameter, $[O_3]_0$, is obtained by measuring the O_3 concentration using the ozone monitor. The accuracy of the ozone monitor is 2%. Since the reading on the ozone monitor agrees with the ozone concentration measured by photoionization to within 20% (see supplementary material)³⁰, we adopt a 20% uncertainty on the ozone concentration. Given a 20% uncertainty in the ozone concentration the uncertainty in modeled $[OH](t)$ is 12% and

for $[O(^3P)](t)$ it is 3%. Second, the fraction of O_3 photodissociated can be measured directly from the initial depletion in the O_3 signal. The uncertainty in the measured photodissociation fraction is less than 1% propagating to less than 1% impact on modeled OH and $O(^3P)$ profiles. Lastly, the $O(^1D)$ quantum yield from photolysis of ozone at 248 nm is $90 \pm 9\%$ (1σ). The result of varying the $O(^1D)$ quantum yield $\pm 1\sigma$ is a 5% standard deviation in $[OH](t)$. $[O(^3P)](t)$ is rather insensitive to this yield, because a large fraction of $O(^3P)$ atoms are formed from collisional deactivation of $O(^1D)$ by O_2 .

Instrumental sources of systematic error in the absolute photoionization cross section of OH are mostly from measuring the OH cross section relative to the reference compound, xenon. The xenon cross section at discrete VUV photon energies is very well-known (1–2% error). However, uncertainty in the mass flows of xenon results in 40% standard deviation in the xenon concentration. We measured the concentration of xenon in the reactor, relative to $O(^3P)$, during single-energy experiments conducted at 14.193 eV, finding a consistent deviation between the measured and flowed concentration. The measured xenon concentration was $89 \pm 1\%$ of the requested flow, well within the expected uncertainty of the mass flow controller. Therefore, the uncertainty in the OH photoionization cross section at 13.436 eV is still dominated by the above uncertainty in the modeled $O(^3P)$ chemistry.

The absolute cross section of OH was measured nine times at 13.436 eV and four times at 14.193 eV, and we report the average for each energy. The precision of these measurements were 2% and 4%, respectively. The measurement precision of $O(^3P)$, which was used as the photoionization standard at 14.193 eV, was 8%. Summing the $O(^3P)$ random error, modeled concentration errors, and literature cross section uncertainty in quadrature results in an overall uncertainty for $O(^3P)$ as a photoionization cross section reference of $\pm 30\%$. At 14.193 eV, the uncertainty in the OH photoionization cross section comes from the $O(^3P)$ error, as well as the OH measurement and modeling errors, resulting in an overall error of $\pm 36\%$. At 13.436 eV, the uncertainty in the OH cross section includes the same sources of error, in addition to the very small uncertainty in the xenon absolute photoionization cross section, and we assign a $\pm 36\%$ uncertainty to the OH cross section at this energy. The absolute cross

sections for the OH radical are listed in Table III, along with these uncertainty values. The consistency between the kinetic model, in which we have altered no bimolecular rate coefficients, and the time-dependent signals of O₃, OH, and O(³P), coupled with the agreement of our O(³P) absolute photoionization cross section with literature values, provides support for the accuracy of our OH photoionization cross section.

4 Discussion

Figure 4 shows the photoionization spectrum measured in this work. We also present the high-resolution spectrum reported by Dehmer,¹⁵ scaled arbitrarily. Dehmer created OH radicals from H atoms generated in a microwave discharge that later reacted with NO₂, and used a high-intensity helium continuum light source to create tunable VUV radiation. There is good agreement between the shape of our spectrum and the Dehmer spectrum (Cutler et al.¹⁶ also noted excellent agreement with Dehmer's spectrum). Due to the energy resolution used in this work, the resolved peaks in Dehmer's spectrum merge into a single feature with FWHM of about 80 meV. The onset of ionization also agrees very well between the two spectra. The features we observe at 13.663, 13.813, and 14.213 eV are all present as medium intensity features in the high-resolution literature spectra, however, they have not been assigned to a Rydberg series.^{15,16}

The O(³P) photoionization spectrum and its absolute cross section have been measured previously. Figure 5 (red line) shows the literature high-resolution absolute spectrum. The literature spectrum is an evaluation by Fennelly and Torr⁵⁴ of a high resolution (~6 meV) relative spectrum reported by Dehmer *et al.*⁵⁵ Fennelly used the absolute cross sections reported by Angel and Samson⁵³ (based on prior work by Samson and Pareek)⁵⁶ to place the Dehmer spectrum on an absolute ordinate. The absolute photoionization cross section reported by Angel and Samson at 14.25 eV was 3.1 ± 0.3 Mb. Unlike absolute cross section measurements by Angel and Samson, Kohl *et al.*,⁵⁷ and Comes *et al.*,⁵⁸ we have sufficient energy resolution to capture the strong resonance (at 14.113 eV) of the metastable autoionization states observed by Dehmer and Chupka.⁵⁹

5 Conclusions

We report the first absolute VUV photoionization spectrum for the hydroxyl radical. This cross section will have practical importance for the measurement of product branching ratios and mole fraction determinations of OH via photoionization mass spectrometry in kinetics and flame studies. From a fundamental point of view, the experimental OH radical cross section is a tractable target and important benchmark species for computation of absolute photoionization cross sections from first principles.^{36,60-67}

6 References

1. Atkinson, R.; Arey, J., Atmospheric Degradation of Volatile Organic Compounds. *Chem. Rev.* **2003**, *103*, 4605-4638.
2. Heard, D. E.; Pilling, M. J., Measurement of OH and HO₂ in the Troposphere. *Chem. Rev.* **2003**, *103*, 5163-5198.
3. Finlayson-Pitts, B. J.; Pitts Jr., J. N., *Chemistry of the Upper and Lower Atmosphere: Theory, Experiments, and Applications*. Academic Press: 1999.
4. Miller, J. A.; Pilling, M. J.; Troe, J., Unravelling Combustion Mechanisms Through a Quantitative Understanding of Elementary Reactions. *Proc. Combust. Inst.* **2005**, *30*, 43-88.
5. Weinreb, S.; Barrett, A. H.; Meeks, M. L.; Henry, J. C., Radio Observations of OH in the Interstellar Medium. *Nature* **1963**, *200*, 829-831.
6. Ray, A. W.; Taatjes, C. A.; Welz, O.; Osborn, D. L.; Meloni, G., Synchrotron Photoionization Measurements of OH-Initiated Cyclohexene Oxidation: Ring-Preserving Products in OH + Cyclohexene and Hydroxycyclohexyl + O₂ Reactions. *J. Phys. Chem. A* **2012**, *116*, 6720-6730.
7. Meloni, G.; Selby, T. M.; Osborn, D. L.; Taatjes, C. A., Enol Formation and Ring-Opening in OH-Initiated Oxidation of Cycloalkenes. *J. Phys. Chem. A* **2008**, *112*, 13444-13451.
8. Dodson, L. G.; Shen, L.; Savee, J. D.; Eddingsaas, N. C.; Welz, O.; Taatjes, C. A.; Osborn, D. L.; Sander, S. P.; Okumura, M., VUV Photoionization Cross Sections of HO₂, H₂O₂, and H₂CO. *J. Phys. Chem. A* **2015**, *119*, 1279-1291.
9. Wiedmann, R. T.; Tonkyn, R. G.; White, M. G.; Wang, K.; McKoy, V., Rotationally Resolved Threshold Photoelectron Spectra of OH and OD. *J. Chem. Phys.* **1992**, *97*, 768-772.
10. Dyke, J. M.; Gamblin, S. D.; Morris, A.; West, J. B.; Wright, T. G., Photoelectron Spectroscopy of Reactive Intermediates. *AIP Conf. Proc.* **1998**, *454*, 81-88.
11. Barr, J. D.; De Fanis, A.; Dyke, J. M.; Gamblin, S. D.; Hooper, N.; Morris, A.; Stranges, S.; West, J. B.; Wright, T. G., Study of the OH and OD Radicals with Photoelectron Spectroscopy Using Synchrotron Radiation. *J. Chem. Phys.* **1999**, *110*, 345-354.

12. West, J. B.; Dyke, J. M.; Morris, A.; Wright, T. G.; Gamblin, S. D., Photoelectron Spectroscopy of Short-Lived Molecules Using Synchrotron Radiation. *J. Phys. B: At. Mol. Opt. Phys.* **1999**, *32*, 2763.
13. Garcia, G. A.; Tang, X.; Gil, J.-F.; Nahon, L.; Ward, M.; Batut, S.; Fittschen, C.; Taatjes, C. A.; Osborn, D. L.; Loison, J.-C., Synchrotron-Based Double Imaging Photoelectron/Photoion Coincidence Spectroscopy of Radicals Produced in a Flow Tube: OH and OD. *J. Chem. Phys.* **2015**, *142*, 164201.
14. Stranges, S.; Richter, R.; Alagia, M., High-Resolution Inner-Shell Photoabsorption of the OH and OD Free Radicals. *J. Chem. Phys.* **2002**, *116*, 3676-3680.
15. Dehmer, P. M., Photoionization of OH in the Region 750–950 Å. *Chem. Phys. Lett.* **1984**, *110*, 79-84.
16. Cutler, J. N.; He, Z. X.; Samson, J. A. R., Relative Photoionization Cross Section Study of OH and OD from 68 nm to 95 nm. *J. Phys. B: At. Mol. Opt. Phys.* **1995**, *28*, 4577.
17. Innocenti, F.; Zuin, L.; Costa, M. L.; Dias, A. A.; Morris, A.; Paiva, A. C. S.; Stranges, S.; West, J. B.; Dyke, J. M., Photoionization Studies of the Atmospherically Important Species N and OH at the Elettra Synchrotron Radiation Source. *J. Electron Spectrosc. Relat. Phenom.* **2005**, *142*, 241-252.
18. Jones, I. T. N.; Bayes, K. D., Detection of Steady-State Free-Radical Concentrations by Photoionization. *J. Am. Chem. Soc.* **1972**, *94*, 6869-6871.
19. Sablier, M.; Fujii, T., Mass Spectrometry of Free Radicals. *Chem. Rev.* **2002**, *102*, 2855-2924.
20. Slagle, I. R.; Yamada, F.; Gutman, D., Kinetics of Free Radicals Produced by Infrared Multiphoton-Induced Decompositions. 1. Reactions of Allyl Radicals with Nitrogen Dioxide and Bromine. *J. Am. Chem. Soc.* **1981**, *103*, 149-153.
21. Slagle, I. R.; Gutman, D., Kinetics of Polyatomic Free Radicals Produced by Laser Photolysis. 5. Study of the Equilibrium Methyl + Oxygen \rightleftharpoons CH₃O₂ Between 421 and 538 °C. *J. Am. Chem. Soc.* **1985**, *107*, 5342-5347.
22. Timonen, R. S.; Ratajczak, E.; Gutman, D.; Wagner, A. F., The Addition and Dissociation Reaction Atomic Hydrogen + Carbon Monoxide \rightleftharpoons Oxomethyl. 2. Experimental Studies and Comparison with Theory. *J. Phys. Chem.* **1987**, *91*, 5325-5332.
23. Fockenberg, C.; Bernstein, H. J.; Hall, G. E.; Muckerman, J. T.; Preses, J. M.; Sears, T. J.; Weston, R. E., Repetitively Sampled Time-of-Flight Mass Spectrometry for Gas-Phase Kinetics Studies. *Rev. Sci. Instrum.* **1999**, *70*, 3259-3264.
24. Eskola, A. J.; Timonen, R. S., Kinetics of the Reactions of Vinyl Radicals with Molecular Oxygen and Chlorine at Temperatures 200-362 K. *Phys. Chem. Chem. Phys.* **2003**, *5*, 2557-2561.
25. Blitz, M. A.; Goddard, A.; Ingham, T.; Pilling, M. J., Time-of-Flight Mass Spectrometry for Time-Resolved Measurements. *Rev. Sci. Instrum.* **2007**, *78*, 034103.

26. Baeza-Romero, M. T.; Blitz, M. A.; Goddard, A.; Seakins, P. W., Time-of-Flight Mass Spectrometry for Time-Resolved Measurements: Some Developments and Applications. *Int. J. Chem. Kin.* **2012**, *44*, 532-545.
27. Osborn, D. L.; Zou, P.; Johnsen, H.; Hayden, C. C.; Taatjes, C. A.; Knyazev, V. D.; North, S. W.; Peterka, D. S.; Ahmed, M.; Leone, S. R., The Multiplexed Chemical Kinetic Photoionization Mass Spectrometer: A New Approach to Isomer-Resolved Chemical Kinetics. *Rev. Sci. Instrum.* **2008**, *79*, 104103.
28. Taatjes, C. A.; Hansen, N.; Osborn, D. L.; Kohse-Hoinghaus, K.; Cool, T. A.; Westmoreland, P. R., "Imaging" Combustion Chemistry via Multiplexed Synchrotron-Photoionization Mass Spectrometry. *Phys. Chem. Chem. Phys.* **2008**, *10*, 20-34.
29. Berkowitz, J., Absolute Partial Photoionization Cross Sections of Ozone. *Int. J. Mass Spectrom.* **2008**, *271*, 8-14.
30. See supplementary material at [URL] for further discussion of how the initial ozone concentration was determined and for the tabulated photoionization spectra.
31. Savee, J. D.; Soorkia, S.; Welz, O.; Selby, T. M.; Taatjes, C. A.; Osborn, D. L., Absolute Photoionization Cross-Section of the Propargyl Radical. *J. Chem. Phys.* **2012**, *136*, 134307-10.
32. Welz, O.; Savee, J. D.; Osborn, D. L.; Vasu, S. S.; Percival, C. J.; Shallcross, D. E.; Taatjes, C. A., Direct Kinetic Measurements of Criegee Intermediate (CH_2OO) Formed by Reaction of CH_2I with O_2 . *Science* **2012**, *335*, 204-207.
33. Taatjes, C. A., How does the Molecular Velocity Distribution Affect Kinetics Measurements by Time-Resolved Mass Spectrometry? *Int. J. Chem. Kin.* **2007**, *39*, 565-570.
34. Lide, D. R., Section 10, Atomic, Molecular, and Optical Physics, Ionization Potentials of Atoms and Atomic Ions. In *CRC Handbook of Chemistry and Physics*, 84th ed.; CRC Press: Boca Raton, Florida, 2003.
35. Melania Oana, C.; Krylov, A. I., Dyson Orbitals for Ionization from the Ground and Electronically Excited States Within Equation-of-Motion Coupled-Cluster Formalism: Theory, Implementation, and Examples. *J. Chem. Phys.* **2007**, *127*, 234106.
36. Gozem, S.; Gunina, A. O.; Ichino, T.; Osborn, D. L.; Stanton, J. F.; Krylov, A. I., Photoelectron Wave Function in Photoionization: Plane Wave or Coulomb Wave? *J. Phys. Chem. Lett.* **2015**, *6*, 4532-4540.
37. Gozem, S.; Krylov, A. I. ezDyson User's Manual. <http://iopenshell.usc.edu/downloads/>.
38. Shao, Y.; Gan, Z.; Epifanovsky, E.; Gilbert, A. T. B.; Wormit, M.; Kussmann, J.; Lange, A. W.; Behn, A.; Deng, J.; Feng, X., et al., Advances in Molecular Quantum Chemistry Contained in the Q-Chem 4 Program Package. *Mol. Phys.* **2015**, *113*, 184-215.
39. Chai, J.-D.; Head-Gordon, M., Long-Range Corrected Hybrid Density Functionals with Damped Atom-Atom Dispersion Corrections. *Phys. Chem. Chem. Phys.* **2008**, *10*, 6615-6620.
40. Mozhayskiy, V.; Krylov, A. I. ezSpectrum User's Manual. <http://iopenshell.usc.edu/downloads/>.

41. Matsumi, Y.; Kawasaki, M., Photolysis of Atmospheric Ozone in the Ultraviolet Region. *Chem. Rev.* **2003**, *103*, 4767-4782.
42. Atkinson, R.; Baulch, D. L.; Cox, R. A.; Crowley, J. N.; Hampson, R. F.; Hynes, R. G.; Jenkin, M. E.; Rossi, M. J.; Troe, J., Evaluated Kinetic and Photochemical Data for Atmospheric Chemistry: Volume I - Gas Phase Reactions of O_x, HO_x, NO_x and SO_x Species. *Atmos. Chem. Phys.* **2004**, *4*, 1461-1738.
43. Sander, S. P.; Abbatt, J.; Barker, J. R.; Burkholder, J. B.; Friedl, R. R.; Golden, D. M.; Huie, R. E.; Kolb, C. E.; Kurylo, M. J.; Moortgat, G. K., et al., Chemical Kinetics and Photochemical Data for Use in Atmospheric Studies, Evaluation Number 17. *JPL Publication 10-6* **2011**.
44. Ianni, J. C. *Kintecus*, Windows Version 2.80; <http://www.kintecus.com>, 2002.
45. Gericke, K. H.; Comes, F. J.; Levine, R. D., Energy partitioning in the reaction $^{16}\text{O}(^1\text{D})+\text{H}_2^{18}\text{O}\rightarrow^{16}\text{OH}+^{18}\text{OH}$. II. The distribution of ^{16}OH and ^{18}OH . *J. Chem. Phys.* **1981**, *74*, 6106-6112.
46. Comes, F. J.; Gericke, K. H.; Manz, J., Energy partitioning in the reaction $^{16}\text{O}(^1\text{D})+\text{H}_2^{18}\text{O}\rightarrow^{16}\text{OH}+^{18}\text{OH}$. IV. Microscopic probabilities for $^{16}\text{OH}+^{18}\text{OH}$ coincident pairs. *J. Chem. Phys.* **1981**, *75*, 2853-2863.
47. Butler, J. E.; Talley, L. D.; Smith, G. K.; Lin, M. C., Rotational and vibrational energy distributions of $^{16}\text{OH}(X^2\Pi)$ and $^{18}\text{OH}(X^2\Pi)$ produced in the reaction of O(¹D) with H₂O and H₂¹⁸O. *J. Chem. Phys.* **1981**, *74*, 4501-4508.
48. Guillory, W. A.; Gericke, K. H.; Comes, F. J., The dynamics of the reaction of $^{16}\text{O}(^1\text{D})+\text{D}_2^{18}\text{O}\rightarrow^{16}\text{OD}+^{18}\text{OD}$. *J. Chem. Phys.* **1983**, *78*, 5993-6001.
49. Cleveland, C. B.; Wiesenfeld, J. R., Nascent product population distribution in the reaction $^{16}\text{O}(^1\text{D}_2)+\text{H}_2^{18}\text{O}\rightarrow^{16}\text{OH}+^{18}\text{OH}$. *J. Chem. Phys.* **1992**, *96*, 248-255.
50. Sauder, D. G.; Stephenson, J. C.; King, D. S.; Casassa, M. P., Nascent product states in the photoinitiated reaction of O₃ and H₂O. *J. Chem. Phys.* **1992**, *97*, 952-961.
51. Dodd, J. A.; Lipson, S. J.; Blumberg, W. A. M., Formation and Vibrational Relaxation of OH ($X^2\Pi_{i,v}$) by O₂ and CO₂. *J. Chem. Phys.* **1991**, *95*, 5752-5762.
52. Samson, J. A. R.; Stolte, W. C., Precision Measurements of the Total Photoionization Cross-Sections of He, Ne, Ar, Kr, and Xe. *J. Electron Spectrosc. Relat. Phenom.* **2002**, *123*, 265-276.
53. Angel, G. C.; Samson, J. A. R., Total Photoionization Cross Sections of Atomic Oxygen from Threshold to 44.3 Å. *Phys. Rev. A* **1988**, *38*, 5578-5585.
54. Fennelly, J. A.; Torr, D. G., Photoionization and Photoabsorption Cross Sections of O, N₂, O₂, and N for Aeronomic Calculations. *At. Data Nucl. Data Tables* **1992**, *51*, 321-363.
55. Dehmer, P. M.; Berkowitz, J.; Chupka, W. A., Photoionization of Atomic Oxygen from 920 to 650 Å. *J. Chem. Phys.* **1973**, *59*, 5777-5786.
56. Samson, J. A. R.; Pareek, P. N., Absolute Photoionization Cross Sections of Atomic Oxygen. *Phys. Rev. A* **1985**, *31*, 1470-1476.

57. Kohl, J. L.; Lafyatis, G. P.; Palenius, H. P.; Parkinson, W. H., Absolute Cross Section for Photoionization of Atomic Oxygen. *Phys. Rev. A* **1978**, *18*, 571-574.
58. Comes, F. J.; Speier, F.; Elzer, A., Photoionization Studies of Atomic Radiation 2. Ionization Cross Section of Atomic Oxygen. *Z. Naturforsch., A: Phys. Sci.* **1968**, *23a*, 125-133.
59. Dehmer, P. M.; Chupka, W. A., Nonstatistical Emission From Metastable Autoionizing States of OI. *J. Chem. Phys.* **1975**, *62*, 584-591.
60. Fronzoni, G.; Stener, M.; Decleva, P., Valence and core photoionization dynamics of acetylene by TD-DFT continuum approach. *Chem. Phys.* **2004**, *298*, 141-153.
61. Natalense, A. P. P.; Lucchese, R. R., Cross Section and Asymmetry Parameter Calculation for Sulfur 1s Photoionization of SF₆. *J. Chem. Phys.* **1999**, *111*, 5344-5348.
62. Cacelli, I.; Moccia, R.; Rizzo, A., Gaussian-type-orbital Basis Sets for the Calculation of Continuum Properties in Molecules: The Differential Photoionization Cross Section of Molecular Nitrogen. *Phys. Rev. A* **1998**, *57*, 1895-1905.
63. Cukras, J.; Decleva, P.; Coriani, S., A coupled-cluster study of Photodetachment Cross Sections of Closed-shell Anions. *J. Chem. Phys.* **2014**, *141*, 174315.
64. Cukras, J.; Coriani, S.; Decleva, P.; Christiansen, O.; Norman, P., Photoionization Cross Section by Stieltjes Imaging Applied to Coupled Cluster Lanczos Pseudo-spectra. *J. Chem. Phys.* **2013**, *139*, 094103.
65. Ruberti, M.; Yun, R.; Gokhberg, K.; Kopelke, S.; Cederbaum, L. S.; Tarantelli, F.; Averbukh, V., Total Molecular Photoionization Cross-sections by Algebraic Diagrammatic Construction-Stieltjes-Lanczos Method: Benchmark Calculations. *J. Chem. Phys.* **2013**, *139*, 144107.
66. Ruberti, M.; Averbukh, V.; Decleva, P., B-spline Algebraic Diagrammatic Construction: Application to Photoionization Cross-sections and High-order Harmonic Generation. *J. Chem. Phys.* **2014**, *141*, 164126.
67. Oana, C. M.; Krylov, A. I., Cross Sections and Photoelectron Angular Distributions in Photodetachment from Negative Ions Using Equation-of-motion Coupled-cluster Dyson Orbitals. *J. Chem. Phys.* **2009**, *131*, 124114.
68. Forster, R.; Frost, M.; Fulle, D.; Hamann, H. F.; Hippler, H.; Schlegel, A.; Troe, J., High Pressure Range of the Addition of HO to HO, NO, NO₂, and CO. I. Saturated Laser Induced Fluorescence Measurements at 298 K. *J. Chem. Phys.* **1995**, *103*, 2949-2958.
69. Michael, J. V.; Su, M. C.; Sutherland, J. W.; Carroll, J. J.; Wagner, A. F., Rate Constants For H + O₂ + M → HO₂ + M in Seven Bath Gases. *J. Phys. Chem. A* **2002**, *106*, 5297-5313.
70. Huie, R. E.; Herron, J. T.; Davis, D. D., Absolute Rate Constants for the Reaction O + O₂ + M → O₃ + M Over the Temperature Range 200-346 K. *J. Phys. Chem.* **1972**, *76*, 2653-2658.

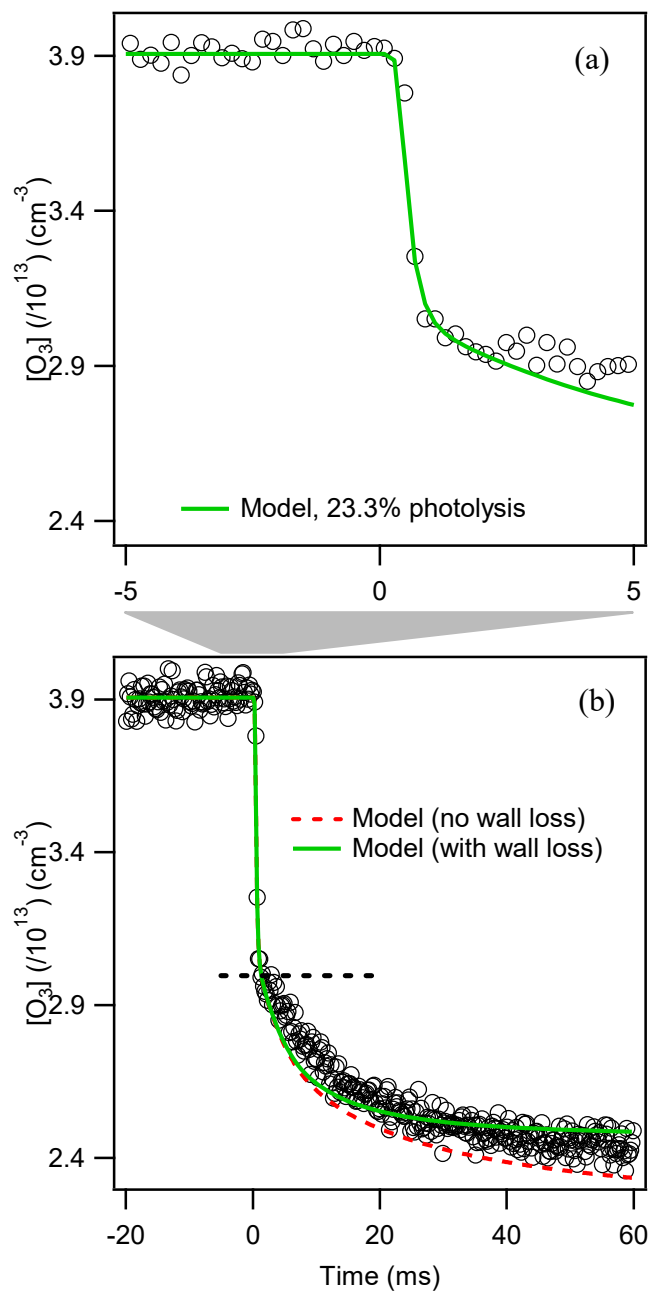


Figure 1. Observed O_3 depletion. (a) The initial depletion at $t = 0$ is from photolysis. The green line shows the fitted depletion due to initial photolysis (23.3 ± 0.1 % photolysis) and subsequent depletion by secondary chemistry. (b) Showing subsequent removal of O_3 , primarily from reaction with H atoms at early times, with additional removal by reaction with OH. The red dashed line shows the simulated kinetics model in the absence of any wall loss. The green solid line shows the kinetics model with an OH wall loss rate of 27.9 s^{-1} . The black dashed line shows the 23.3% photolytic depletion of O_3 . Additional removal of O_3 past this level is from secondary chemistry. Data taken from Experiment 4.

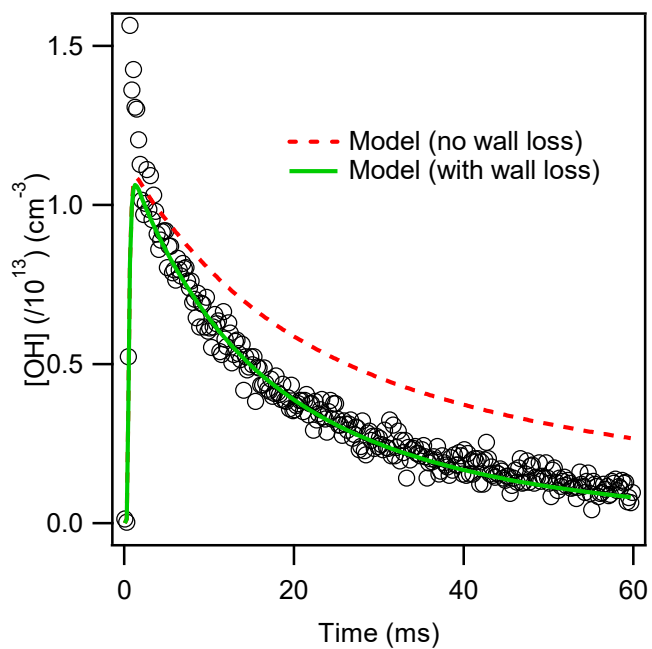


Figure 2. Observed OH decay. The red dashed line shows the simulated kinetics model in the absence of any adjustments to the kinetics model. The green solid line shows the kinetics model fitted with an OH wall loss rate ($28 \pm 6 \text{ s}^{-1}$). The fit was performed from 5–20 ms, which excluded the initial spike, attributed to relaxation of vibrationally-excited OH, observed in the first few milliseconds. Data taken from Experiment 4.

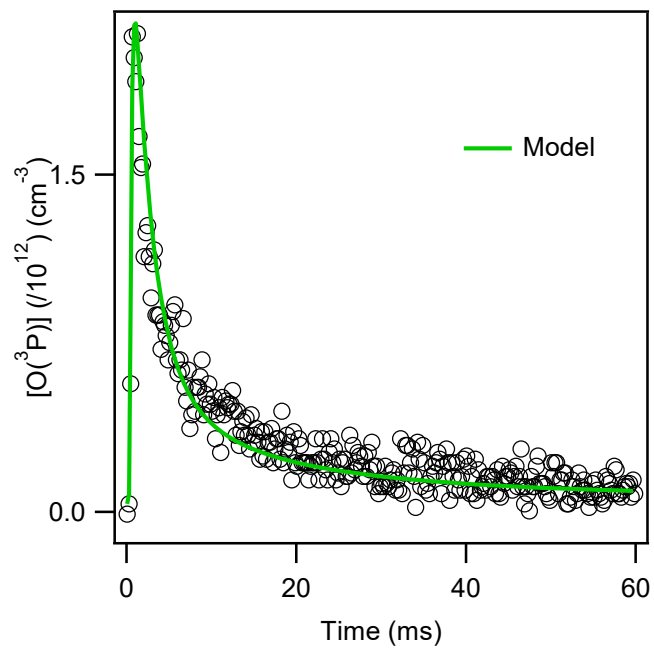


Figure 3. Observed $O(^3P)$ decay. The absolute concentrations of the data points (open points) are scaled to fit the kinetics model (green line). Data taken from Experiment 11.

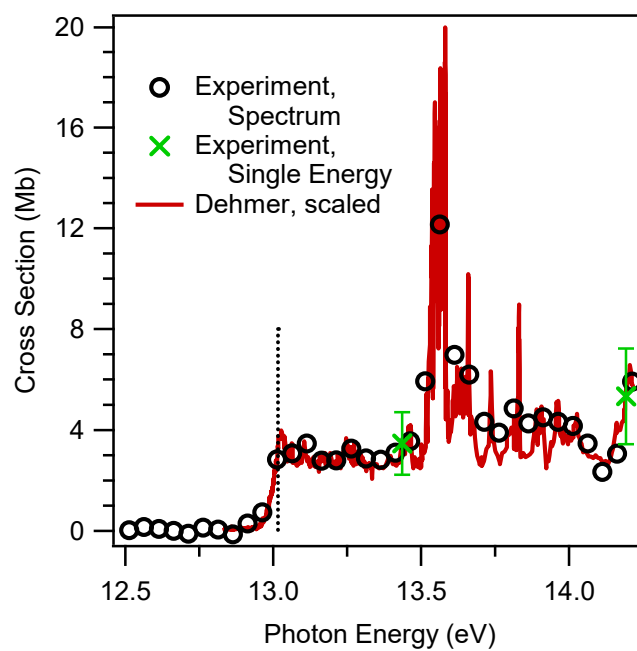


Figure 4. Absolute photoionization spectrum of OH. Open circles are the data obtained from the energy-dependent scan in the current work, scaled to the absolute cross section measurements made at 13.436 and 14.193 eV (indicated with green x's, shown with error bars, as listed in Table III). The tabulated OH spectrum is reported in the supplementary material. The green line is the high-resolution spectrum taken from Dehmer,¹⁵ scaled to match the absolute cross sections determined in this work. Data taken from Experiment 16.

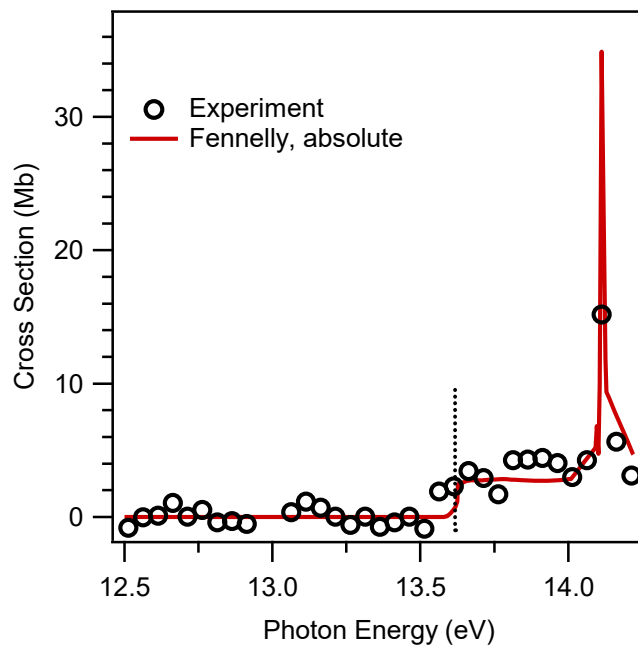


Figure 5. Absolute photoionization spectrum of $O(^3P)$. Shown here (black circles) is the absolute energy-resolved cross section of $O(^3P)$ atoms formed in this experiment. The literature evaluated absolute photoionization spectrum is shown (red line).⁵⁴ Data taken from Experiment 16.

Table 1. Conditions for each experiment. Photon energies and initial concentrations for all experiments. All experiments were performed at 298 K. Experiments were performed at 8 Torr and 200 sccm total flow rate. $[O(^1D)]_0$ is the initial number of $O(^1D)$ atoms formed from photolysis of O_3 , from the measured photodissociation of ozone and expected quantum yield. The error bars are the uncertainty in the fit (2σ) from the depletion data, and do not include the systematic errors. The OH concentration is the peak OH value from each model simulation.

Experiment	Photon energy (eV)	$[O_3]$ ($/10^{13}$) (cm^{-3})	$[O_2]$ ($/10^{15}$) cm^{-3}	$[H_2O]$ ($/10^{15}$) cm^{-3}	$[O(^1D)]_0$ ($/10^{12}$) cm^{-3}	$[OH]$ (peak) ($/10^{12}$) cm^{-3}
1	13.113	3.55	3.55	...	9.68 ± 0.05	...
2	13.436	2.56	2.06	2.24	5.36 ± 0.02	8.2
3	13.436	3.91	3.53	2.17	8.18 ± 0.04	11
4	13.436	6.10	5.11	2.23	12.79 ± 0.06	15
5	13.436	4.40	3.65	2.17	9.37 ± 0.04	12
6	13.436	1.50	1.14	2.22	3.19 ± 0.02	5.4
7	13.436	0.90	0.69	2.23	1.91 ± 0.02	3.4
8	13.436	2.54	1.98	1.03	5.33 ± 0.04	6.9
9	13.436	2.55	2.00	0.52	5.27 ± 0.03	5.2
10	14.193	0.90	0.80	2.20	1.92 ± 0.01	3.4
11	14.193	6.43	5.24	2.23	12.17 ± 0.06	14
12	14.193	4.11	3.09	2.20	8.43 ± 0.04	12
13*	14.193	4.11	3.09	2.19	4.91 ± 0.03	7.0
14*	13.436	0.93	0.68	2.20	1.20 ± 0.02	2.2
15*	14.193	0.93	0.68	2.23	1.20 ± 0.02	2.2
16	12.513– 14.213	3.92	2.94	2.23

*Experiments conducted with a mesh attenuator to reduce the excimer laser fluence.

Table 2. The reactions used to simulate the concentration-dependent profiles. Pressure-dependent rate constants are for 8 Torr. All rate constants are taken from the NASA Data Evaluation,⁴³ unless otherwise noted.

		$k_{298\text{K}}$ ($\text{cm}^3 \text{s}^{-1}$)	Ref
(1)	$\text{O}_3 + h\nu(248 \text{ nm}) \rightarrow \text{O}(^1\text{D}) + \text{O}_2$	90±9 %	
	$\rightarrow \text{O}(^3\text{P}) + \text{O}_2$	10±9 %	
(2)	$\text{O}(^1\text{D}) + \text{H}_2\text{O} \rightarrow 2\text{OH}$	$2.0_{-0.1}^{+0.2} \times 10^{-10}$	
(3)	$\text{O}(^1\text{D}) + \text{O}_2 \rightarrow \text{O}(^3\text{P}) + \text{O}_2$	$3.95 \pm 0.4 \times 10^{-11}$	
(4)	$\text{OH} + \text{O}(^3\text{P}) \rightarrow \text{H} + \text{O}_2$	$3.3_{-0.4}^{+0.5} \times 10^{-11}$	
(5)	$\text{OH} + \text{OH} \rightarrow \text{H}_2\text{O} + \text{O}(^3\text{P})$	$1.8_{-0.4}^{+0.5} \times 10^{-12}$	a
	$\xrightarrow{\text{M}} \text{H}_2\text{O}_2$	9.6×10^{-14}	
(6)	$\text{H} + \text{O}_3 \rightarrow \text{OH} + \text{O}_2$	$2.9 \pm 0.3 \times 10^{-11}$	
(7)	$\text{OH} + \text{O}_3 \rightarrow \text{HO}_2 + \text{O}_2$	$7.3_{-1.0}^{+1.1} \times 10^{-14}$	
(8)	$\text{O}(^3\text{P}) + \text{O}_3 \rightarrow 2\text{O}_2$	$8.0_{-0.7}^{+0.8} \times 10^{-15}$	
(9)	$\text{H} + \text{O}_2 \xrightarrow{\text{M}} \text{HO}_2$	$4.7 \pm 0.3 \times 10^{-15}$	b
(10)	$\text{O}(^1\text{D}) + \text{O}_3 \rightarrow 2\text{O}_2$	$1.2 \pm 0.2 \times 10^{-10}$	
	$\rightarrow 2\text{O}(^3\text{P}) + \text{O}_2$	$1.2 \pm 0.2 \times 10^{-10}$	
(11)	$\text{O}(^3\text{P}) + \text{O}_2 \xrightarrow{\text{M}} \text{O}_3$	$8.6 \pm 0.5 \times 10^{-17}$	c
(12)	$\text{OH} + \text{HO}_2 \rightarrow \text{H}_2\text{O} + \text{O}_2$	$1.1_{-0.1}^{+0.2} \times 10^{-10}$	
(13)	$\text{OH} + \text{H}_2\text{O}_2 \rightarrow \text{HO}_2 + \text{H}_2\text{O}$	$1.8_{-0.2}^{+0.3} \times 10^{-12}$	
(14)	$\text{O}(^3\text{P}) + \text{HO}_2 \rightarrow \text{OH} + \text{O}_2$	$5.9 \pm 0.3 \times 10^{-11}$	
(15)	$\text{O}(^3\text{P}) + \text{H}_2\text{O}_2 \rightarrow \text{OH} + \text{HO}_2$	$1.7 \pm 0.3 \times 10^{-15}$	

	$\text{H} + \text{HO}_2 \rightarrow 2\text{OH}$	$7.2_{-1.2}^{+1.4} \times 10^{-11}$
(16)	$\rightarrow \text{O}({}^3\text{P}) + \text{H}_2\text{O}$	$1.6_{-0.5}^{+0.8} \times 10^{-12}$
	$\rightarrow \text{H}_2 + \text{O}_2$	$6.9_{-2.0}^{+2.8} \times 10^{-12}$
(17)	$\text{HO}_2 + \text{HO}_2 \rightarrow \text{H}_2\text{O}_2 + \text{O}_2$	$1.4 \pm 0.2 \times 10^{-12}$
(18)	$\text{O}_3 + \text{HO}_2 \rightarrow \text{OH} + 2\text{O}_2$	$1.9_{-0.2}^{+0.3} \times 10^{-15}$

^aTermolecular OH + OH reaction rate in He from Forster et al., computed at 8 Torr.⁶⁸

^bTermolecular H + O₂ reaction rate in He from Michael et al., computed at 8 Torr.⁶⁹

^cTermolecular O(³P) + O₂ reaction rate in He from Huie et al., computed at 8 Torr.⁷⁰

Table 3. Photoionization cross sections for the reference compounds used in this work and the average single-energy OH cross sections measured here. Xenon cross sections were taken from Samson and Stolte.⁵² The literature O(³P) cross section was taken from Angel and Samson, for a photon energy equal to 14.25 eV.⁵³ The reported OH cross section uncertainties come from the systematic and random errors in the measurement, and are on the order of 36%.

Photon energy (eV)	Xe (Mb) ^a	O(³ P) (Mb) ^b	OH (Mb)
13.436	65.3	...	3.6 ± 1.3
14.193	63.7	3.1	5.5 ± 2.0

^aTaken from Samson and Stolte.⁵²

^bTaken from Angel and Samson.⁵³

7 Supporting Information

7.1 Determining the ozone concentration

In order to determine the OH absolute photoionization cross section, the concentration of OH in the flow tube—relative to the concentration of the photoionization reference compounds (xenon and O(³P))—had to be known accurately. The modeled time profiles, [OH](*t*), are very sensitive to the initial O(¹D) number density, formed directly from photolysis of O₃. [O(¹D)]₀ depends on the initial ozone concentration [O₃](*t* < 0) and the fractional photolytic ozone depletion. We measured the photolytic ozone depletion using the instantaneous depletion observed in the O₃⁺ signal at *m/z* = 48 caused by the excimer laser-initiated photolysis with uncertainties (precision) in the fractional depletions of less than 1% (2σ).

To quantify the initial ozone concentration, there are two possible methods. The first method uses the literature value for the absolute ozone photoionization spectrum, recently evaluated by Berkowitz (Figure S1).¹ The Mocellin/Berkowitz spectrum (green pluses) was reported by Berkowitz by scaling the total ion yield spectrum reported by Mocellin *et al.*² (energy resolution 20–40 meV) to the total photoionization cross section reported by Cook.³⁻⁴ The Weiss/Berkowitz spectrum (red line) was then obtained by Berkowitz by scaling the relative spectrum (5–10 meV resolution) reported by Weiss *et al.*⁵ to the O₃⁺ spectrum from Mocellin. Berkowitz does not provide an error estimate for these spectra.

The initial ozone concentration could also be determined by using the reading of the ozone monitor and the measured mass flows. The ozone concentration measured by the ozone monitor was significantly higher than the range recommended by the factory specifications. However, if the concentration reported by the ozone monitor is used to evaluate the O₃ absolute cross section relative to that of xenon or O(³P),⁶ the resulting absolute photoionization spectrum (shown in Figure S1, black open circles) agrees well, both in terms of shape and absolute magnitude (to within 20%), with the Weiss/Berkowitz spectrum. The ozone concentration measured by the ozone monitor was used in the analysis described in the main text.

7.2 The tabulated photoionization spectrum of OH

The absolute photoionization spectrum of OH is reported as tabulated data in Table S1.

7.3 References

1. Berkowitz, J., Absolute Partial Photoionization Cross Sections of Ozone. *Int. J. Mass Spectrom.* **2008**, *271*, 8-14.
2. Mocellin, A.; Wiesner, K.; Burmeister, F.; Björneholm, O.; Naves de Brito, A., Experimental Study of Photoionization of Ozone in the 12 to 21 eV Region. *J. Chem. Phys.* **2001**, *115*, 5041-5046.
3. Cook, G. R., Photoionization and Absorption Cross Sections of Ozone. *Trans. Am. Geophys. Union* **1968**, *49*, 736A.
4. Cook, G. R., Photoionization of Ozone with Mass Analysis. In *Recent Developments in Mass Spectroscopy*, Ogata, K.; Hayakawa, T., Eds. University Park Press: Japan, 1970; pp 761-764.
5. Weiss, M. J.; Berkowitz, J.; Appelman, E. H., Photoionization of Ozone: Formation of O_4^+ and O_5^+ . *J. Chem. Phys.* **1977**, *66*, 2049-2053.
6. Samson, J. A. R.; Stolte, W. C., Precision Measurements of the Total Photoionization Cross-Sections of He, Ne, Ar, Kr, and Xe. *J. Electron Spectrosc. Relat. Phenom.* **2002**, *123*, 265-276.

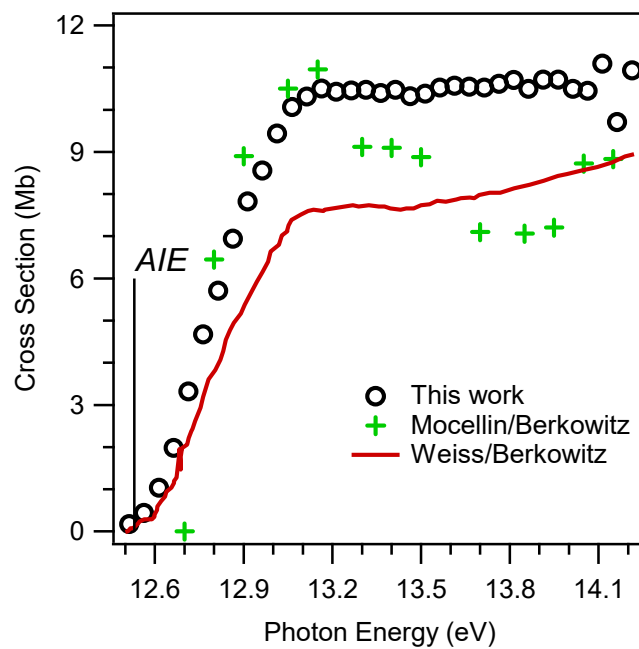


Figure S1. Absolute photoionization spectrum of ozone. Shown here (black circles) is the absolute photoionization spectrum of ozone measured in this work, which assumes that the reading of the ozone monitor is accurate.⁶ Also shown here are the literature absolute photoionization spectra of ozone of Mocellin² (green pluses) and Weiss⁵ (red line), as evaluated by Berkowitz.¹

Table S1. Absolute photoionization spectrum of OH. A relative spectrum was scaled to absolute measurements as outlined in the text.

Photon energy (eV)	OH (Mb)	Photon energy (eV)	OH (Mb)
12.513	0.028	13.413	3.099
12.563	0.155	13.463	3.556
12.613	0.068	13.513	5.925
12.663	-0.008	13.563	12.160
12.713	-0.119	13.613	6.978
12.763	0.127	13.663	6.201
12.813	0.052	13.713	4.328
12.863	-0.142	13.763	3.896
12.913	0.293	13.813	4.857
12.963	0.725	13.863	4.264
13.013	2.826	13.913	4.495
13.063	3.069	13.963	4.318
13.113	3.468	14.013	4.160
13.163	2.775	14.063	3.457
13.213	2.787	14.113	2.333
13.263	3.258	14.163	3.059
13.313	2.864	14.213	5.916
13.363	2.817		

KINETICS AND BRANCHING FRACTION OF THE ETHYL PEROXY RADICAL SELF-REACTION MEASURED USING VUV PHOTOIONIZATION MASS SPECTROMETRY

1 Introduction

Peroxy radicals in the atmosphere play an important role in ozone concentrations worldwide.¹ The ethyl peroxy radical ($C_2H_5O_2$) self-reaction has been poorly constrained, both in terms of the kinetic rate of self-reaction and the products that are formed.²⁻¹²

The ethyl peroxy self-reaction goes as reaction (1).



The evaluated³ rate coefficient for this reaction is $6.8_{-3.4}^{+6.8} \times 10^{-14} \text{ cm}^3 \text{ s}^{-1}$ (1σ error limits), independent of temperature. All past work investigating the rate coefficient for reaction (1) used ultraviolet absorbance to monitor $C_2H_5O_2$ concentrations with time. A complication to the use of absorbance in the ultraviolet comes from interference by other peroxy radicals which typically have overlapping absorption features. The broad B–X transition of most peroxy radicals falls in this region.¹ Interference by HO_2 is inevitable since it is formed both as a byproduct of the ethyl peroxy self-reaction and as a direct product from the bimolecular reaction between ethyl radicals and oxygen. Noell et al. attempted to correct for the presence of HO_2 by simultaneously monitoring the HO_2 features in the near-infrared region.¹² The resulting self-reaction rate constant is dramatically different than other reports.

There are three channels by which the ethyl peroxy self-reaction is expected to react. Reaction (1a) produces two ethoxy radicals, reaction (1b) forms ethanol and acetaldehyde, whereas reaction (1c) forms the dialkyl peroxide ROOR. The branching fraction of reaction (1a) is of particular interest as it produces alkoxy radicals which may go on to react with O₂ to form HO₂ (reaction (2)).



HO₂ formation is important atmospherically and from an analytical standpoint. Not only does the HO₂ ultraviolet absorption interfere with quantification of the ethyl peroxy radical, but cross-reactions of HO₂ with C₂H₅O₂ (reaction (3)) can be very fast, contributing to the overall observed decay of the peroxy radical.



The other two product channels—reactions (1b) and (1c)—form closed-shell products. Reaction (1b) is a chain-terminating step in the atmosphere. Reaction (1c) forms a peroxide product which could serve as a radical reservoir, releasing radicals to the atmosphere upon photolysis, or as a radical sink through heterogeneous removal processes. Reaction (1c) has been constrained to an upper limit of 6% of the total yield.¹³⁻¹⁴

The branching fraction of the alkoxy radical channel (α_{alkoxy}) is given by equation (I).

$$\alpha_{\text{alkoxy}} = \frac{k_{1a}}{k_{1a} + k_{1b} + k_{1c}} \quad (I)$$

The value for α_{alkoxy} is especially poorly-understood. Literature measurements for the alkoxy radical product channel range from 0.28 to 0.76.^{5,12-14} The current IUPAC² and JPL³ recommendations for α_{alkoxy} at 298 K are 0.62±0.1 and 0.60, respectively. In the experimental studies leading to these yields, Niki et al.¹³ and Wallington et al.¹⁴ both used

FTIR to detect the products of the reaction whereas Anastasi et al. used gas chromatography/mass spectrometry to observe products while simultaneously monitoring the ultraviolet absorption.⁵ As described previously, Noell et al. observed both $C_2H_5O_2$ decay and HO_2 formation to determine the branching fraction, resulting in a drastically different value for the branching fraction.¹² Preliminary work in this group used an earlier version of the MPIMS instrument to measure the branching fractions of the ethyl peroxy self-reaction. The initial report observed a low branching ratio for the radical channel (1a).¹⁵

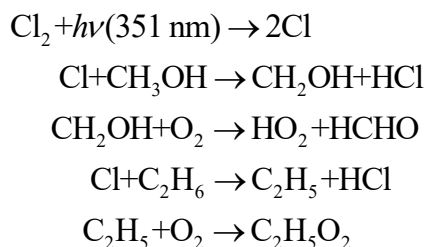
The large uncertainties in the rate constant and product distribution call for a rigorous study of the ethyl peroxy radical self-reaction. Given that neither the rate constant nor branching fraction are well-constrained, it is necessary to utilize a technique which has capabilities of observing both reactant and product concentrations in real-time. Previous techniques have mostly monitored only the disappearance of $C_2H_5O_2$ but the expected formation of large amounts of HO_2 along with the probable contribution of the $HO_2 + C_2H_5O_2$ cross-reaction complicates matters. In this study, multiplexed photoionization mass spectrometry was used to monitor the destruction and formation of reactants, intermediates, and products of the ethyl peroxy radical self-reaction. This method is preferred because its high mass resolution allows for the simultaneous detection of many species of interest, with excellent time resolution in the temporal window when the self-reaction processes occur. The decay of the ethyl peroxy radical (through detection of $C_2H_5^+$ ions formed from $C_2H_5O_2^+$ fragmentation¹⁶) was monitored while concurrent ethanol, acetaldehyde, and other secondary product formations were observed.

2 Experimental methods

Time-resolved experiments were carried out on the Multiplexed Photoionization Mass Spectrometer (MPIMS) at the Advanced Light Source (ALS), which was described in detail in Chapter 3 and in previous publications.¹⁷⁻¹⁸ Reactions of ethyl peroxy radicals were studied at 8 Torr at room temperature in a flow reactor. Flash photolysis of Cl_2 at 351 nm generated the radicals of interest and reactant decay and product formation was observed with a time-of-flight (TOF) mass spectrometer.

Two different peroxy radical reactions were investigated in this study; $\text{C}_2\text{H}_5\text{O}_2 + \text{HO}_2$, and $\text{C}_2\text{H}_5\text{O}_2 + \text{C}_2\text{H}_5\text{O}_2$. HO_2 and $\text{C}_2\text{H}_5\text{O}_2$ were produced from reactions of Cl with methanol or ethane respectively (see Scheme 1).

Scheme 1:



2.1 Experimental conditions

Typical gas concentrations for measuring the cross reaction were, in units of molecules cm^{-3} $[\text{Cl}_2] = 7.8 \times 10^{14}$, $[\text{CH}_3\text{OH}] = 3.2 \times 10^{14}$, $[\text{C}_2\text{H}_6] = 1.3 \times 10^{14}$, $[\text{O}_2] = 7.8 \times 10^{14}$, and $[\text{He}] = 1.8 \times 10^{17}$, and for the $\text{C}_2\text{H}_5\text{O}_2$ self-reaction $[\text{Cl}_2] = 7.8 \times 10^{14}$, $[\text{C}_2\text{H}_6] = 1.3 \times 10^{14}$, $[\text{O}_2] = (6.5\text{--}10.4) \times 10^{15}$, and $[\text{He}] = (1.5\text{--}2.5) \times 10^{17}$. Table 1 is a list of all experiments from which data was taken to determine the ethyl peroxy radical self-reaction rate constant. Table 2 describes the experiment from which data was taken to determine the cross-reaction between $\text{C}_2\text{H}_5\text{O}_2$ and HO_2 (experiment 17).

All reagents were introduced to the system from pre-mixed gas cylinders with gas flows controlled via mass flow controller. The buffer gas was helium (Matheson Tri-Gas, 99.9999%) and the radical precursor was Cl_2 (Matheson Tri-Gas, 1% Cl_2 in He). Starting reagents were either C_2H_6 and O_2 for self-reaction studies or C_2H_6 , CH_3OH , and O_2 for the HO_2 cross-reaction.

Ethyl peroxy radicals were produced from hydrogen abstraction of ethane by Cl produced by photolysis of Cl_2 at 351 nm. With the large excess of ethane compared to Cl present in the reaction cell, H-abstraction occurs nearly instantaneously and completely (i.e. $[\text{C}_2\text{H}_5] = [\text{Cl}]$). In a similar way HO_2 was produced from H-abstraction of methanol

followed by reaction of the methanol radical with O₂. The radical concentration was determined in two ways for the given set of experiments (as described previously¹⁹); calculated using the photolysis rate of Cl₂ based off of the photon flux of the excimer laser at 351 nm and from the observed depletion of Cl₂ and/or other precursors such as methanol in the TOF at a given *m/z*. The *in-situ* method of monitoring the Cl₂ depletions to obtain the initial Cl atom concentration for each experiment was preferred.

Data was collected for 20 ms before the excimer was fired to establish a baseline for each mass, then data was collected for 130 ms after the excimer, to observe the decay and rise of reactants and products simultaneously. Data points were 0.2 ms apart after binning. The number of counts of all products decreased and reached the baseline by the end of data collection, indicating that all products were fully removed from the reaction region before beginning the next data collection.

2.2 Photoionization spectra

The photons from the synchrotron source can also be scanned (i.e. here from 8.7–11.45 eV in steps of 0.025 eV) resulting in a three-dimensional data set of time-resolved mass spectra as a function of photoionization energy.

Absolute photoionization cross sections of acetaldehyde, ethanol, ethylene, and chloroethane were measured relative to that of propene using gas mixtures of known concentrations as described previously. Absolute cross sections were determined from the ratio of integrated photoion counts of the analyte to propene, which is referenced to its absolute photoionization spectrum.²⁰ Duplicate tanks of each gas were prepared and each tank was run in duplicate.

For products that were not available as pure samples, we determined the photoionization cross sections for these species at single photon energies by fitting their time-dependent signals with a kinetics model (described below), simulated based on other species with well-constrained chemistry and cross sections. The relative photoionization spectra collected during kinetics experiments were scaled to the single-energy determinations.

2.3 Kinetics model

Time-dependent concentration profiles were simulated using the Kintecus modeling software package²¹ and an extensive kinetics model (see Table 3). Briefly, experimental data was fit with simulated kinetics traces using a fitting algorithm in Matlab, holding all well-known rates constant and allowing the program to iteratively solve for the best fit of the unknown rate constant(s). The model listed in Table 3 includes only the most important reactions; the full model used to simulate the data was much more comprehensive, but will not be listed here. The heterogeneous loss rates for HO₂ and H₂O₂, as measured in Chapter 4, were included in this kinetics model.

3 Results

To obtain accurate branching fractions for the ethyl peroxy radical self-reaction, a number of variables needed to be constrained. First, the concentration of the ethyl peroxy radical must be known to low degree of uncertainty as the observed rate of decay of the ethyl peroxy radical and the formation of the products are dependent on the ethyl peroxy radical concentration. Second, since the self-reaction cannot be isolated from reaction with HO₂, as HO₂ is produced from the reaction of ethoxy with O₂ (reaction (2)) (past experiments monitored the disappearance of C₂H₅O radicals in excess O₂),²²⁻²⁴ k_2 must be well-known. In addition, at the low pressure and relatively low O₂ concentrations used in these experiments, reaction of ethyl radicals with O₂ will not always to stabilized peroxy radicals, but can provide an additional source of reactive HO₂ radicals. It is important to quantify the amount of prompt HO₂ in this experiment to again understand the involvement of HO₂ in the radical decays.

3.1 Photoionization spectra

The identity and concentration of products formed in the kinetics experiments described here can be determined by comparing the energy-dependent photoionization signals with measured or literature absolute photoionization spectra. In this work, we measured the absolute photoionization spectra of acetaldehyde, ethanol, ethylene, and chloroethane, relative to propene, using authentic samples of each compound, as discussed previously for

the measurement of methanol in Chapter 4. The absolute photoionization spectra obtained experimentally in this work for acetaldehyde, ethanol, and ethylene agree with literature.²⁵⁻²⁶ There are no literature reports of the photoionization spectrum of chloroethane. The random error from multiple measurements of all four photoionization spectra was less than 2%, but the literature propene absolute spectrum has 20% uncertainty,²⁰ which is propagated into this measurement resulting in a 20% uncertainty for each absolute cross section reported in this chapter.

Figure 1 demonstrates how the shape of the photoionization spectra obtained with pure samples of acetaldehyde, ethanol, ethylene, and chloroethane, in addition to the literature spectrum for formaldehyde, compare to the spectra obtained at the mass peaks *in-situ* during ethyl peroxy self-reaction experiments. At photon energies below 11 eV, the spectra at the masses corresponding to CH₃CHO (m/z 44, Figure 1(a)), C₂H₅OH (m/z 46, Figure 1(b)) and C₂H₄ (m/z 28, Figure 1(c)) all agree extremely well with the shapes of the corresponding literature spectra; however, above 11 eV, all three spectra collected during kinetics experiments rise somewhat faster than the pure sample spectra, indicating the likely appearance daughter ions from the dissociative ionization of higher-mass products, or parent ionization of an isobaric species that has an ionization energy around 11 eV. For this reason, we only used data from experiments conducted at photon energies < 11.0 eV for quantitative measurements of these three molecules. Similarly, the spectrum collected at m/z 30 (corresponding to formaldehyde, Figure 1(d)), does not agree with the published photoionization spectrum below 10.8 eV, again suggesting that another species is present at this mass. We did not use formaldehyde as a constraint on the chemistry of this system. Figure 1(e) demonstrates the excellent agreement that can be achieved when only one species is present at a mass—the spectrum at m/z 64 matches that of C₂H₅Cl (formed from reaction of Cl₂ with C₂H₅) perfectly. These spectra demonstrate the importance of tunable VUV radiation from the synchrotron source—if we did not have the capability to identify the species in our system, or to recognize when another species might be contaminating a mass of interest, we might obtain erroneous results.

Panel (f)—the photoionization spectrum collected during kinetics experiments at m/z 62—will be discussed below in section 3.8.

3.2 C₂H₅O₂ + HO₂ cross-reaction

The cross-reaction rate constant for the reaction of ethyl peroxy radicals with HO₂ has been tested here. The JPL³ evaluated value (with 1σ error limits) for this rate constant is $8_{-3}^{+4} \times 10^{-12}$ cm³ molecule⁻¹ s⁻¹. By monitoring the C₂H₅OOH, and HO₂, signals (see Figure 2), the data was fit using a kinetic model, iteratively solving for k_3 . We recently reported the absolute photoionization cross sections for HO₂,¹⁹ enabling the HO₂ kinetics to be fit terms of absolute concentrations. The rate constant found here was $(6 \pm 1) \times 10^{-12}$ cm³ molecule⁻¹ s⁻¹, in good agreement with the evaluated rate. The error includes the uncertainty in the Cl radical concentrations, uncertainties from kinetics modeling, and error in the absolute cross sections.

3.3 Prompt C₂H₄ and HO₂ formation

Collisional deactivation of the ROO* complexes formed upon reaction of alkyl radicals with O₂ has been an open question in combustion chemistry. Reaction of ethyl radicals with O₂ has been one of the most carefully-studied ROO* systems.²⁷⁻³³ At high pressure and low temperature, ROO* is efficiently stabilized into the peroxy radical potential well with nearly 100% yield, but below 10 Torr, the direct reaction products, HO₂ + C₂H₄ start to appear (reaction (4)). In this work, experiments were carried out at 8 Torr with 0.6–3.6 Torr O₂, and reaction of ethyl radicals with O₂ was expected to form a not-insignificant amount of prompt HO₂ + C₂H₄. At 10 Torr, Clifford et al. observed 8.0 ± 0.8% yield for reaction (4) at 294 K.²⁹ Wagner et al. report a reaction (4) yield of 9.1% at 296 K at 11 Torr.³⁰ Kaiser et al. noted that ROO* interactions with uncoated reactor wall appeared to reduce the yield of reaction (4).²⁸ Not only are peroxy radicals lost to heterogeneous wall reactions, the chemically-activated complex may also be stabilized by wall collisions.



In this study, we were able to detect both C₂H₄ (at low photon energies, Figure 3(a)) and HO₂ (at high photon energies (Figure 3(b))). The VUV photoionization cross sections for both species have been measured and can be used to quantitatively measure the yield of reaction (4). The photoionization cross section for C₂H₄ at 10.7 eV is 5.19±0.06 Mb and the photoionization cross section for HO₂ is 1.3±0.3 Mb at 11.4 eV. The data points are shown with error bars, indicating the error associated with measuring the concentrations of both species. The best fit to the data is a 2.3±0.2 (2σ)% yield for reaction (4) at 8 Torr. The error in the reported yield was evaluated to include the error in the photoionization cross sections and the root N error in the ion counting.

3.4 C₂H₅O₂ self-reaction rate constant

The ethyl peroxy radical self-reaction rate constant could not be determined in this work because of the contribution of heterogeneous wall chemistry. However, assuming that no stabilized RO₂ radicals undergo heterogeneous chemistry upon interacting with reactor walls enabled us to provide an upper limit for the self-reaction. Figure 4 shows representative data from experiments designed to measure the alkoxy radical yield from the ethyl peroxy radical self-reaction, taken from Experiment 4 (10.7 eV). Acetaldehyde (*m/z* 44) was formed from two main sources: directly from reaction 1(b), as well as from secondary reactions of alkoxy radicals with O₂. There was some initial rapid formation of acetaldehyde, which was well-described by including reactions of lingering Cl atoms with ethoxy radicals in our kinetics model. Ethanol (*m/z* 46, panel (b)) had only one source in this reaction system: it is formed as a product in only one product channel in the ethyl peroxy radical self-reaction. Both acetaldehyde and ethanol are reported in terms of absolute concentrations, because of their measured photoionization cross sections. Although we do not detect the parent ion for ethyl peroxy radicals (the cation is dissociative¹⁶) we can observe the C₂H₅⁺ daughter ion at low photon energies (where it is not obscured by other species that form C₂H₅⁺ daughter ions with higher photoionization energies). Figure 4(c) shows the time-dependent C₂H₅⁺, which we assume is representative of the ethyl peroxy radical decays. The simulated C₂H₅O₂ kinetics agree well with the data. Finally, we observed the product of reaction (3), C₂H₅OOH. Enough HO₂ was formed during these experiments to create > 10¹² C₂H₅OOH cm⁻³. Scaling

the m/z 62 data relative to the simulated C_2H_5OOH model, we see that the time-dependent traces agree very well.

If we were to use the much faster rate (closer to $1 \times 10^{-13} \text{ cm}^3 \text{ s}^{-1}$) reported by Adachi et al.⁴ and Noell et al.¹², the observed ethyl peroxy radical decays would have to be significantly faster, complemented by faster product formation. The dotted lines in Figure 4 show the simulated error limits from the JPL evaluation ($k_1 = 6.8_{-3.4}^{+6.8} \times 10^{-14} \text{ cm}^3 \text{ s}^{-1}$), assuming the same initial conditions as the model.

3.5 Branching fraction of the ethoxy channel (α_{alkoxy})

The branching fraction of the ethoxy channel was determined with a kinetic model by constraining all rate constants in the kinetics model to literature values and the derived rates discussed above, and allowing the branching fractions of the two product channels (1a) and (1b) to vary, iteratively solving for the best fit. We obtained the time-dependent ratio, $R(t)$, of the acetaldehyde concentration over that of ethanol from our data, which was a straight line between 10 and 60 ms (shown, Figure 5).

$$R(t) = \frac{[CH_3CHO](t)}{[C_2H_5OH](t)} \quad (\text{II})$$

Several of the previous studies,^{5,13} including the preliminary work in this group,¹⁵ used the ratio of these two products, along with the following analytical model relating the time-independent ratio R , at steady state, to the branching fraction of the alkoxy channel.

$$\alpha_{eq} = \frac{R - 1}{R + 1} \quad (\text{III})$$

This model, detailed by Sander and Watson for the methyl peroxy radical self-reaction,³⁴ assumes that reaction of alkoxy radicals with O_2 and peroxy radicals with HO_2 are very fast, and that the alkoxy radical is in an equilibrium created by radical formation from the peroxy radical self-reaction and alkoxy radical destruction by reaction with O_2 . To test this model,

we defined $\alpha_{\text{alkoxy}} = 0.60$ and simulated $R(t)$ for a typical set of experimental conditions used in this work. Figure 6 shows modeled α_{eq} , as defined by equations II and III above. Also shown is the data collected for the same experimental conditions. Even though we have set α_{alkoxy} equal to 0.6 in our model the equilibrium value, α_{eq} does not equal 0.6 (indicated by the green line). The model levels off between 0.70 and 0.65. The analytical model therefore fails to reproduce the alkoxy radical branching fraction for the conditions used in this work. Even though our experimental data has $\alpha_{eq} = 0.6$, we did not find that $\alpha_{eq} = \alpha_{\text{alkoxy}}$ here, rather we obtain a smaller value $\alpha_{\text{alkoxy}} = 0.47 \pm 0.01$ for this set of conditions (described below).

To determine the value for α_{alkoxy} for each data set, we compared the experimental and simulated values for $R(t)$ (equation II). Figure 6 shows an example of this data. We used a fitting algorithm to vary the branching fraction for alkoxy radicals and compared the two ratios. This method was very sensitive to the branching fraction. Fitting only data collected at photon energies less than 11.0 eV to minimize impurities, we obtained the branching fraction of the ethoxy channel, $\alpha_{\text{alkoxy}} = 0.52 \pm 0.05$ from the weighted average of measurements made with oxygen concentrations (Figure 7). The error reported here is the 2σ error in the weighted average of each independent determination of α_{alkoxy} . Each independent determination of α_{alkoxy} plotted in Figure 7 is shown with error bars that represent the uncertainty in the fit, on the order of 15%, coming primarily from the uncertainty in the $\text{C}_2\text{H}_5\text{OH}$ counting statistics (the lower concentration of $\text{C}_2\text{H}_5\text{OH}$ ions, from the lower concentration of $\text{C}_2\text{H}_5\text{OH}$ formed in the flow reactor, and the lower $\text{C}_2\text{H}_5\text{OH}$ photoionization cross section gave it the largest contribution to the overall uncertainty).

3.6 Dialkyl peroxide formation

Formation of the diethyl peroxide $\text{C}_2\text{H}_5\text{OOC}_2\text{H}_5$ (ROOR) has been predicted to be of small importance for the ethyl peroxy self-reaction. Niki et al. put an upper limit on ROOR of 9% and Wallington et al. decreased this upper limit to 6%.¹³⁻¹⁴ The peroxide may be formed in

other ways, such as from peroxy radical reaction with the alkoxy radical, but it is unknown which channel contributed to ROOR detection in previous studies. Here, we observed product formation at m/z 90 (Figure 8(a)), growing in slowly at a rate quite similar to that observed for C_2H_5OH . We believe that the formation of the dialkyl peroxide product should have the same rate as C_2H_5OH because both species have only one source: self-reaction of $C_2H_5O_2$. We propose that $C_2H_5OOC_2H_5$ was detected at its parent ion mass (m/z 90) by the TOF at m/z 90. The photoionization spectrum at m/z 90 is shown in Figure 8(b). The ionization onset energy of the trace at m/z 90 is consistent with the expected adiabatic ionization energy of 8.87 eV (calculated at CBS-QB3, discussed in Appendix B) for a dialkyl peroxide molecule.

3.7 Photoionization spectrum of C_2H_5OOH

During the experiments described in this chapter, we obtained the relative photoionization spectrum at m/z 62, which we assumed to be methyl hydroperoxide, C_2H_5OOH , formed primarily from reaction of ethyl peroxy radicals with HO_2 . This spectrum is presented in Figure 1(f). Assuming we were able to quantitatively predict the C_2H_5OOH concentrations in our experiments, we scaled the m/z 62 ion signal to the model simulation for C_2H_5OOH (as shown in Figures 2(b) and 4(d)), and obtained an absolute cross section of 7.1 ± 1.4 Mb for this molecule at 10.7 eV, relative to the reference compound at each energy where kinetics experiments were conducted (similar to the procedures used in Chapters 4 and 5). The spectrum shown in Figure 1(f) has been scaled to single-energy determinations of the absolute cross section of C_2H_5OOH , yielding the absolute photoionization spectrum, with uncertainties in the cross sections of 20%, propagated from the uncertainty in the reference cross section measurement.

4 Discussion

The formation of prompt $C_2H_4 + HO_2$ in this study is significantly lower than yields suggested by all previous studies (here 2.5% formation of prompt chemistry at 8 Torr where typical values range from 8 – 10% at 10 Torr).²⁹⁻³¹ The role of collisional deactivation of the ROO^* intermediate is expected to decrease significantly as pressure decreases so this result disagrees with previous estimates. Kaiser et al. noted a surface-dependence in the formation

of C₂H₄ in their low pressure experiments.²⁸ They note that coating the walls of their reactor with a fluorocarbon coating increased the yield of C₂H₄ by a factor of 2. We similarly coat our reactor; however, formed radicals interact with the walls many times as they travel down the flow tube and we cannot rule out the possibility of enhanced collisional deactivation of ROO* caused by these collisions.

Several parameters were observed to strongly impact the ethyl peroxy and branching fraction. In obtaining the branching fraction α_{alkoxy} the most important parameter at 22.5% O₂ concentrations and greater was the relative ratio of acetaldehyde to ethanol. As a result, the cross sections obtained here played a large role in determining the final branching ratio. The cross sections of acetaldehyde and ethanol were both measured relative to the absolute photoionization spectrum of propene. As we discussed in Chapter 4, Section 3.4, the uncertainty in the propene literature absolute spectrum is 20%.²⁰ Measuring cross sections relative to propene introduces the same systematic error in the absolute cross sections of acetaldehyde and ethanol. However, since we obtained the branching fraction α_{alkoxy} from the ratio of acetaldehyde to ethanol, this systematic error is canceled out, and we are left only with the random error from several cross section measurements and the root N error in ion counting. The random error in both measurements was less than 2%, so the primary source of uncertainty in measuring the branching fraction was the ion counting error in the C₂H₅OH signal. Our result for the alkoxy radical yield from the self-reaction of ethyl peroxy radicals, $\alpha_{\text{alkoxy}} = 0.55 \pm 0.05$, agrees with the majority of past experimental measurements and with the branching fraction typically included in atmospheric models.

The results reported in this work disagree with preliminary results presented as part of the groundwork in Noell's thesis, which tentatively assigned an alkoxy radical yield on the order of 30%.¹⁵ The Sandia group implemented a key instrumental change that enabled the accurate measurements presented in this thesis: they incorporated an orthogonal acceleration time-of-flight detection system into the MPIMS to replace the magnetic sector mass spectrometer (described by Savee et al.).³⁵ This change resulted in much higher mass resolution, enabling complete separation of mass peaks less than 1 mass unit apart. Noell

observed significant overlap between nearby peaks, seriously hindering his ability to quantitatively measure the products in the very congested mass spectrum.

5 Conclusions

Using multiplexed photoionization mass spectrometry, we measured the branching fraction for the radical forming channel of the ethyl peroxy self-reaction. We present an alkoxy radical yield, $\alpha_{\text{alkoxy}} = 0.52 \pm 0.05$, in good agreement with most previous reports. The yield of $\text{HO}_2 + \text{C}_2\text{H}_4$ from the $\text{C}_2\text{H}_5 + \text{O}_2$ reaction has been constrained to $2.3 \pm 0.2\%$ at 8 Torr in helium. Finally, this study has obtained photoionization efficiencies of $\text{C}_2\text{H}_5\text{OH}$, CH_3CHO , C_2H_4 , $\text{C}_2\text{H}_5\text{Cl}$, and $\text{C}_2\text{H}_5\text{OOH}$ at energies up to 11.45 eV.

6 References

1. Lightfoot, P. D.; Cox, R. A.; Crowley, J. N.; Destriau, M.; Hayman, G. D.; Jenkin, M. E.; Moortgat, G. K.; Zabel, F., Organic Peroxy Radicals: Kinetics, Spectroscopy and Tropospheric Chemistry. *Atmos. Environ., Part A* **1992**, *26*, 1805-1961.
2. Atkinson, R.; Baulch, D. L.; Cox, R. A.; Crowley, J. N.; Hampson, R. F.; Hynes, R. G.; Jenkin, M. E.; Rossi, M. J.; Troe, J.; Subcommittee, I., Evaluated Kinetic and Photochemical Data for Atmospheric Chemistry: Volume II – Gas Phase Reactions of Organic Species. *Atmos. Chem. Phys.* **2006**, *6*, 3625-4055.
3. Sander, S. P.; Abbatt, J.; Barker, J. R.; Burkholder, J. B.; Friedl, R. R.; Golden, D. M.; Huie, R. E.; Kolb, C. E.; Kurylo, M. J.; Moortgat, G. K., et al., Chemical Kinetics and Photochemical Data for Use in Atmospheric Studies, Evaluation Number 17. *JPL Publication 10-6* **2011**.
4. Adachi, H.; Basco, N.; James, D. G. L., The Ethylperoxy Radical Spectrum and Rate Constant for Mutual Interaction Measured by Flash Photolysis and Kinetic Spectroscopy. *Int. J. Chem. Kinet.* **1979**, *11*, 1211-1229.
5. Anastasi, C.; Waddington, D. J.; Woolley, A., Reactions of Oxygenated Radicals in the Gas Phase. Part 10. – Self-reactions of Ethylperoxy Radicals. *J. Chem. Soc., Faraday Trans. 1* **1983**, *79*, 505-516.
6. Cattell, F. C.; Cavanagh, J.; Cox, R. A.; Jenkin, M. E., A Kinetics Study of Reactions of HO_2 and $\text{C}_2\text{H}_5\text{O}_2$ using Diode Laser Absorption Spectroscopy. *J. Chem. Soc., Faraday Trans. 2* **1986**, *82*, 1999-2018.
7. Munk, J.; Pagsberg, P.; Ratajczak, E.; Sillesen, A., Spectrokinetic Studies of Ethyl and Ethylperoxy Radicals. *J. Phys. Chem.* **1986**, *90*, 2752-2757.
8. Wallington, T. J.; Dagaut, P.; Kurylo, M. J., Measurements of the Gas Phase UV Absorption Spectrum of $\text{C}_2\text{H}_5\text{O}_2\cdot$ Radicals and of the Temperature Dependence of the Rate Constant for their Self-reaction. *J. Photochem. Photobiol., A* **1988**, *42*, 173-185.

9. Fenter, F. F.; Catoire, V.; Lesclaux, R.; Lightfoot, P. D., The Ethylperoxy Radical: Its Ultraviolet Spectrum, Self-reaction, and Reaction with Hydroperoxy, Each Studied as a Function of Temperature. *J. Phys. Chem.* **1993**, *97*, 3530-3538.
10. Bauer, D.; Crowley, J. N.; Moortgat, G. K., The UV Absorption Spectrum of the Ethylperoxy Radical and its Self-reaction Kinetics Between 218 and 333 K. *J. Photochem. Photobiol., A* **1992**, *65*, 329-344.
11. Atkinson, D. B.; Hudgens, J. W., Chemical Kinetic Studies Using Ultraviolet Cavity Ring-Down Spectroscopic Detection: Self-Reaction of Ethyl and Ethylperoxy Radicals and the Reaction $O_2 + C_2H_5 \rightarrow C_2H_5O_2$. *J. Phys. Chem. A* **1997**, *101*, 3901-3909.
12. Noell, A. C.; Alconcel, L. S.; Robichaud, D. J.; Okumura, M.; Sander, S. P., Near-Infrared Kinetic Spectroscopy of the HO_2 and $C_2H_5O_2$ Self-Reactions and Cross Reactions. *J. Phys. Chem. A* **2010**, *114*, 6983-6995.
13. Niki, H.; Maker, P. D.; Savage, C. M.; Breitenbach, L. P., Fourier Transform Infrared Studies of the Self-reaction of $C_2H_5O_2$ Radicals. *J. Phys. Chem.* **1982**, *86*, 3825-3829.
14. Wallington, T. J.; Gierczak, C. A.; Ball, J. C.; Japar, S. M., Fourier Transform Infrared Study of the Self Reaction of Ethylperoxy ($C_2H_5O_2$) Radicals in Air at 295 K. *Int. J. Chem. Kinet.* **1989**, *21*, 1077-89.
15. Noell, A. C. Laboratory Studies of the Self and Cross Reactions of Atmospheric Peroxy Radicals. Dissertation (Ph.D.), California Institute of Technology, 2010.
16. Meloni, G.; Zou, P.; Klippenstein, S. J.; Ahmed, M.; Leone, S. R.; Taatjes, C. A.; Osborn, D. L., Energy-Resolved Photoionization of Alkylperoxy Radicals and the Stability of Their Cations. *J. Am. Chem. Soc.* **2006**, *128*, 13559-13567.
17. Osborn, D. L.; Zou, P.; Johnsen, H.; Hayden, C. C.; Taatjes, C. A.; Knyazev, V. D.; North, S. W.; Peterka, D. S.; Ahmed, M.; Leone, S. R., The Multiplexed Chemical Kinetic Photoionization Mass Spectrometer: A New Approach to Isomer-Resolved Chemical Kinetics. *Rev. Sci. Instrum.* **2008**, *79*, 104103.
18. Taatjes, C. A.; Hansen, N.; Osborn, D. L.; Kohse-Hoinghaus, K.; Cool, T. A.; Westmoreland, P. R., "Imaging" Combustion Chemistry via Multiplexed Synchrotron-Photoionization Mass Spectrometry. *Phys. Chem. Chem. Phys.* **2008**, *10*, 20-34.
19. Dodson, L. G.; Shen, L.; Savee, J. D.; Eddingsaas, N. C.; Welz, O.; Taatjes, C. A.; Osborn, D. L.; Sander, S. P.; Okumura, M., VUV Photoionization Cross Sections of HO_2 , H_2O_2 , and H_2CO . *J. Phys. Chem. A* **2015**, *119*, 1279-1291.
20. Welz, O.; Zador, J.; Savee, J. D.; Ng, M. Y.; Meloni, G.; Fernandes, R. X.; Sheps, L.; Simmons, B. A.; Lee, T. S.; Osborn, D. L., et al., Low-Temperature Combustion Chemistry of Biofuels: Pathways in the Initial Low-Temperature (550 K-750 K) Oxidation Chemistry of Isopentanol. *Phys. Chem. Chem. Phys.* **2012**, *14*, 3112-3127.
21. Ianni, J. C. *Kintecus*, Windows Version 2.80; <http://www.kintecus.com>, 2002.

22. Gutman, D.; Sanders, N.; Butler, J. E., Kinetics of the Reactions of Methoxy and Ethoxy Radicals with Oxygen. *J. Phys. Chem.* **1982**, *86*, 66-70.
23. Hartmann, D.; Karthäuser, J.; Sawerysyn, J. P.; Zellner, R., Kinetics and HO₂ Product Yield of the Reaction C₂H₅O + O₂ between 295 and 411 K. *Ber. Bunsen-Ges. Phys. Chem.* **1990**, *94*, 639-645.
24. Zabarnick, S.; Heicklen, J., Reactions of Alkoxy Radicals with O₂. I. C₂H₅O Radicals. *Int. J. Chem. Kinet.* **1985**, *17*, 455-476.
25. Cool, T. A.; Wang, J.; Nakajima, K.; Taatjes, C. A.; McIlroy, A., Photoionization Cross sections for Reaction Intermediates in Hydrocarbon Combustion. *Int. J. Mass Spectrom.* **2005**, *247*, 18-27.
26. Cool, T. A.; Nakajima, K.; Mostefaoui, T. A.; Qi, F.; McIlroy, A.; Westmoreland, P. R.; Law, M. E.; Poisson, L.; Peterka, D. S.; Ahmed, M., Selective Detection of Isomers with Photoionization Mass Spectrometry for Studies of Hydrocarbon Flame Chemistry. *J. Chem. Phys.* **2003**, *119*, 8356-8365.
27. Dobis, O.; Benson, S. W., Reaction of the Ethyl Radical with Oxygen at Millitorr Pressures at 243-368 K and a Study of the Cl + HO₂, Ethyl + HO₂, and HO₂ + HO₂ reactions. *J. Am. Chem. Soc.* **1993**, *115*, 8798-8809.
28. Kaiser, E. W.; Lorkovic, I. M.; Wallington, T. J., Pressure Dependence of the Ethene Yield from the Reaction Ethyl Radical + Oxygen. *J. Phys. Chem.* **1990**, *94*, 3352-3354.
29. Clifford, E. P.; Farrell, J. T.; DeSain, J. D.; Taatjes, C. A., Infrared Frequency-Modulation Probing of Product Formation in Alkyl + O₂ Reactions: I. The Reaction of C₂H₅ with O₂ between 295 and 698 K. *J. Phys. Chem. A* **2000**, *104*, 11549-11560.
30. Wagner, A. F.; Slagle, I. R.; Sarzynski, D.; Gutman, D., Experimental and Theoretical Studies of the Ethyl + Oxygen Reaction Kinetics. *J. Phys. Chem.* **1990**, *94*, 1853-1868.
31. Bozzelli, J. W.; Dean, A. M., Chemical Activation Analysis of the Reaction of Ethyl Radical with Oxygen. *J. Phys. Chem.* **1990**, *94*, 3313-3317.
32. Taatjes, C. A., Uncovering the Fundamental Chemistry of Alkyl + O₂ Reactions via Measurements of Product Formation. *J. Phys. Chem. A* **2006**, *110*, 4299-4312.
33. DeSain, J. D.; Klippenstein, S. J.; Miller, J. A.; Taatjes, C. A., Measurements, Theory, and Modeling of OH Formation in Ethyl + O₂ and Propyl + O₂ Reactions. *J. Phys. Chem. A* **2003**, *107*, 4415-4427.
34. Sander, S. P.; Watson, R. T., Kinetics Studies of the Reactions of CH₃O₂ with NO, NO₂, and CH₃O₂ at 298 K. *J. Phys. Chem.* **1980**, *84*, 1664-1674.
35. Savee, J. D.; Soorkia, S.; Welz, O.; Selby, T. M.; Taatjes, C. A.; Osborn, D. L., Absolute Photoionization Cross-Section of the Propargyl Radical. *J. Chem. Phys.* **2012**, *136*, 134307-10.
36. Eskola, A. J.; Lozovsky, V. A.; Timonen, R. S., Kinetics of the Reactions of C₂H₅, *n*-C₃H₇, and *n*-C₄H₉ Radicals with Cl₂ at the Temperature Range 190–360 K. *Int. J. Chem. Kinet.* **2007**, *39*, 614-619.

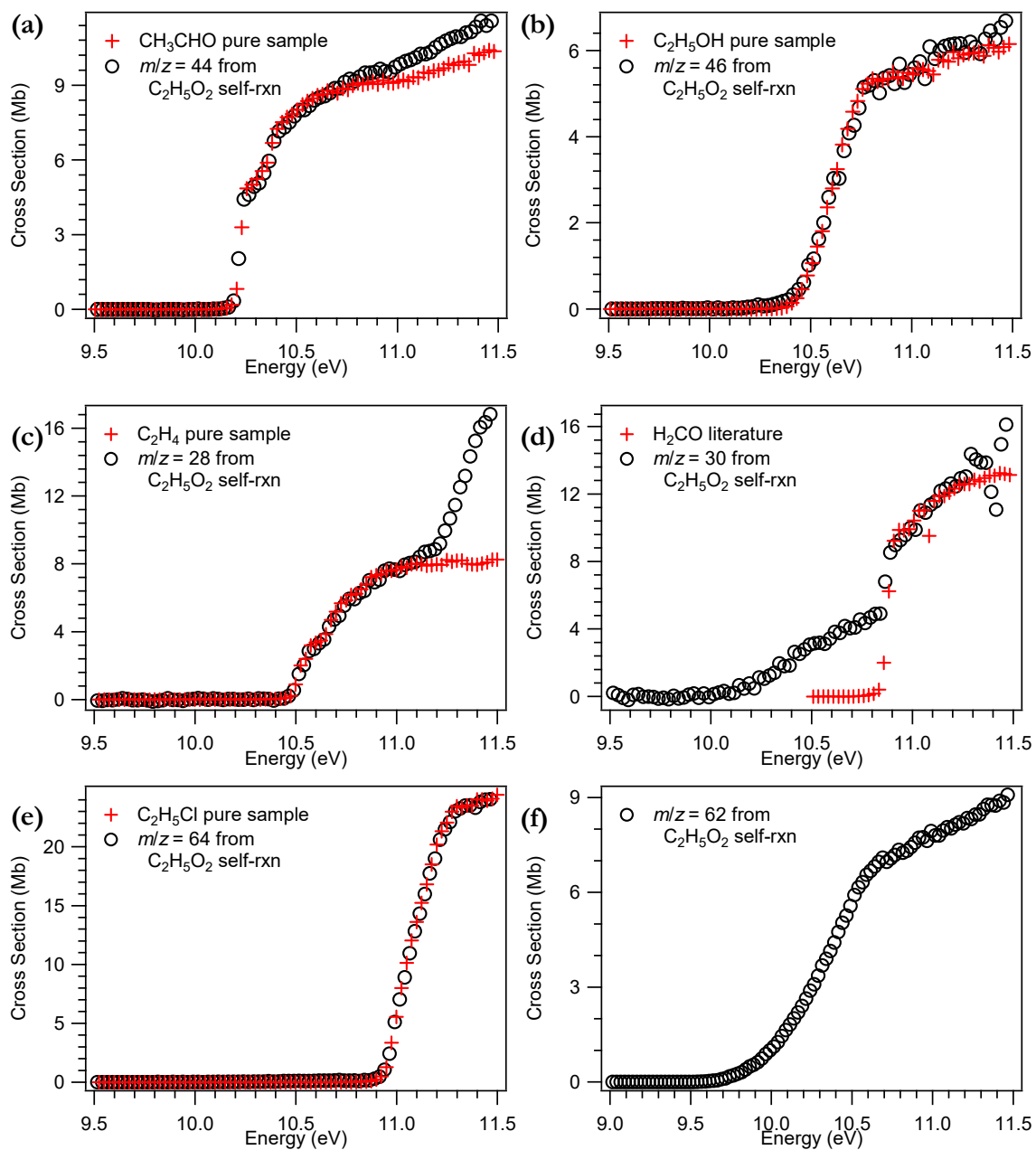


Figure 1. Absolute photoionization cross section (black diamonds) of (a) acetaldehyde, (b) ethanol, (c) ethylene, (d) formaldehyde, and (e) chloroethane and normalized signal for (a) m/z 44, (b) m/z 46, (c) m/z 28, (d) m/z 30, (e) m/z 64. Also shown (on an expanded x-axis plotted from 9–11.5 eV) is the m/z 62 spectrum, corresponding to C₂H₅OOH.

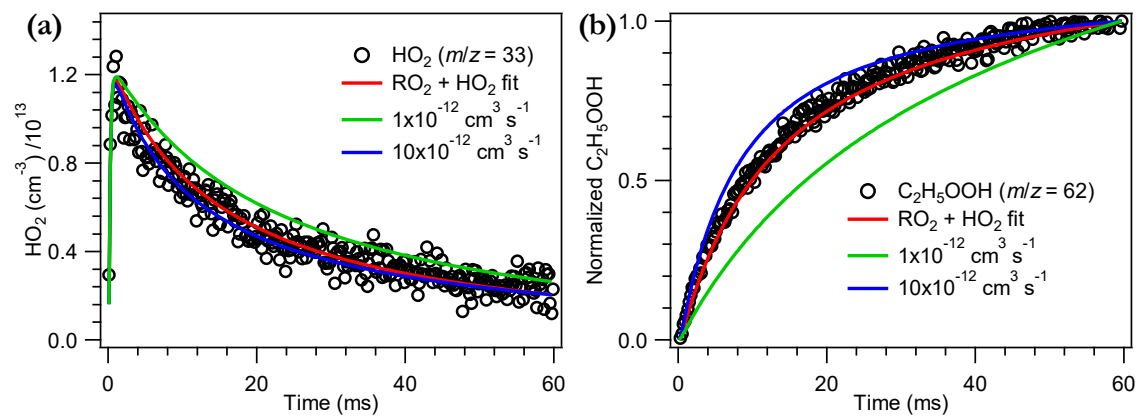


Figure 2. Experimental data (black circles) and kinetic fit (red line) of $C_2H_5O_2 + HO_2$ cross-reaction. Each panel displays the fit to the data for the species ((a) HO_2 (b) C_2H_5OOH).

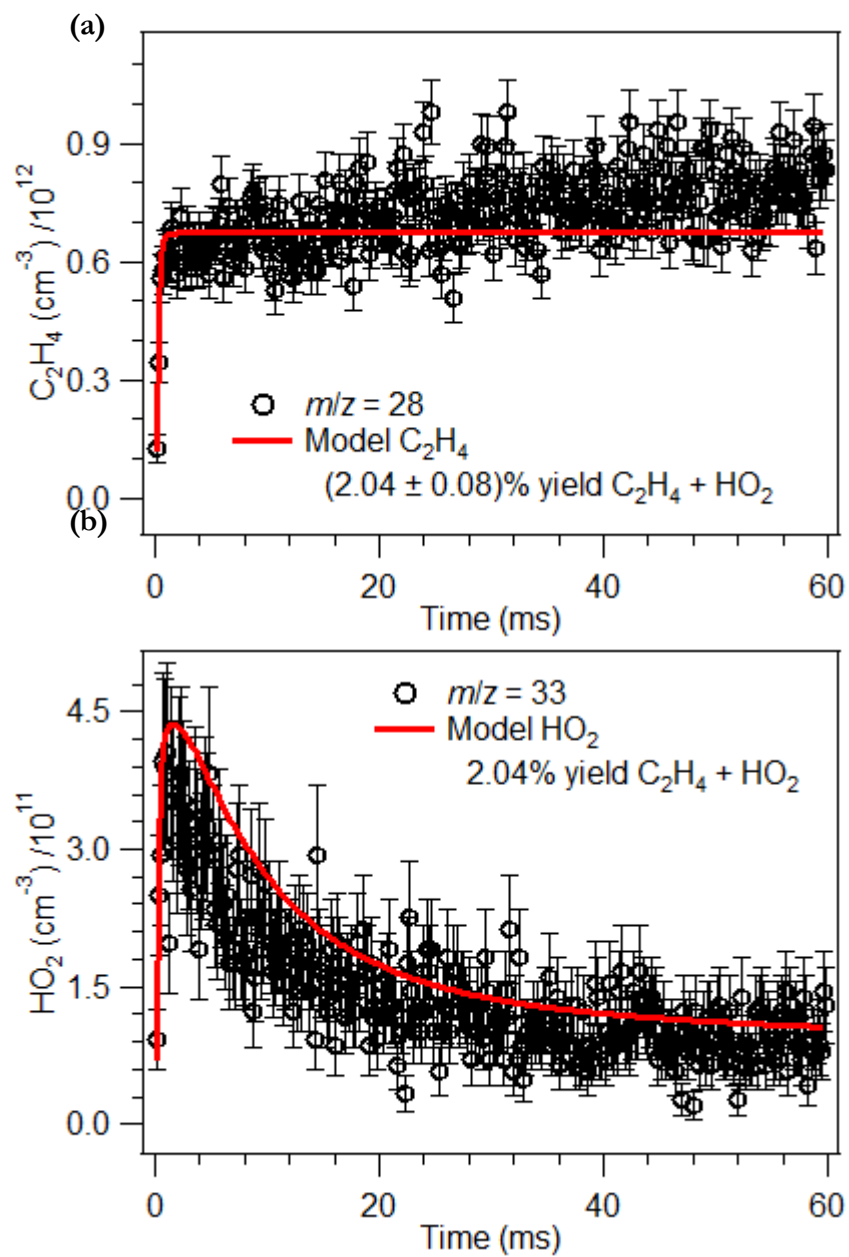


Figure 3. Experimental kinetic traces for m/z 28 (C_2H_4 , top panel) and m/z 33 (HO_2 , bottom panel), formed from reaction of C_2H_5 radicals and O_2 . The red line is the result of fitting the yield of reaction (4) to the C_2H_4 formation.

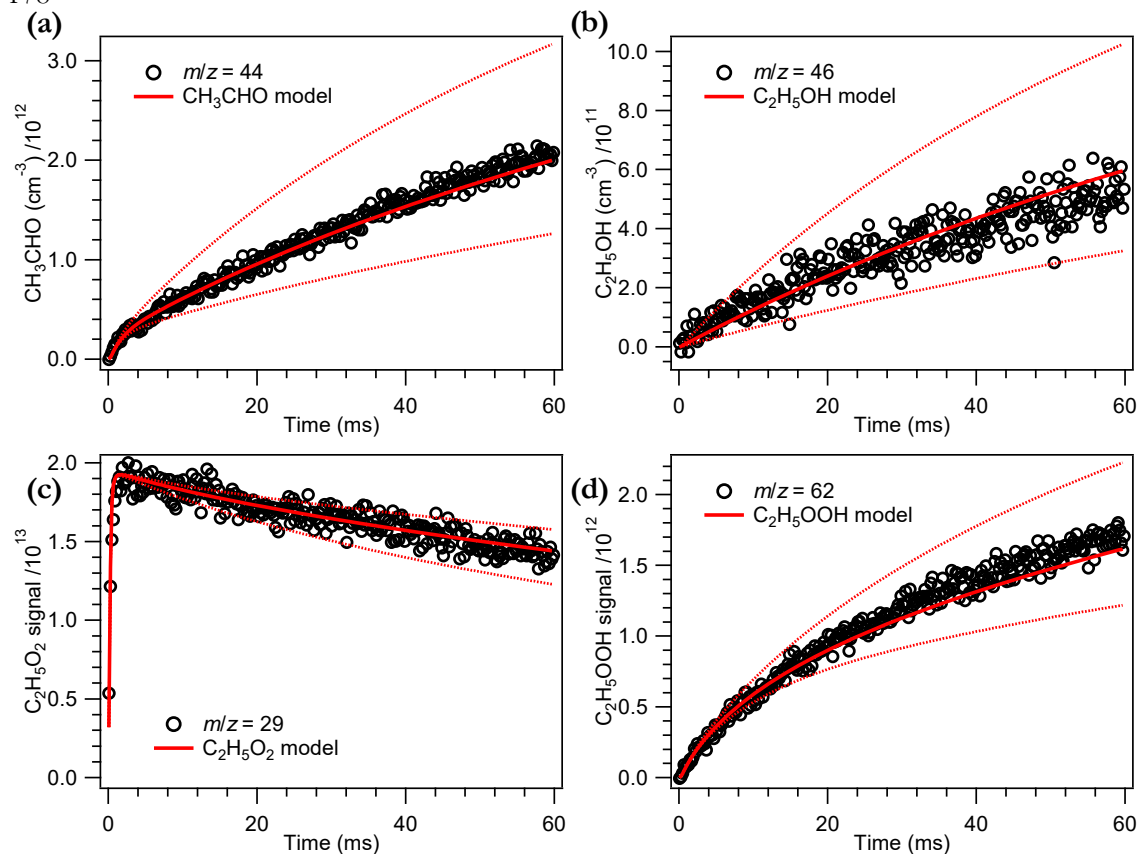


Figure 4. Kinetics from the ethyl peroxy radical self-reaction. Shown are the experimental data (open circles) for (a) m/z 44 (CH_3CHO), (a) m/z 46 ($\text{C}_2\text{H}_5\text{OH}$), (a) m/z 29 (C_2H_5^+ from $\text{C}_2\text{H}_5\text{O}_2$), and (d) m/z 62 ($\text{C}_2\text{H}_5\text{OOH}$). The solid red line shows the result of the simulation, using $k_1 = 6.8 \times 10^{-14} \text{ cm}^3 \text{ s}^{-1}$ and $\alpha_{\text{alkoxy}} = 0.50$. The thin dotted lines are simulations using the error limits for k_1 taken from the JPL evaluation.

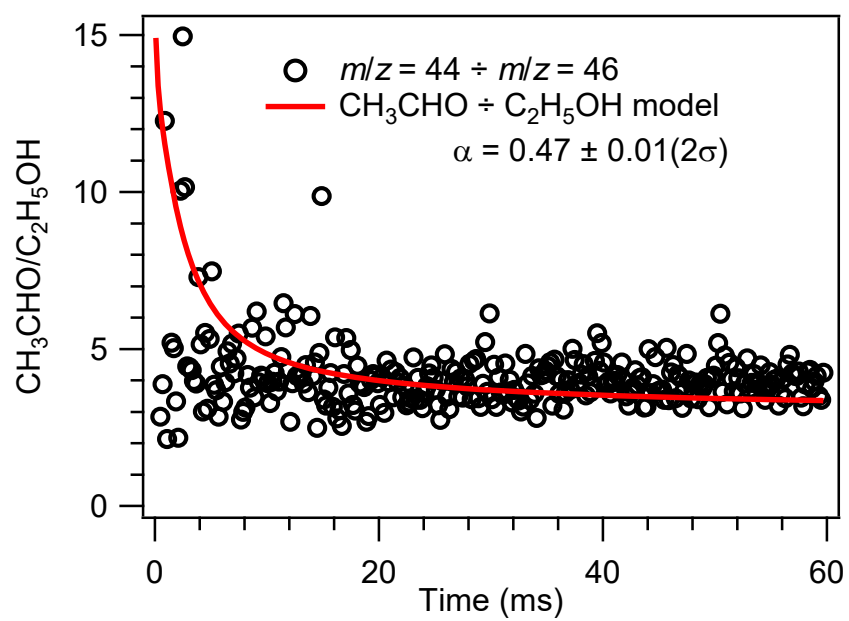


Figure 5. Ratio of acetaldehyde/ethanol in the ethyl peroxy radical self-reaction.

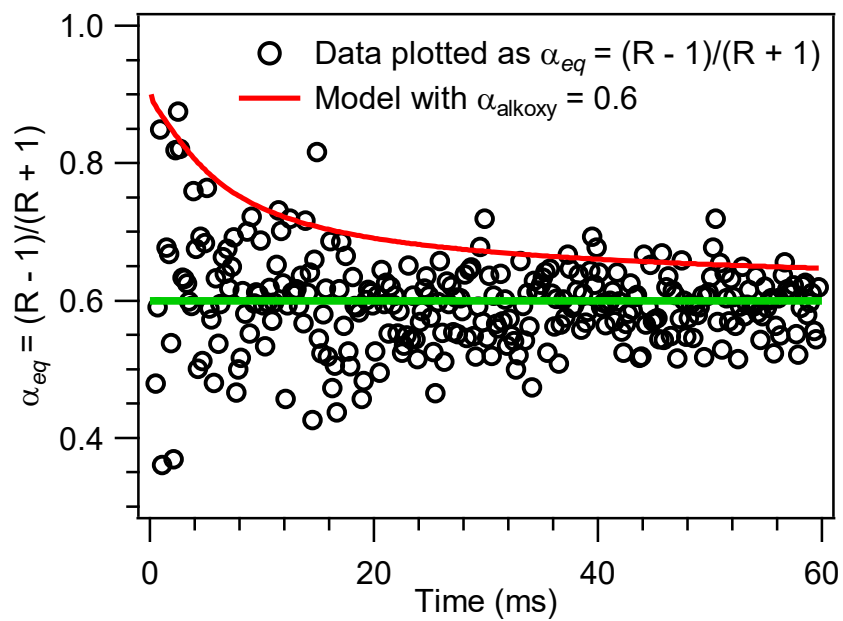


Figure 6. Time-dependent ratio of $\text{CH}_3\text{CHO} \div \text{C}_2\text{H}_5\text{OH}$ in the ethyl peroxy radical self-reaction.

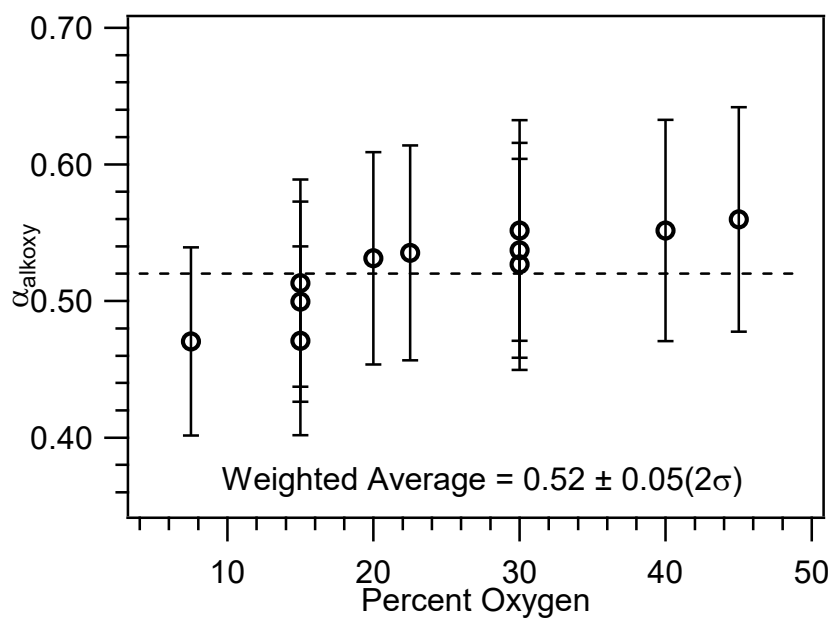


Figure 7. Fitted alkoxy yields as a function of % O₂. The weighted average of all experimental data was $\alpha_{\text{alkoxy}} = 0.52 \pm 0.05$ (this 2σ error is the weighted error in the fits, which include the measurement uncertainty).

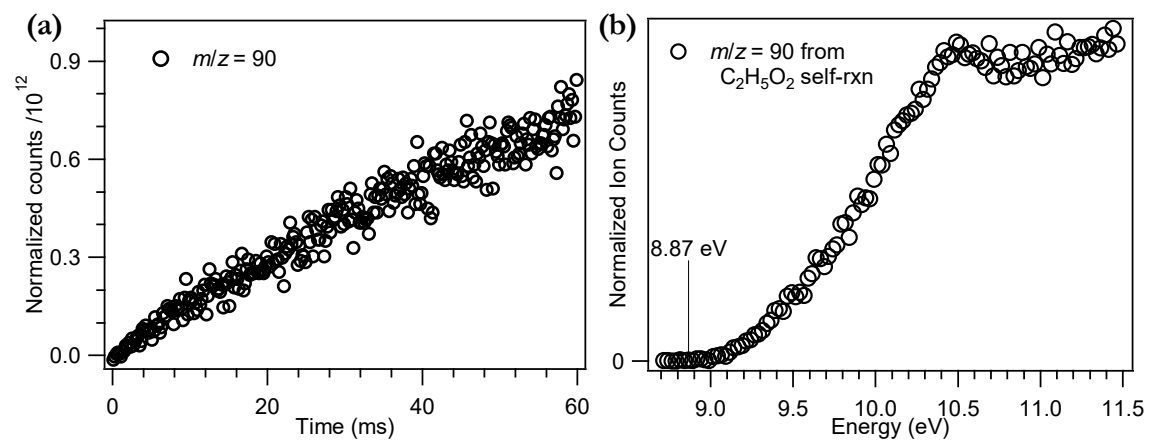


Figure 8. Kinetics and spectroscopy at m/z 90.

Table 1. List of experimental parameters for the ethyl peroxy radical self-reaction. All experiments were at 8 Torr and 298 K.

Experiment	Photon energy (eV)	[C ₂ H ₆] ^a	[O ₂] ^a	[Cl ₂] ^a	[Cl] ^a
1	10.7	1.3×10 ¹⁵	6.48×10 ¹⁵	7.8×10 ¹⁴	2.2±0.2×10 ¹³
2	10.7	1.3×10 ¹⁵	1.94×10 ¹⁶	7.8×10 ¹⁴	1.2±0.2×10 ¹³
3	11.4	1.3×10 ¹⁵	1.94×10 ¹⁶	7.8×10 ¹⁴	1.2±0.2×10 ¹³
4	10.7	1.3×10 ¹⁵	3.89×10 ¹⁶	7.8×10 ¹⁴	1.6±0.2×10 ¹³
5	11.4	1.3×10 ¹⁵	3.89×10 ¹⁶	7.8×10 ¹⁴	1.6±0.2×10 ¹³
6	10.7	1.3×10 ¹⁵	5.18×10 ¹⁶	7.8×10 ¹⁴	1.7±0.2×10 ¹³
7	11.0	1.3×10 ¹⁵	5.18×10 ¹⁶	7.8×10 ¹⁴	1.7±0.2×10 ¹³
8	11.4	1.3×10 ¹⁵	5.18×10 ¹⁶	7.8×10 ¹⁴	1.7±0.2×10 ¹³
9	10.7	1.3×10 ¹⁵	5.83×10 ¹⁶	7.8×10 ¹⁴	1.6±0.2×10 ¹³
10	11.4	1.3×10 ¹⁵	5.83×10 ¹⁶	7.8×10 ¹⁴	1.6±0.2×10 ¹³
11	10.7	1.3×10 ¹⁵	7.78×10 ¹⁶	7.8×10 ¹⁴	1.6±0.2×10 ¹³
12	11.0	1.3×10 ¹⁵	7.78×10 ¹⁶	7.8×10 ¹⁴	1.7±0.2×10 ¹³
13	11.4	1.3×10 ¹⁵	7.78×10 ¹⁶	7.8×10 ¹⁴	1.6±0.2×10 ¹³
14	10.7	1.3×10 ¹⁵	1.04×10 ¹⁷	7.8×10 ¹⁴	1.7±0.2×10 ¹³
15	11.0	1.3×10 ¹⁵	1.04×10 ¹⁷	7.8×10 ¹⁴	1.7±0.2×10 ¹³
16	11.4	1.3×10 ¹⁵	1.04×10 ¹⁷	7.8×10 ¹⁴	1.7±0.2×10 ¹³

^a in molecules cm⁻³

Table 2. List of experimental parameters for the HO₂ + C₂H₅O₂ cross-reaction. All experiments were at 8 Torr and 298 K.

Experiment	Photon energy (eV)	[CH ₃ OH] ^a	[C ₂ H ₆] ^a	[O ₂] ^a	[Cl ₂] ^a	[Cl] ^a
17	11.45	3.24 × 10 ¹⁴	1.3 × 10 ¹⁴	7.78 × 10 ¹⁶	7.8 × 10 ¹⁴	1.2 ± 0.2 × 10 ¹³

^a in molecules cm⁻³

Table 3. Kinetics model for the C₂H₅O₂ self-reaction. Rate coefficients are taken from the JPL evaluation³, unless otherwise noted, with 1σ errors.

	$k_{298\text{K}}$ (cm ³ molecule ⁻¹ s ⁻¹)	Ref
$\text{Cl}_2 \xrightarrow{h\nu} 2\text{Cl}$	---	
$\text{C}_2\text{H}_6 + \text{Cl} \rightarrow \text{C}_2\text{H}_5 + \text{HCl}$	$5.7 \pm 0.4 \times 10^{-11}$	
$\text{C}_2\text{H}_5 + \text{O}_2 \rightarrow \text{C}_2\text{H}_5\text{O}_2$	$4.6 \pm 0.9 \times 10^{-12}$	
$\text{C}_2\text{H}_5 + \text{O}_2 \rightarrow \text{C}_2\text{H}_4 + \text{HO}_2$	determined here	
$\text{C}_2\text{H}_5\text{O}_2 + \text{C}_2\text{H}_5\text{O}_2 \rightarrow 2\text{C}_2\text{H}_5\text{O} + \text{O}_2$	determined here	
$\text{C}_2\text{H}_5\text{O}_2 + \text{C}_2\text{H}_5\text{O}_2 \rightarrow \text{C}_2\text{H}_5\text{OH} + \text{CH}_3\text{CHO} + \text{O}_2$	determined here	
$\text{C}_2\text{H}_5\text{O}_2 + \text{HO}_2 \rightarrow \text{C}_2\text{H}_5\text{OOH} + \text{O}_2$	determined here	
$\text{C}_2\text{H}_5\text{O} + \text{O}_2 \rightarrow \text{HO}_2 + \text{CH}_3\text{CHO}$	$1.0 \pm 0.5 \times 10^{-14}$	
$\text{C}_2\text{H}_5\text{O}_2 + \text{C}_2\text{H}_5\text{O} \rightarrow \text{C}_2\text{H}_5\text{OOH} + \text{CH}_3\text{CHO}$	$1.54 \pm 0.7 \times 10^{-11}$	a
$\text{HO}_2 + \text{HO}_2 \rightarrow \text{H}_2\text{O}_2 + \text{O}_2$	$1.4 \pm 0.2 \times 10^{-12}$	
$\text{C}_2\text{H}_5 + \text{Cl}_2 \rightarrow \text{C}_2\text{H}_5\text{Cl} + \text{Cl}$	$1.45 \pm 0.04 \times 10^{-11}$	b

^aTaken from Noell et al.¹² ^bTaken from Eskola et al.³⁶

PRODUCT YIELD STUDIES OF THE REACTIONS OF ACETYL RADICALS WITH O₂ AND ACETYL PEROXY RADICALS WITH HO₂ USING VUV PHOTOIONIZATION MASS SPECTROMETRY

1 Introduction

Hydroxyl radicals (OH) control daytime oxidation of volatile organic compounds because of their high reactivity, leading to air pollution and aerosol formation.¹⁻² Yet photochemical models fail to reproduce measurements of OH concentrations in remote regions rich in biogenic emissions.³ In order to resolve this discrepancy, efforts have been made to identify missing or incorrect chemistry that could account for higher OH levels through radical regeneration mechanisms.⁴ One suggested route by which OH radicals may be recycled in remote regions is regeneration of OH radicals from reaction of HO₂ with carbonyl-containing peroxy radicals. This mechanism depends on competition between several accessible product channels for such reactions.

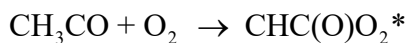
The acetyl peroxy radical, CH₃C(O)O₂ is an important intermediate in the oxidation of isoprene and other biogenic emissions. Reaction of this carbonyl-containing peroxy radical with HO₂ can proceed via three channels:



Most simple peroxy radicals react with HO₂ exclusively via H-atom transfer, analogous to reaction (1a), on the triplet surface, leading to hydroperoxide product formation – a radical chain-terminating step in the atmosphere. In the case of acetyl peroxy radicals, stabilization of reactant intermediates by the carbonyl functional group α - to the peroxy radical moiety

opens up the singlet reaction surface.⁵ Reaction (1b) becomes accessible on this surface through a 7-member transition state, forming the acetic acid product along with O₃ through a 3,4 sigmatropic rearrangement. Also on the singlet surface, the acetoxy radical, CH₃C(O)O, forms as a co-product with OH through hemolytic O–O cleavage, stabilized by hydrogen bonding, by reaction (1c). Experimental measurements of the yield of reaction (1c) have ranged from <10% up to 70% (not including the three studies prior to 2000 that were unaware of the existence of product channel (1c)⁶⁻⁸).^{4-5,9-14} Table 1 summarizes their results.

Reaction of acetyl radicals with O₂ forms the chemically-activated ROO* complex.



Collision with bath gas molecules stabilizes the intermediate down into the peroxy radical potential energy well, whereas direct reaction forms OH radicals plus a coproduct.¹⁵⁻²¹



Several questions remain for this reaction: what is the pressure-dependent yield of each channel, what is the co-product of the OH channel, and are there any other possible product channels? At low pressure, where fewer collisional partners exist to quench the ROO* species down into the peroxy well, the yield for the bimolecular channel increases, but to what extent remains an open question. Low pressure measurements disagree on the yield below 10 Torr. Figure 1 shows the potential energy surface computed by Carr et al. (2011), calculating stationary points at G3X(MP2)-RAD and using CASPT2 on some parts of the potential energy surface. Master equation calculations using this potential energy surface support the experimental findings by Blitz et al., Carr et al. (2007), and Carr et al. (2011) indicating a measured OH yield of significantly less than 100%. However, the potential energy surface computed by Maranzana et al. supports experiments that measured nearly unity yield of reaction (b).

2 Experimental Methods

The experiments described in this chapter used the same instrumentation described in the previous three chapters. Reactants, intermediates, and products were formed and detected in the Multiplexed Photoionization Mass Spectrometer (MPIMS) using the synchrotron radiation available on the Chemical Dynamics beamline at the Advanced Light Source at Lawrence Berkeley National Laboratory.²²⁻²³ We again performed our experiments in a Teflon-coated quartz reactor at room temperature and 8.00 ± 0.04 Torr total pressure, 200 ± 1.2 sccm total flow, and He bath gas. Cl₂ gas was photodissociated using excimer light at 351 nm to form Cl atoms. Cl atoms reacted with precursor molecules (CH₃CHO and CH₃OH) in the presence of oxygen to form the CH₃C(O)O₂ and HO₂ radicals.

Typical gas concentrations for experiments on the acetyl radical reaction with O₂ were, in units of molecules cm⁻³: [Cl₂] = 7.8×10^{14} , [CH₃CHO] = 2.6×10^{14} , [O₂] = $(1.3-7.7) \times 10^{16}$, and [He] = $(1.8-7.7) \times 10^{17}$. Experiments to measure the branching fractions of the product channels of the cross reaction used the following conditions, in units of molecules cm⁻³: [Cl₂] = 7.8×10^{14} , [CH₃CHO] = $(0.8-2.6) \times 10^{14}$, [CH₃OH] = $(4.4-12.7) \times 10^{14}$, [O₂] = 7.7×10^{16} , and [He] = 1.8×10^{17} .

As described in previous chapters, the complex chemistry of these systems necessitates the use of chemical kinetics modeling software to numerically simulate the time-dependence of the chemical system.²⁴ Table 2 lists the most important reactions included in the kinetics model. We also included the heterogeneous wall chemistry for HO₂ and OH radicals, described in Chapters 4 and 5, in the kinetics simulations.

3 Results

The ultimate goal of this study was to measure the branching fraction of the radical channel for the cross-reaction between HO₂ and CH₃C(O)O₂. Several determinations had to be made first. In order to quantify the yield of the radical channel, we needed to identify a product of this reaction that could be measured quantitatively. Under the experimental conditions described here, the lifetime of the OH radicals was quite short, given the high concentration of OH reaction partners, such as acetaldehyde and methanol. Additionally, the co-product of

the radical channel, the acetoxy radical, is known to decompose rapidly to form CO_2 and CH_3 radicals. Since the mass of carbon monoxide (m/z 44) is the same as the acetaldehyde precursor, we could not detect it in our mass spectrometer. But we can quantify the yield of this channel through quantitative measurement of CH_3O_2 and CH_3Cl , which are formed rapidly from CH_3 reactions with high concentrations of O_2 and Cl_2 . Finally, using the results from the measured methyl peroxy radical absolute spectrum, we can investigate the reactions of acetyl peroxy radicals in our experiments. We first determined the yield of acetyl peroxy radicals from the reaction of acetyl radicals with O_2 , and, using quantitative concentrations of radical reactants and products, fit experimental results from the cross-reaction between acetyl peroxy radicals and HO_2 .

3.1 Absolute photoionization cross section of CH_3O_2

Quantitative measurement of the methyl peroxy radical was central to constraining the kinetics of all of the chemical systems discussed here. Using several different chemical systems, we measured the absolute photoionization cross section for the methyl peroxy radical at several photon energies to place the relative photoionization spectrum of the radical on an absolute scale. Unlike most other peroxy radicals, the methyl peroxy radical features a bound cation, enabling its detection at the parent mass.²⁵ The relative spectrum we measured matches the previously-reported spectrum. Figure 2(a) shows the absolute photoionization spectrum of the methyl peroxy radical. Table 3 lists the cross sections from 8.7–11.5 eV. The random error in the methyl peroxy radical cross section measurement was 6%. Added in quadrature to the 20% error propagated from the original propene cross section measurement (against which all hydrocarbon cross sections were measured in this thesis) resulted in an overall uncertainty for the methyl peroxy radical cross section of 21%.

3.2 Acetyl peroxy yield from $\text{CH}_3\text{CO} + \text{O}_2$

In our experiment, acetyl peroxy radicals were formed from reaction of acetyl radicals with O_2 . Given the literature disagreements regarding the yield of acetyl peroxy radicals (reaction (2a)), compared to that of the bimolecular reaction products (reaction (2b)), we performed a measurement of the branching fraction of acetyl peroxy radicals from this reaction under the experimental conditions used here. To measure this yield, we produced acetyl peroxy radicals

from the chlorine-initiated oxidation of acetaldehyde in the presence of O₂, without added HO₂. Under these conditions, CH₃C(O)O₂ primarily reacted with itself to form acetoxy radicals (CH₃C(O)O) and O₂ (reaction (3)).



The acetoxy radicals decomposed to form methyl radicals and CO₂. We detected the methyl radicals as either methyl peroxy or chloromethane.

To measure the yield of acetyl peroxy radicals from reaction (2), we quantified the acetyl peroxy reaction products, CH₃O₂ and CH₃Cl. Figure 3 shows the oxygen dependence of the CH₃O₂ kinetics traces. The open circles are the data collected at five different oxygen concentrations. The solid black lines are the corresponding simulated kinetics. As the number density of oxygen increases, the peak concentration of CH₃O₂ increases, because O₂ competes with Cl₂ for reaction with the CH₃ radicals. We fit each kinetics trace, varying the yield of reaction (2a) to achieve the best fit of the simulated CH₃O₂ kinetics to the data. The left ordinate Figure 4 shows the result of each fit, demonstrating the fitted yield of acetyl peroxy radicals from reaction (2), α_{2a} (defined in equation (I)), for each oxygen concentration.

$$\alpha_{2a} = \frac{k_{2a}}{k_{2a} + k_{2b}} \quad (I)$$

The error bars for each fitted value for α_{2a} are on the order of 40%. This comes from the 5% random error in our CH₃O₂ cross section measurement—the yield of reaction (2a) is very sensitive to the methyl peroxy radical concentration, leading to rather large uncertainty in this measurement. The weighted average of all measurements led to an acetyl peroxy radical yield of $\alpha_{2a} = 0.49 \pm 0.17$ (2σ) at 8 Torr in Helium. These simulations assumed that there is only one other product channel for reaction (2), which produces OH radicals and an inert co-product.

We separately measured the yield of OH radicals from reaction (2), α_{2b} , by fitting the acetaldehyde depletion in each experiment. If the yield of OH radicals is high, a large amount of radical recycling will occur leading to additional removal of acetaldehyde molecules after the initial photolysis laser pulse. By varying α_{2b} (assuming that the balance of reaction (2) resulted in the formation of a peroxy radical), we fit the acetaldehyde depletion with the kinetics model for a range of oxygen concentrations. The result of these fits are shown in Figure 4; the weighted average is $\alpha_{2b} = 0.38 \pm 0.01$ (2σ) at 8 Torr in He. This measurement does not depend on any cross section measurements, so the statistical uncertainty in this measurement is smaller than that for reaction (2a).

The OH yield from reaction (2) is observed to be dependent on the percentage oxygen in the flow reactor. As the oxygen number density increases, the OH yield decreases. We do not observe an oxygen dependence in the formation of CH_3O_2 radicals. At low oxygen concentrations, where the buffer gas is primarily helium, the yields of reactions (2a) and (2b), fit separately, add up to unity. However, at conditions where O_2 makes up significant fractions of the molecules in the flow reactor, the yields add up to significantly less than 1.

3.3 Co-product of OH

The theoretical calculations for reaction of acetyl radicals with O_2 all determine that the co-product of OH, formed from reaction (b) is α -acetolactone. However, this product is formed with so much internal energy, that it is expected to decompose to formaldehyde and CO and has never been detected. Experiments by Devolder et al. searched for formaldehyde to test this mechanism, but did not see any evidence for prompt H_2CO formation.²⁶ In the present work, we are very sensitive to H_2CO detection and can quantify its formation using our recently-reported H_2CO photoionization cross section.²⁷ Figure 5 shows the time-dependent formaldehyde concentration in the $\text{CH}_3\text{C}(\text{O})\text{O}_2$ self-reaction experiments described in the previous section, at two oxygen concentrations, 16% O_2 and 30% O_2 . If the lactone does not decompose promptly to form H_2CO , the simulated H_2CO (dotted lines) grows in slowly, formed primarily as a product from self-reaction of the CH_3O_2 radicals that come from the acetoxy radical decomposition (described above). If we assume that α -acetolactone

immediately decomposes into formaldehyde and carbon monoxide, H₂CO forms promptly, as shown in the solid lines in Figure 5. However, the models predict significantly more H₂CO formation; these traces have been multiplied by a factor of 0.3, for visualization purposes. Prompt H₂CO clearly forms in our experiments, but cannot fully be described by lactone decomposition.

3.4 Ketene product channel

The potential energy surface shown in Figure 1 indicates a slightly exothermic product channel leading to formation of HO₂ + ketene (CH₂CO) (reaction (4)).



Experimental evidence for this channel does not exist and we do not expect it to be thermodynamically favorable. Nevertheless, the incredible detection sensitivity of the MPIMS instrument, along with the fortuitously-large ketene photoionization cross section (at 10.5 eV its cross section is 25 Mb!),²⁸ enables us to detect even a small concentration of the product and quantify its formation rate. Ketene formation is observed to be oxygen-dependent, as seen in Figure 6; we formed about 10¹¹ cm⁻³ ketene during these experiments, corresponding to a bimolecular rate constant, k_{2c} , of 2.5×10⁻¹⁴ cm³ s⁻¹ at 30% O₂. Interestingly, the measured ketene concentration decreases with increasing O₂ concentration. Compared to the other product channels (stabilization to form CH₃C(O)O₂ or bimolecular reaction to form OH), this is a very insignificant channel, but quantifying its contribution provides useful information in verifying the potential energy surface.

3.5 Reaction of CH₃C(O)O₂ with HO₂

The rate coefficients for two of the product channels for reaction of acetyl peroxy radicals with HO₂ were measured at a range of [HO₂]/[CH₃C(O)O₂] ratios by varying the initial acetaldehyde and methanol concentrations. The branching fraction for product channels (1b) and (1c) were measured by directly measuring the products or secondary products of these reactions: acetic acid (CH₃C(O)OH) from channel (1b) and methyl peroxy radical (CH₃O₂)—formed after reaction of CH₃ radicals with O₂—to quantify channel (1c). Initial

radical concentrations were determined quantitatively by fitting the depletions of the precursors (Cl_2 , CH_3CHO , and CH_3OH), given the known partial pressures of reactants present in the flow reactor. Typically, about 1% of the Cl_2 molecules were photodissociated, forming 10^{13} Cl atoms. Using the absolute cross sections for the two investigated products, $\text{CH}_3\text{C}(\text{O})\text{OH}$ and CH_3O_2 , along with the quantitative measurement of the initial radical concentrations, we measured the rate coefficients for reactions (1b) and (1c).

Figure 7 shows an example of the data obtained in this experiment. This data was taken at a $[\text{HO}_2]/[\text{CH}_3\text{C}(\text{O})\text{O}_2]$ initial ratio equal to 10, as determined from the initial acetaldehyde and methanol concentrations. Panel (a) shows the appearance of acetic acid, $\text{CH}_3\text{C}(\text{O})\text{OH}$, measured at m/z 60. The acetic acid trace levels off as all of the acetyl peroxy radicals are consumed (under these conditions, $\text{CH}_3\text{C}(\text{O})\text{O}_2$ has a lifetime of 5 ms) and plateaus around $1.5 \times 10^{11} \text{ cm}^{-3}$. This data was fit with the simulated model, varying the rate coefficient k_{1b} to find the best fit to the data (the result was $(2.4 \pm 0.4) \times 10^{-12} \text{ cm}^3 \text{ s}^{-1}$). Panel (b) shows the time-dependent trace for methyl peroxy radicals, observed at their parent mass of m/z 47. The formed methyl peroxy radicals reach a peak concentration of $4 \times 10^{11} \text{ cm}^{-3}$ at around 5 ms and then decay as they are no longer produced from acetyl peroxy radicals, and the $\text{CH}_3\text{O}_2 + \text{HO}_2$ reaction begins to consume the radicals. This data was similarly fit with a model, solving for the k_{1c} rate coefficient (the best fit for this data was $(1.2 \pm 0.2) \times 10^{-11} \text{ cm}^3 \text{ s}^{-1}$).

Panels (c) and (d) of Figure 7 show the data and models for CH_3Cl and H_2CO , respectively. These simulations were from the fitted experimental models that were constrained by the products measured in panels (a) and (b). Panel (c) demonstrates a disagreement between CH_3O_2 and CH_3Cl – both species come from reactions of CH_3 radicals, which are formed as a product from acetyl peroxy radical reactions. The disagreement between data and model for CH_3Cl suggests that either our absolute cross sections for CH_3O_2 and/or CH_3Cl are wrong, or the rate constants for reaction of CH_3 with O_2 and/or Cl_2 are wrong. Panel (d) shows the formation of formaldehyde – which comes primarily from the self-reaction of HO_2 radicals. The excellent agreement between the data and model immediately after photolysis

lends support to our quantification of the initial number of radicals formed from photodissociation of Cl₂.

Figure 8 shows the results of the fits for a range (from 1–10) of initial [HO₂]/[CH₃C(O)O₂] values. Figure 8(a) shows the rate coefficient for formation of product channel (1b), formation of acetic acid and ozone. The fitted rates were found by varying the rate coefficient, k_{1b} , and fitting the modeled CH₃C(O)OH kinetics trace to the observed CH₃C(O)OH kinetics at m/z 60. At the same time, the rate coefficient for the radical channel (1c) was varied and the simulated CH₃O₂ kinetics trace was fit to the CH₃O₂ observed kinetics at m/z 47 to find the fitted value for the radical channel k_{1c} (Figure 8(b)). Both rate coefficients, k_{1b} and k_{1c} , were iteratively varied to find the best fit to the experimental kinetics traces for CH₃C(O)OH and CH₃O₂. We were unable to detect the peracetic acid (CH₃C(O)OOH) product of channel (1a). In fitting, we simply assumed that the rate coefficient for reaction (1a) was the remainder of the total rate for reaction (1), $k_{1a} = k_1 - k_{1b} - k_{1c}$ using the overall rate $k_1 = 1.4 \times 10^{-11} \text{ cm}^3 \text{ s}^{-1}$. However, k_{1a} had little impact on the overall fits described here. The weighted averages for the two rate coefficients from all experiments shown in Figure 8 are as follows: $k_{1b} = (2.0 \pm 0.3) \times 10^{-12} \text{ cm}^3 \text{ s}^{-1}$ and $k_{1c} = (1.0 \pm 0.2) \times 10^{-11} \text{ cm}^3 \text{ s}^{-1}$. The reported error bars are the 1 σ error limits. For the acetic acid measurement, the primary source of uncertainty was the 40% uncertainty in our measured acetyl + O₂ branching fraction, propagated into the kinetics model for simulating the kinetics model. The larger uncertainty in the radical channel comes from both the uncertainty in the acetyl + O₂ branching fraction, as well as the 5% random error in the CH₃O₂ cross section.

4 Discussion

In order to measure the yield of the radical channel from reactions of acetyl peroxy radicals with HO₂, we had to measure several things first, not least among them was the absolute cross section of the methyl peroxy radical. The random error in the methyl peroxy radical cross section measurements was much larger than that usually obtained from measurements of pure samples of closed-shell molecules. Since the measured concentration of methyl peroxy radicals was the key factor in quantifying many things in this experiment, the large

random error in the methyl peroxy radical cross section led to significant uncertainty in the branching fractions reported in this chapter.

If the total rate constant for reaction (1) is $1.4 \times 10^{-11} \text{ cm}^3 \text{ s}^{-1}$, then the branching fractions for the two channels are $(14 \pm 2)\%$ and $(74 \pm 11)\%$ for channels (1b) and (1c), respectively. The measured yield for the acetic acid + ozone channel (1b) is in good agreement with most of the past measurements. The yield of the radical channel is somewhat higher than past reports, but is generally within the generous mutual 2σ error limits of the most recent values.

5 Conclusions

In this chapter, we reported the absolute photoionization spectrum of the methyl peroxy radical. Using this absolute spectrum to quantify the amount of methyl peroxy radicals formed in our experiment, we measured a yield of acetyl peroxy radicals from reaction of acetyl radicals with O_2 of 0.49 ± 0.17 (1σ) %. Then, using the CH_3O_2 cross section and the measured absolute spectra of closed-shell molecules like $\text{CH}_3\text{C}(\text{O})\text{OH}$, CH_3Cl , and H_2CO , we investigated the rate coefficients of two of the three product channels of the cross reaction between acetyl peroxy and HO_2 radicals, finding a rate coefficient for the acetic acid channel, $k_{1b} = (2.0 \pm 0.3) \times 10^{-12} \text{ cm}^3 \text{ s}^{-1}$, and for the radical channel, $k_{1c} = (1.0 \pm 0.2) \times 10^{-11} \text{ cm}^3 \text{ s}^{-1}$. Given a total k_1 rate constant of $1.4 \times 10^{-11} \text{ cm}^3 \text{ s}^{-1}$, these two channels have the following yields: $(14 \pm 2)\%$ and $(74 \pm 11)\%$, for the acetic acid and radical channels, respectively.

6 References

1. Finlayson-Pitts, B. J.; Pitts, J., James N., *Chemistry of the Upper and Lower Atmosphere*. Academic Press: San Diego, California, 2000.
2. Atkinson, R.; Arey, J., Atmospheric Degradation of Volatile Organic Compounds. *Chem. Rev.* **2003**, *103*, 4605-4638.
3. Lelieveld, J.; Butler, T. M.; Crowley, J. N.; Dillon, T. J.; Fischer, H.; Ganzeveld, L.; Harder, H.; Lawrence, M. G.; Martinez, M.; Taraborrelli, D., et al., Atmospheric Oxidation Capacity Sustained by a Tropical Forest. *Nature* **2008**, *452*, 737-740.
4. Taraborrelli, D.; Lawrence, M. G.; Crowley, J. N.; Dillon, T. J.; Gromov, S.; Grosz, C. B. M.; Vereecken, L.; Lelieveld, J., Hydroxyl Radical Buffered by Isoprene Oxidation over Tropical Forests. *Nat. Geosci.* **2012**, *5*, 190-193.

5. Hasson, A. S.; Kuwata, K. T.; Arroyo, M. C.; Petersen, E. B., Theoretical Studies of the Reaction of Hydroperoxy Radicals (HO_2) with Ethyl Peroxy ($\text{CH}_3\text{CH}_2\text{O}_2$), Acetyl Peroxy ($\text{CH}_3\text{C}(\text{O})\text{O}_2$), and Acetonyl Peroxy ($\text{CH}_3\text{C}(\text{O})\text{CH}_2\text{O}_2$) Radicals. *J. Photochem. Photobiol. A* **2005**, *176*, 218-230.
6. Niki, H.; Maker, P. D.; Savage, C. M.; Breitenbach, L. P., FTIR Study of the Kinetics and Mechanism for Chlorine-Atom-Initiated Reactions of Acetaldehyde. *J. Phys. Chem.* **1985**, *89*, 588-591.
7. Moortgat, G. K.; Veyret, B.; Lesclaux, R., Kinetics of the Reaction of HO_2 with $\text{CH}_3\text{C}(\text{O})\text{O}_2$ in the Temperature Range 253–368 K. *Chem. Phys. Lett.* **1989**, *160*, 443-447.
8. Crawford, M. A.; Wallington, T. J.; Szente, J. J.; Maricq, M. M.; Francisco, J. S., Kinetics and Mechanism of the Acetylperoxy + HO_2 Reaction. *J. Phys. Chem. A* **1999**, *103*, 365-378.
9. Hasson, A. S.; Tyndall, G. S.; Orlando, J. J., A Product Yield Study of the Reaction of HO_2 Radicals with Ethyl Peroxy ($\text{C}_2\text{H}_5\text{O}_2$), Acetyl Peroxy ($\text{CH}_3\text{C}(\text{O})\text{O}_2$), and Acetonyl Peroxy ($\text{CH}_3\text{C}(\text{O})\text{CH}_2\text{O}_2$) Radicals. *J. Phys. Chem. A* **2004**, *108*, 5979-5989.
10. Le Crâne, J.-P.; Rayez, M.-T.; Rayez, J.-C.; Villenave, E., A Reinvestigation of the Kinetics and the Mechanism of the $\text{CH}_3\text{C}(\text{O})\text{O}_2 + \text{HO}_2$ Reaction using Both Experimental and Theoretical Approaches. *Phys. Chem. Chem. Phys.* **2006**, *8*, 2163-2171.
11. Jenkin, M. E.; Hurley, M. D.; Wallington, T. J., Investigation of the Radical Product Channel of the $\text{CH}_3\text{C}(\text{O})\text{O}_2 + \text{HO}_2$ Reaction in the Gas Phase. *Phys. Chem. Chem. Phys.* **2007**, *9*, 3149-3162.
12. Dillon, T. J.; Crowley, J. N., Direct Detection of OH Formation in the Reactions of HO_2 with $\text{CH}_3\text{C}(\text{O})\text{O}_2$ and Other Substituted Peroxy Radicals. *Atmos. Chem. Phys.* **2008**, *8*, 4877-4889.
13. Groß, C. B. M.; Dillon, T. J.; Schuster, G.; Lelieveld, J.; Crowley, J. N., Direct Kinetic Study of OH and O_3 Formation in the Reaction of $\text{CH}_3\text{C}(\text{O})\text{O}_2$ with HO_2 . *J. Phys. Chem. A* **2014**, *118*, 974-985.
14. Winiberg, F. A. F.; Dillon, T. J.; Orr, S. C.; Groß, C. B. M.; Bejan, I.; Brumby, C. A.; Evans, M. J.; Smith, S. C.; Heard, D. E.; Seakins, P. W., Direct Measurements of OH and Other Product Yields from the $\text{HO}_2 + \text{CH}_3\text{C}(\text{O})\text{O}_2$ reaction. *Atmos. Chem. Phys.* **2016**, *16*, 4023-4042.
15. Groß, C. B. M.; Dillon, T. J.; Crowley, J. N., Pressure Dependent OH Yields in the Reactions of CH_3CO and HOCH_2CO with O_2 . *Phys. Chem. Chem. Phys.* **2014**, *16*, 10990-10998.
16. Kovács, G.; Zádor, J.; Farkas, E.; Nádasdi, R.; Szilágyi, I.; Dóbbé, S.; Bérces, T.; Márta, F.; Lendvai, G., Kinetics and Mechanism of the Reactions of CH_3CO and $\text{CH}_3\text{C}(\text{O})\text{CH}_2$ Radicals with O_2 . Low-Pressure Discharge Flow Experiments and Quantum Chemical Computations. *Phys. Chem. Chem. Phys.* **2007**, *9*, 4142-4154.
17. Carr, S. A.; Baeza-Romero, M. T.; Blitz, M. A.; Pilling, M. J.; Heard, D. E.; Seakins, P. W., OH Yields from the $\text{CH}_3\text{CO} + \text{O}_2$ Reaction using an Internal Standard. *Chem. Phys. Lett.* **2007**, *445*, 108-112.
18. Carr, S. A.; Glowacki, D. R.; Liang, C.-H.; Baeza-Romero, M. T.; Blitz, M. A.; Pilling, M. J.; Seakins, P. W., Experimental and Modeling Studies of the Pressure and Temperature Dependences

- of the Kinetics and the OH Yields in the Acetyl + O₂ Reaction. *J. Phys. Chem. A* **2011**, *115*, 1069-1085.
19. Tyndall, G. S.; Orlando, J. J.; Wallington, T. J.; Hurley, M. D., Pressure Dependence of the Rate Coefficients and Product Yields for the Reaction of CH₃CO Radicals with O₂. *Int. J. Chem. Kin.* **1997**, *29*, 655-663.
20. Blitz, M. A.; Heard, D. E.; Pilling, M. J., OH Formation from CH₃CO+O₂: A Convenient Experimental Marker for the Acetyl Radical. *Chem. Phys. Lett.* **2002**, *365*, 374-379.
21. Maranzana, A.; Barker, J. R.; Tonachini, G., Master Equation Simulations of Competing Unimolecular and Bimolecular Reactions: Application to OH Production in the Reaction of Acetyl Radical with O₂. *Phys. Chem. Chem. Phys.* **2007**, *9*, 4129-4141.
22. Osborn, D. L.; Zou, P.; Johnsen, H.; Hayden, C. C.; Taatjes, C. A.; Knyazev, V. D.; North, S. W.; Peterka, D. S.; Ahmed, M.; Leone, S. R., The Multiplexed Chemical Kinetic Photoionization Mass Spectrometer: A New Approach to Isomer-resolved Chemical Kinetics. *Rev. Sci. Instrum.* **2008**, *79*, 104103.
23. Taatjes, C. A.; Hansen, N.; Osborn, D. L.; Kohse-Hoinghaus, K.; Cool, T. A.; Westmoreland, P. R., "Imaging" Combustion Chemistry via Multiplexed Synchrotron-photoionization Mass Spectrometry. *Phys. Chem. Chem. Phys.* **2008**, *10*, 20-34.
24. Ianni, J. C. *Kintecus*, Windows Version 2.80; <http://www.kintecus.com>, 2002.
25. Meloni, G.; Zou, P.; Klippenstein, S. J.; Ahmed, M.; Leone, S. R.; Taatjes, C. A.; Osborn, D. L., Energy-Resolved Photoionization of Alkylperoxy Radicals and the Stability of Their Cations. *J. Am. Chem. Soc.* **2006**, *128*, 13559-13567.
26. Devolder, P.; Dusanter, S.; Lemoine, B.; Fittschen, C., About the Co-Product of the OH Radical in the Reaction of Acetyl with O₂ below Atmospheric Pressure. *Chem. Phys. Lett.* **2006**, *417*, 154-158.
27. Dodson, L. G.; Shen, L.; Savee, J. D.; Eddingsaas, N. C.; Welz, O.; Taatjes, C. A.; Osborn, D. L.; Sander, S. P.; Okumura, M., VUV Photoionization Cross Sections of HO₂, H₂O₂, and H₂CO. *J. Phys. Chem. A* **2015**, *119*, 1279-1291.
28. Yang, B.; Wang, J.; Cool, T. A.; Hansen, N.; Skeen, S.; Osborn, D. L., Absolute Photoionization Cross-Sections of Some Combustion Intermediates. *Int. J. Mass Spectrom.* **2012**, *309*, 118-128.
29. Sander, S. P.; Abbatt, J.; Barker, J. R.; Burkholder, J. B.; Friedl, R. R.; Golden, D. M.; Huie, R. E.; Kolb, C. E.; Kurylo, M. J.; Moortgat, G. K., et al., Chemical Kinetics and Photochemical Data for Use in Atmospheric Studies, Evaluation Number 17. *JPL Publication 10-6* **2011**.

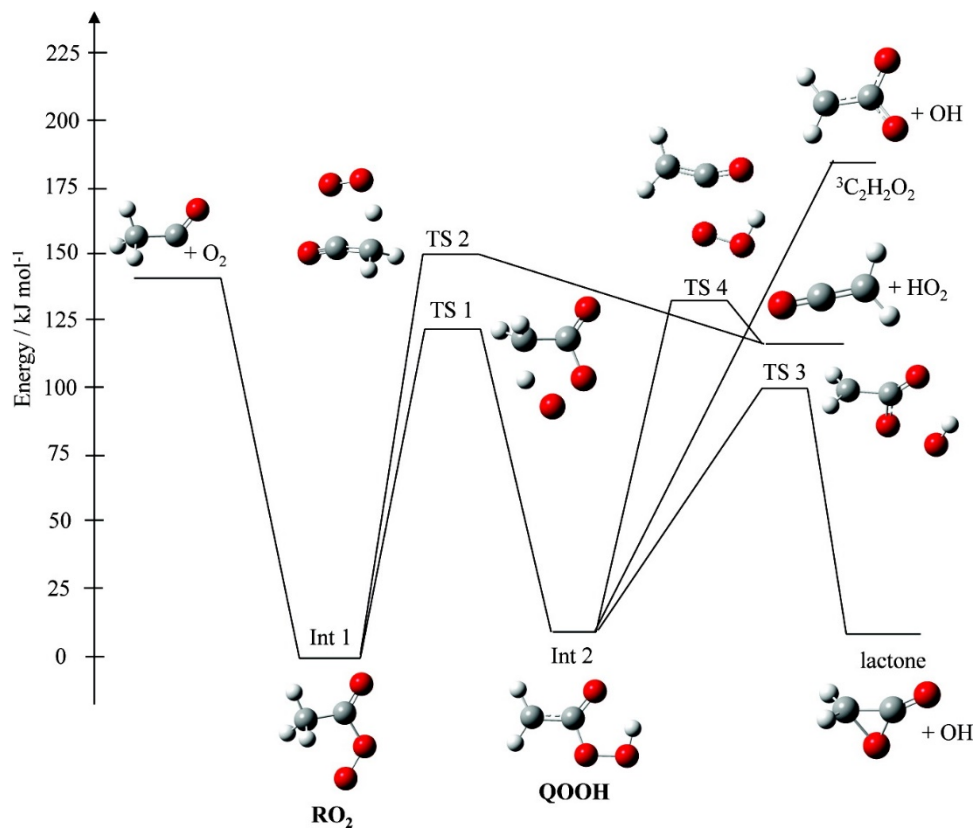


Figure 1. Potential energy surface of the reaction of acetyl radicals with O_2 , taken from Carr et al. (2011).¹⁸

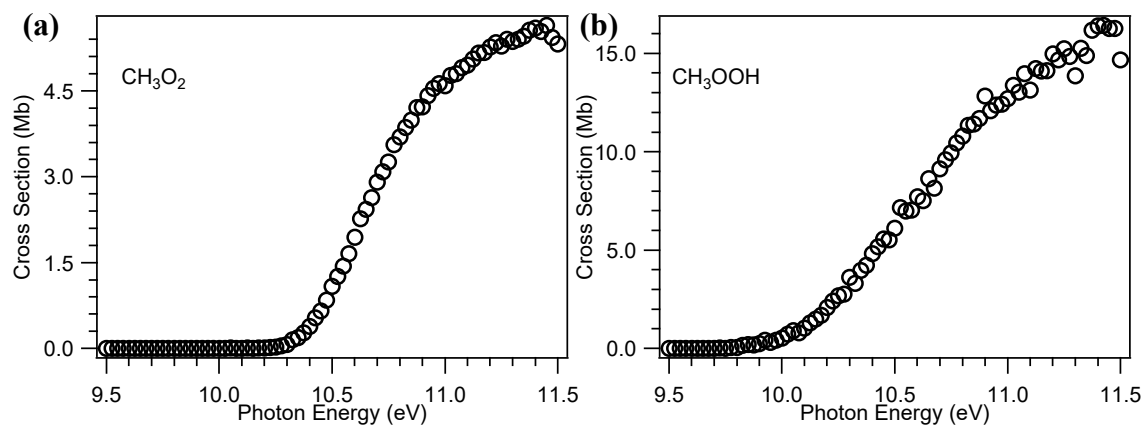


Figure 2. Absolute photoionization spectra of the methyl peroxy radical (CH_3O_2 , panel (a)) and methyl hydroperoxide (CH_3OOH , panel (b)).

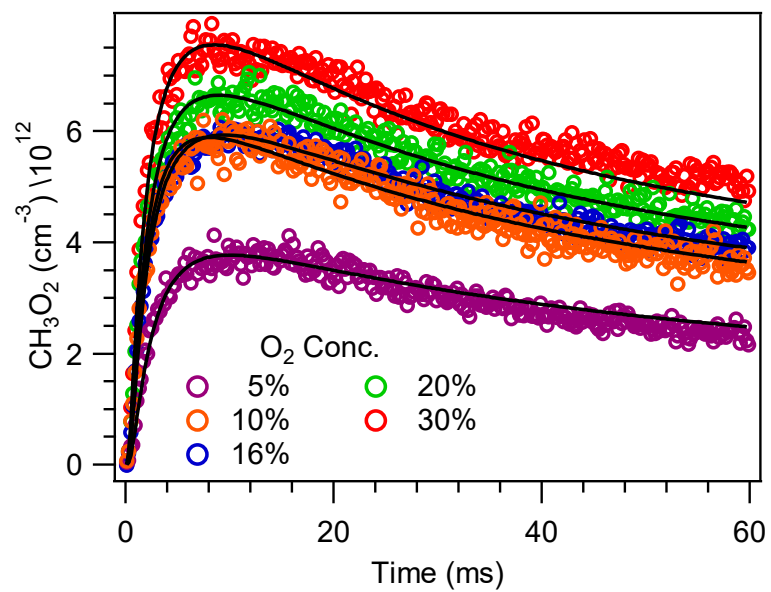


Figure 3. Oxygen-dependent CH_3O_2 formation from the acetyl peroxy radical self-reaction.

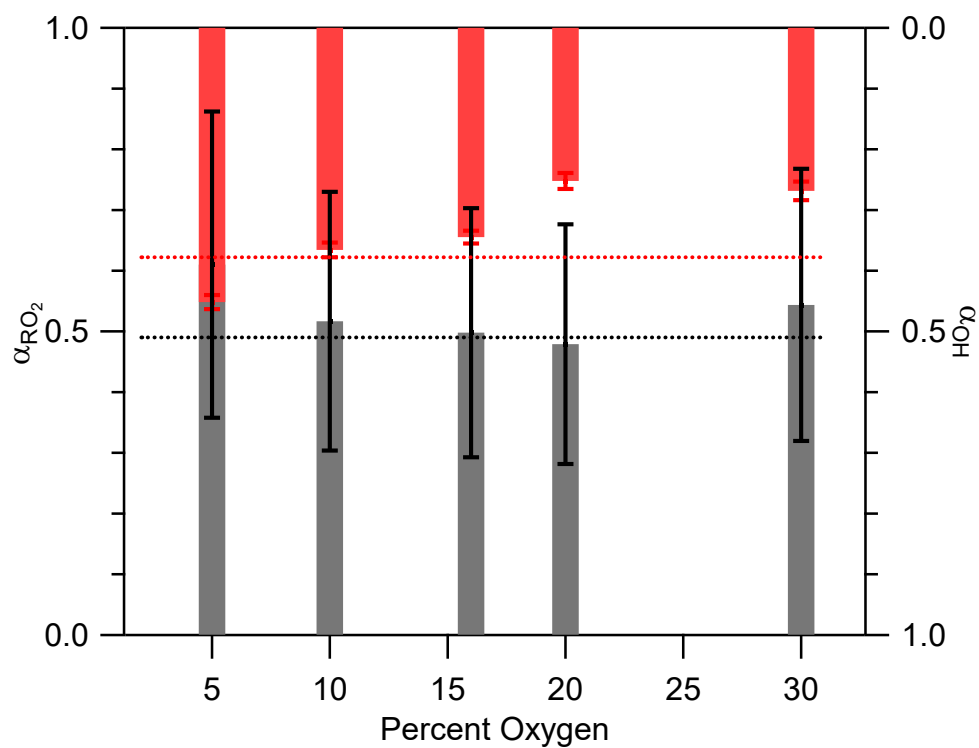


Figure 4. Fitted values for the yield of acetyl peroxy radicals (left ordinate, gray bars) and OH radicals (right ordinate, red bars) from reactions of $CH_3C(O)$ with O_2 as a function of percent oxygen. The dotted lines indicate the value resulting from the weighted average for each reaction, drawn at $\alpha_{2a} = 0.49$ and $\alpha_{2b} = 0.38$.

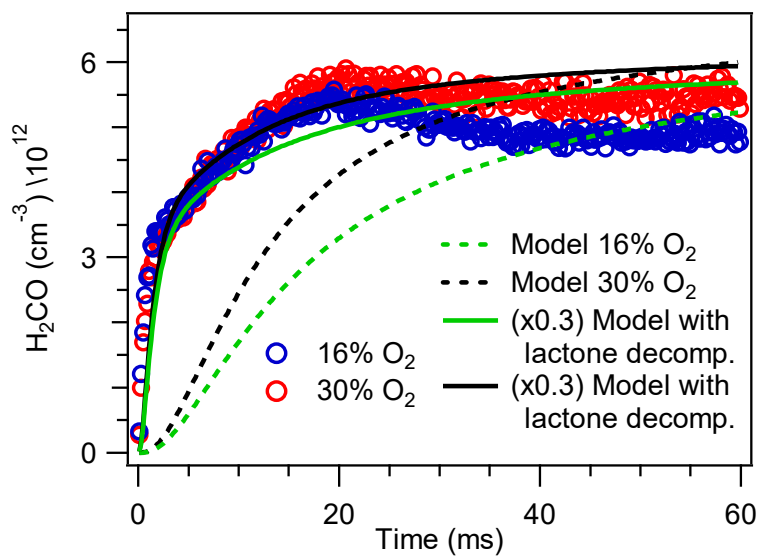


Figure 5. Time-dependent traces of formaldehyde formed during $\text{CH}_3\text{C}(\text{O})\text{O}_2$ self-reaction experiment at two different oxygen conditions. The dashed lines show the simulated H_2CO kinetics without added formaldehyde mechanisms. The solid lines show the simulated H_2CO kinetics, assuming that lactone immediately decomposes to form $\text{H}_2\text{CO} + \text{CO}$. The solid lines have been multiplied by 0.3 for comparison.

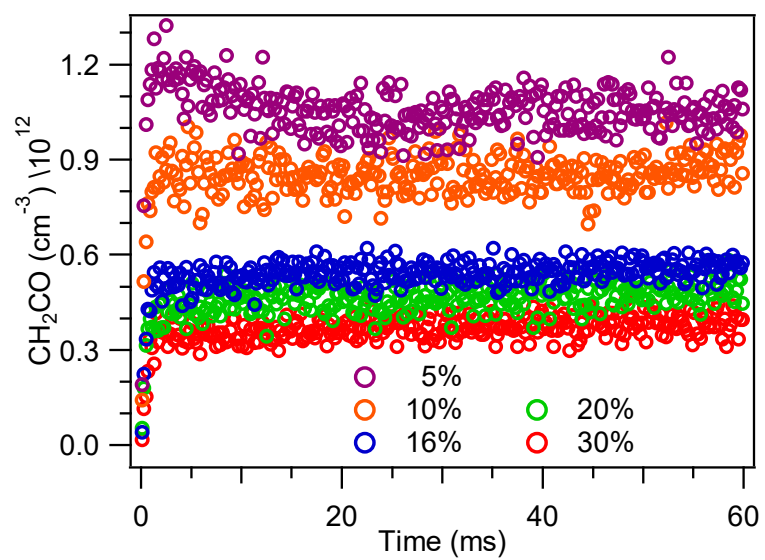


Figure 6. Oxygen-dependent ketene (CH_2CO) formation from $\text{CH}_3\text{C}(\text{O})\text{O}_2$ self-reaction experiment.

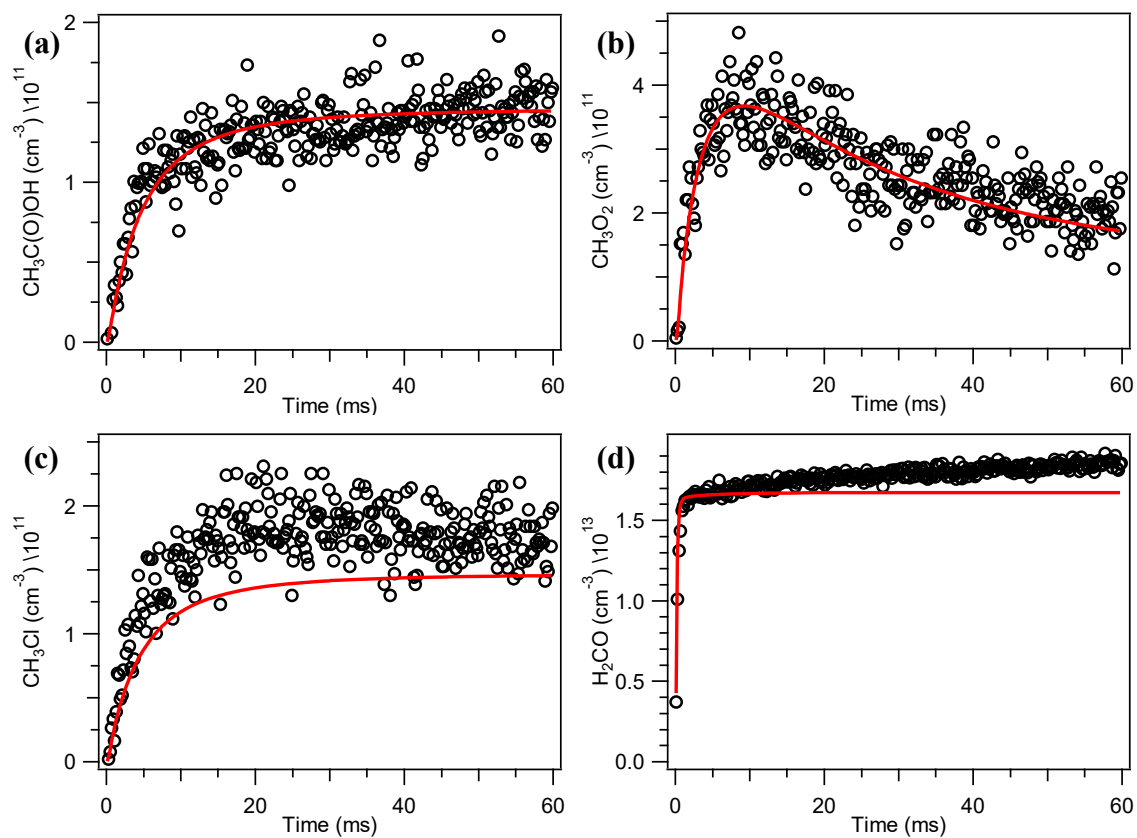


Figure 7. Experimental and simulated kinetics for the $\text{CH}_3\text{C}(\text{O})\text{O}_2 + \text{HO}_2$ cross-reaction. Taken from data where $[\text{HO}_2]/[\text{CH}_3\text{C}(\text{O})\text{O}_2] = 10$. Panel (a) shows the acetic acid data at $m/\bar{\nu} \approx 60$ and the simulated $\text{CH}_3\text{C}(\text{O})\text{OH}$ model, fit to the data with a rate $k_{1b} = (2.4 \pm 0.4) \times 10^{-12} \text{ cm}^3 \text{ s}^{-1}$. Panel (b) shows the methyl peroxy radical data at $m/\bar{\nu} \approx 47$ and the simulated model, fit to the data with a rate coefficient $k_{1c} = (1.2 \pm 0.2) \times 10^{-11} \text{ cm}^3 \text{ s}^{-1}$. Panels (c) and (d) show other reaction products: CH_3Cl and H_2CO .

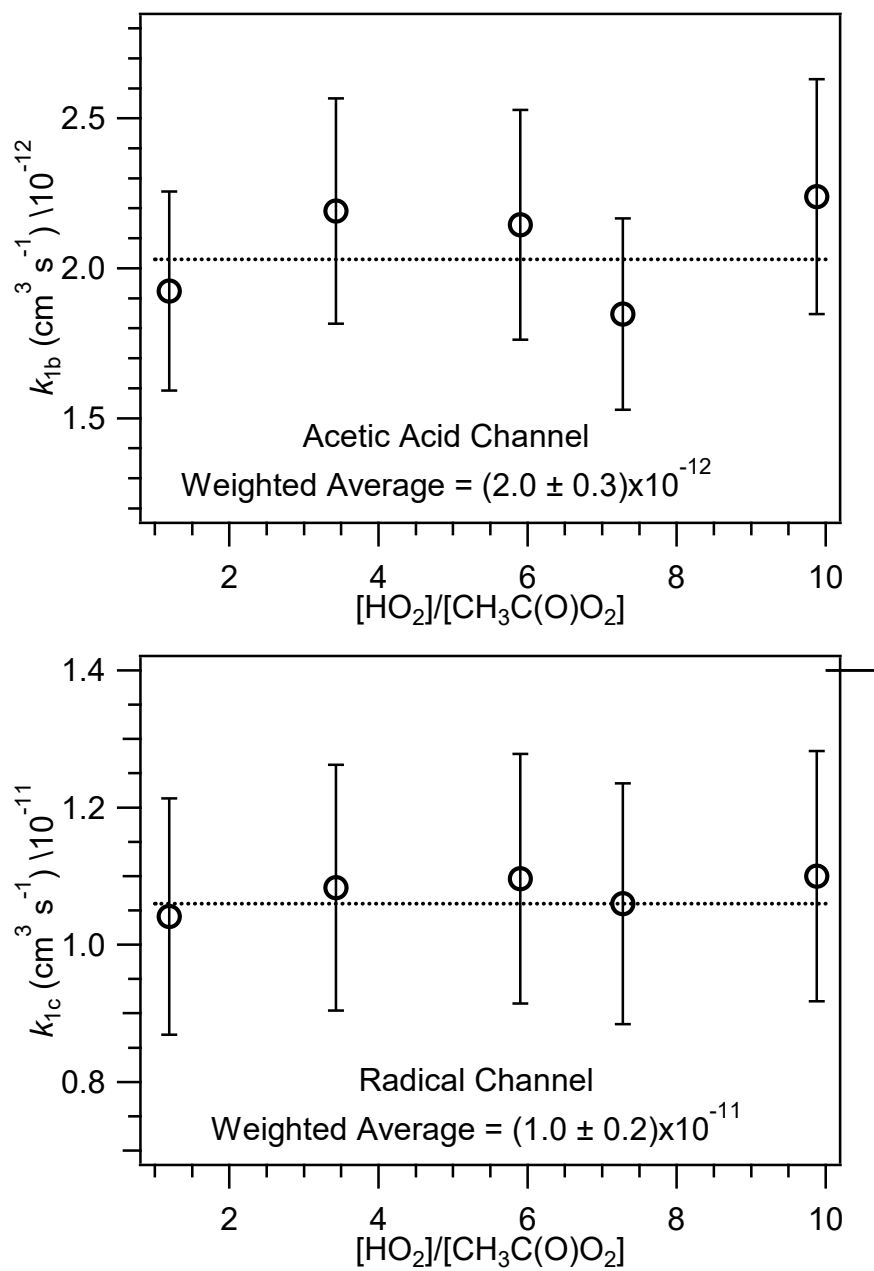


Figure 8. Fitted rate coefficients for the acetic acid and radical channels.

Table 1. Literature results for the branching fractions of the three product channels of reaction of $\text{CH}_3\text{C}(\text{O})\text{O}_2$ with HO_2 .

	Hasson 2004	Hasson 2005	Le Crâne 2006	Jenkin 2007	Dillon 2008	Tara- borrelli 2012	Groß 2014	Winiberg 2016
1a	40	36	---	38	---	12	23	37
1b	20	19	20	12	---	18	16	12
1c	40	46	< 10	43	50	70	61	51

Table 2. Kinetics model, used to simulate the modeled kinetics for acetyl peroxy radical reactions. This list is representative of the most important reactions, but does not include all reactions used in the full simulation. Most rate coefficients were taken from the JPL evaluation,²⁹ although some were taken from various literature sources cited throughout this chapter.

	rate (cm ³ s ⁻¹)
<i>Acetyl peroxy radical reactions</i>	
CH ₃ C(O)O ₂ +HO ₂ →CH ₃ C(O)OOH+O ₂	<i>k</i> _{1a}
CH ₃ C(O)O ₂ +HO ₂ →CH ₃ C(O)OH+O ₃	<i>k</i> _{1b}
CH ₃ C(O)O ₂ +HO ₂ →CH ₃ +CO ₂ +OH+O ₂	<i>k</i> _{1c}
CH ₃ CO+O ₂ →CH ₃ C(O)O ₂	<i>k</i> _{2a}
CH ₃ CO+O ₂ →OH+CH ₂ C(O)O	<i>k</i> _{2b}
CH ₃ CO+O ₂ →HO ₂ +CH ₂ CO	<i>k</i> _{2c}
2CH ₃ C(O)O ₂ →2CH ₃ +2CO ₂ +O ₂	1.5×10 ⁻¹¹
CH ₃ O ₂ +CH ₃ C(O)O ₂ →CH ₃ +CO ₂ +CH ₃ O+O ₂	9.64×10 ⁻¹²
CH ₃ O ₂ +CH ₃ C(O)O ₂ →CH ₃ C(O)OH+H ₂ CO+O ₂	1.07×10 ⁻¹²
CH ₃ CO+O ₃ →CH ₃ +CO ₂ +O ₂	4.4×10 ⁻¹¹
<i>Methyl peroxy radical reactions</i>	
CH ₃ +O ₂ →CH ₃ O ₂ (at 8 Torr)	7.65×10 ⁻¹⁴
CH ₃ O ₂ +CH ₃ O ₂ →CH ₃ O+CH ₃ O+O ₂	1.31×10 ⁻¹³
CH ₃ O ₂ +CH ₃ O ₂ →CH ₃ OH+H ₂ CO+O ₂	2.21×10 ⁻¹³
CH ₃ O+O ₂ →H ₂ CO+HO ₂	1.9×10 ⁻¹⁵
CH ₃ O+CH ₃ O→H ₂ CO+CH ₃ OH	1.3×10 ⁻¹¹
CH ₃ O+HO ₂ →H ₂ CO+H ₂ O ₂	5.08×10 ⁻¹²
CHO ₂ +HO ₂ →CH ₃ OOH+O ₂	5.08×10 ⁻¹²
CH ₃ O+CH ₃ CHO→CH ₃ CO+CH ₃ OH	7.4×10 ⁻¹⁴
<i>HO₂ reactions</i>	
HO ₂ +HO ₂ →H ₂ O ₂ +O ₂	1.41×10 ⁻¹²
HO ₂ +Cl→HCl+O ₂	3.5×10 ⁻¹¹
HO ₂ +Cl→ClO+OH	1×10 ⁻¹¹
HO ₂ +ClO→HOCl+O ₂	6.9×10 ⁻¹²
HO ₂ +H ₂ CO→HOCH ₂ O ₂	7.9×10 ⁻¹⁴
HOCH ₂ O ₂ →HO ₂ +H ₂ CO	150
<i>OH reactions</i>	
OH+OH→H ₂ O ₂	1.63×10 ⁻¹³
OH+OH→H ₂ O+O	1.8×10 ⁻¹²
OH+HO ₂ →H ₂ O+O ₂	1.1×10 ⁻¹⁰
OH+O ₃ →HO ₂ +O ₂	7.3×10 ⁻¹⁴
OH+CH ₃ OH→CH ₂ OH+H ₂ O	7.74×10 ⁻¹³

$\text{OH} + \text{CH}_3\text{OH} \rightarrow \text{CH}_3\text{O} + \text{H}_2\text{O}$	1.37×10^{-13}
$\text{OH} + \text{CH}_3\text{CHO} \rightarrow \text{H}_2\text{O} + \text{CH}_3\text{CO}$	1.2×10^{-11}
$\text{OH} + \text{CH}_3\text{CHO} \rightarrow \text{H}_2\text{O} + \text{CH}_3 + \text{CO}$	3×10^{-12}
$\text{OH} + \text{H}_2\text{CO} \rightarrow \text{H}_2\text{O} + \text{HCO}$	8.5×10^{-12}
$\text{OH} + \text{CH}_3\text{Cl} \rightarrow \text{H}_2\text{O} + \text{CH}_2\text{Cl}$	3.6×10^{-14}
$\text{OH} + \text{CH}_3\text{OOH} \rightarrow \text{H}_2\text{O} + \text{CH}_3\text{O}_2$	5.18×10^{-12}
$\text{OH} + \text{CH}_3\text{OOH} \rightarrow \text{H}_2\text{O} + \text{CH}_2\text{OOH}$	2.22×10^{-12}
<i>Cl reactions</i>	
$\text{Cl}_2 + \text{CH}_3 \rightarrow \text{CH}_3\text{Cl} + \text{Cl}$	1.59×10^{-12}
$\text{Cl} + \text{CH}_3\text{O}_2 \rightarrow \text{CH}_3\text{O} + \text{ClO}$	8×10^{-11}
$\text{Cl} + \text{CH}_3\text{O}_2 \rightarrow \text{CH}_2\text{O}_2 + \text{HCl}$	8×10^{-11}
$\text{Cl}_2 + \text{CH}_3\text{CO} \rightarrow \text{CH}_3\text{COCl} + \text{Cl}$	3×10^{-11}
$\text{Cl} + \text{H}_2\text{CO} \rightarrow \text{HCO} + \text{HCl}$	7.2×10^{-11}
$\text{Cl} + \text{CH}_3\text{OH} \rightarrow \text{CH}_2\text{OH} + \text{HCl}$	5.5×10^{-11}
$\text{Cl} + \text{CH}_2\text{OH} \rightarrow \text{HCl} + \text{H}_2\text{CO}$	3×10^{-10}
$\text{Cl}_2 + \text{CH}_2\text{OH} \rightarrow \text{ClCH}_2\text{OH} + \text{Cl}$	2.9×10^{-11}
$\text{Cl} + \text{CH}_3\text{CHO} \rightarrow \text{CH}_3\text{CO} + \text{HCl}$	8×10^{-11}
$\text{ClO} + \text{CH}_3\text{O}_2 \rightarrow \text{ClO}_2 + \text{CH}_3\text{O}$	1.61×10^{-12}
$\text{ClO} + \text{CH}_3\text{O}_2 \rightarrow \text{CH}_3\text{OCl} + \text{O}_2$	3.3×10^{-13}

Table 3. Photoionization spectrum for CH₃O₂ and CH₃OOH. The random error in the CH₃O₂ absolute spectrum is 5% and for CH₃OOH it is 13%.

Energy (eV)	CH ₃ O ₂ (Mb)	CH ₃ OOH (Mb)	Energy (eV)	CH ₃ O ₂ (Mb)	CH ₃ OOH (Mb)
8.7	0	0	10.125	0.004	1.288
8.725	0	0	10.15	0.003	1.482
8.75	0	0	10.175	0.004	1.685
8.775	0	0	10.2	0.004	2.070
8.8	0	0	10.225	0.013	2.398
8.825	0	0.0126	10.25	0.026	2.677
8.85	0	0	10.275	0.048	2.755
8.875	0	0	10.3	0.068	3.615
8.9	0	0	10.325	0.148	3.300
8.925	0	0	10.35	0.189	3.973
8.95	0	0.0118	10.375	0.274	4.235
8.975	0	0	10.4	0.384	4.813
9	0	0	10.425	0.533	5.166
9.025	0.0012	0	10.45	0.657	5.550
9.05	0	0	10.475	0.845	5.521
9.075	0	0	10.5	1.083	6.100
9.1	0	0	10.525	1.253	7.160
9.125	0	0	10.55	1.439	6.974
9.15	0	0	10.575	1.657	7.024
9.175	0	0	10.6	1.938	7.704
9.2	0	0	10.625	2.264	7.509
9.225	0	0	10.65	2.430	8.618
9.25	0	0	10.675	2.633	8.151
9.275	0	0	10.7	2.901	9.130
9.3	0	0	10.725	3.083	9.590
9.325	0	0	10.75	3.260	9.934
9.35	0	0	10.775	3.562	10.453
9.375	0.0011	0	10.8	3.697	10.788
9.4	0	0	10.825	3.856	11.342
9.425	0	0	10.85	3.988	11.409
9.45	0	0	10.875	4.204	11.680
9.475	0	0	10.9	4.223	12.833
9.5	0	0	10.925	4.415	12.090
9.525	0	0	10.95	4.546	12.368
9.55	0	0	10.975	4.624	12.407
9.575	0	0.0093	11	4.590	12.692
9.6	0	0	11.025	4.771	13.382

9.625	0	0	11.05	4.802	13.030
9.65	0	0.0091	11.075	4.906	13.957
9.675	0	0	11.1	4.953	13.132
9.7	0	0.0090	11.125	5.057	14.228
9.725	0.0010	0.0178	11.15	5.163	14.102
9.75	0	0	11.175	5.169	14.112
9.775	0	0.0355	11.2	5.263	14.966
9.8	0	0.0442	11.225	5.340	14.677
9.825	0	0.1581	11.25	5.281	15.230
9.85	0	0.2014	11.275	5.405	14.835
9.875	0	0.1658	11.3	5.362	13.866
9.9	0	0.2439	11.325	5.404	15.261
9.925	0.0009	0.4269	11.35	5.456	14.876
9.95	0	0.3043	11.375	5.561	16.173
9.975	0	0.4179	11.4	5.595	16.390
10	0.0009	0.5301	11.425	5.535	16.419
10.025	0.0009	0.7320	11.45	5.643	16.269
10.05	0.0038	0.9076	11.475	5.435	16.270
10.075	0	0.7853	11.5	5.322	14.668
10.1	0.0019	1.0318			

DESIGN AND PERFORMANCE OF A TEMPERATURE CONTROLLED FLOW REACTOR FOR LOW-TEMPERATURE RADICAL KINETICS

1 Introduction

The Sandia Multiplexed Chemical Kinetics Reactor was built to study low-temperature (meaning $T < 1000$ K) combustion processes.¹⁻² As such, the original design supported temperature controlled experiments at a range of temperatures from 300–1050 K, with uniform temperatures stabilized to ± 4 K. Such conditions were achieved by wrapping heating tape around the quartz reactor through which current could flow to provide heating along the full axis of the tube. The temperature in the reactor was controlled using a proportional–integral–derivative controller that responded to a thermocouple temperature measurement made in the center of the reactor.

The aim in this work was to design a flow reactor that can be seamlessly integrated into the existing Multiplexed Photoionization Mass Spectrometer (MPIMS) to enable kinetics experiments at temperatures below 300 K while the instrument is connected to the Chemical Dynamics Beamline at the Advanced Light Source (ALS) at Lawrence Berkeley National Laboratory.³ The Sandia group had previously attempted several designs to achieve such conditions, but faced serious difficulties in cooling the entire length of the flow tube. The technical challenge is to control the temperature along the entire length of the flow tube while still enabling access to the side-sampled pinhole. Additionally, the MPIMS machine was designed for experiments that are carried out on the millisecond timescale; the lifetime of HO₂ radicals in the experiments described in Chapter 4 were on the order of 40 ms, so as much of the reactor must be cooled as uniformly as possible. Typical experiments were conducted at 8 Torr with a total flow of 200 sccm through the reactor. At these conditions, gases flowed through the reactor at speeds of 0.366 cm ms^{-1} . In order to have 60 ms of useable kinetics data, the tube must be cooled uniformly for > 9 inches above the pinhole.

Construction and implementation of the low-temperature flow reactor presented here could not have been accomplished without the groundwork and assistance of Sandia engineer Howard Johnsen, who is now retired.

2 Low-temperature reactor design

The Okumura group low-temperature reactor is a stainless steel flow tube featuring an outer jacket through which almost any coolant can flow. Figure 1 conceptualizes the temperature-controlled apparatus tested as part of this thesis. Here house nitrogen, which is readily available at the ALS, is delivered by a large (30 standard liters per minute (slm) maximum) mass flow controller to a coil of ¼” copper tubing which is submerged in a liquid nitrogen bath. Using the mass flow controller, the flow rate of the nitrogen gas through the system can be varied; increasing the flow results in colder reactor temperatures. The cooled nitrogen gas is fed to the chamber through a liquid nitrogen feedthrough; the gas then flows through insulated flexible tubing to the top of the temperature-controlled flow reactor. After the cooled nitrogen exits the flow reactor, it travels through insulated flexible tubing and exits the MPIMS chamber through the second port on the liquid nitrogen feedthrough. From here, the nitrogen is vented to the air (care must be taken that this port does not become sealed with ice).

2.1 Inner tube design

The temperature-controlled flow reactor is comprised of two concentric stainless steel tubes and was machined by Moore Machine in Livermore, CA. The inner tube, shown in Figure 2, is designed to fit the Sandia MPIMS machine in exactly the same way that their typical reactor tubes fit. During use, reactant gases are introduced into the flow tube through ports connected to the top of the tube. Gas flows down the tube, is side-sampled by the orifice, and is pumped out the bottom of the tube. The low-temperature tube is a stainless steel 0.5” OD hollow tube with 0.049” wall thickness. It is 24.25” long, with a small (500 µm ID) orifice drilled and countersunk 14.75” from the top end of the tube. To provide access between this pinhole and the MPIMS skimmer, a short section of 0.375” OD tube was welded perpendicular to the tube axis, as shown. The top part of this piece was welded to the outer

tube (described in the next paragraph), forming a sealed jacket that allows coolant to surround as much of the reaction tube as possible, without blocking access to the pinhole.

2.2 Outer tube design

To uniformly cool the reaction tube, coolant flows through an outer jacket that is constructed of 15.68"-long stainless steel tube (Figure 3). The tube is 0.75" OD with wall thickness 0.035". A 0.375" ID hole was cleared 10.33" from the top end; the short 0.375" OD tubing section on the inner tube was welded to the outer tube at this joint. The size of the jacket and clearance hole were designed so that the MPIMS skimmer can be brought as close as possible to the orifice drilled into the inner tube without any surfaces clashing between the cooled reactor and the machine. Figure 4 is a picture of the pinhole region in the final reactor.

2.3 Assembly of reactor

The ends of the outer tube coolant jacket were sealed to the outer wall of the inner reactor tube using a bored-through Swagelok reducing union. The outer tube was sealed to the 3/4" end of the union, with the inner tube running through the interior of the union and sealing on the 1/2" end. A 1/4" port was welded to the side of the union, and a hole was drilled through to the center of the union so that coolant could flow into/out of the jacket without leaking into the reactor. Figure 5 shows a drawing of the final assembly of the low-temperature flow reactor. Figure 6 shows a photograph of the full temperature-controlled reactor after it has been assembled. The inner surface of the inner tube was coated with the same DuPont AF 400S2-100-1 fluoroplastic resin used on the quartz reactors in Chapters 4 and 5.

3 Low-temperature reactor performance

Two metrics were considered in testing the performance of the cooled flow reactor: temperature stability and temperature gradient. The reactor must maintain a single temperature throughout experiments, with good repeatability and stability. Also, since kinetics experiments sampled reacting gases as they traveled down the length of the flow reactor, the temperature must be uniform over the kinetic range ($> 9''$ above the sampling orifice).

The design discussed in section 2 relies on a stable flow of gas through the liquid nitrogen cooling vessel and few environmental impacts to produce a stable reactor temperature. Figure 7 shows a time series of the temperature (measured at the pinhole, with 200 sccm He gas flowing through the reactor, held at 8 Torr) inside the flow reactor. For the first 30 minutes of this time series, the cooled nitrogen flow is held constant at 5.0 slm, resulting in a reactor temperature of $-8\text{ }^{\circ}\text{C}$. The temperature varies less than $1\text{ }^{\circ}\text{C}$ over 30 minutes. Thirty minutes into the measurement, the flow rate was increased to 5.5 slm, leading to a slow decrease in reactor temperature down to $-18\text{ }^{\circ}\text{C}$ after one hour. The temperature variability after reaching equilibrium was again less than $1\text{ }^{\circ}\text{C}$.

The primary difficulty in past low-temperature tube designs was to maintain a reasonably constant temperature along the vertical axis of the flow tube. Glass tube designs that left too much uncooled area around the pinhole region resulted in huge temperature gradients (temperature increases larger than $5\text{ }^{\circ}\text{C}$ within one inch above the pinhole). In the design presented here, only a small area around the pinhole is not jacketed. This, combined with the the increased thermal conductivity of stainless steel compared to glass, resulted in an excellent temperature profile (shown in Figure 8). The reactor tube pressure was maintained at 8 Torr, with 200 sccm He flowing through, while a long thermocouple was randomly moved up and down the vertical tube axis making measurements every 0.5" in the center of the reactor. From almost ten inches above the sampling orifice to several inches below, the temperature slowly increases, resulting in a total temperature change of less than $4\text{ }^{\circ}\text{C}$ over about 15 inches.

4 PID control

The reactor described in section 2 and tested in section 3 had no mechanism for active temperature stabilization, but stable flows appeared to produce very stable temperature profiles. However, all tests described in section 3 were conducted with only helium present and laser-initiated chemistry. During kinetics experiments, the same thermocouple used to control the temperature in the Sandia heated tube was inserted through the bottom end of the flow reactor; a metal hood shields the end of the thermocouple to block excimer light from directly irradiating the probe. This temperature measurement drifted significantly during

experiments, typically warming by several degrees. This observation, combined by a desire to shorten the amount of time required to change the reactor temperature, prompted the development of a PID-controlled heater to further stabilize the temperature and decrease equilibration times.

The goal was to obtain a very stable reactor temperature by setting the cooled nitrogen flow to a rate that produced a temperature somewhat lower than the desired set point and then, using the PID-controlled heater, the reactor could be warmed up and the desired temperature maintained using the active feedback of the PID controller. This goal was accomplished by controlling the temperature of the stainless steel Swagelok union on the input port of the cooled jacket. The thermal conductivity of stainless steel is $0.14 \text{ W cm}^{-1} \text{ K}^{-1}$ and the approximate volume of stainless steel in the union was 9 cm^3 . An input of 1.4 W was estimated to heat this metal block by $10 \text{ }^\circ\text{C}$. A 10 W/in^2 Kapton insulated flexible heater ($4'' \times \frac{1}{2}''$) (Omega KHLV-0504/10-P) was wrapped around the $\frac{3}{4}''$ nut of the union (shown in Figure 9). Then, a thermistor (Omega SA1-TH-44004-40-T) was secured with Kapton tape just below the heater on the outside wall of the jacket, as indicated. The response of this thermistor to current flowing through the heater was used as the PID controller signal. Current flow through the heater was varied using a PID controller (Figure 10). A DC power supply (Delta AA15S2400A, 24 VDC, 625 mA, 15 W) was switched on and off by a solid state relay (Omron G3NA-205B) controlled by a commercial PID controller (Omega CN32PT-224-C24).

The PID-controlled low-temperature tube demonstrated improved stability over the cooled tube without active feedback, with no change in the vertical temperature gradient profile. Figure 11 shows a time series of the flow reactor, measured with the hooded thermocouple inserted through the bottom of the tube. Cooled nitrogen was flowing at 7.5 slm, leading to an initial tube temperature of $-30 \text{ }^\circ\text{C}$. The PID controller was set to increase the temperature by $+10 \text{ }^\circ\text{C}$. The temperature of the reactor (at 8 Torr, 200 sccm He) was stabilized at $-19.87 \pm 0.09 \text{ }^\circ\text{C}$ over more than one hour. The time series reveals that an increase in temperature was observed every time the excimer laser was firing (indicated by the grey shading on the

time series). This temperature increase was not observed by a thermocouple that was located further down the exhaust line, indicating that the increase in temperature was not reflective of an increase in the temperature of the reacting gases, but was probably caused by heating of the thermocouple surface due to irradiation by the excimer laser photons.

In principle, the temperature range accessible to the flow reactor is limited only by the coolant. The boiling point of liquid nitrogen is $-196\text{ }^{\circ}\text{C}$. During tests, we managed to cool the gas inside the flow reactor to $-150\text{ }^{\circ}\text{C}$ using a coolant flow rate of 20 slm (we did not attempt to go further). Table 1 lists the temperatures achieved at a range of flows, without any temperature stabilization or use of the PID-controlled heater. At the highest coolant flow rates, the liquid nitrogen dewar had to be refilled regularly (every ~ 30 mins), but improved insulation of the dewar should decrease that need. Ultimately, the useful temperature range for this apparatus will be limited by the chemical environment of the performed experiments – since the MPIMS was designed to measure first-order rate coefficients up to 2000 s^{-1} , this imposes a practical limit for radical reactions that become very fast at lower temperatures.

5 Low-temperature study of the HO_2 self-reaction

The first experimental system we tested in the low-temperature reactor was the HO_2 self-reaction. The temperature dependence of this reaction is well-established (see Sander et al.⁴ and Atkinson et al.⁵ and references therein), and we recently performed a room-temperature study of this reaction, measuring reactants, intermediates, and products using the MPIMS instrument.⁶ We measured the VUV photoionization cross sections of HO_2 , H_2O_2 , and H_2CO , as well as the room-temperature wall loss rates for HO_2 and H_2O_2 .

We revisited the HO_2 self-reaction system with our new low-temperature flow reactor for two reasons: (1) to test the performance of the reactor and (2) to investigate the possible formation of complexes. In the upper troposphere/lower stratosphere (UT/LS), where temperatures range from 190–250 K, HO_2 becomes the dominant member of the HO_x family (over OH, which reigns in the lower troposphere). The HO_2 self-reaction is the primary source of H_2O_2 in the UT/LS; H_2O_2 serves as a reservoir for HO_x species and is used to infer HO_2 concentrations in the UT/LS. However, increasing theoretical evidence suggests that

H₂O₂ may not be the only accessible product channel for the HO₂ self-reaction at low temperature.⁷⁻¹⁵ Formation of the H₂O₄ adduct from HO₂ association would represent a much less-stable reservoir for HO_x species that could thermally or photochemically decompose to recycle radicals in the UT/LS. However, the only experimental detection of H₂O₄ has been in matrix experiments using Raman spectroscopy. An H₂O₄ binding energy of ~16.5 kcal mol⁻¹ suggests that this adduct could play a role in radical recycling in the UT/LS and could ultimately explain discrepancies between modeled and observed H₂O₂ concentrations in the UT/LS.^{14,16-17}

Preliminary density functional theory calculations (described in Appendix X) using the B3LYP functional and the 6-311+G(3df,2p) basis set revealed that the H₂O₄⁺ cation is bound and is stable compared to decomposition, although it exhibited a large geometry change from the neutral species (Figure 12). The extreme differences between the two structures resulted in over 1 eV difference between the computed vertical ionization energy (11.69 eV) and the adiabatic ionization energy (10.44 eV). The Franck-Condon factors between the neutral and cation are very weak, much like those seen in H₂O₂ which faces similar geometry changes.¹⁸ We expected to see a spectrum quite similar to that of H₂O₂, with a slow onset starting at 10.44 eV, increasing in intensity up to the adiabatic ionization energy at 11.69 eV.

Initial MPIMS experiments using the temperature-controlled reactor revealed an increase in the relative signal at *m/z* 66 with decreasing temperature (Figure 13). The signal appeared to be time-dependent (forming only after the photolysis laser fired), but we had insufficient signal-to-noise to determine the identity of this species. Repeated experiments with significant signal averaging revealed that the species formed as a step function immediately after photolysis, and not with a formation rate that matches the HO₂ decays, as would be expected for a product of the HO₂ self-reaction. These signal-averaged experiments also enabled a more precise measurement of the peak center for *m/z* 66, finding an exact mass of 65.987 rather than that expected for H₂O₄ (65.995). The final piece of evidence contradicting the hypothesis that the *m/z* 66 peak comes from H₂O₄ is the experimental photoionization spectrum, which is shown in Figure 14. This spectrum features a sharp onset at 11 eV, which

is more suggestive of a species with very similar neutral and cation structures, with good Franck-Condon overlap between the ground states of the two species. We tentatively propose the identity of the species at mass 66 may be ClCH₂OH, formed promptly after photolysis by reaction of Cl₂ with CH₂OH radicals. This species would have very strong overlap between the neutral and cation states because the structures are nearly identical, with no change in the primary dihedral angle and only slight (<4%) decreases in the C–O and Cl–C bond lengths upon ionization. Preliminary calculations (at B3LYP/6-311+G(3df,2p)) found an adiabatic ionization energy of 10.58 eV.

Encouragingly, the HO₂ decay rates increased as expected with decreasing temperature; however, these decays were complicated by temperature dependence of the heterogeneous wall loss processes. Figure 15 demonstrates the HO₂ + HO₂ kinetics, using the same reaction conditions as those described in Chapter 4, carried out in the stainless-steel flow reactor described in the current chapter without any temperature control (i.e. at room temperature). Shown are the H₂CO, HO₂, and H₂O₂ time-dependent ion signals at room temperature. A sharp spike appears at early times ($t < 5$ ms) in the H₂CO and HO₂ signals, which has previously been thought to be related to the alignment of the photolysis laser when this feature appeared in photolysis experiments using quartz flow reactors. We were unable to completely remove this spike, although repeated attempts were made to realign the excimer laser. A photolysis gradient was also necessary to fit the $t = 5$ –60 ms portions of the H₂CO, Cl₂, and CH₃OH traces, as described in Chapter 4. The gradient was on the same order as that observed for the quartz reactors used in Chapter 4. Heterogeneous loss of HO₂ and H₂O₂ also occurred – the green traces in Figure 15 show the simulated HO₂ and H₂O₂ kinetics in the absence of added loss processes. The red traces show the fitted simulations, using rates of 7 s^{-1} for both HO₂ and H₂O₂ wall loss, in good agreement with the values measured for both species at room temperature in the coated quartz reactors.

We carried out kinetics experiments at several different temperatures using the stainless-steel temperature-controlled reactor. Figure 16 shows the HO₂ + HO₂ kinetics carried out at –20 °C. To model this reaction system, we used the kinetics model listed in Chapter 4, updated

with the temperature-dependent rate constants listed in Table 2 to simulate the time dependence of H₂CO, HO₂, and H₂O₂ at -20 °C. The HO₂ signal decay increases as the self-reaction speeds up at lower temperatures. However, the observed decays of HO₂ and H₂O₂ are faster than those predicted by the model. The red traces in Figure 16 show the kinetics traces for HO₂ and H₂O₂, simulated using the same heterogeneous wall loss rates measured for this reactor at room temperature (7 s⁻¹ for both HO₂ and H₂O₂ wall loss). The blue traces show the time-dependent kinetics of HO₂ and H₂O₂, fit with faster wall loss rates: 20 s⁻¹ for HO₂ and 15 s⁻¹ for H₂O₂. The heterogeneous wall loss processes are temperature-dependent.

6 Discussion

In this chapter, we described the development and testing of a new low-temperature temperature-controlled flow reactor for use in the Sandia Multiplexed Chemical Kinetics Reactor. The reactor is cooled with any fluid that flows through a jacket, with active temperature control feedback supplied by a PID controller. The reactor was tested using cooled nitrogen gas, with temperatures ranging down to nearly liquid nitrogen temperatures, and is well-suited to detect novel low-temperature products. However, its use in measuring temperature-dependent rate constants is complicated by our observation of temperature dependence in the heterogeneous loss processes for sticky molecules.

7 References

1. Osborn, D. L.; Zou, P.; Johnsen, H.; Hayden, C. C.; Taatjes, C. A.; Knyazev, V. D.; North, S. W.; Peterka, D. S.; Ahmed, M.; Leone, S. R., The Multiplexed Chemical Kinetic Photoionization Mass Spectrometer: A New Approach to Isomer-Resolved Chemical Kinetics. *Rev. Sci. Instrum.* **2008**, *79*, 104103.
2. Taatjes, C. A.; Hansen, N.; Osborn, D. L.; Kohse-Hoinghaus, K.; Cool, T. A.; Westmoreland, P. R., "Imaging" Combustion Chemistry via Multiplexed Synchrotron-Photoionization Mass Spectrometry. *Phys. Chem. Chem. Phys.* **2008**, *10*, 20-34.
3. Leone, S. R.; Ahmed, M.; Wilson, K. R., Chemical Dynamics, Molecular Energetics, and Kinetics at the Synchrotron. *Phys. Chem. Chem. Phys.* **2010**, *12*, 6564-6578.
4. Sander, S. P.; Abbatt, J.; Barker, J. R.; Burkholder, J. B.; Friedl, R. R.; Golden, D. M.; Huie, R. E.; Kolb, C. E.; Kurylo, M. J.; Moortgat, G. K., et al., Chemical Kinetics and Photochemical Data for Use in Atmospheric Studies, Evaluation Number 17. *JPL Publication 10-6* **2011**.
5. Atkinson, R.; Baulch, D. L.; Cox, R. A.; Crowley, J. N.; Hampson, R. F.; Hynes, R. G.; Jenkin, M. E.; Rossi, M. J.; Troe, J., Evaluated Kinetic and Photochemical Data for Atmospheric

Chemistry: Volume I - Gas Phase Reactions of O_x, HO_x, NO_x and SO_x Species. *Atmos. Chem. Phys.* **2004**, *4*, 1461-1738.

6. Dodson, L. G.; Shen, L.; Savee, J. D.; Eddingsaas, N. C.; Welz, O.; Taatjes, C. A.; Osborn, D. L.; Sander, S. P.; Okumura, M., VUV Photoionization Cross Sections of HO₂, H₂O₂, and H₂CO. *J. Phys. Chem. A* **2015**, *119*, 1279-1291.
7. Sprague, M. K.; Irikura, K. K., Thermochemistry of HO₂ + HO₂ → H₂O₄: Does HO₂ Dimerization Affect Laboratory Studies? *J. Phys. Chem. A* **2015**, *119*, 7052-7062.
8. Kircher, C. C.; Sander, S. P., Kinetics and Mechanism of Hydroperoxo and Hydroperoxo-d Disproportionations. *J. Phys. Chem.* **1984**, *88*, 2082-2091.
9. Benson, S. W., On the Existence of Polyoxides of Hydrogen. *J. Chem. Phys.* **1960**, *33*, 306-307.
10. Arnau, J. L.; Giguère, P. A., Studies on Hydrogen–Oxygen Systems in the Electrical Discharge. VI. Detection by Laser Raman Spectroscopy of O₂ and O₃ Trapped at 80 °K. *Can. J. Chem.* **1973**, *51*, 1525-1529.
11. Arnau, J. L.; Giguère, P. A., Vibrational Analysis and Molecular Structure of the Hydrogen Polyoxides, H₂O₃, H₂O₄, D₂O₃, and D₂O₄. *J. Chem. Phys.* **1974**, *60*, 270-273.
12. Mozurkewich, M.; Benson, S. W., Self-Reaction of HO₂ and DO₂: Negative Temperature Dependence and Pressure Effects. *Int. J. Chem. Kin.* **1985**, *17*, 787-807.
13. Patrick, R.; Barker, J. R.; Golden, D. M., Computational Study of the Hydroperoxo + Hydroperoxo and Hydroperoxo-d + Hydroperoxo-d Reactions. *J. Phys. Chem.* **1984**, *88*, 128-136.
14. Anglada, J. M.; Olivella, S.; Solé, A., New Insight into the Gas-Phase Bimolecular Self-Reaction of the HOO Radical. *J. Phys. Chem. A* **2007**, *111*, 1695-1704.
15. Hollman, D. S.; Schaefer, H. F., In Search of the Next Holy Grail of Polyoxide Chemistry: Explicitly Correlated *ab initio* Full Quartic Force Fields for HOOH, HOOOH, HOOOOH, and their Isotologues. *J. Chem. Phys.* **2012**, *136*, 084302.
16. Denis, P. A.; Ornellas, F. R., Theoretical Characterization of Hydrogen Polyoxides: HOOH, HOOOH, HOOOOH, and HOOO. *J. Phys. Chem. A* **2009**, *113*, 499-506.
17. Bales, R. C.; McConnell, J. R.; Losleben, M. V.; Conklin, M. H.; Fuhrer, K.; Neftel, A.; Dibb, J. E.; Kahl, J. D. W.; Stearns, C. R., Diel Variations of H₂O₂ in Greenland: A Discussion of the Cause and Effect Relationship. *J. Geophys. Res.: Atmos.* **1995**, *100*, 18661-18668.
18. Litorja, M.; Ruscic, B., A Photoionization Study of the Hydroperoxyl Radical, HO₂, and Hydrogen Peroxide, H₂O₂. *J. Electron Spectrosc. Relat. Phenom.* **1998**, *97*, 131-146.
19. Morajkar, P.; Schoemaeker, C.; Okumura, M.; Fittschen, C., Direct Measurement of the Equilibrium Constants of the Reaction of Formaldehyde and Acetaldehyde with HO₂ Radicals. *Int. J. Chem. Kin.* **2014**, *46*, 245-259.

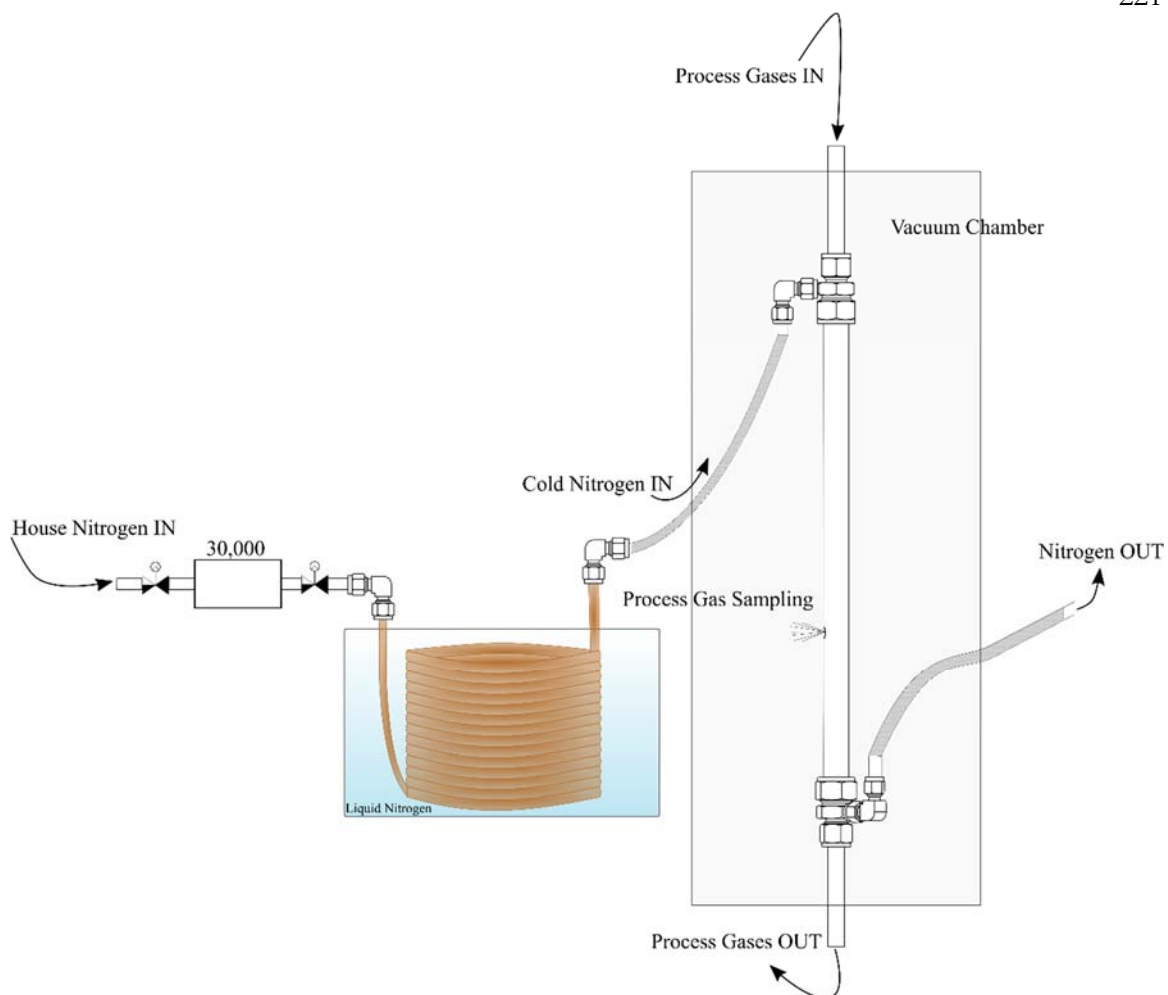


Figure 1. Conceptualization of cooled temperature-controlled flow reactor for low-temperature kinetics experiments. A controlled flow of nitrogen flows through copper coils submerged in liquid nitrogen. The cooled nitrogen flows through a jacket surrounding the reaction tube.

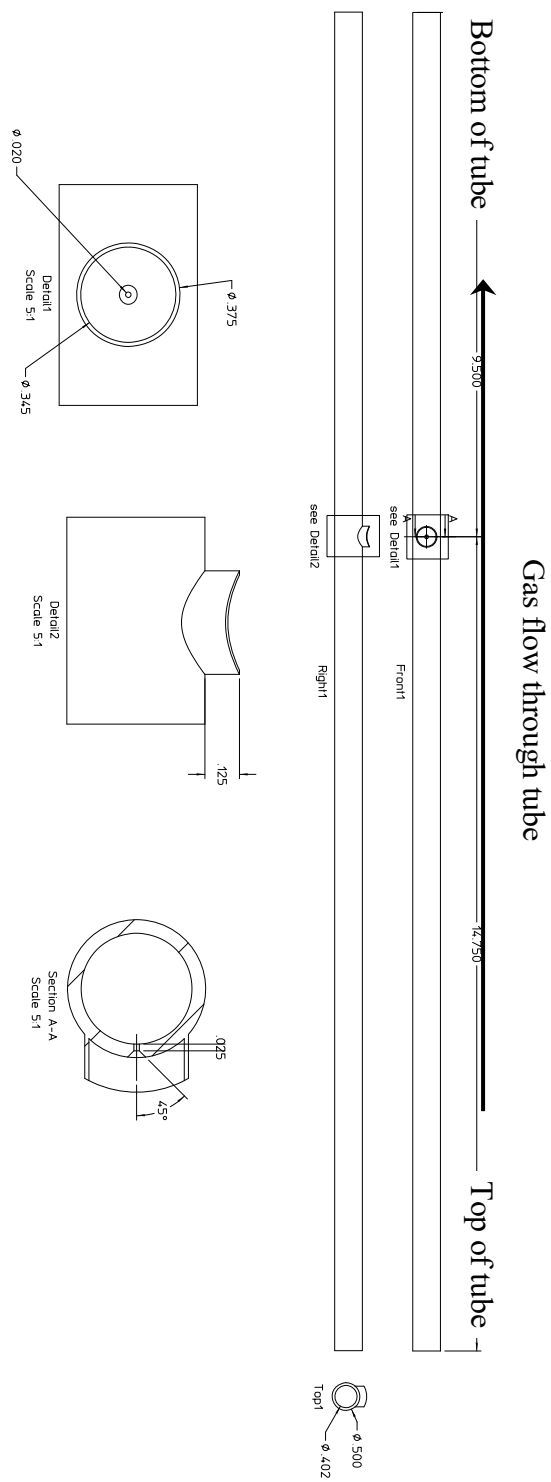


Figure 2. Drawing of the inner flow tube of the low-temperature reactor. All parts are stainless steel.

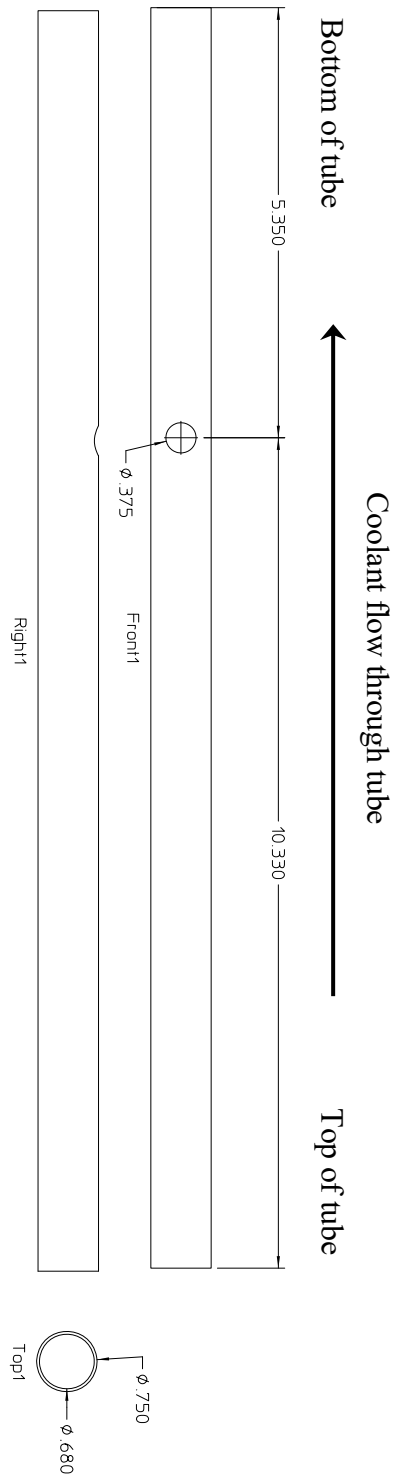


Figure 3. Outer tube of temperature-controlled flow tube. All parts are stainless steel.



Figure 4. Photograph of the pinhole region of the low-temperature flow tube, showing the counter-sunk 500 μm orifice in the inner tube, with a clearance space in the outer coolant jacket allowing for access to the pinhole by the skimmer without greatly impacting the temperature profile near the pinhole.

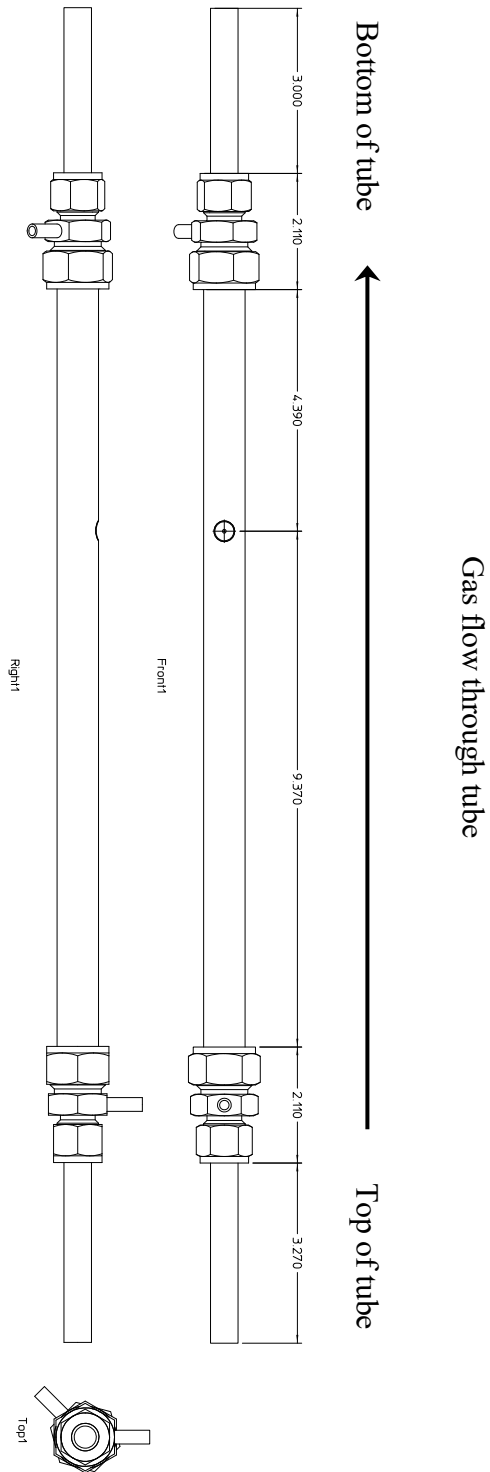


Figure 5. Overall drawing of Okumura group temperature-controlled tube.



Figure 6. Photograph of final assembled low-temperature flow reactor.

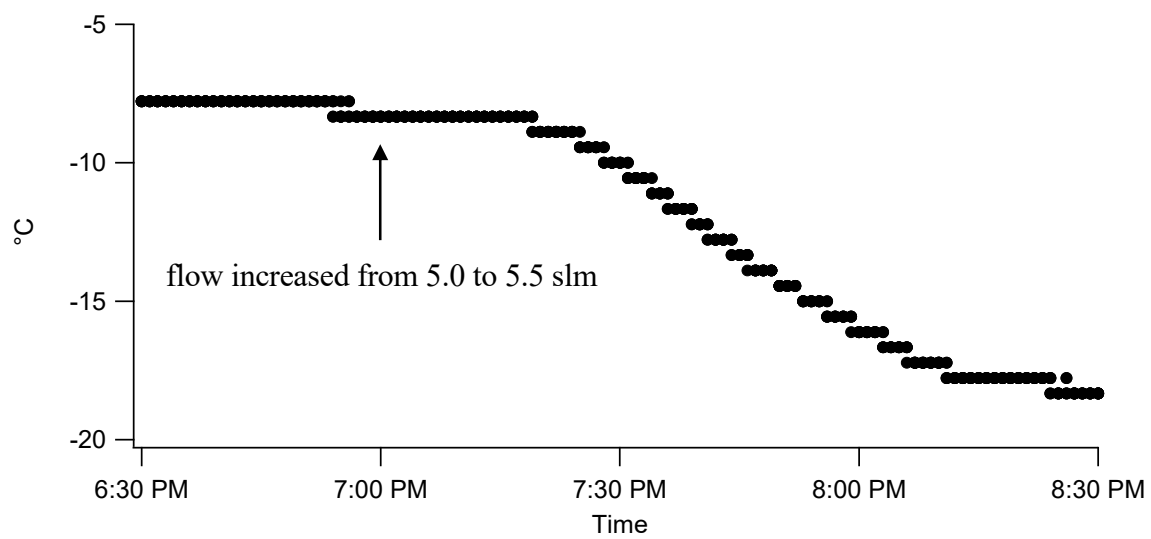


Figure 7. Temperature stability of low-temperature flow reactor without active feedback. For the first 30 minutes of this time series, the flow of cooled nitrogen through the reactor was maintained at 5.0 slm. The cooled nitrogen flow was increased to 5.5 slm at 7:00 pm.

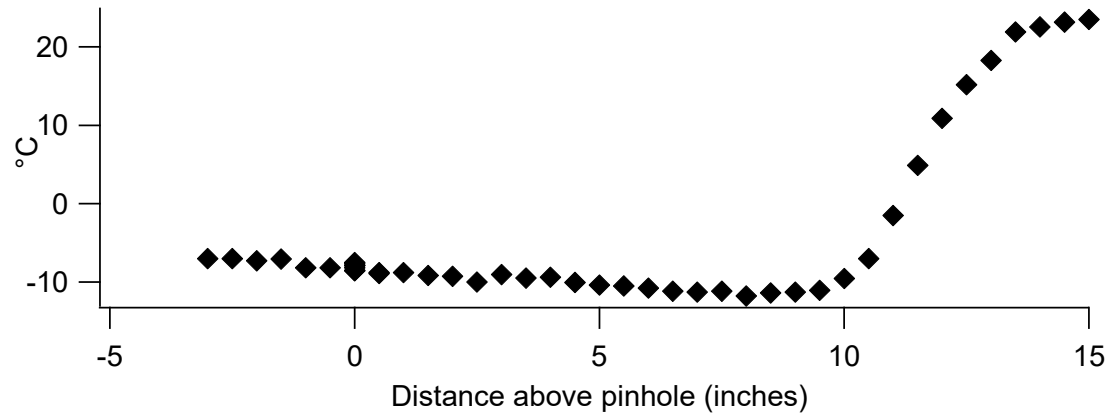


Figure 8. Temperature profile along the vertical axis of the cooled flow tube (without active feedback). The flow of the cooled nitrogen was kept constant at 5.0 slm and the temperature was measured along the axis randomly at 0.5" intervals.

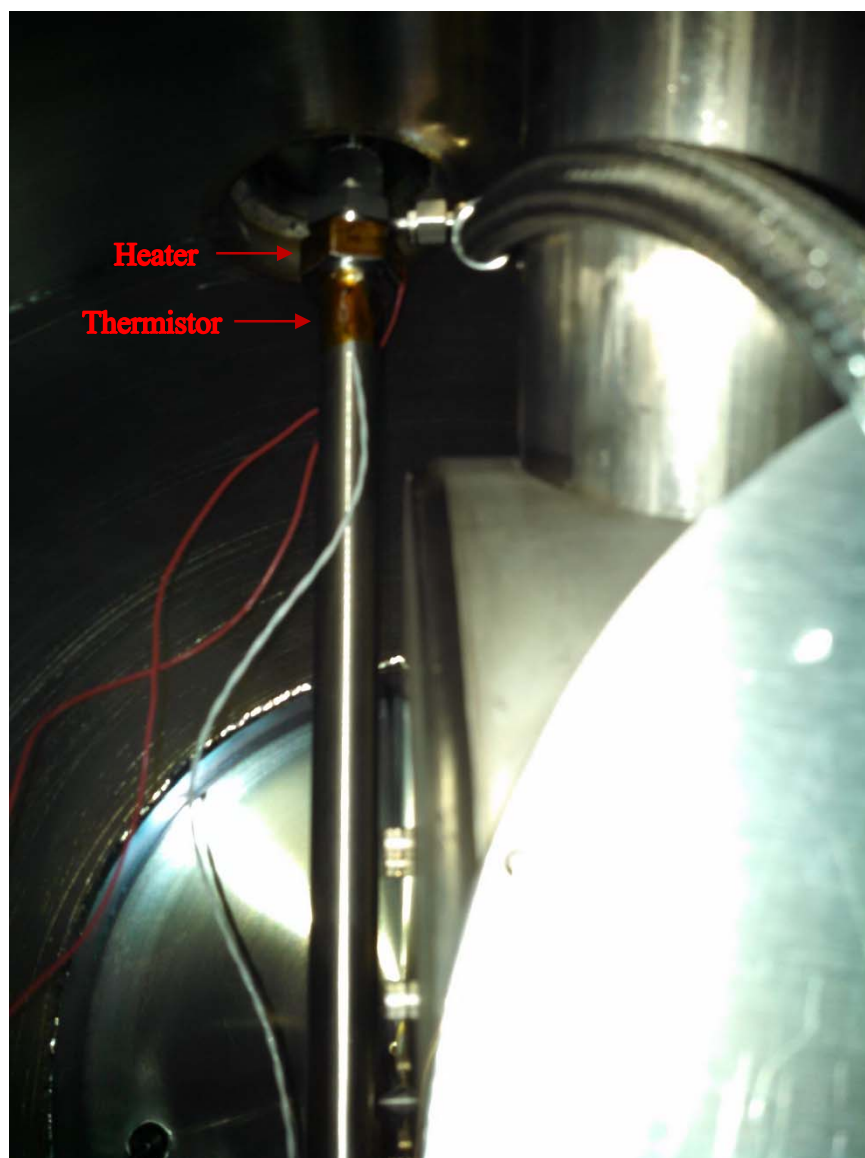


Figure 9. Photograph of PID-controlled heating of low-temperature tube.

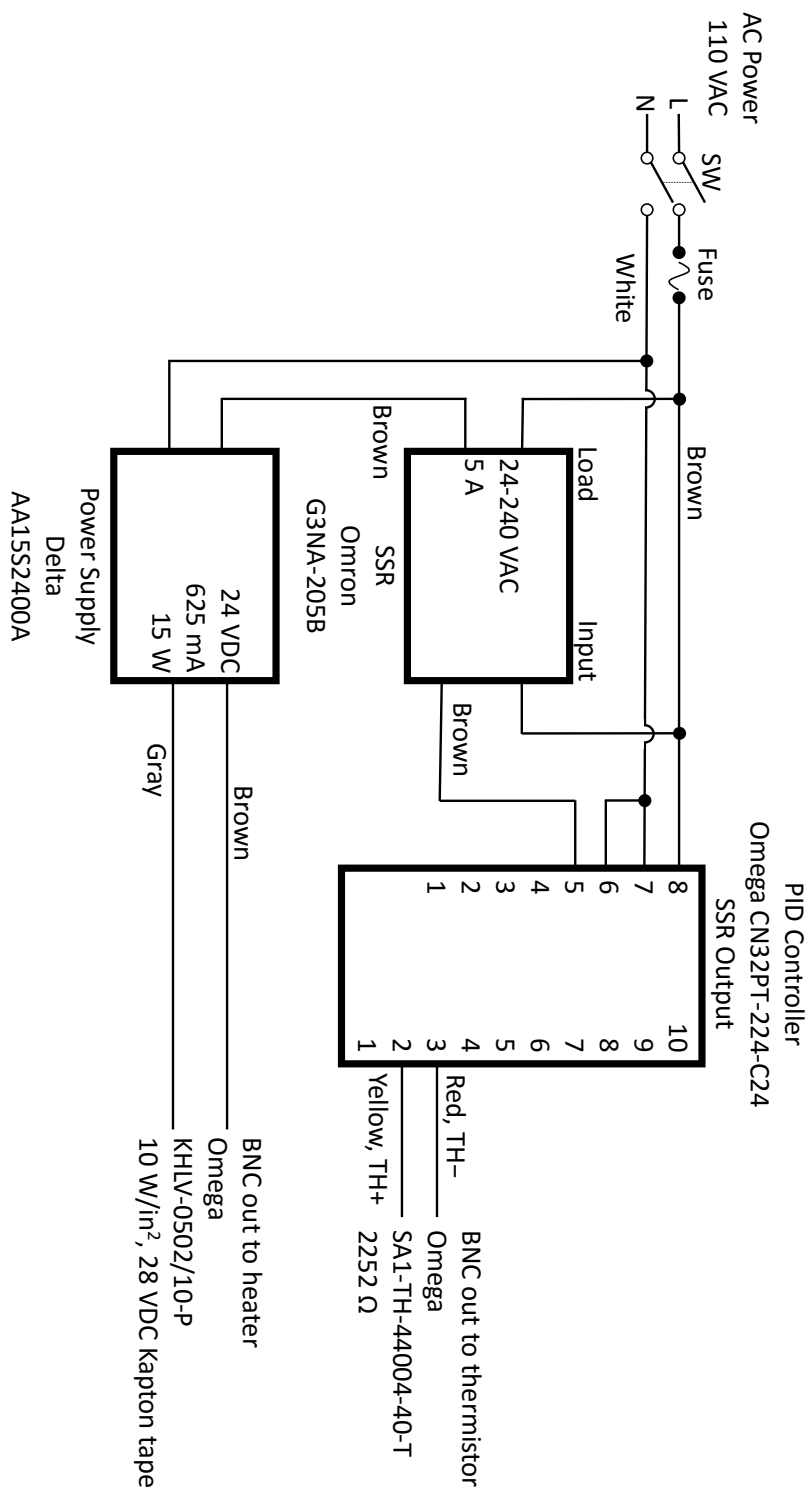


Figure 10. Schematic of PID controlled-heater.

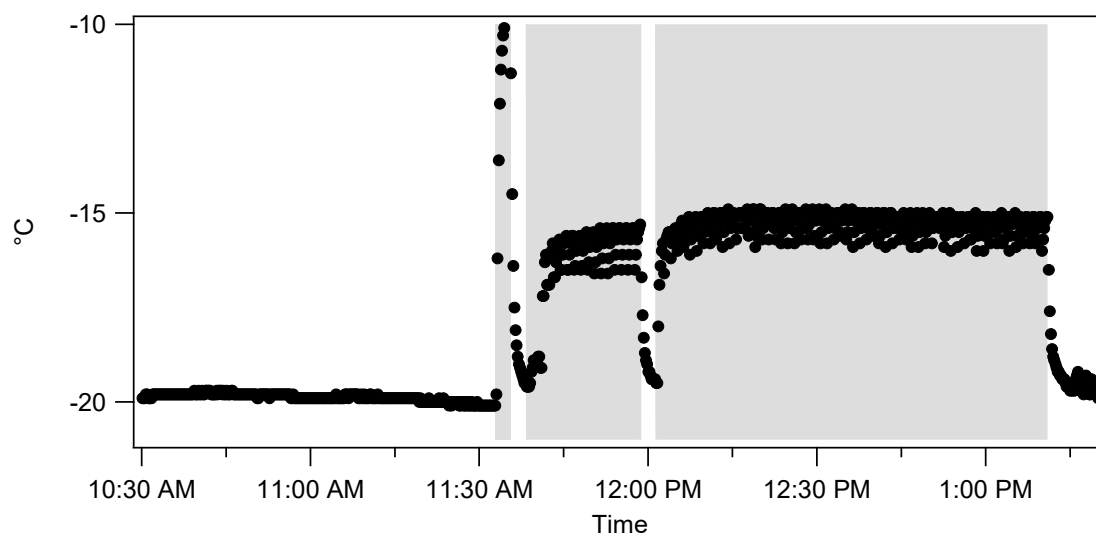


Figure 11. Temperature stability of PID-controlled reactor. The light grey portions of the time series indicate times when the excimer laser was firing.

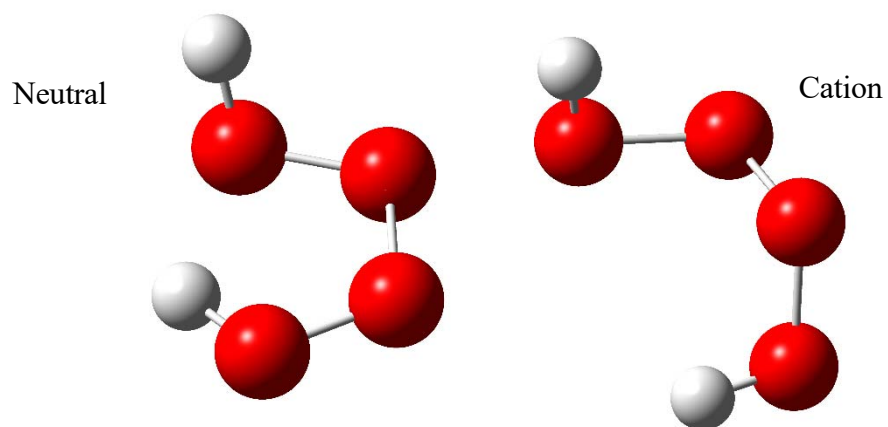


Figure 12. Neutral and cation structures for one H_2O_4 structure. Calculated at B3LYP/6-311+G(3df,2p).

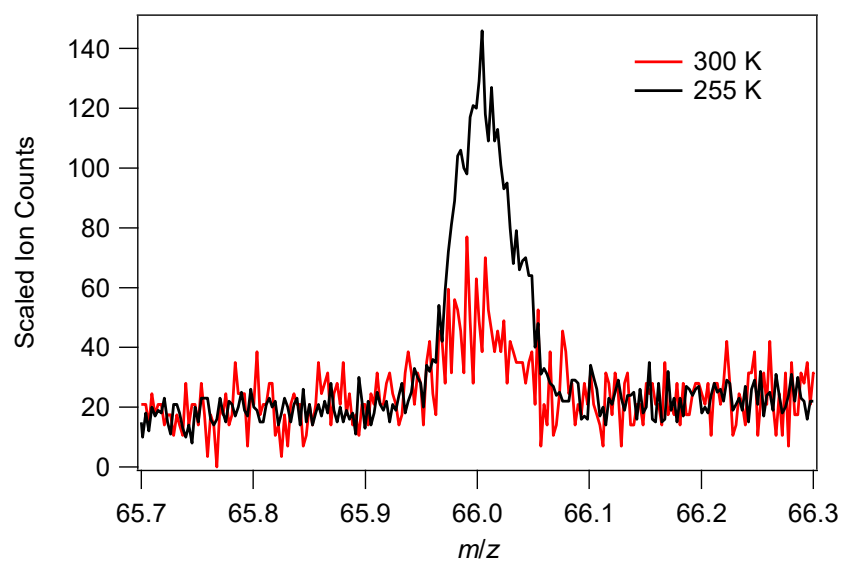


Figure 13. The relative signal at $m/z \approx 66$, with decreasing temperature.

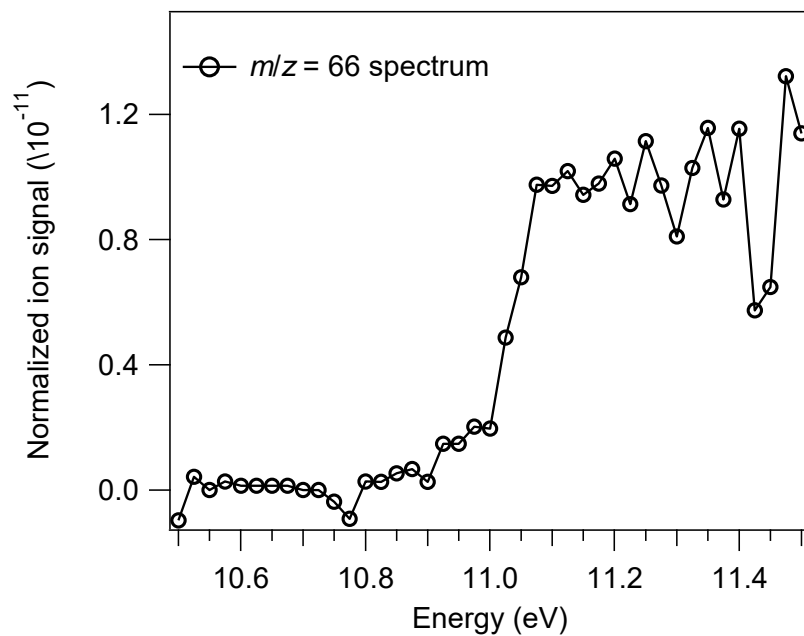


Figure 14. The photoionization spectrum of m/z 66.

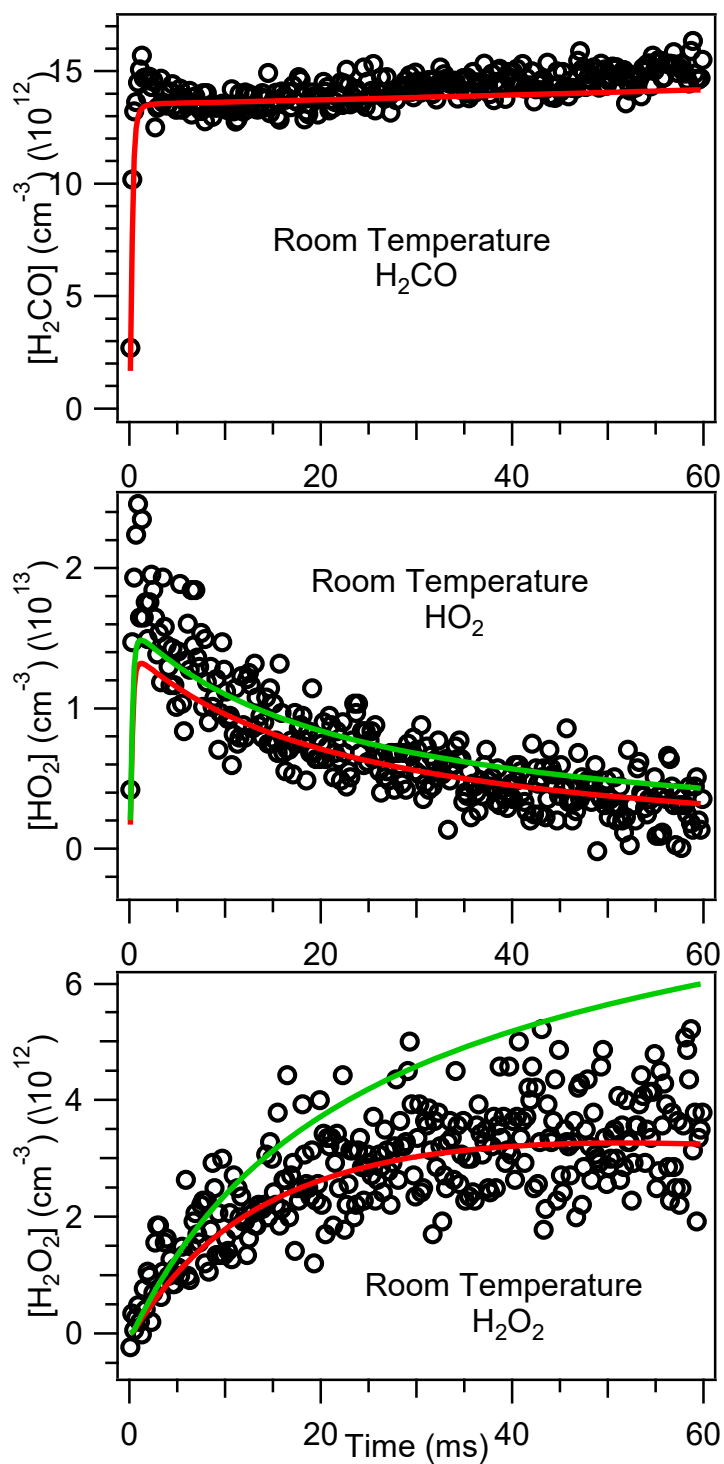


Figure 15. Room temperature $\text{HO}_2 + \text{HO}_2$ kinetics carried out in the temperature-controlled flow tube. The H_2CO , HO_2 , and H_2O_2 traces are fit with the kinetics model, including 7 s^{-1} wall loss terms for both HO_2 and H_2O_2 (red lines). The green lines are the model without heterogeneous wall loss terms.

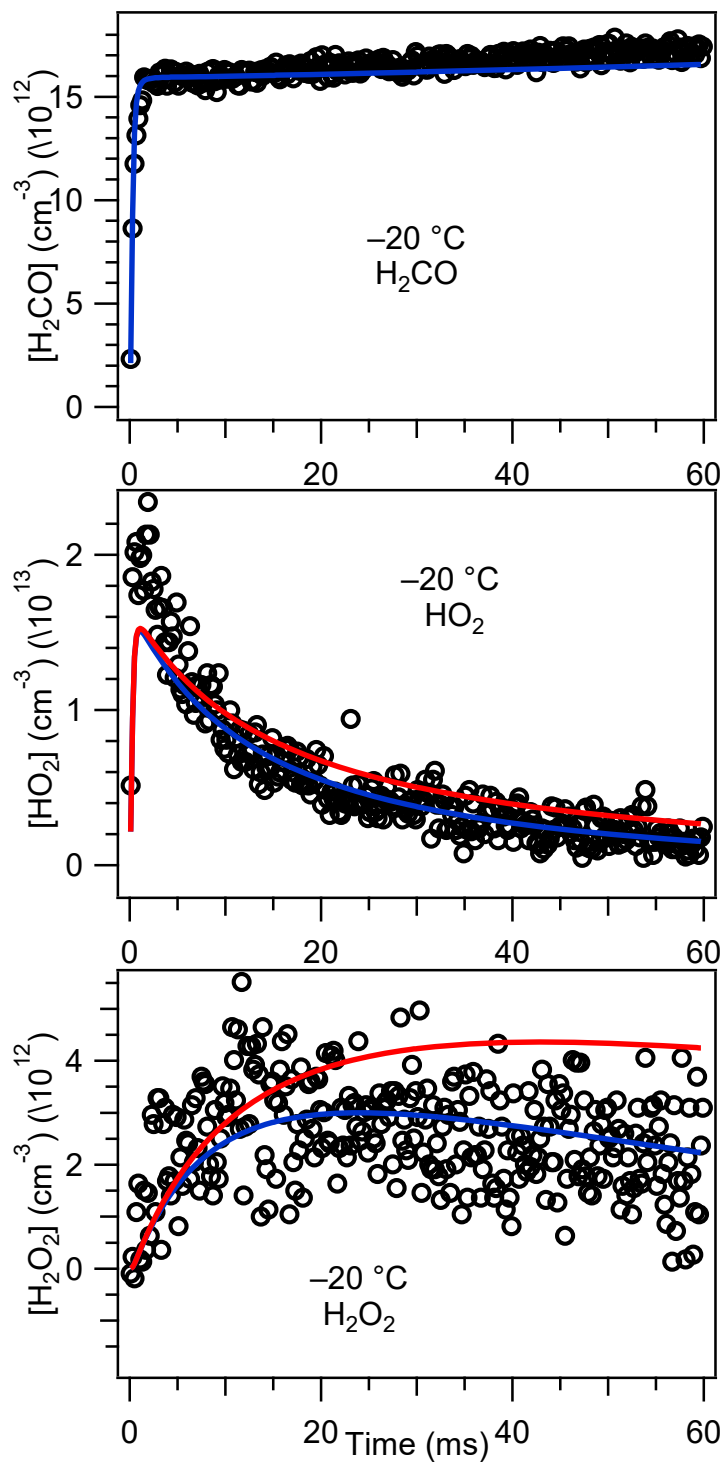


Figure 16. $\text{HO}_2 + \text{HO}_2$ kinetics measured at -20°C . The H_2CO , HO_2 , and H_2O_2 kinetics traces are fit with the kinetics model, including a 20 s^{-1} HO_2 wall loss term and a 15 s^{-1} H_2O_2 wall loss rate (blue lines). These traces are compared to the model including the wall loss rates (7 s^{-1} for both HO_2 and H_2O_2), measured at room temperature (red line).

Table 1. Flow reactor temperatures (in °C) achieved for various liquid nitrogen coolant flow rates (slm). These temperatures were achieved without active temperature feedback or heating.

Flow (slm)	Temperature (°C)
2	6
5	-7
8	-60
12.5	-123
15	-140
20	-150

Table 2. Temperature-dependent rate constants in the HO₂ + HO₂ reaction system. All values are taken from the JPL Evaluation⁴ unless otherwise noted. Arrhenius A-factors are given in cm³ molecule⁻¹ s⁻¹. The temperature dependence is listed as an E/R temperature, in Kelvin, as described by the JPL Evaluation.

	A	E/R	Ref
HO ₂ + HO ₂ → H ₂ O ₂ + O ₂	3.0×10 ⁻¹³	-460	
HO ₂ + HO ₂ \xrightarrow{M} H ₂ O ₂ + O ₂	2.1×10 ⁻³³ [M]	-920	
HO ₂ + H ₂ CO → HOCH ₂ O ₂	3.7×10 ⁻¹⁵	-637	a
HOCH ₂ O ₂ → HO ₂ + H ₂ CO	1.4×10 ¹⁵	9160	a
HO ₂ + Cl → HCl + O ₂	1.4×10 ⁻¹¹	-270	
HO ₂ + Cl → OH + ClO	3.6×10 ⁻¹¹	375	
HO ₂ + ClO → HOCl + O ₂	2.6×10 ⁻¹²	-290	
H ₂ O ₂ + Cl → HCl + HO ₂	1.1×10 ⁻¹¹	980	
H ₂ CO + Cl → HCl + HCO	8.1×10 ⁻¹¹	30	

^aTaken from Morajkar et al.¹⁹

EXPERIMENTAL MEASUREMENT OF THE RATE COEFFICIENT FOR REACTION OF THE SIMPLEST CRIEGEE CH₂OO WITH OZONE

1 Introduction

Direct experimental gas phase measurements of Criegee Intermediate (C.I.) bimolecular reactions, once illusive, are now being frequently reported in the literature. First theorized by Rudolf Criegee, this intermediate forms in the atmosphere during ozonolysis of unsaturated hydrocarbons.¹ Since the discovery of a direct route to formation of C.I. from photolysis of suitable iodinated precursors,² the bimolecular reaction rate constants of C.I. with a plethora of reaction partners have been measured. Two reviews detail the recent progress on the entire body of work.³⁻⁴

The recent measurements of the rate constant for reaction of CH₂OO with (H₂O)₂ ($4-6.5 \times 10^{-12} \text{ cm}^3 \text{ s}^{-1}$) demonstrated that CH₂OO will predominantly react with water dimer in the atmosphere.⁵⁻⁷ Earlier theoretical work by Vareaecken et al. predicted, using a large rate coefficient ($7 \times 10^{-11} \text{ cm}^3 \text{ s}^{-1}$) for reaction of CH₂OO + (H₂O)₂, that most of CH₂OO loss will be by reaction with the water dimer in the atmosphere.⁸ For larger C.I. species, (e.g. (CH₃)₂COO), with potentially slower reaction rates with (H₂O)₂, other bimolecular reactions play a larger role in controlling atmospheric lifetimes. Additionally, they note that laboratory ozonolysis experiments, conducted in the absence of water dimer, have C.I. lifetimes primarily dictated by reaction with precursor species.

Laboratory ozonolysis experiments are typically conducted with high levels of ozone and hydrocarbons, since the O₃ + alkene reaction occurs very slowly (see e.g. Kroll et al.⁹), so bimolecular C.I. reaction with precursor species should be considered. The recent work by Womack et al. highlights this necessity.¹⁰ In this work, CH₂OO, formed by ozonolysis of ethylene, was observed by Fourier transform microwave spectroscopy. The authors quantified the number density of CH₂OO from the signal of the rotational line and compare

the line intensity with that predicted by a steady-state model, finding reasonable agreement (within a factor of 2). The dominant method of CH₂OO removal in their experiment was assumed to be reaction with O₃, using the CH₂OO + O₃ rate coefficient and products computed by Vereecken et al ($1 \times 10^{-12} \text{ cm}^3 \text{ s}^{-1}$ at 300 K)⁸. If reaction between the C.I. and ozone had not been this fast, the observed number of CH₂OO molecules would have been significantly higher (this assumes no other reaction partners).

Quantum chemical calculations on C.I.s have been notoriously difficult.¹¹ The determination that the electronic structure of C.I. is mostly zwitterionic in nature, and likely contains only minimal biradical character, has simplified things somewhat, but calculating accurate electronic potentials remains a challenge, especially when reaction coordinates go through intermediates that are biradical in nature. Recently, three groups sought to address computationally the possibility of reactions between CH₂OO and ozone.^{8,12-13} A key feature of the potential energy surface identified by Vereecken et al. was the barrierless formation of a pre-reactive complex due to the electrostatic attraction between the partial charges on CH₂OO and O₃ (both are zwitterions). This mechanism is different from that suggested by Kjaergaard et al., which proposed direct cycloaddition between the two reactants, but could not identify the transition state of such a process.¹² The reaction pathway proposed by Vereecken et al. leads to a relatively fast rate coefficient with a negative temperature dependence ($k_1(T) = 3 \times 10^{-14} \exp(1068/T) \text{ cm}^3 \text{ s}^{-1}$) with two O₂ elimination steps leading ultimately to the product H₂CO (reaction (1)). Likewise, Kjaergaard et al. identified the same final products of this reaction, but could only provide a lower limit on k_1 of $10^{-18} \text{ cm}^3 \text{ s}^{-1}$.



In the present work, building on past success using a time-resolved broadband cavity enhanced absorption spectrometer to detect various C.I. species,¹⁴⁻¹⁵ we measured the rate of reaction of ozone with the smallest C.I., CH₂OO and found it to be in good agreement with the theoretical work by Vereecken et al.⁸ For reaction (1), we assumed the ultimate products of this reaction are formaldehyde and two oxygen molecules, in keeping with theoretical work by Vereecken et al, although the aim of this work was not to identify the products of

this reaction, nor was that a crucial issue in measuring the rate constant. Under our experimental conditions, the primary removal mechanism for CH₂OO was self-reaction (reaction (2)), as well as diffusion out of the detection region.



Again, we adopt the reaction products as determined computationally by Vereecken et al.

2 Experiment

The experiments described below were carried out in the time-resolved broadband cavity enhanced absorption spectrometer (BB-CEAS), which has been described elsewhere,^{14,16} at 291 K and 10 Torr total pressure. The chemical reaction is initiated and sampled through the center of a 3-cm inner diameter, 120 cm long flow tube. A broadband Xe arc lamp (Oriel Research Arc Lamp Housing Model 67005) is focused into a low-finesse cavity through $99.5 \pm 0.2\%$ (300–450 nm) mirrors (JDSU, Inc.), spaced 147 cm apart. The light exiting the cavity is filtered by a Schott Glass BG3 filter, reflected by a mirror rotating at 2 Hz, and finally reflected by a grating, dispersing the broadband light in the horizontal direction. The light is focused and sweeps vertically across a CCD camera (Andor Technology), providing two-dimensional images of probe light intensity as a function of wavelength (horizontal axis) and time (vertical axis).

Radicals are generated by a collimated laser pulse (Continuum Surelite III, 266 nm, 2 Hz) propagating at a small angle relative to the BB-CEAS sampling, providing an overlap pathlength of 80 cm. The laser is synchronized to the rotating mirror, enabling control of the CCD time axis. The YAG laser is pulsed just after the CCD is first illuminated, providing a few milliseconds of background signal before the reaction is initiated. Typically, the YAG is pulsed for 60 seconds, followed by 60 seconds of data collection in the absence of photolysis. The stray light that is transmitted straight through the cavity without any reflections ($I_{sp}(\lambda, t)$) is subtracted from the two “laser on” ($I_{on}(\lambda, t)$) and “laser off” ($I_{off}(\lambda, t)$) integrated two-dimensional images, resulting in the time-dependent absorption spectrum ($OD(\lambda, t)$) using the following expression:

$$\text{OD}(\lambda, t) = -\ln \left(\frac{I_{on}(\lambda, t) - I_{sp}(\lambda, t)}{I_{off}(\lambda, t) - I_{sp}(\lambda, t)} \right)$$

This procedure is repeated six times for each set of reaction conditions, resulting in an average of 720 laser shots accumulated for each.

Reactants are injected at one end of the flow tube and are pumped out at the other end by a roots pump, throttled by a butterfly valve to maintain constant pressure (10 Torr). All gases flow in to the reactor by means of calibrated mass flow controllers.

Before entering the reactor, helium (Matheson, 99.9999%) and oxygen (Matheson, 99.999%) are routed through an ozone generator (Orec Model V5-0) that creates ozone by a silent arc discharge. The ozone production efficiency (thus the ozone concentration entering the reactor) is varied by changing the pressure inside the ozone generator by means of a needle valve on the input of the reactor. The output flow from the ozone generator is a mixture of helium, oxygen, and ozone; this flow is further diluted with additional O₂ and passes through a small (37.1-cm long) glass tube where the ozone concentration is measured. The light from a lamp (Oriel Instruments Hg(Ar) Spectral Calibration Lamp) passes through quartz windows on the ends of the glass tube and the intensity of the 253.65 nm line (O₃ cross section $1.148 \times 10^{-17} \text{ cm}^2$)¹⁷ is monitored as a function of pressure inside the ozonator by a spectrometer (ThorLabs CCS200) to determine the ozone concentration.

A helium flow saturated with CH₂I₂ (Sigma Aldrich, 99%) carries the C.I. precursor into the cell from a fritted bubbler. The CH₂I₂ dilution within the flow is modulated by adjusting the pressure above the liquid using a needle valve at the entrance to the reactor. The concentration of CH₂I₂ in the flow is measured in the same way as ozone, using the 253.65 nm line and the cross section of CH₂I₂ ($1.395 \times 10^{-19} \text{ cm}^2$)¹⁷ and a 10.2 cm long absorption cell.

3 Results

3.1 CH₂I₂ + O(³P) rate constant

The primary source of CH₂OO in our CH₂OO + O₃ experiments was reaction of CH₂I₂ with O(³P) to form CH₂I radicals that react immediately with O₂ to form the desired CH₂OO (reaction (3)).



The O(³P) was formed from collisional deactivation of the O(¹D) atoms generated from O₃ photodissociation at 266 nm. One literature measurement exists for the reaction rate of O(³P) atoms with CH₂I₂.¹⁸ This measurement found a rate constant of $k_3 = (7.36 \pm 0.31) \times 10^{-11} \text{ cm}^3 \text{ s}^{-1}$. Formed CH₂I radicals react with O₂, leading to the desired C.I. through reaction (4).



The product channels that compete with reaction (4) (e.g. reaction (5)) will be discussed later.

Our measurement of the reaction rate of O₃ with CH₂OO relied heavily on our knowledge of the k_3 , so we endeavored to measure this rate again. The formation rates of CH₂OO and IO were obtained by varying the initial CH₂I₂ and O₃ concentrations while maintaining the same number of estimated CH₂I radicals formed both from direct CH₂I₂ photolysis and from reaction of CH₂I₂ with O(³P).

Typically, data collected using the BB-CEAS can be fit using a simple double exponential function describing formation and depletion of a species ($S(t)$),

$$S(t) = S_0 \frac{k_b}{k_b - k_a} (e^{k_a t} - e^{-k_b t}) + y_0$$

which is convolved with an instrument function

$$e^{-[(t-t_0)/width]^2}$$

where S_0 is related to the initial radical concentration, k_a and k_b are rate constants, and y_0 is a constant y-axis offset to account for baseline effects. Figure 1 shows (a) CH₂OO and (b) IO kinetics at a range of CH₂I₂ concentrations. For CH₂OO, the kinetics traces were summed over the wavelength interval 340 to 360 nm, minimizing spectral contributions from both CH₂I₂ and IO. IO data was obtained from 415 to 433 nm.

We used very low initial CH₂I₂ ($(1.3\text{--}9.1)\times 10^{13}\text{ cm}^{-3}$) along with high O₂ ($6.3\times 10^{16}\text{ cm}^{-3}$) in order to determine the rate for reaction (3), so that we could decouple the IO that was formed during the reaction we are attempting to measure (k_3) from IO radicals formed in a competitive CH₂I reaction, reaction (5).



By design, the latter reaction was nearly instantaneous (the literature rate of reaction of CH₂I with O₂ is $(1.1 \pm 0.2)\times 10^{-12}\text{ cm}^3\text{ s}^{-1}$,¹⁹ yielding formation rates greater than 100 ms^{-1}), so appearance of IO was limited by reaction (3). In addition to varying [CH₂I₂], we also varied [O₃] from $(2\text{--}11)\times 10^{13}\text{ cm}^{-3}$ (keeping it relatively low to minimize additional IO formation from reaction of I atoms with O₃, reaction (6)), in order to keep a consistent number of estimated initial CH₂I radicals ($[\text{CH}_2\text{I}]_0 \approx 9\times 10^{11}\text{ cm}^{-3}$) in each experiment. With these considerations, we were able to fit CH₂OO and IO at the same time to obtain the rate of reaction (3) from a global fit of all conditions.

For each CH₂I₂ concentration, we fit for the formation rate of CH₂OO and IO as linked variables. All other parameters were allowed to vary independently, except for those describing the instrument function, which were linked amongst all kinetic traces in the global fit. As the initial CH₂I₂ concentration increased, the product formation rate also increased. Removal of CH₂OO was primarily due to self-reaction; IO was similarly removed through reaction with other IO radicals.

Figure 2 shows the dependence on the formation rate of CH₂OO and IO as a function of initial CH₂I₂ concentration. The error bars on the k_a formation rate coefficient are 20% error

bars. The result of the linear fit of k_a versus CH_2I_2 concentration finds a $\text{CH}_2\text{I}_2 + \text{O}(^3\text{P})$ rate constant of $k_3 = (6.8 \pm 0.9) \times 10^{-11} \text{ cm}^3 \text{ s}^{-1}$ with a y-intercept of $0.4 \pm 0.02 \text{ ms}^{-1}$. This value is within reasonable agreement with that of Teruel et al.,¹⁸ and was used in analyzing the $\text{CH}_2\text{OO} + \text{O}_3$ rate constant, discussed next.

3.2 $\text{CH}_2\text{OO} + \text{O}_3$ rate constant

In order to measure the title reaction rate k_1 , we operated under experimental conditions that promoted reaction (1), while minimizing secondary chemistry. To measure the bimolecular reaction rate, we varied the ozone concentration and maintained the same number of initial CH_2OO molecules. In order to vary ozone but not the initial number of CH_2I radicals formed (since most of the CH_2I came from reactions of CH_2I_2 with $\text{O}(^3\text{P})$ (formed indirectly from photolysis of ozone), we had to also vary the photolysis laser fluence, decreasing the laser fluence while raising the ozone concentration. We varied the ozone concentration from 2×10^{13} – $1 \times 10^{15} \text{ cm}^{-3}$ with the initial CH_2I concentration maintained at around $1 \times 10^{12} \text{ radicals cm}^{-3}$. A global fit of the CH_2OO kinetics traces was performed, allowing both the formation and decay rates to float but constraining the instrument response function parameters. Figure 3 shows an example of a global fit for nine of the initial ozone concentrations. As the initial ozone concentration increased, the decay rate of CH_2OO also increased. Figure 4 demonstrates the linear dependence between the fitted CH_2OO decay rates and the initial ozone concentration. From this data, we obtained a rate constant for $\text{CH}_2\text{OO} + \text{O}_3$ of $k_1 = (7.9 \pm 0.7) \times 10^{-13} \text{ cm}^3 \text{ s}^{-1}$ with a y-intercept of $0.29 \pm 0.03 \text{ ms}^{-1}$. The scatter in the data is significant, however.

3.3 Time-dependent spectrum simulations

One difficulty in conducting the experiments described in this chapter was an increasingly-crowded spectrum. Figure 5 shows the three species that primarily absorbed light between 300 and 440 nm: CH_2I_2 and IO (taken from Sander et al.¹⁷) and CH_2OO (taken from Ting et al.¹⁹). All three species overlap spectrally. Previous work on this apparatus operated under conditions that minimized the contributions of CH_2I_2 and IO to the kinetics trace of CH_2OO – specifically operating with very little IO formation. In this work, we formed a significant amount of IO which complicated spectral deconvolution. To achieve this, we modeled the

time evolution of each species using a kinetics model (Table 1) and numerical simulation program.²⁰ We used the modeled time traces along with the literature spectra to reconstruct the time-dependent spectrum.

3.3.a CH₂OO Self-Reaction Simulation

To test this procedure, we first carried out experiments on the C.I. self-reaction, duplicating previous work on the instrument.¹⁴⁻¹⁵ The Criegee intermediate was formed from reaction of O₂ with CH₂I radicals created directly by photolysis of CH₂I₂. Figure 6(a) shows the two-dimensional image obtained from these experiments, showing the time-evolution of the spectrum. The photolysis laser fires at 0 milliseconds, after the spectrometer has collected over 1 ms of background signal. The spectra presented here have been background-subtracted, to remove absorbance from the CH₂I₂ signal. The broad signal appearing upon photolysis between 300–390 nm is primarily from absorption by the Criegee intermediate. The sharp lines > 400 nm are the IO radical, which is formed in small quantities in competition with CH₂OO from the CH₂I + O₂ reaction.

Using the kinetics model listed in Table 1 and the literature spectra of absorbers present in this system, shown in Figure 5, we simulated (Figure 6(b)) the same two-dimensional image that was presented in panel (a). Given the concentration of CH₂I₂ in the reactor, the measured laser fluence, and the CH₂I₂ photodissociation cross section, we modeled the number of CH₂I radicals present after photolysis. With these starting conditions we modeled the kinetics of the absorbers in the system (CH₂I₂, CH₂OO, and IO), and reproduced the spectrum as a simulated optical density plot. Absorption by CH₂I and H₂CO have negligible contribution to the spectra. The two images shown in Figure 6 have good qualitative agreement, both showing the broad absorption from the C.I. that decays almost completely by 5 ms after photolysis. Above 400 nm, the sharp features from IO appear, looking to be present from 0 – 5 ms without dramatic changes in concentration. The absolute intensity (z-axis) of both three-dimensional plots is on the same scale, reported in optical density units. If the modeled concentrations and cross sections properly reproduce the experimental conditions, then the absolute intensity of the simulation should match that of the experiment.

In order to assess the spectra reconstruction, we take a snapshot of the experimental and modeled spectra, integrating from 0–1 ms (Figure 7). The experimental spectrum (black dots) is dominated by the broad CH₂OO absorption, with small contributions evident > 400 nm from IO. The simulated spectrum (red line) agrees extremely well with that from experiment at wavelengths greater than 350 nm. However, the simulation underrepresents the intensity below 350 nm. The uncertainty in the simulated spectrum from uncertainty in the rate constants shown in Table 1 (demonstrated as the shaded grey area) is not enough to explain this discrepancy.

Figure 8 shows the kinetic traces for (a) CH₂OO (summed from 340–360 nm) and (b) IO (summed from 415–433 nm), compared with the simulation over the same ranges. For both molecules, diffusion out of the probe region was taken into consideration. In principle, diffusion can and has been modeled for this reactor. The modeled diffusion rate for CH₂OO formed in this reactor was found²¹ to be ~150 s⁻¹ using the Comsol software package. Diffusion terms of 100 and 50 s⁻¹ for CH₂OO and IO, respectively, were used to fit the data shown in Figure 8, in good agreement with modeling. IO, as a larger molecule, should have a slower diffusion rate compared to CH₂OO. This modeling demonstrates that we can reproduce the experimental time-dependent spectrum of the C.I. self-reaction conditions quite well above 350 nm.

3.3.b CH₂OO + O₃ Simulation

For experiments measuring the CH₂OO + O₃ rate constant, we followed the same procedure described above, using the rate constant reported in section 3.2 ($k_1 = (7.9 \pm 0.7) \times 10^{-13} \text{ cm}^3 \text{ s}^{-1}$) to simulate the time-dependent spectrum. Figure 9 shows the simulated CH₂I₂, O₃, CH₂OO, and IO contributions to the spectrum, before background subtraction for an experiment with $4.4 \times 10^{13} \text{ CH}_2\text{I}_2 \text{ cm}^{-3}$ and $5.6 \times 10^{13} \text{ O}_3 \text{ cm}^{-3}$. Peak optical densities for each species in this spectra window are: CH₂I₂ – 1×10^{-2} , O₃ – 1.5×10^{-3} , CH₂OO – 4×10^{-4} , IO – 1×10^{-3} . The CH₂I₂ is very optically-thick, but is rather time-independent (less than 2% of the initial CH₂I₂ is removed by photolysis or chemistry) and could be subtracted from the final two-dimensional image to reveal the underlying chemistry. The optical density of IO is also very high, with more than double the intensity of peak CH₂OO. Figure 10 compares the

experimental two-dimensional background-subtracted data (panel (a)) with the simulated spectrum in panel (b). The simulated spectrum was produced by adding the four spectra from Figure 9 to yield the total time vs. wavelength vs. optical density plot which was then treated the same way as the experimental spectrum and background-subtracted. Here we can see that the C.I. is much shorter-lived than in the self-reaction experiments and that there is significantly more IO present. Looking just at the CH₂OO and IO kinetics in Figure 11 (summed over the same wavelength region as before) shows that although the CH₂OO decay rate agrees between experiment and simulation, the absolute intensity of CH₂OO is underestimated in the simulation. At the same time, the simulated IO trace decays more rapidly than experiment.

3.3.c Spectral Analysis

The experiments described here relied primarily on analyzing the CH₂OO and IO kinetics using data from small ~20 nm windows in the spectrum, as indicated in Figure 5. The assumption is that absorption in these two regions depends almost entirely on those two species alone. However, both regions clearly include contributions from other species: CH₂I₂, CH₂OO, and IO all absorb between 340 – 360 nm and both CH₂OO and IO absorb in the 415–433 nm region. To assess the impact such spectral overlap has on measured kinetics, we modeled the CH₂OO spectral region at two extreme scenarios: (1) an experiment with low initial CH₂I₂ ($1.3 \times 10^{13} \text{ cm}^{-3}$) and O₃ ($2.7 \times 10^{13} \text{ cm}^{-3}$) (and subsequently minimal formation of IO) and (2) an experiment with comparatively high initial reactant conditions ($[\text{CH}_2\text{I}_2]_0 = 9.2 \times 10^{13} \text{ cm}^{-3}$) and $[\text{O}_3]_0 = 6.7 \times 10^{14} \text{ cm}^{-3}$) and significant IO formation. Figure 12(a) shows scenario (1). Using the kinetics model and the absorption cross sections for the species that absorb in this region, we simulated the time-dependence of the absorption (in units of optical density). The red line is the modeled CH₂OO kinetics, purple is the IO kinetics, and green is the background-subtracted CH₂I₂ kinetics. IO and CH₂I₂ contribute minimally to the sum of all kinetics traces (black line). We then fit both the black (summed) and red (CH₂OO-only) traces with the double exponential formula described in section 3.1 and obtained nearly the same fitted values. This demonstrates that at conditions with low initial reactant

concentrations we can expect that a fit to the data summed between 340–360 nm will be reasonably representative of the CH₂OO kinetics.

On the other hand, reaction conditions that begin with high initial reactant concentrations may result in incorrect reaction rate measurements if fit in this same window without consideration of the spectral interference by CH₂I₂ and IO. Figure 12(b) shows the CH₂OO (red), IO (purple), background-subtracted CH₂I₂ (green), and summed (black) kinetics traces for scenario (2) (described above). Here, a very large number of IO radicals are formed promptly (primarily from reaction (6): I + O₃); few IO radicals are subsequently removed after this initial influx of absorbers. Even though the absorption cross section for IO is less than 2.5×10^{-18} cm² in this spectral region, absorption by IO cannot be ignored here. Fitting the black (summed) and red (CH₂OO) traces to the same double-exponential fitting function results in statistically-significant changes in the formation and decay rates. In the summed model, the formation rate is about 15% faster than that of CH₂OO alone. Similarly, the decay rate of the summed model is about 10% slower than that of the CH₂OO trace.

Unless a spectral window can be identified that isolates CH₂OO from significant overlap with other absorbers, a multi-spectrum fitting approach may be the only way to properly obtain reaction rates for experimental conditions with high concentrations of CH₂I₂ and IO. However, our current inability to reproduce the full spectrum through simulation (as seen in the discrepancy below 350 nm in Figure 7) hinders such analysis. Although the cross sections of CH₂I₂ and IO are very low, their high concentrations in our experiments necessitates a good understanding of those spectra in the region where CH₂OO also absorbs. Improvements could be made in our measurement of both CH₂I₂ and IO, either by developing a better understanding of the BB-CEAS mirror reflectivity¹⁶ or by obtaining better reference spectra. An example of an improvement that could be made is the behavior of the IO spectrum at wavelengths smaller than 340 nm. The IO spectrum shown in Figure 5 drops to zero just below 340 nm, since the JPL evaluation whence the IO literature spectrum cuts out at 339 nm. A better constraint on the IO spectrum below 350 nm may lead to improved agreement between the simulated intensities and experimental data.

4 Discussion

Using time-resolved broadband cavity enhances absorption spectroscopy, we measured the rate coefficients for reaction of CH₂I₂ with O(³P) and reaction of CH₂OO with O₃. The rate for the former reaction has been measured experimentally in the past, and our value of $(6.8 \pm 0.9) \times 10^{-11} \text{ cm}^3 \text{ s}^{-1}$ is in good agreement with the literature value $((7.36 \pm 0.31) \times 10^{-11} \text{ cm}^3 \text{ s}^{-1})$. Unlike the O(³P) reaction with CH₂I₂, no direct experimental measurement of the reaction of C.I. with ozone exists in the literature, but quantum chemistry calculations predict a rate coefficient for CH₂OO + O₃ of $1 \times 10^{-12} \text{ cm}^3 \text{ s}^{-1}$. In this work, we experimentally measure the CH₂OO + O₃ rate coefficient by measuring the CH₂OO decay rate as a function of ozone concentration. The resulting rate constant was $(7.9 \pm 0.7) \times 10^{-13} \text{ cm}^3 \text{ s}^{-1}$, which is in reasonable agreement with the theoretical prediction. However, significant scatter in the data, along with observed perturbation of the CH₂OO kinetics by other absorbers, suggests that additional work should be done to improve the credibility of this result.

5 References

1. Criegee, R., Mechanism of Ozonolysis. *Angew. Chem. Int. Ed.* **1975**, *14*, 745-752.
2. Welz, O.; Savee, J. D.; Osborn, D. L.; Vasu, S. S.; Percival, C. J.; Shallcross, D. E.; Taatjes, C. A., Direct Kinetic Measurements of Criegee Intermediate (CH₂OO) Formed by Reaction of CH₂I with O₂. *Science* **2012**, *335*, 204-207.
3. Osborn, D. L.; Taatjes, C. A., The Physical Chemistry of Criegee Intermediates in the Gas Phase. *Int. Rev. Phys. Chem.* **2015**, *34*, 309-360.
4. Taatjes, C. A.; Shallcross, D. E.; Percival, C. J., Research Frontiers in the Chemistry of Criegee Intermediates and Tropospheric Ozonolysis. *Phys. Chem. Chem. Phys.* **2014**, *16*, 1704-1718.
5. Chao, W.; Hsieh, J.-T.; Chang, C.-H.; Lin, J. J.-M., Direct Kinetic Measurement of the Reaction of the Simplest Criegee Intermediate with Water Vapor. *Science* **2015**, *347*, 751-754.
6. Lewis, T. R.; Blitz, M. A.; Heard, D. E.; Seakins, P. W., Direct Evidence for a Substantive Reaction Between the Criegee Intermediate, CH₂OO, and the Water Vapour Dimer. *Phys. Chem. Chem. Phys.* **2015**, *17*, 4859-4863.
7. Okumura, M., Just Add Water Dimers. *Science* **2015**, *347*, 718-719.
8. Vereecken, L.; Harder, H.; Novelli, A., The Reactions of Criegee Intermediates with Alkenes, Ozone, and Carbonyl Oxides. *Phys. Chem. Chem. Phys.* **2014**, *16*, 4039-4049.

9. Kroll, J. H.; Clarke, J. S.; Donahue, N. M.; Anderson, J. G., Mechanism of HO_x Formation in the Gas-Phase Ozone – Alkene Reaction. 1. Direct, Pressure-Dependent Measurements of Prompt OH Yields. *J. Phys. Chem. A* **2001**, *105*, 1554-1560.
10. Womack, C. C.; Martin-Drumel, M.-A.; Brown, G. G.; Field, R. W.; McCarthy, M. C., Observation of the Simplest Criegee Intermediate CH₂OO in the Gas-phase Ozonolysis of Ethylene. *Sci. Adv.* **2015**, *1*.
11. Vereecken, L.; Francisco, J. S., Theoretical Studies of Atmospheric Reaction Mechanisms in the Troposphere. *Chem. Soc. Rev.* **2012**, *41*, 6259-6293.
12. Kjaergaard, H. G.; Kurtén, T.; Nielsen, L. B.; Jørgensen, S.; Wennberg, P. O., Criegee Intermediates React with Ozone. *J. Phys. Chem. Lett.* **2013**, *4*, 2525-2529.
13. Wei, W.-m.; Zheng, R.-h.; Pan, Y.-l.; Wu, Y.-k.; Yang, F.; Hong, S., Ozone Dissociation to Oxygen Affected by Criegee Intermediate. *J. Phys. Chem. A* **2014**, *118*, 1644-1650.
14. Sheps, L., Absolute Ultraviolet Absorption Spectrum of a Criegee Intermediate CH₂OO. *J. Phys. Chem. Lett.* **2013**, *4*, 4201-4205.
15. Sheps, L.; Scully, A. M.; Au, K., UV Absorption Probing of the Conformer-Dependent Reactivity of a Criegee Intermediate CH₃CHOO. *Phys. Chem. Chem. Phys.* **2014**, *16*, 26701-26706.
16. Sheps, L.; Chandler, D. W., *Time-Resolved Broadband Cavity-Enhanced Absorption Spectroscopy for Chemical Kinetics*. SAND2013-2664, Sandia National Laboratories, Livermore, CA, 2013.
17. Sander, S. P.; Abbatt, J.; Barker, J. R.; Burkholder, J. B.; Friedl, R. R.; Golden, D. M.; Huie, R. E.; Kolb, C. E.; Kurylo, M. J.; Moortgat, G. K., et al., Chemical Kinetics and Photochemical Data for Use in Atmospheric Studies, Evaluation Number 17. *JPL Publication 10-6* **2011**.
18. Teruel, M. A.; Dillon, T. J.; Horowitz, A.; Crowley, J. N., Reaction of O(³P) with the alkyl iodides: CF₃I, CH₃I, CH₂I₂, C₂H₅I, 1-C₃H₇I and 2-C₃H₇I. *Phys. Chem. Chem. Phys.* **2004**, *6*, 2172-2178.
19. Ting, W.-L.; Chang, C.-H.; Lee, Y.-F.; Matsui, H.; Lee, Y.-P.; Lin, J. J.-M., Detailed Mechanism of the CH₂I + O₂ Reaction: Yield and Self-reaction of the Simplest Criegee Intermediate CH₂OO. *J. Chem. Phys.* **2014**, *141*, 104308.
20. Ianni, J. C. *Kintecus*, Windows Version 2.80; <http://www.kintecus.com>, 2002.
21. Antonov, I., Personal Communication. 2015.
22. Chhantyal-Pun, R.; Davey, A.; Shallcross, D. E.; Percival, C. J.; Orr-Ewing, A. J., A Kinetic Study of the CH₂OO Criegee Intermediate Self-reaction, Reaction with SO₂ and Unimolecular Reaction Using Cavity Ring-down Spectroscopy. *Phys. Chem. Chem. Phys.* **2015**, *17*, 3617-3626.
23. Atkinson, R.; Baulch, D. L.; Cox, R. A.; Crowley, J. N.; Hampson, R. F.; Hynes, R. G.; Jenkin, M. E.; Rossi, M. J.; Troe, J., Evaluated Kinetic and Photochemical Data for Atmospheric Chemistry: Volume III – Gas Phase Reactions of Inorganic Halogens. *Atmos. Chem. Phys.* **2007**, *7*, 981-1191.

24. Baulch, D. L.; Duxbury, J.; Grant, S. J.; Montague, D. C., Evaluated Kinetic Data for High Temperature Reactions. Volume 4: Homogeneous Gas Phase Reactions of Halogen- and Cyanide-Containing Species. In *J. Phys. Chem. Ref. Data*, 1981; Vol. 10, Supplement No. 1.

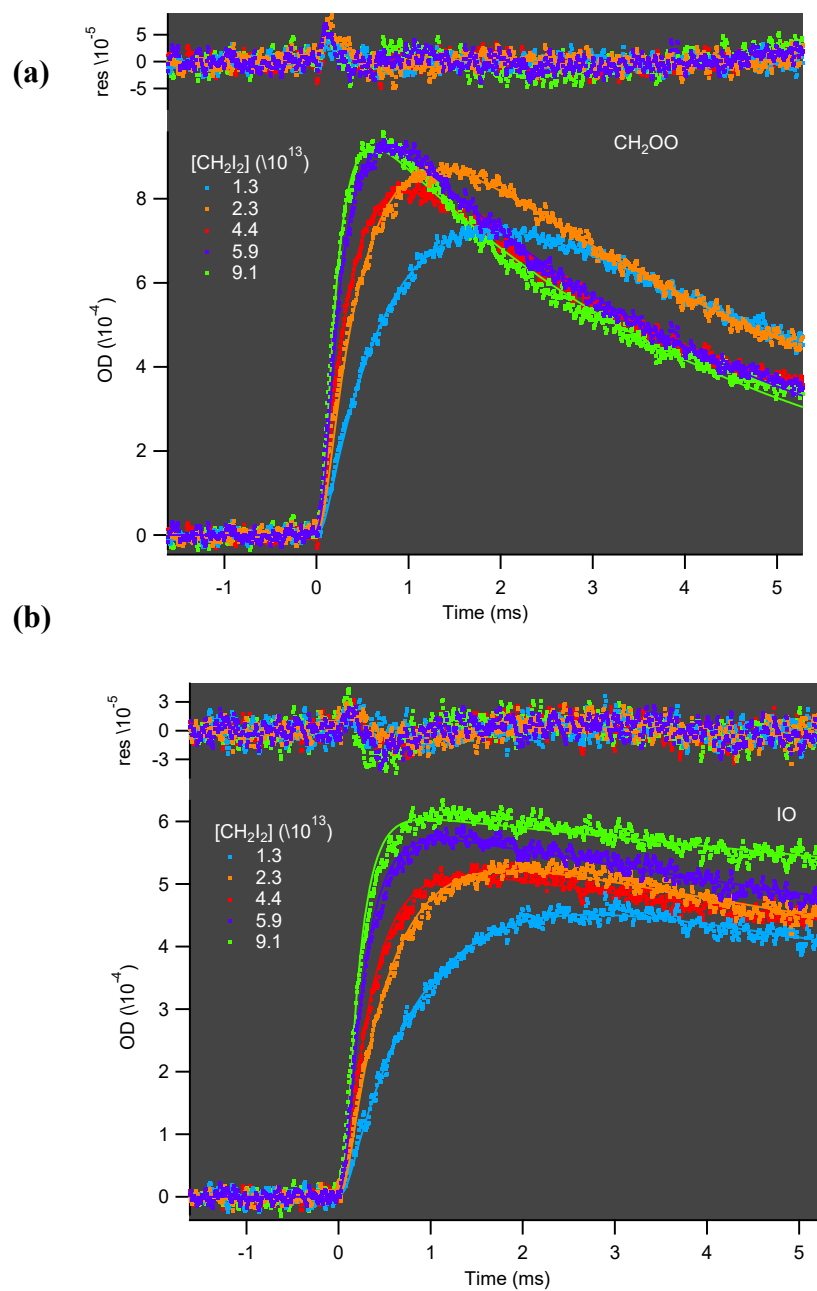


Figure 1. Kinetics traces for CH_2OO and IO formed from reaction of $\text{O}(^3\text{P})$ with CH_2I_2 , at a range of initial CH_2I_2 concentrations ($(1.3\text{--}9.1) \times 10^{13} \text{ cm}^{-3}$). The data (dots) have been fit to a global fit to the function described in the text, which was convolved with an instrument function, incorporating both species simultaneously and all CH_2I_2 concentrations. The model is shown as a solid line; the residuals (data minus model) are shown as dots above each plot.

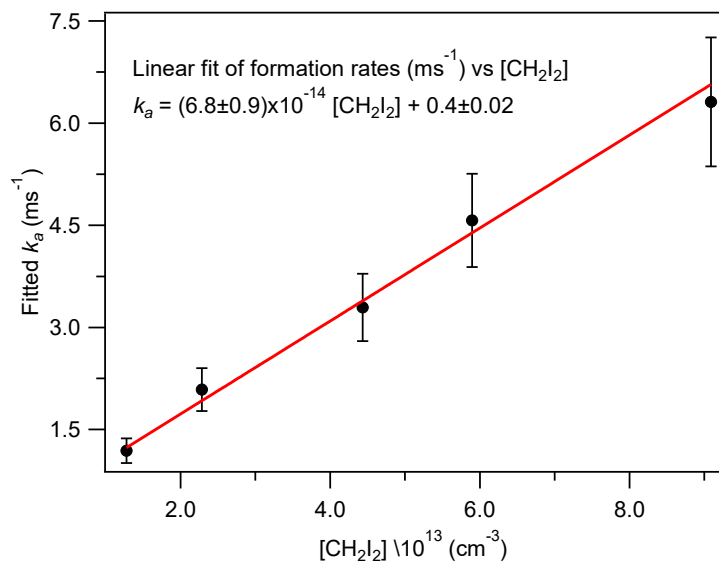


Figure 2. Dependence of CH_2OO and IO formation rates on $[\text{CH}_2\text{I}_2]$. A linear fit obtains $k_a = (6.8 \pm 0.9) \times 10^{-14} \text{ cm}^3 \text{ ms}^{-1}$ with a y-intercept of $0.4 \pm 0.02 \text{ ms}^{-1}$. The error bars in the data points represent the estimated 20% error in determining k_a .

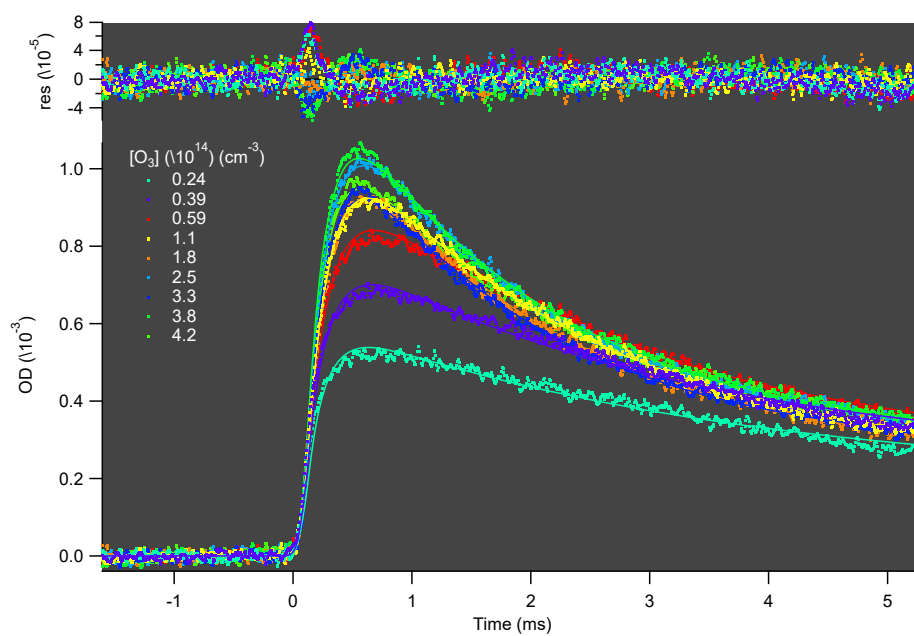


Figure 3. Kinetics traces for CH_2OO formed from reaction of $O(^3P)$ with CH_2I_2 , at a range of initial O_3 concentrations ($(0.24\text{--}4.2) \times 10^{14} \text{ cm}^{-3}$). The data (dots) have been fit to a global fit to the function described in the text, which was convolved with an instrument function, including all O_3 concentrations. The model is shown as a solid line; the residuals (data minus model) are shown as dots above each plot.

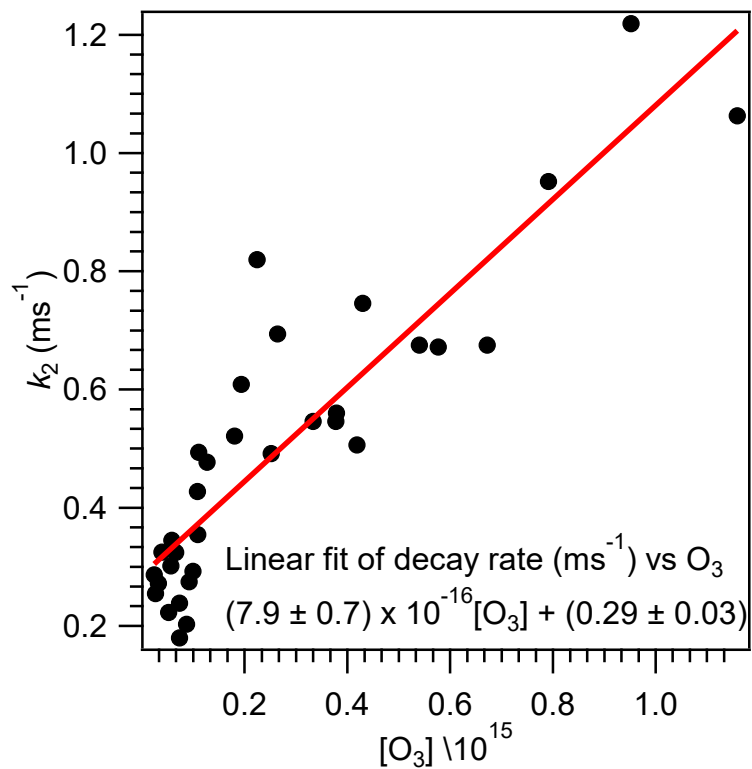


Figure 4. Ozone dependence of the CH_2OO decay rates (in ms^{-1}), as determined from a double-exponential fit of the CH_2OO experimental kinetics traces. The fitted decay rates are plotted as a function of ozone concentration, and are fit with a line. The rate coefficient k_1 from this data is $(7.9 \pm 0.7) \times 10^{-16} \text{ cm}^3 \text{ ms}^{-1}$ and a y-intercept of $0.29 \pm 0.03 \text{ ms}^{-1}$.

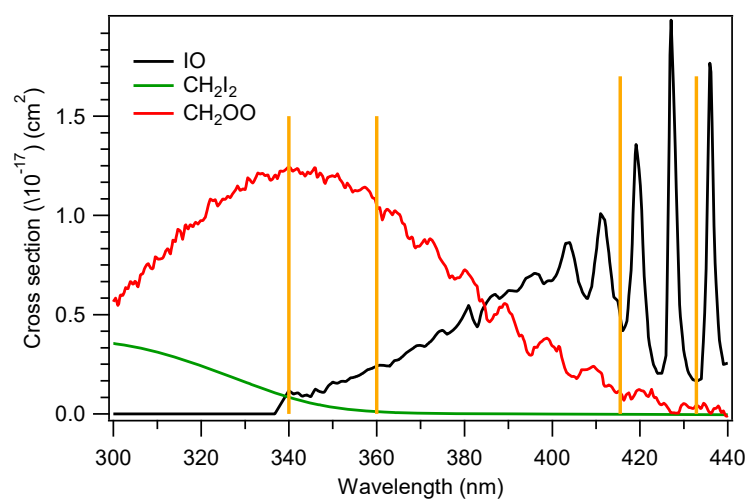


Figure 5. Absorption cross sections of relevant species present during experiments that absorb between 300–440 nm. The CH₂I₂ and IO spectra were taken from Sander et al.¹⁷ The CH₂OO spectrum was taken from Ting et al.¹⁹ The vertical orange lines indicate the regions where CH₂OO (340–360 nm) and IO (415–433 nm) kinetics traces were obtained.

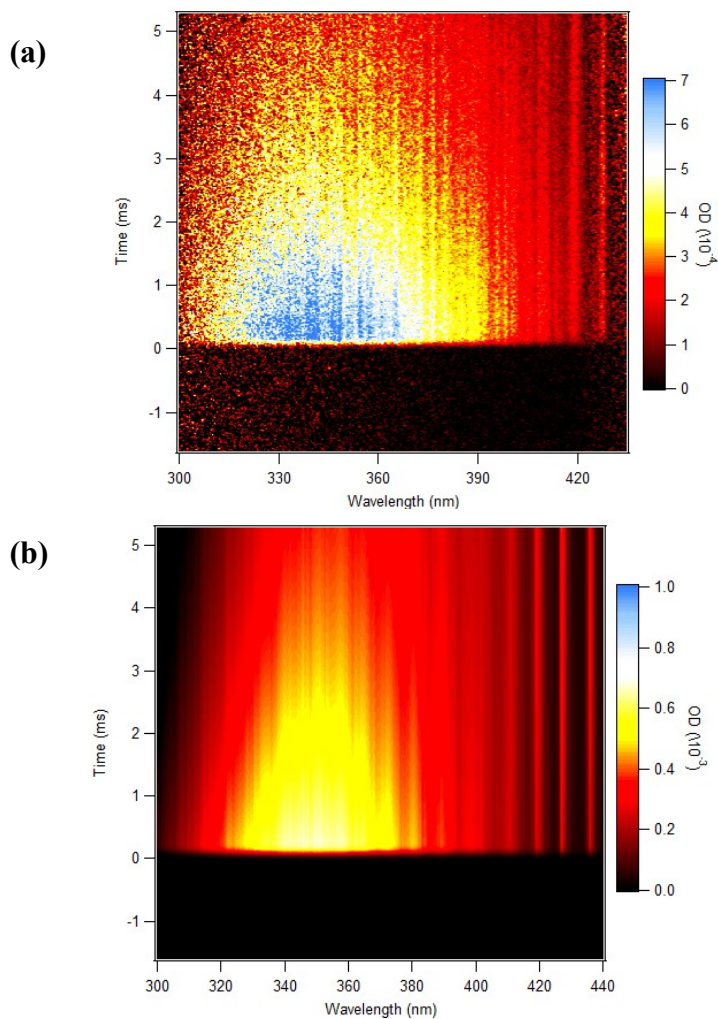


Figure 6. Two-dimensional images showing the time-dependence of the spectrum during $\text{CH}_2\text{OO} + \text{CH}_2\text{OO}$ experiments. Panel (a) shows the experimental spectrum. The pulsed photolysis laser fired at 0 ms forming radicals that are apparent as an increase in optical density where they absorb. Panel (b) shows the modeled spectrum, taking into account the literature absorption spectra and the kinetics model. Both images have been background-subtracted. Both panels are plotted on the same x,y,z axis scales.

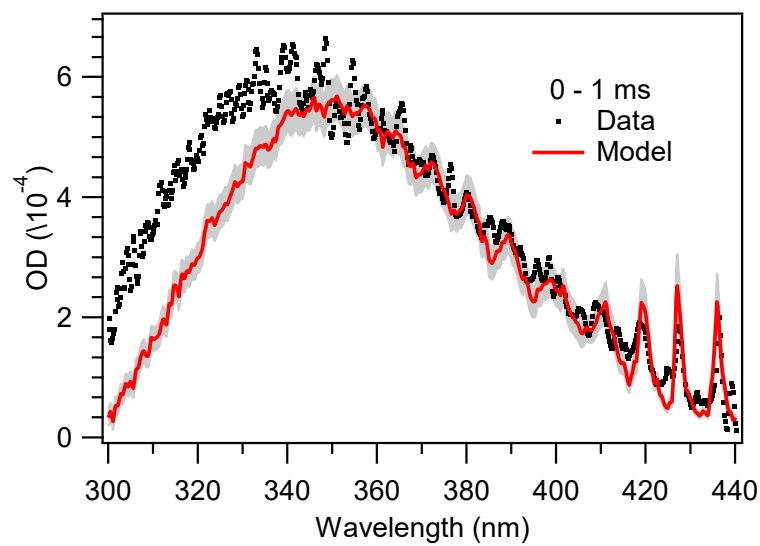


Figure 7. One-dimensional images showing the experimental (dots) and modeled (red line) spectrum of the CH_2OO self-reaction, integrated from 0–1 ms. The grey area represents the error in the simulated spectrum that comes from uncertainty in the kinetics model.

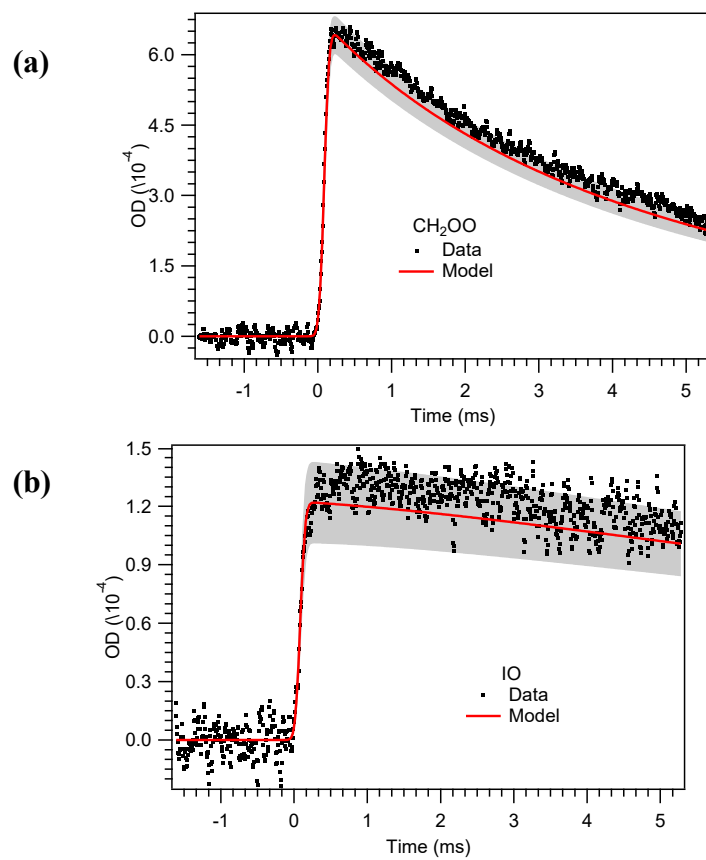


Figure 8. CH_2OO self-reaction kinetics traces for (a) CH_2OO and (b) IO formed during CH_2I_2 photolysis in the presence of O_2 .

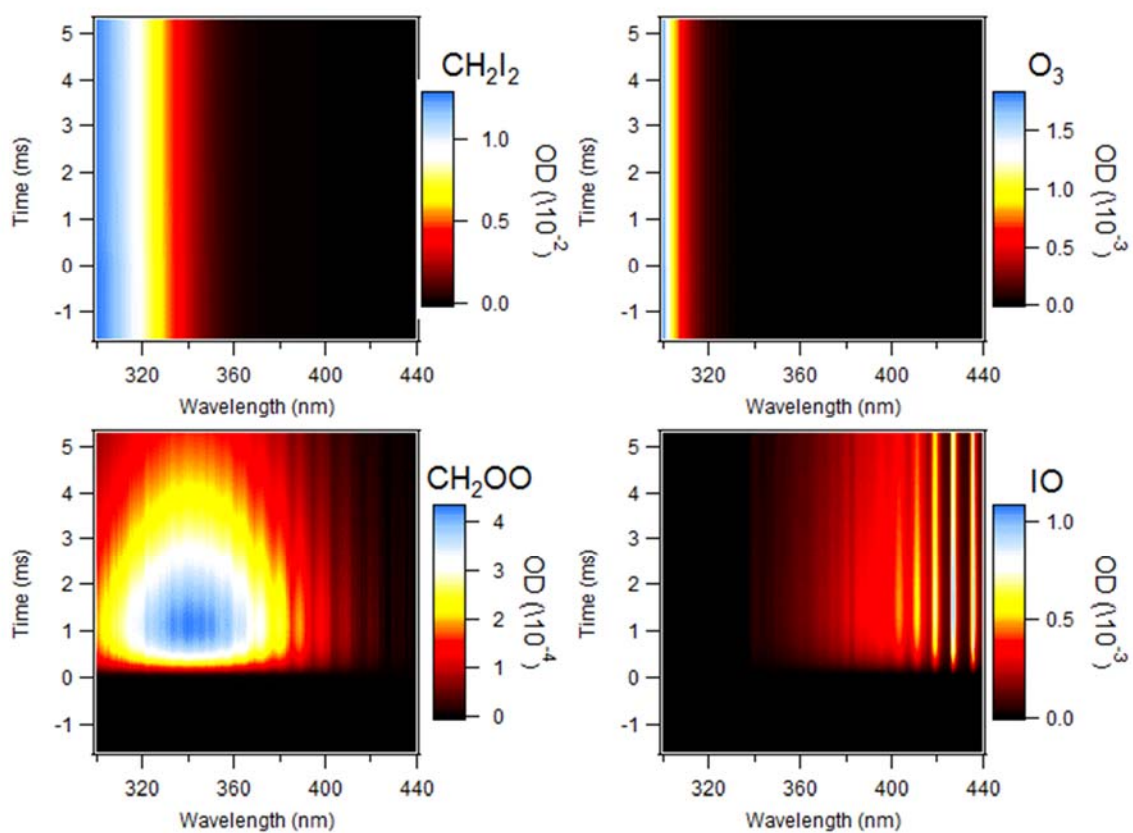


Figure 9. The four simulated spectra of absorbers in the CH₂OO + O₃ experiment. CH₂I₂ and O₃ are both present before photolysis. CH₂OO and IO grow in rapidly at $t = 0$.

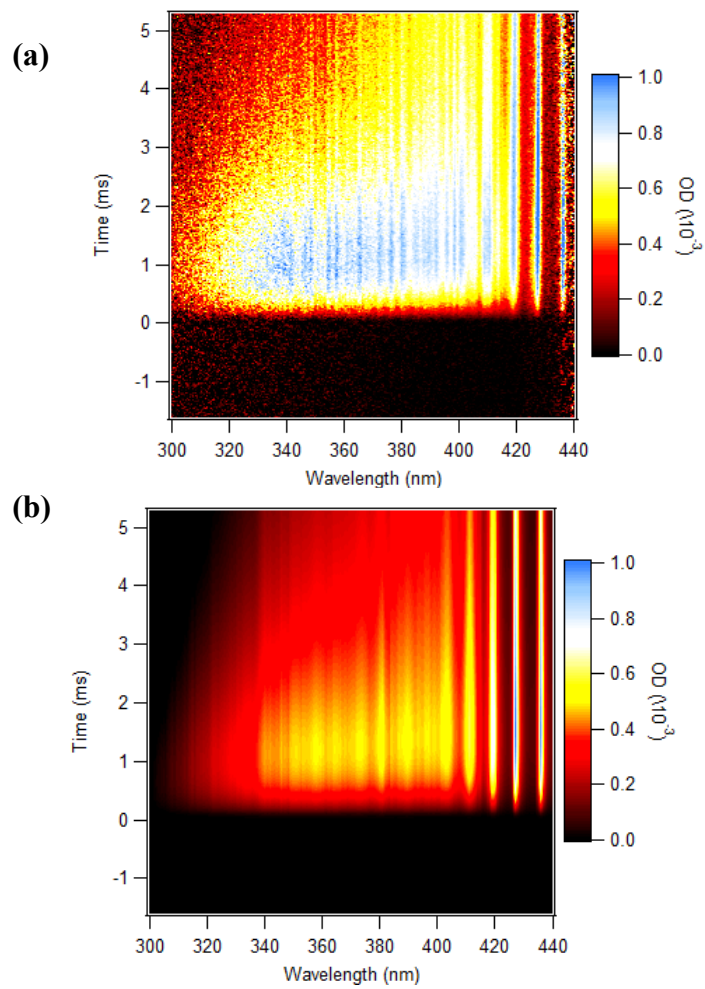


Figure 10. Two-dimensional plots of the (a) experimental and (b) simulated time-dependent spectra obtained during $\text{CH}_2\text{OO} + \text{O}_3$ experiments. Both images have been background subtracted.

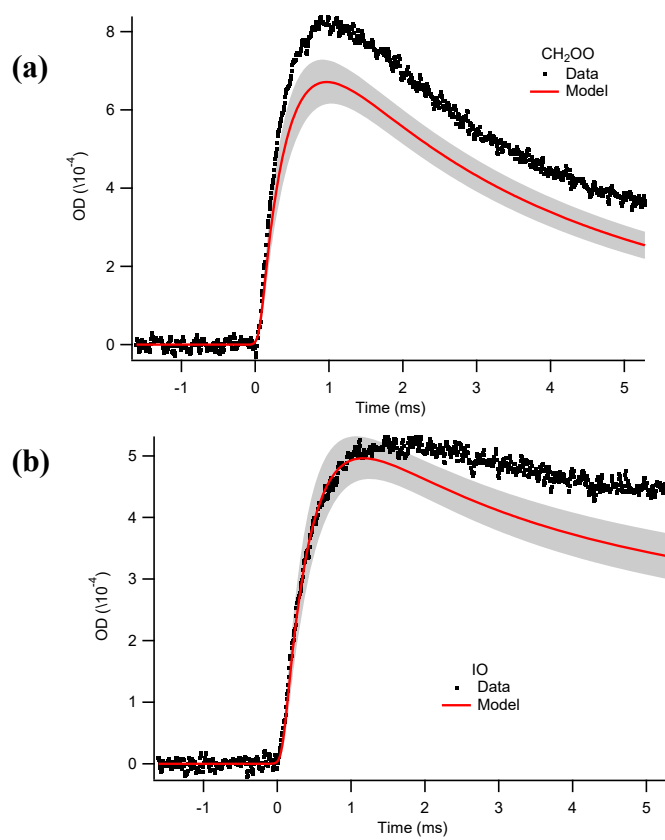


Figure 11. Experimental and simulated kinetics of CH_2OO and IO in $\text{CH}_2\text{OO} + \text{O}_3$ experiments.

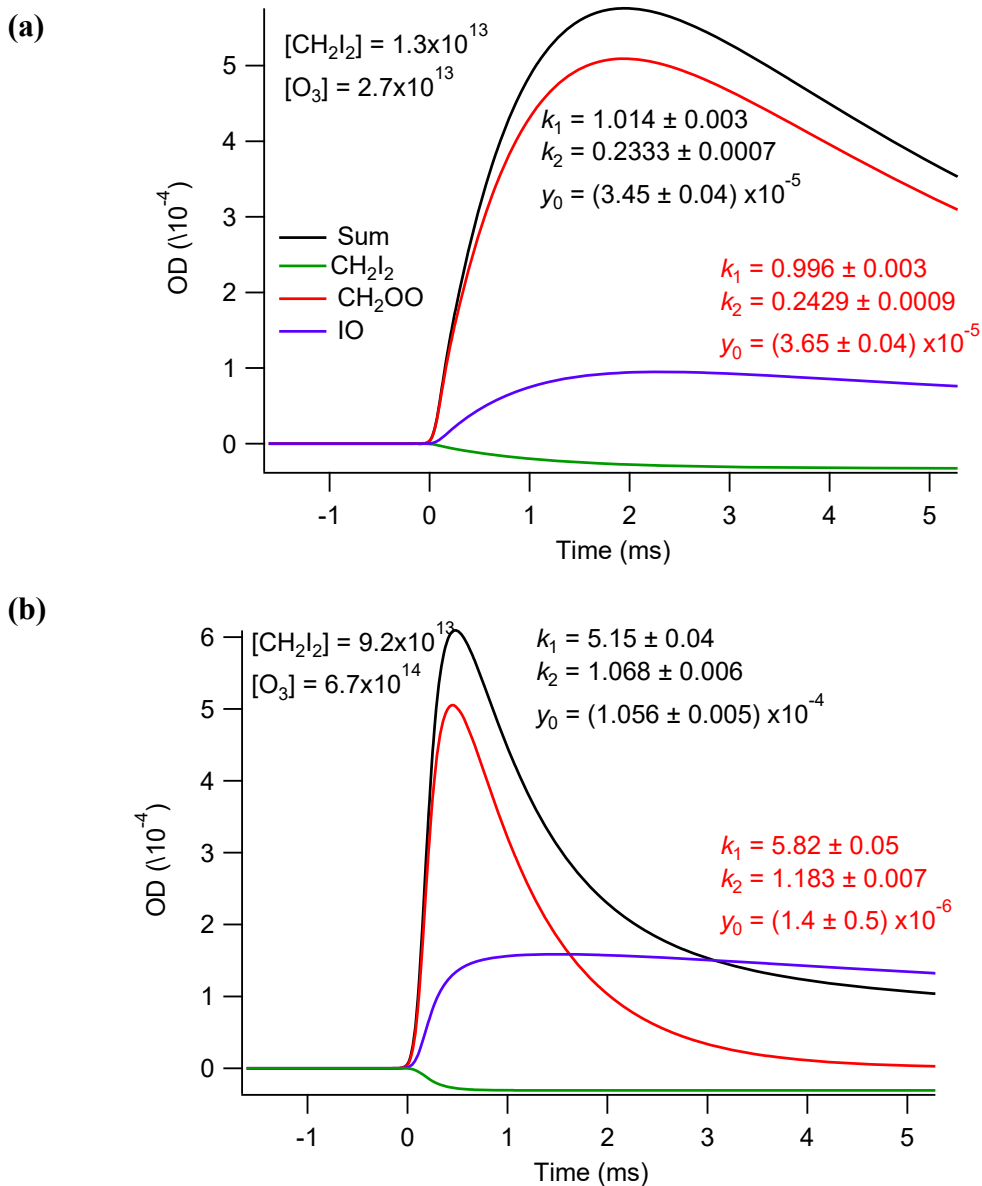


Figure 12. Assessment of the perturbation to CH_2OO fits cause by absorption of other species like IO and CH_2I_2 . (a) Simulated kinetics with initial reaction conditions: $[\text{CH}_2\text{I}_2]_0 = 1.3 \times 10^{13} \text{ cm}^{-3}$, $[\text{O}_3]_0 = 2.7 \times 10^{13} \text{ cm}^{-3}$. The summed model has a fitted formation rate of $1.014 \pm 0.003 \text{ ms}^{-1}$ and decay rate of $0.2333 \pm 0.0007 \text{ ms}^{-1}$. CH_2OO by itself has a fitted formation rate of $0.996 \pm 0.003 \text{ ms}^{-1}$ and decay rate of $0.2429 \pm 0.0009 \text{ ms}^{-1}$. (b) Simulated kinetics with initial reaction conditions: $[\text{CH}_2\text{I}_2]_0 = 9.2 \times 10^{13} \text{ cm}^{-3}$, $[\text{O}_3]_0 = 6.7 \times 10^{14} \text{ cm}^{-3}$. The summed model has a fitted formation rate of $5.15 \pm 0.04 \text{ ms}^{-1}$ and decay rate of $1.069 \pm 0.006 \text{ ms}^{-1}$. CH_2OO by itself has a fitted formation rate of $5.82 \pm 0.05 \text{ ms}^{-1}$ and decay rate of $1.183 \pm 0.007 \text{ ms}^{-1}$.

Table 1. Kinetics model. Rate constants are reported in $\text{cm}^3 \text{s}^{-1}$. The rates of termolecular reactions are reported at 10 Torr.

Reaction	Rate	Ref
(1) $\text{CH}_2\text{OO} + \text{O}_3 \rightarrow \text{H}_2\text{CO} + 2\text{O}_2$	---	this work
(2) $\text{CH}_2\text{OO} + \text{CH}_2\text{OO} \rightarrow 2\text{H}_2\text{CO} + \text{O}_2$	$(7.4 \pm 0.6) \times 10^{-11}$	a
(3) $\text{CH}_2\text{I}_2 + \text{O}({}^3\text{P}) \rightarrow \text{CH}_2\text{I} + \text{IO}$	---	this work
(4) $\text{CH}_2\text{I} + \text{O}_2 \rightarrow \text{CH}_2\text{OO} + \text{I}$	$(1.1 \pm 0.2) \times 10^{-12}$	b
(5) $\text{CH}_2\text{I} + \text{O}_2 \rightarrow \text{H}_2\text{CO} + \text{IO}$	$(2.5 \pm 0.5) \times 10^{-13}$	b
(6) $\text{I} + \text{O}_3 \rightarrow \text{IO} + \text{O}_2$	$(1.2 \pm 0.2) \times 10^{-12}$	c
(7) $\text{I} + \text{CH}_2\text{OO} \rightarrow \text{CH}_2\text{I} + \text{O}_2$	8.0×10^{-11}	b
(8) $\text{I} + \text{CH}_2\text{OO} \rightarrow \text{CH}_2\text{IOO}$	2.8×10^{-12}	b
(9) $\text{I} + \text{CH}_2\text{OO} \rightarrow \text{H}_2\text{CO} + \text{IO}$	9.0×10^{-12}	b
(10) $\text{IO} + \text{O} \rightarrow \text{O}_2 + \text{I}$	$(1 \pm 1) \times 10^{-10}$	c
(11) $\text{IO} + \text{IO} \rightarrow 2\text{I} + \text{O}_2$	$(6 \pm 2) \times 10^{-11}$	d
(12) $\text{IO} + \text{IO} \rightarrow \text{OIO} + \text{I}$	$(4 \pm 1) \times 10^{-11}$	d
(13) $\text{I}_2 + \text{O} \rightarrow \text{IO} + \text{I}$	$(1.4 \pm 0.6) \times 10^{-10}$	c
(14) $\text{I} + \text{I} \rightarrow \text{I}_2$	$(2.7 \pm 0.8) \times 10^{-15}$	e
(15) $\text{O}({}^1\text{D}) + \text{O}_2 \rightarrow \text{O}({}^3\text{P}) + \text{O}_2$	$(4.0 \pm 0.4) \times 10^{-11}$	c
(16) $\text{O}({}^1\text{D}) + \text{O}_3 \rightarrow 2\text{O}_2$	$(1.2 \pm 0.2) \times 10^{-10}$	c
(17) $\text{O}({}^1\text{D}) + \text{O}_3 \rightarrow \text{O}_2 + 2\text{O}({}^3\text{P})$	$(1.2 \pm 0.2) \times 10^{-10}$	c
(18) $\text{O}({}^3\text{P}) + \text{O}_2 \rightarrow \text{O}_3$	$(2.0 \pm 0.2) \times 10^{-16}$	c
(19) $\text{O}({}^3\text{P}) + \text{O}_3 \rightarrow 2\text{O}_2$	$(8.0 \pm 0.8) \times 10^{-15}$	c
(20) $\text{CH}_2\text{I}_2 + h\nu \rightarrow \text{CH}_2\text{I} + \text{I}$		
(21) $\text{O}_3 + h\nu \rightarrow \text{O}({}^1\text{D}) + \text{O}_2$		

^aTaken from Chhantyal-Pun et al.²² ^bTaken from Ting et al.¹⁹ ^cTaken from the Sander et al..¹⁷

^dTaken from Atkinson et al.²³ ^eTaken from Baulch et al.²⁴

6 Supporting Information

6.1 Igor procedure file for simulating 2D spectra for BB-CEAS

The time-dependent reaction systems described in the previous chapter were modeled with Kintecus using the mechanism listed in Table 1. The CH₂I₂, O₃, CH₂OO, and IO simulated kinetics traces were then imported into IgorPro where they could be convolved with the instrument function and easily converted into two-dimension plots for direct comparison with experimental data. Convolution of the kinetics traces with the instrument function was accomplished using the `convolve_kintecus(w,p)` function, shown below, where `w` is the Kintecus simulated output wave and `p` is a 4×1 dimensional wave prepared with the instrument response function parameters and initial conditions. The `simulate_2D(CH2OO, XS_CH2OO, IO, XS_IO, CH2I2, XS_CH2I2, O3, XS_O3, coef, wavelength)` function takes simulated kinetics traces, convolves them with the instrument response function through the `convolve_kintecus` function, and then using provided reference spectra, simulates the two-dimensional image of the time-evolution of the absorption spectrum. It creates four individual two-dimensional images, one for each of the following species: CH₂I₂, O₃, CH₂OO, and IO. Then, it sums the four two dimensional spectra, resulting in one final summed spectrum that it background subtracts, using a function available in Sheps's original TR-BB-CEAS Procedures IgorPro procedure file.

The two functions, `convolve_kintecus` and `simulate_2D` are given below.

```
#pragma rtGlobals=3    // Use modern global access method and strict wave access.
```

```
Function convolve_kintecus(w,p)
```

```
// This function takes the kinetics model output from Kintecus and convolves it with
the instrument response function. User must supply the modeled Kintecus trace as a wave
w and a 4×1 dimensional wave p containing the instrument response function parameters
and initial conditions.
```

```
p[0] = to (ms-1)
p[1] = width (ms-1)
p[2] = step size (ms-1)
p[3] = concentration of species at t < 0
```

```
Wave w, p
```

```
// Make gaussian instrument response function
```

```
make/o/d/n=201 resp_func
SetScale/p x, (-100*p[2]), p[2], resp_func
resp_func = exp(-((x-p[1])/p[0])^2)
```

```
make/o/d/n=240 pre_phot
pre_phot = p[3]
```

```
// Convolve the kinetics trace with the instrument response function
```

```
make/o/d/n=1024 temp
concatenate/o {pre_phot,w}^24, temp
SetScale/P x -1.61502,0.00674,"", temp
convolve/a resp_func, temp
Redimension/N=1064 w
w = temp/sum(resp_func)
```

```
w[0,190] = p[3]
SetScale/P x -1.61502,0.00674,"", w
```

```
KillWaves temp,pre_phot,resp_func
end
```

```
Function simulate_2D(CH2OO, XS_CH2OO, IO, XS_IO, CH2I2, XS_CH2I2, O3,
XS_O3, coef, wavelength)
```

```
// This function simulates the 2-dimensional image from a kinetics model (modeling the
concentrations of CH2OO, IO, CH2I2, and O3) and determines the time evolution of the
spectrum using input absorption spectra (XS_CH2OO, XS_IO, XS_CH2I2, XS_O3).
coef is 4×1 dimensional wave containing the same parameters as those listed for wave p
in the convolve_kintecus function. Wavelength is the wave which was calibrated to
convert index to wavelength.
```

```
wave
CH2OO,XS_CH2OO,IO,XS_IO,CH2I2,XS_CH2I2,O3,XS_O3,coef,wavelength
```

```

variable i,j
Duplicate/o coef, temp_coef
Duplicate/o CH2OO, kin_CH2OO
Duplicate/o IO, kin_IO
Duplicate/o CH2I2, kin_CH2I2
Duplicate/o O3, kin_O3

convolve_kintecus(kin_CH2I2,coef)
temp_coef[3] = coef[4]
convolve_kintecus(kin_O3,temp_coef)
temp_coef[3] = 0
convolve_kintecus(kin_CH2OO,temp_coef)
convolve_kintecus(kin_IO,temp_coef)

Make/O/N=(1023,1024) OD_2D = 0 //x axis (dimension 1) = negative time axis, y
axis (dimension 2) = negative energy axis
Make/O/N=(1023,1024) CH2OO_2D = 0
Make/O/N=(1023,1024) IO_2D = 0
Make/O/N=(1023,1024) CH2I2_2D = 0
Make/O/N=(1023,1024) O3_2D = 0
Make/O/N=1024 time_axis
time_axis = 5.28-(p*coef[2])
for(i=0;i<1023;i+=1) //i counts through time delay
  for(j=0;j<1024;j+=1) //at a set time delay, j counts through spectrum
    CH2OO_2D[i][j] = XS_CH2OO[j]*kin_CH2OO[1023-i]*80
    IO_2D[i][j] = XS_IO[j]*kin_IO[1023-i]*80
    CH2I2_2D[i][j] = XS_CH2I2[j]*kin_CH2I2[1023-i]*80
    O3_2D[i][j] = XS_O3[j]*kin_O3[1023-i]*80
  endfor
endfor
OD_2D = CH2OO_2D + IO_2D + CH2I2_2D + O3_2D
Display;AppendImage OD_2D vs {time_axis,wavelength}
ModifyImage OD_2D ctab= {0,0.001,BlueHot,0}
ModifyImage OD_2D ctabAutoscale=1,lookup= "$"
SetAxis left 300,440.24228
ModifyGraph swapXY=1
Label bottom "Wavelength (nm)";Label left "Time (ms)"
Duplicate/o OD_2D, OD_2D_copy
pretrigger_subtract("OD_2D",900) //Function is in Lenny's original procedure file

KillWaves temp_coef,kin_CH2OO,kin_IO,kin_CH2I2,kin_O3,OD_2D_copy
end

```

CHANGES MADE TO THE PULSED CAVITY RINGDOWN APPARATUS AFTER MOVING FROM NOYES TO LINDE+ROBINSON

1 Introduction

In November 2011, the pulsed cavity ringdown experiment that had been located in 105 Noyes for more than 10 years was moved to B212A Linde+Robinson to join the newly-commissioned multidisciplinary Linde Center for Global Environmental Science. This appendix documents all equipment that was moved and various changes that were made to instrumentation within the first year after the move.

2 Relocated instruments

The pulsed cavity ringdown apparatus was described in Andre Deev and Kana Takematsu's theses.^{1,2} A pulsed Nd:YAG laser (Continuum NY61) generates 1064 nm laser light (500 mJ pulse⁻¹, 5 Hz), which is frequency doubled with a built-in second harmonic generator to create 532 nm light (150 mJ pulse⁻¹). This light pumps a tunable dye laser (Continuum TDL51), creating a wide range of visible light from 583–653 nm using various dyes. The visible laser light then passes through a multipass 88"-long steel tube that is filled with > 200 Psi hydrogen gas. The second Stokes-shifted light is selected by filters to obtain tunable near-infrared pulsed laser light from 7000–9000 cm⁻¹ (~1 mJ pulse⁻¹, typical). The excimer laser, Lambda Physik LPF 220, was relocated as well, although significant changes had to be made to the relative orientation of all lasers to accommodate the smaller lab space. Computers, digital delay generators, and all other equipment were moved to the new Linde+Robinson lab. During the move, all of this equipment was moved by a professional moving company, along with the 12'×4' laser table on which it rests. The original cavity ringdown mirror mounts, designed and built by Deev, were maintained, but a new pulsed photolysis stainless steel flow cell was designed by postdoctoral scholar Nathan C. Eddingsaas for use after the

move. This design was adopted by several other group members who needed photolysis flow cells. Overall, very few serious problems arose as a result of the move.

After relocating to Linde+Robinson, all lasers were installed and aligned. Specifically, the position of the monochromator grating in the tunable dye laser was randomly oriented after being moved and needed to be calibrated. To achieve a coarse alignment of the dye laser monochromator, we used a Jarrell Ash 82-000 W-mode monochromator. First, we aligned the Jarrell Ash monochromator to the output of the HeNe. Then, we performed a rough calibration on the dye laser monochromator using the Jarrell Ash monochromator. Precision alignment of the dye laser was then carried out using optogalvanic spectroscopy, as described in Takematsu's thesis.

Several times we dealt with the Marx bank, responsible for generating the very short, high-voltage pulse to switch the Pockels cell, failing to operate. This could be quickly diagnosed by the noticeable absence of the audible clicking (at the Q-switch rate, 5–20 Hz) that should come from the Marx bank as soon as the power supply is turned on. In some cases, this was caused by faulty wiring (Marx banks from different YAGs had previously been altered for incorporation into this model), but in others cases, there was no obvious explanation and the Marx bank simply had to be replaced. Parts can still be ordered from Continuum (PN 504-3100, \$236.00) if more replacements are need. After repair, we tested the YAG for breakthrough using a reversed-bias diode, finding that breakthrough did not begin until increasing the voltage above 1.58 kV.

3 Single-wavelength kinetics

Prior to the move from Noyes, the majority of the experiments performed on this apparatus focused on obtaining spectra of atmospheric radicals such as peroxy radicals and NO_3 . While this work continued, we also became interested in using this instrument for kinetics measurements. To such an end, preliminary experiments were carried out by setting a delay time between the photolysis (excimer) and probe (Nd:YAG) laser pulses, collecting a spectrum (which usually took about 30 minutes), and then manually changing the delay time (controlled by a digital delay generator) and repeating the process. Figure 1 shows an

example of such data, collected over the ethyl peroxy radical origin region. Fitting the decays of the ethyl peroxy radical with time was complicated by several issues, not least the problems associated with performing one kinetics experiment over the course of several hours, and it became clear that the apparatus needed to be redesigned to support kinetics experiments that could be carried out rapidly at one wavelength. Therefore, we set up remote control of the digital delay generator by the computer and wrote a new Labview program that allowed for single-wavelength kinetics experiments (like those shown for the isoprene peroxy radical in Chapter 3, Figures 6 and 7). For each set of experimental conditions, collecting 100 delay times with 30 averages of the excimer on and off takes about 15 minutes, significantly cutting down in the data collection time and enabling data sets like that shown in Chapter 3 Figure 7 to be collected in less than a day. Figure 2 shows the front panel of “Kinetics program.vi”. The user can request a dye laser wavelength, and, in providing a text file of the requested delay times, signal average for a preselected number of laser shots.

Kinetics experiments should be carried out with good control over reactant concentrations, flows, and pressures. To enable the researcher to record all pertinent data, such as the flow rate of the reactant gases through each of the mass flow meters, without any added effort, we installed a new data acquisition card and wrote Labview software that records relevant information. Figure 3 shows “DAQ_conversion.vi” which enables the user to set the parameters for the seven input channels on the new data acquisition card. This merely enables the program to write out flow rates or pressures based on calibrations of the mass flow meters, controllers, and pressure transducers instead of reporting voltages. The spectroscopy and kinetics Labview programs were rewritten so that the cell pressure, temperature, and mass flow meter flow rates are recorded after every block (during the wait time while either the laser either moves to a new wavelength or the digital delay generator is set to a new delay time). We also installed a new joulemeter (Coherent J-50MUV-248 EnergyMax Sensor) to measure the excimer laser power behind the flow cell for monitoring changes in the excimer laser fluence on the short and long timescales during photolysis experiments.

Kinetics experiments were also made easier by the adoption of Cl_2 as the Cl atom precursor for chlorine-initiated oxidation experiments. Previously, we used photolysis of oxalyl chloride at 248 nm as the radical precursor. Although oxalyl chloride has some unique benefits as a radical precursor (for example, it diminishes radical recycling mechanisms that arise when Cl_2 is used), its practical use is limited when it comes to extensive, continual, and convenient use, since it cannot be purchased as a dilute gas cylinder. Cl_2 is an attractive precursor because it can be purchased in high-purity gas cylinders; but more important for our applications, it can be photolyzed using 351 nm excimer light. This was critical to our success in conducting experiments on molecules such as isoprene, which absorb weakly at 248 nm, catalyzing an unacceptable amount of polymer formation. We previously limited ourselves to only using the Lambda Physik LPF 220 excimer laser at 193 and 248 nm because it was advertised as being designed only for use at 193 nm. However, discussions with an excimer laser technician led us to simply make an attempt to run the laser at 351 nm with the appropriate gas mixture, to great success. Presumably, this means that the mirrors inside the LPF 220 are simply silver mirrors and are not coated for any specific wavelength.

4 Lambda Physik dye laser installation

Several problems arose with the Continuum TDL51 dye laser that had been used historically as a part of this apparatus. This dye laser had always been difficult to work with (see Takematsu's thesis), especially when it came to replacing the laser dye. Unlike many dye laser models, in order to replace a dye, the current dye had to be pumped out and the entire system had to be flushed with several liters of solvent. Not only is this a technical issue (fully removing all traces of the previous dye is not easy but is critical when switching between different types of dye), but it is also a safety hazard, considering the toxic and carcinogenic nature of the dyes and solvents. Alignment of the Continuum laser was also not trivial, considering the extreme number of adjustable optics inside the laser; many had to be aligned by placing one's hand directly within the beam path. But what finally prompted us to retire this dye laser was the death of the oscillator/amplifier laser dye circulator.

Taking parts from two old Lambda Physik FL3002 dye lasers (one from Geoff Blake's lab and one from Paul Wennberg's lab), we cobbled together one working dye laser. Like many

other dye laser models, this dye laser has removable dye cells, making the switch between different dyes much easier. This dye laser was designed to operate with an excimer pump laser, but with the right optics can be used with an Nd:YAG with 532 nm pumping. Alignment of this laser is significantly easier, with only a small number of conveniently-located adjustment knobs. The greatest difficulty we faced was in communicating with the dye laser—the Molecular Dynamics News mailing list came to the rescue here, providing us with missing critical pieces of source code for communicating with this laser via GPIB. Figure 4 shows the front panel of “FL3002_move.vi”, where the user can request a desired wavelength. The address (6) is the GPIB address for scan control, and the grating order depends on the desired wavelength (here, to achieve dye laser lasing at 640 nm, the grating order is set to 4). Lambda zero is the calibrated zero point when the monochromator grating is move to the zero position. This value should be changed to reflect changes in the grating alignment. Figure 5 shows the Labview Library that now runs all of the data acquisition.

It should be noted that this dye laser came equipped with an etalon and the necessary motor driver that can be used to further narrow the linewidth of the output radiation (at the expense of scanning range). The etalon is currently in storage and can be installed should the need arise.

5 References

1. Deev, A. Cavity Ringdown Spectroscopy of Atmospherically Important Radicals. Dissertation (Ph.D.), California Institute of Technology, 2005. <http://resolver.caltech.edu/CaltechETD:etd-03172005-154741>
2. Takematsu, K. Cavity Ringdown Spectroscopy of the Nitrate and Peroxy Radicals. Dissertation (Ph.D.), California Institute of Technology, 2011. <http://resolver.caltech.edu/CaltechTHESIS:06012011-114553466>

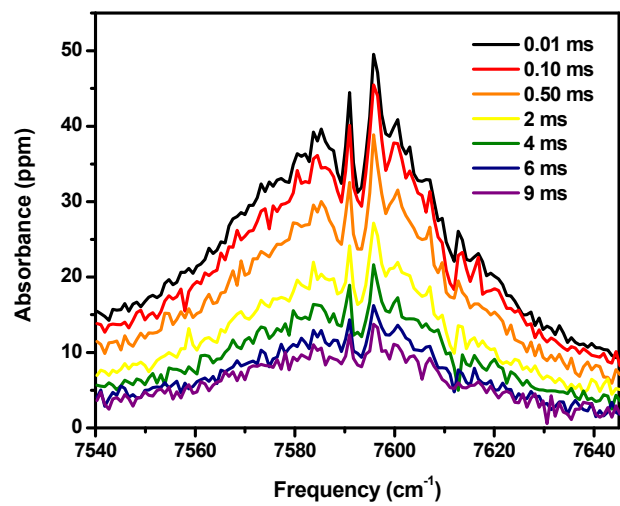


Figure 1. Example of data collected for kinetics measurements that measured the decay of a spectral feature.

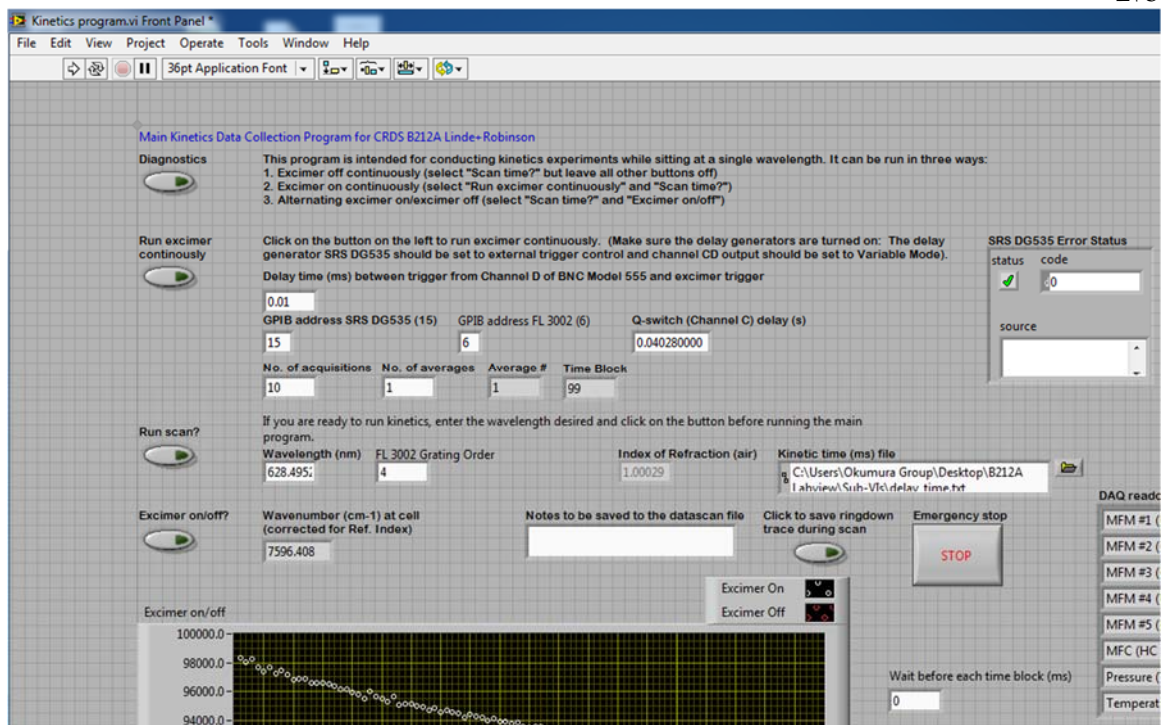


Figure 2. Front panel of the kinetics acquisition Labview program.

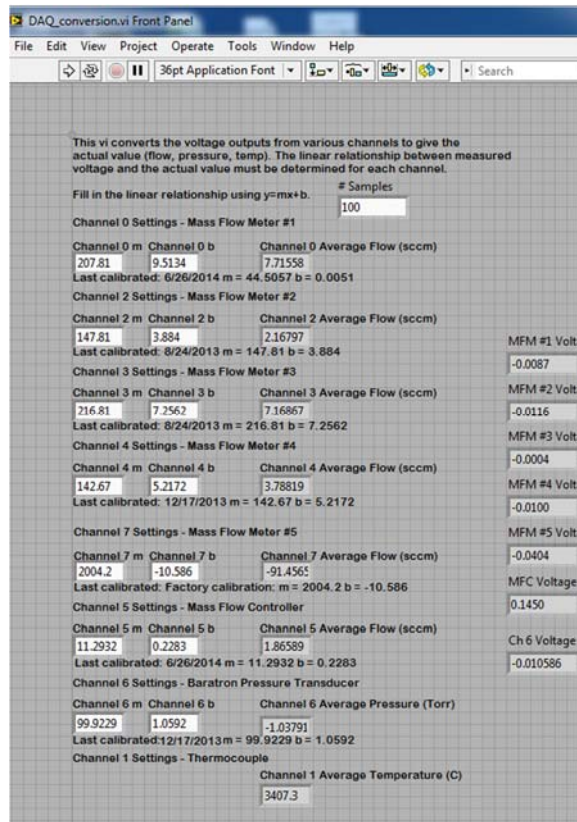


Figure 3. DAQ conversion program.

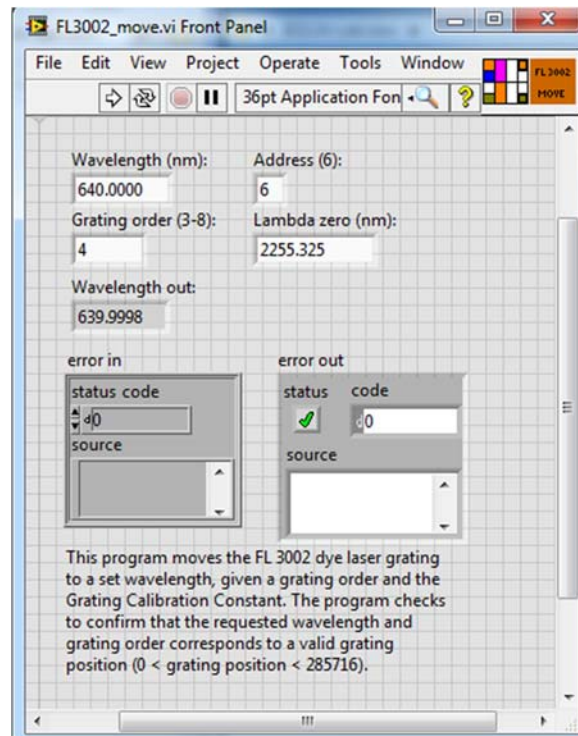


Figure 4. Front panel of the Labview program that moves the dye laser grating.

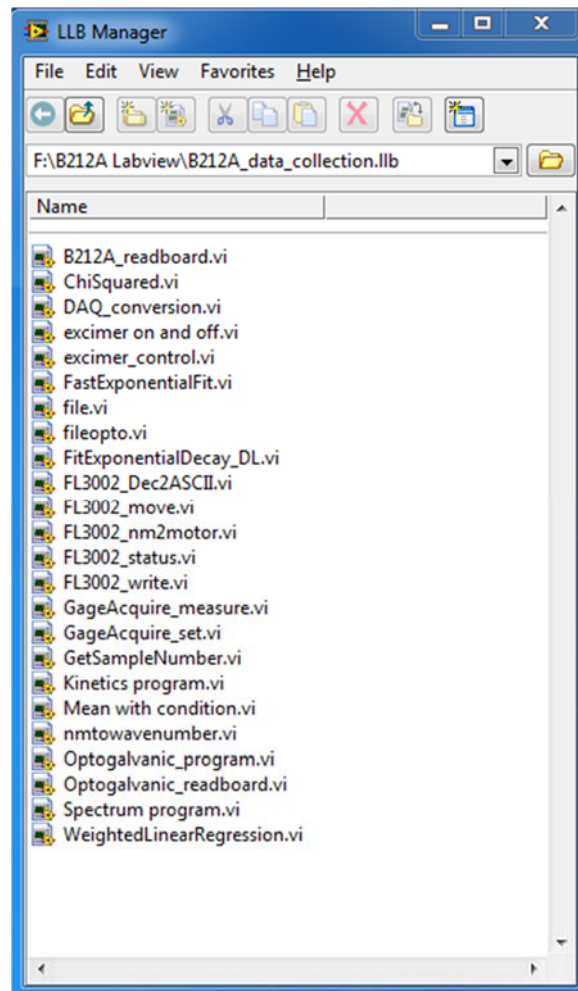


Figure 5. Labview Library File.

PREDICTING VIBRATIONALLY-RESOLVED A–X ELECTRONIC AND PHOTOIONIZATION SPECTRA USING QUANTUM CHEMICAL METHODS

1 Introduction

This appendix contains methods for using Gaussian 09 and CFOUR to calculate vibrationally-resolved electronic spectra. In addition, it presents a description of how to similarly calculate adiabatic ionization energies and predict photoionization spectra. These methods were used to assign the peroxy radical near-infrared cavity ringdown spectra presented as part of this thesis, and to identify absorbers in the photoionization spectra measured in other parts of this thesis.

2 Calculation of electronically excited states

The A–X electronic transition was calculated for several peroxy radicals. Appendix C of Matthew K. Sprague’s thesis describes several methods for obtaining excited states for molecules.¹ The majority of the peroxy radicals addressed in the current work have conformers that can be described as having C_1 symmetry, meaning that the symmetry tricks described in part 3 of Appendix C of Sprague’s thesis cannot be used here. Instead of exploiting the differences in ground and excited state symmetries to compute the two electronic states, we must use other methods, such as time-dependent (described in part 2 of Appendix C of Sprague’s thesis) or equation of motion methods. Specifically, time-dependent density functional theory was used to obtain vibrational frequencies for X and A states independently. The EOMEE method was used to produce the most accurate adiabatic A–X transition energies for the smallest (C2) chlorine-substituted peroxy radical addressed in this work. For larger peroxy radicals observed in this work, the EOMEE method was too computationally expensive. A single-point A state energy calculation for the chloro-ethyl peroxy radical takes about one minute to finish on the Okumura group computational computer when running a TD-DFT calculation using the B3LYP functional and the aug-cc-

pVDZ basis set. The same A state energy calculation computed at EOMEE-CCSD with the same aug-cc-pVDZ basis set takes just under 3 hours.

3 Identification of local minimum structures

Multiple conformers were expected as the number of atoms increases for each peroxy radical studied in this work. To find all of the possible absorbers in our spectra, we performed potential energy surface scans of the major dihedral angles, as described in the text, for both the ground and first excited state. For the chloro-ethyl peroxy radical, we have identified two torsion angles, identified as α (C–C–O–O) and β (Cl–C–C–O) (see Figure 1).

For the chloro-ethyl peroxy radical, we identified six local minimum conformations from potential energy surface scans across both torsion angles at B3LYP/6-31+g(d,p); there were two pairs of conformations that are related by symmetry, resulting in four unique conformations. Figure 2 shows the result of the potential energy surface scan across the two torsion angles. At room temperature, the ground state conformers can easily interconvert and will be present in ratios dictated by their relative energetics. Ground state energy differences amongst the conformers are calculated using the G2 compound method.

We also completed a potential energy surface scan of the excited state across the two torsion angles using TD-DFT at B3LYP/6-31+g(d,p) to obtain excited state energies. Figure 3 shows the potential energy surface map that results. The map of the excited state is quite similar to that of the ground state: again there are four unique conformations of the α and β torsion angles that have similar geometries to the minima identified in the ground state. The barrier heights to interconversion amongst the four conformers are about three times higher in the excited state than those in the ground state.

4 Calculation of A–X adiabatic transitions

Several different methods were investigated for calculating the adiabatic A–X electronic transition of peroxy radicals. For each method, the ethyl peroxy radical was used as a test case because extensive experimental and computational work has been performed on this species.²⁻⁴ Correction scaling factors were obtained for each method and basis set by

comparing the adiabatic A–X transition from the ethyl peroxy radical calculations with the experimentally-observed origin transition, following the method described in detail by Sprague, et al.^{1,5}

4.1 TD-DFT

Time-dependent density functional theory is the first method discussed here. First, ground state structures were reoptimized (using the `opt=verytight` and `int=ultrafine` protocols to invoke extremely tight optimization convergence criteria) at the chosen level of theory and basis set (typically, using the B3LYP functional and a series of basis sets including two Pople basis sets 6-31+G(d,p) and 6-311+G(3df,2p), and the correlation-consistent basis set aug-cc-pVDZ). Figure 4 demonstrates an example input file that performs an X state geometry optimization, along with a frequency calculation, for the ethyl peroxy radical. Rupper et al. performed equation of motion ionization potential coupled cluster with singles and doubles (EOMIP-CCSD) calculations on the ethyl peroxy radical and compared their results with the experimental spectrum obtained by that group. They identified two unique conformers, one with a C–C–O–O torsion angle equal to 60° (which they call the G conformer) and a second, the T conformer, with a C–C–O–O torsion angle equal to 180° , whose ground state lies $+81\text{ cm}^{-1}$ higher in energy than the G conformer. Here, DFT calculations identify the T conformer as the lowest energy structure. Beginning with the structures optimized for the ground state, we performed TD-DFT geometry optimizations using the same functional and basis sets using the `td=(nstates=1)` command. Figure 5 shows an example input file for requesting a TD-DFT geometry optimization and frequency calculation. The adiabatic zero-point energy corrected A–X excitation energies are listed in Table 1. The experimentally-identified T and G origin frequencies appear at 7362 and 7592 cm^{-1} , respectively, with the difference in energy between the two peaks equaling 230 cm^{-1} . TD-DFT overpredicts the position of the origin transition by more than 1000 cm^{-1} and, like EOMIP, underpredicts the length of the O–O bond in the excited state, which is expected to increase to longer than 1.4 \AA . However, invoking scaling factors like those described in Sprague’s thesis enables us to still use this method. Table 1 lists the scale factors for each basis set; these values are presented as the conformer-specific experimental origin frequency divided by the theoretical A–X value

computed for the corresponding structure. A trend is observed where the scale factors for the two conformers converge to the same value with increasing correlation in the basis set. An ideal method would find the same scaling factor for each conformer.

4.2 EOMEE-CCSD

The second method used in this thesis to investigate electronically-excited states was equation of motion excitation energies using coupled cluster with singles and doubles (EOMEE-CCSD). These calculations were completed using CFOUR. Figure 6 shows an example CFOUR input file for the ethyl peroxy radical. Ground state geometries were optimized using CCSD, with ground state energy differences between the two conformers that are more in line with the result presented by Rupper et al.² CCSD calculations with the aug-cc-pVDZ basis set find the T conformer lying +26 cm⁻¹ above the G conformer. Frequency calculations were not carried out at the CCSD level, so no energies discussed in this section have been corrected for zero-point energies.

EOMEE-CCSD calculations predict A–X electronic transition energies much closer to the observed experimental value. Figure 7 shows an example CFOUR input file for an EOMEE-CCSD calculation of the ethyl peroxy radical. The computed adiabatic energies are within 400 cm⁻¹ of the experimental value and have almost exactly the same scaling factor. The excited state O–O bond length is > 1.4 Å, a much more reasonable value for the peroxy radical \tilde{A} state. EOMEE-CCSD calculations are much more accurate, both in terms of absolute energies, bond lengths, and treatment of asymmetric structures.

5 Simulation of vibrationally-resolved electronic spectra

Vibrationally-resolved excited state spectra, including Franck-Condon overlap integrals, can be simulated in Gaussian 09. The protocol for producing these spectra was described in detail by Barone et al.⁶ First, frequency calculations are carried out for both the ground and excited states, by requesting freq=SaveNM, as shown in Figures 4 and 5. The modifier SaveNM is necessary to save the normal modes to the checkpoint files, so that Gaussian can access them directly. One problem to avoid is using dissimilar geometry coordinates between the two states, which can make it difficult for the program to match normal modes. Figure 8 shows

an example input file. This file requests a computation of the Franck-Condon overlap integral using the Herzberg-Teller approximation (FCHT) between the ethyl peroxy X and A states optimized in the last step for all transitions whose energy falls between 6000 and 10000 cm^{-1} . For peroxy radicals, it is helpful to perform the FCHT calculation, which includes the first two terms of the Taylor expansion of the transition dipole moment, rather than the FC calculation (only the first term), because of the weak dipole transitions.

The computed Franck-Condon overlap intensities are reported in the Gaussian output file, as shown in Figure 9. The ZPE-corrected energy of the origin transition is listed (8921.8502 cm^{-1}) along with its intensity (0.6586E-06). After this, Gaussian reports the computed intensities for each active mode in order of transition energy; here, the first is excitation from the vibrational ground state of the X state to one quanta of vibration in mode 1 (which has a vibrational frequency of 134.8529 cm^{-1}) with an intensity of 0.9573E-07. Gaussian continues to list all transitions with intensities greater than 1% of the intensity of the origin transition, including transitions that have more than one excited vibrational mode in the A state.

For the chlorine-substituted peroxy radicals reported in this thesis, the frequency of the origin transition was scaled using the scale factor found for the ethyl peroxy system. Then, the vibrational transitions were each scaled by the recommended scale factor for the basis set used. The cross section for each origin transition was assumed to be unity, and the spectra were weighted by the ground state Boltzmann factors computed at the G2 level.

6 Computing ionization energies and photoionization spectra

To support the photoionization mass spectrometry experiments carried out in Chapters 4–8, we used quantum chemical calculations to predict the ionization energies and photoionization spectra for hypothesized species. This was often useful in predicting whether we should expect to see specific ions in the mass spectrometer by determining whether a stable cation structure could be formed or estimating the ionization energy or photoionization spectrum of previously unreported molecules. The Sandia group has established methodologies for predicting adiabatic ionization energies and photoionization spectra (see,

for example, references 7–9) using the CBS-QB3 compound method. This method is available in Gaussian 09.

We used quantum chemical calculations to predict the adiabatic ionization energy of the proposed peroxide species investigated as part of this thesis ($\text{C}_2\text{H}_5\text{OOC}_2\text{H}_5$ in Chapter 6 and H_2O_4 in Chapter 8) as well as assessing the possible identity of other unknown products. Figure 10 shows the neutral $\text{C}_2\text{H}_5\text{OOC}_2\text{H}_5$ global minimum structure (geometries optimized using CBSB7), identified by a potential energy surface scan of the major dihedral angles. Upon ionization, the major dihedral angles change significantly; the C–O–O–C torsion angle increases from -128° to -178° . One of the C–C–O–O angles also changes significantly, from -178° to 90° . However, the diethyl peroxide cation is clearly a stable molecule; the O–O bond distance increases slightly from 1.32 to 1.46 Å. Decomposition to form the ethoxy radical plus the ethoxy cation ($\text{C}_2\text{H}_5\text{O} + \text{C}_2\text{H}_5\text{O}^+$) was somewhat thermodynamically favorable; the adiabatic ionization energy for $\text{C}_2\text{H}_5\text{OOC}_2\text{H}_5$ was 8.87 eV and the calculated appearance energy for was 8.53 eV (computed at CBS-QB3). Formation of $\text{C}_2\text{H}_5\text{O}^+$ through decomposition of higher-mass products at moderate photon energies (e.g. 10.7 eV) perhaps explains presence of a peak in the mass spectrum at m/z 45 whose kinetics do not match that of the ethoxy radical, nor does the intensity match that of $^{13}\text{CH}_3\text{CHO}$.

The Franck-Condon simulation program in Gaussian can also be used to generate the photoelectron spectrum. Integration of this photoelectron spectrum along the energy axis yields the predicted photoionization spectrum. However, it is important to remember that many species, or multiple isomers, could be present at any given mass, making simulating photoionization spectra quite difficult.

7 References

1. Sprague, M. K. Cavity Ringdown Spectroscopy, Kinetics, and Quantum Chemistry of Atmospherically Relevant Reactions. Dissertation (Ph.D.), California Institute of Technology, 2012. <http://resolver.caltech.edu/CaltechTHESIS:05282012-184532561>
2. Rupper, P.; Sharp, E. N.; Tarczay, G.; Miller, T. A., Investigation of Ethyl Peroxy Radical Conformers via Cavity Ringdown Spectroscopy of the $\tilde{A}-\tilde{X}$ Electronic Transition. *J. Phys. Chem. A* **2007**, *111*, 832-840.

3. Just, G. M. P.; Rupper, P.; Miller, T. A.; Meerts, W. L., High-resolution Cavity Ringdown Spectroscopy of the Jet-cooled Ethyl Peroxy Radical $C_2H_5O_2$. *J. Chem. Phys.* **2009**, *131*, 184303.
4. Melnik, D.; Chhantyal-Pun, R.; Miller, T. A., Measurements of the Absolute Absorption Cross Sections of the $\tilde{A} \leftarrow \tilde{X}$ Transition in Organic Peroxy Radicals by Dual-Wavelength Cavity Ring-Down Spectroscopy. *J. Phys. Chem. A* **2010**, *114*, 11583-11594.
5. Sprague, M. K.; Mertens, L. A.; Widgren, H. N.; Okumura, M.; Sander, S. P.; McCoy, A. B., Cavity Ringdown Spectroscopy of the Hydroxy-Methyl-Peroxy Radical. *J. Phys. Chem. A* **2013**, *117*, 10006-10017.
6. Barone, V.; Bloino, J.; Biczysko, M., Vibrationally-Resolved Electronic Spectra in GAUSSIAN 09. GAUSSIAN 09 Revision A.02, **2009**.
7. Welz, O.; Savee, J. D.; Osborn, D. L.; Vasu, S. S.; Percival, C. J.; Shallcross, D. E.; Taatjes, C. A., Direct Kinetic Measurements of Criegee Intermediate (CH_2OO) Formed by Reaction of CH_2I with O_2 . *Science* **2012**, *335*, 204-207.
8. Welz, O.; Zador, J.; Savee, J. D.; Ng, M. Y.; Meloni, G.; Fernandes, R. X.; Sheps, L.; Simmons, B. A.; Lee, T. S.; Osborn, D. L., et al., Low-Temperature Combustion Chemistry of Biofuels: Pathways in the Initial Low-Temperature (550 K-750 K) Oxidation Chemistry of Isopentanol. *Phys. Chem. Chem. Phys.* **2012**, *14*, 3112-3127.
9. Savee, J. D.; Papajak, E.; Rotavera, B.; Huang, H.; Eskola, A. J.; Welz, O.; Sheps, L.; Taatjes, C. A.; Zádor, J.; Osborn, D. L., Direct Observation and Kinetics of a Hydroperoxyalkyl Radical (QOOH). *Science* **2015**, *347*, 643-646.

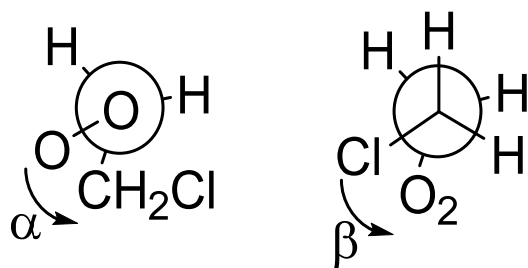


Figure 1. Definition of α and β torsion angles in the chloro-ethyl peroxy radical.

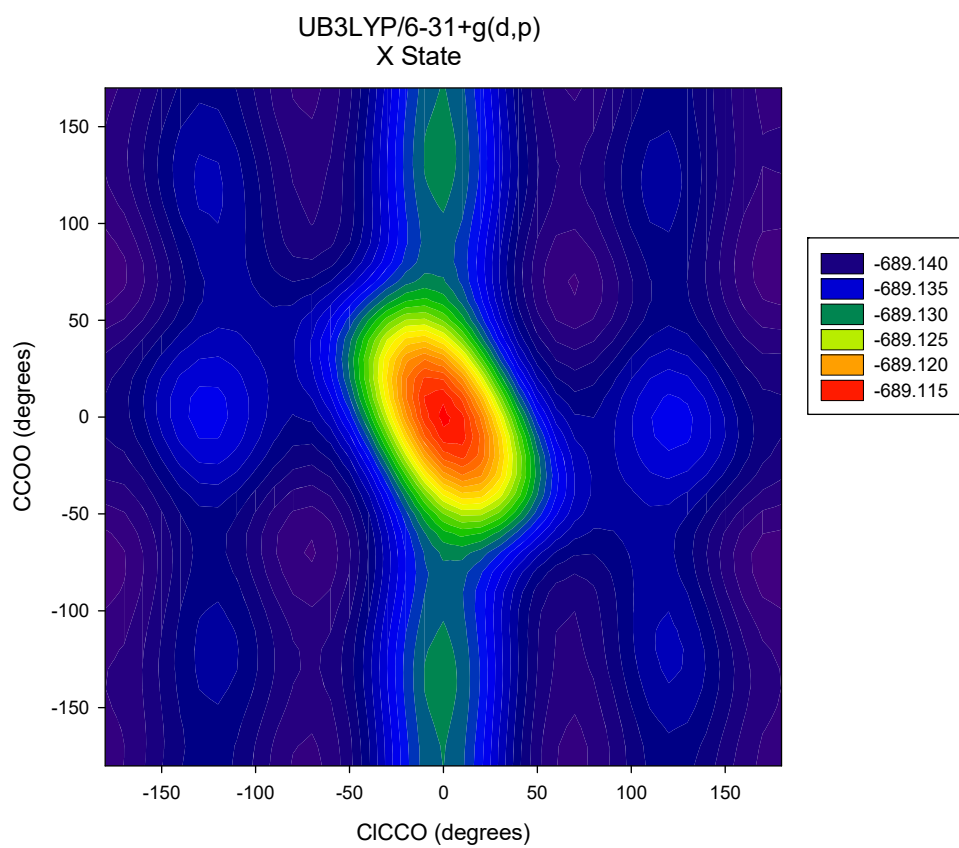


Figure 2. Chloro-ethyl peroxy radical ground state potential energy surface scan across the α (C-C-O-O) and β (Cl-C-C-O) torsion angles at B3LYP/6-31+g(d,p).

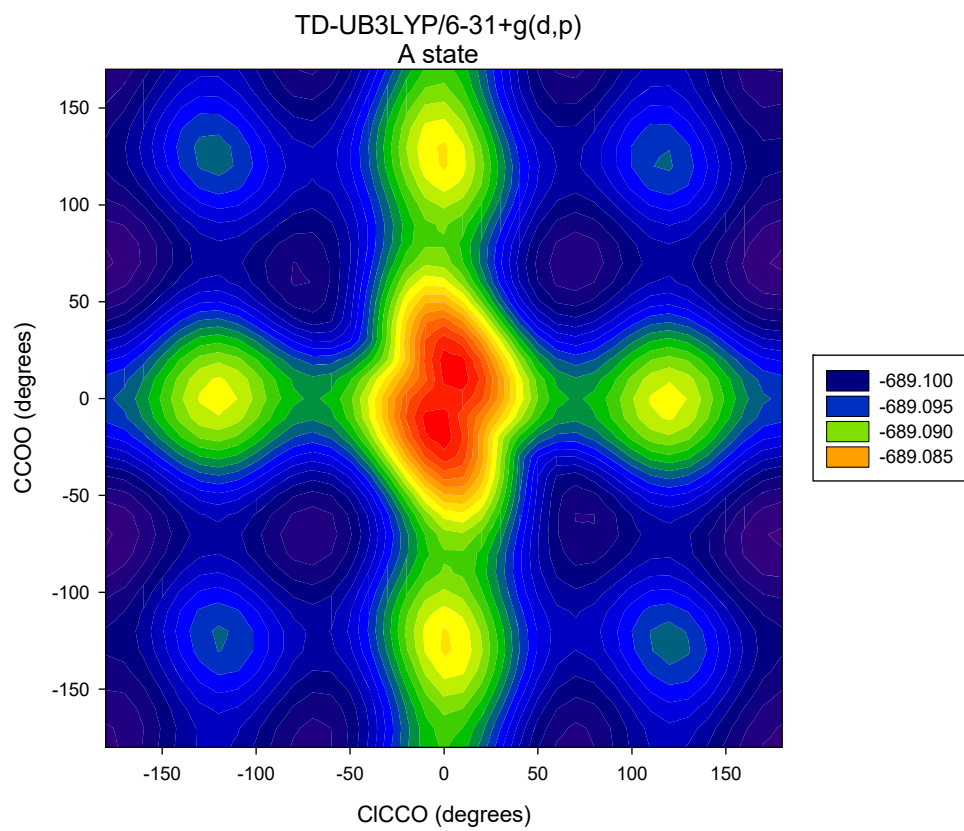


Figure 3. Chloro-ethyl peroxy radical A state potential energy surface scan across the α (C–C–O–O) and β (Cl–C–C–O) torsion angles at TD-B3LYP/6-31+g(d,p).

```
%chk=/home/sprague/Desktop/EP/DFT/EP_B3LYP_G.chk
#p opt=verytight freq=SaveNM int=ultrafine b3lyp/aug-cc-pVDZ nosymm
```

```
EP B3LYP/aug-cc-pVDZ opt and freq G conformer
```

```
0 2
```

```
C
H          1          B1
H          1          B2  2          A1
C          1          B3  3          A2  2          D1  0
H          4          B4  1          A3  3          D2  0
H          4          B5  1          A4  3          D3  0
O          4          B6  1          A5  3          D4  0
H          1          B7  4          A6  7          D5  0
O          7          O0  4          C00  1          CC00  0
```

```
B1      1.08551347
B2      1.08621825
B3      1.51669615
B4      1.08755296
B5      1.08809894
B6      1.45362022
B7      1.08551347
O0      1.31533493
A1     110.00286679
A2     111.44240269
A3     111.95771365
A4     111.78165865
A5     109.40776542
A6     109.34694579
C00    111.56929036
D1     -123.39352177
D2     179.62919615
D3     -55.72793107
D4      59.72644297
D5     178.34378870
CC00    75.51780257
```

Figure 4. Example Gaussian 09 input file for requesting a DFT-B3LYP/aug-cc-pVDZ ground state geometry optimization and frequency calculation for the ethyl peroxy radical.

290

```
%chk=/home/sprague/Desktop/EP/DFT/EP_TD_B3LYP_G.chk  
#p opt=verytight td=(nstates=1) freq=SaveNM int=ultrafine b3lyp/aug-cc-pVDZ nosymm
```

```
EP TDB3LYP/aug-cc-pVDZ opt and freq G conformer
```

```
0 2
```

```
C
```

```
H          1          B1  
H          1          B2    2          A1  
C          1          B3    3          A2    2          D1    0  
H          4          B4    1          A3    3          D2    0  
H          4          B5    1          A4    3          D3    0  
O          4          B6    1          A5    3          D4    0  
H          1          B7    4          A6    7          D5    0  
O          7          O0    4          C00   1          CC00  0
```

```
B1      1.08551347
```

```
B2      1.08621825
```

```
B3      1.51669615
```

```
B4      1.08755296
```

```
B5      1.08809894
```

```
B6      1.45362022
```

```
B7      1.08551347
```

```
O0      1.31533493
```

```
A1     110.00286679
```

```
A2     111.44240269
```

```
A3     111.95771365
```

```
A4     111.78165865
```

```
A5     109.40776542
```

```
A6     109.34694579
```

```
C00    111.56929036
```

```
D1     -123.39352177
```

```
D2     179.62919615
```

```
D3     -55.72793107
```

```
D4      59.72644297
```

```
D5     178.34378870
```

```
CC00    75.51780257
```

Figure 5. Example Gaussian 09 input file for requesting a TD-DFT-B3LYP/aug-cc-pVDZ excited state geometry optimization and frequency calculation for the ethyl peroxy radical.

```

ethyl peroxy, G CCSD/aug-cc-pVDZ opt
C
H 1 B1*
H 1 B2* 2 A1*
C 1 B3* 3 A2* 2 D1*
H 4 B4* 1 A3* 3 D2*
H 4 B5* 1 A4* 3 D3*
O 4 B6* 1 A5* 3 D4*
H 1 B7* 4 A6* 7 D5*
O 7 OO* 4 COO* 1 CCOO*

B1 = 1.100332431097213
B2 = 1.101495722122220
A1 = 109.143044237645029
B3 = 1.522052863560000
A2 = 110.637702298896684
D1 = -121.418977139947316
B4 = 1.099999357019489
A3 = 112.467657182738520
D2 = 178.757606672628327
B5 = 1.100746788405792
A4 = 112.343272363282082
D3 = -56.540212212195676
B6 = 1.461585396579814
A5 = 110.945850310821029
D4 = 58.854031829347051
B7 = 1.102568720860752
A6 = 109.426392990569070
D5 = 178.532682039752160
OO = 1.325372182525668
COO = 109.971960711690471
CCOO = 72.493014358089567

*ACES2 (CALC=CCSD, BASIS=AUG-PVDZ
CHARGE=0, MULT=2, REF=UHF
MEMORY_SIZE=4, MEM_UNIT=GB
CC_CONV=10
CC_MAXCYC=200
GEO_CONV=10
GEO_MAXCYC=200
SCF_CONV=10
SCF_MAXCYC=200
LINEQ_CONV=11
LINEQ_MAXCYC=200)

```

Figure 6. Example CFOUR input file for requesting a CCSD/aug-cc-pVDZ ground state geometry optimization for the ethyl peroxy radical.

```

ethyl peroxy, G EOMEE-CCSD/aug-cc-pVDZ opt
C
H 1 B1*
H 1 B2* 2 A1*
C 1 B3* 3 A2* 2 D1*
H 4 B4* 1 A3* 3 D2*
H 4 B5* 1 A4* 3 D3*
O 4 B6* 1 A5* 3 D4*
H 1 B7* 4 A6* 7 D5*
O 7 OO* 4 COO* 1 CCOO*

B1 = 1.100472290705605
B2 = 1.101029314483652
A1 = 108.770652909757629
B3 = 1.525266022714702
A2 = 110.363328702230916
D1 = -122.394921956839710
B4 = 1.103727576880501
A3 = 112.076748082536128
D2 = 178.396429524527065
B5 = 1.100233834566471
A4 = 111.807084404945940
D3 = -59.096120072450226
B6 = 1.449095471637540
A5 = 112.973789484725330
D4 = 55.384271835453248
B7 = 1.103182418763342
A6 = 109.148433708254160
D5 = 174.884798657944174
OO = 1.407074450539528
COO = 106.212551295860862
CCOO = 68.304656588751243

*ACES2 (CALC=CCSD, BASIS=AUG-PVDZ, EXCITE=EOMEE
CHARGE=0, MULT=2, REF=UHF
MEMORY_SIZE=4, MEM_UNIT=GB
ESTATE_CONV=8
ESTATE_MAXCYC=200
CC_CONV=10
CC_MAXCYC=200
GEO_CONV=10
GEO_MAXCYC=200
SCF_CONV=10
SCF_MAXCYC=200
LINEQ_CONV=11
LINEQ_MAXCYC=200)

```

Figure 7. Example CFOUR input file for requesting an EOMEE-CCSD/aug-cc-pVDZ excited state geometry optimization for the ethyl peroxy radical.

```
%chk=/home/sprague/Desktop/EP/DFT/EP_B3LYP_G.chk  
#p freq=(ReadFC,FC,SaveNM,ReadFCHT) nosymm geom=AllCheck  
  
NORELI00 SPECMIN=6000 SPECMAX=10000 SPECRES=0.1 SPECHWHM=0.1  
  
/home/sprague/Desktop/EP/DFT/EP_TD_B3LYP_G.chk  
.
```

Figure 8. Example Gaussian 09 input file for requesting a Franck-Condon spectrum.

```

-----
  Overlap integrals computation
-----

Energy of the 0-0 transition:   8921.8502 cm(-1)

Notes about the overlap integrals description:
- DeltaE is the relative energy of the transition (wrt 0-0)
- FCI is the Franck-Condon Integral
- Intensity is the line intensity (absolute value)

-- To: vibronic fundamental state --

Initial State: <0|
Final State: |0>
      DeltaE =    0.0000 | TDMI**2 = 0.4927E-04, Intensity =
0.6586E-06
      .....
-----
++ Spectrum progression:  23.76%

-- To: single overtones --

Initial State: <0|
Final State: |1^1>
      DeltaE =   134.8529 | TDMI**2 = 0.5928E-05, Intensity =
0.9573E-07
      .....
Initial State: <0|
Final State: |2^1>
      DeltaE =   221.1214 | TDMI**2 = 0.2223E-05, Intensity =
0.2543E-07
      .....
Initial State: <0|
Final State: |3^1>
      DeltaE =   328.6431 | TDMI**2 = 0.2463E-05, Intensity =

```

Figure 9. A portion of the output of FCHT calculation.

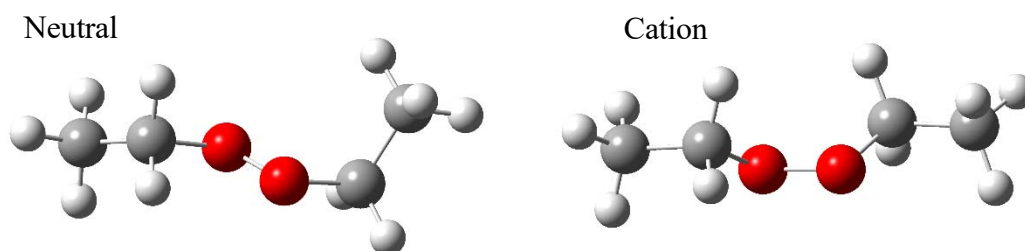


Figure 10. Optimized global minimum C₂H₅OOC₂H₅ neutral and cation structures (at B3LYP/CBSB7 for CBS-QB3 calculations).

Table 1. Comparison of ethyl peroxy radical past experiment and theory with results of methods described in this work.

	<u>Literature</u>				<u>TD-DFT</u>						<u>EOM-CCSD</u>	
	<u>Experiment</u>		<u>Theory</u>		<u>6-31+G(d,p)</u>		<u>6-311+G(3df,2p)</u>		<u>aug-cc-pVDZ</u>		<u>aug-cc-pVDZ</u>	
	T	G	T	G	T	G	T	G	T	G	T	G
0 ⁰ ₀ (cm ⁻¹)	7362	7592	7938	8059	8609	8766	8917	9092	8736	8922	7690	7944
Δ0 ⁰ ₀ (cm ⁻¹)	230		121		157		175		186		254	
Theory – Experiment (cm ⁻¹)			576	467	1247	1174	1555	1500	1374	1330	328	352
Experiment ÷ Theory			0.927	0.942	0.855	0.866	0.826	0.835	0.843	0.851	0.957	0.956
C–O–O bend (cm ⁻¹) (A)	512	457	436	463	428	457	429	457	427	456		
C–C–O bend (cm ⁻¹) (A)		328	285	338	282	331	282	330	281	329		
O–O stretch (cm ⁻¹) (A)	945	915	948	951	1028	1026	1039	1030	1029	1022		
d _{o–o} (Å) (X)			1.322	1.324	1.322	1.324	1.312	1.313	1.316	1.317	1.324	1.325
d _{o–o} (Å) (A)			1.379	1.380	1.383	1.383	1.371	1.371	1.377	1.377	1.406	1.407
C–C–O–O (°) (X)			180	60	180	75	180	75	180	75	180	72
C–C–O–O (°) (A)					180	69	180	68	180	68	180	68
ΔG (cm ⁻¹)			+81		-48		-45		-26		+26	

*Appendix C***MATLAB PROGRAMS USED IN ANALYZING MPIMS DATA****1 Introduction**

This appendix contains the Matlab programs used to analyze the kinetics data obtained during experiments at the ALS on the MPIMS instrument. Below are examples from the ethyl peroxy radical self-reaction system. Other programs exist for different chemical reaction systems.

2 Modeling ALS data

The main use of these programs is to simulate a photolysis gradient, running Kintecus repeatedly with a new initial radical concentration at each time point (representative of an increasing laser fluence from the pinhole to the top of the flow tube). The first program below demonstrates the simulation of kinetics data for the ethyl peroxy radical self-reaction, calling upon five sub-programs listed immediately after. These programs simulate a photolysis gradient and convolve the kinetics model output with the MPIMS instrument response function.

2.1 createConvolvedModelEtO2.m

```
function [new_output, precursor_data] =
createConvolvedModelEtO2(fitParm,initialConc,gradient)
% This program specifically works for the ethyl peroxy system only!
% You can choose to include a photolysis gradient (gradient = 'yes') or
not (gradient = 'no').
% This program calls 5 subprograms that must be in the same directory:
% 1) buildModel
% 2) convolvePrecursor
% 3) convolveModel
% 4) runKintecusEtO2
% 5) photolysis_calc
% Required input:
% initialConc.Cl2 = initial Cl2 concentration (molec/cc)
% initialConc.O2 = initial O2 concentration (molec/cc)
% initialConc.C2H6 = initial C2H6 concentration (molec/cc)
% initialConc.He = initial He concentration (molec/cc)
% fitParm.A = A value for convolution (ex: -1.2)
% fitParm.t0 = t0 value for convolution (ex: -0.6)
% fitParm.delta = time steps (ms) of model (ex: 0.02)
```

298

```
% fitParm.bin = desired time steps (ms) for comparison with data (ex:
0.2)
% fitParm.photolysis = either the photolysis ratio for all time, or the
values defining the linear gradient (ex: [0.0125;1E-5] this means at t
= 0, the photolysis rate is 1.25%, and this rate increases by 1E-3% per
millisecond).

p1_index = 3;
p2_index = 4;
p1_conc0 = initialConc.Cl2;
p2_conc0 = initialConc.C2H6;
file_location = 'C:\Users\Leah\Documents\MATLAB\'; % change to the
location of your Matlab programs
cd(file_location);
kintecus_location = 'C:\Kintecus\';

phot = strcmp('yes',gradient);

% This function runs the Kintecus model. The function is below.
runKintecusEtO2(initialConc,phot);

% This program builds the model including the photolysis gradient
if phot == 1 % use photolysis gradient
    % This program builds the model including the photolysis gradient
    [concatenated_model, header, nspecies] =
buildModel(kintecus_location);
else % don't use photolysis gradient
    % Opens the base file for the run. filepath is the location (e.g.
    % 'C:\Kintecus\').
    location = [kintecus_location 'CONC.txt'];
    Kintecus_conc = importdata(location);
    concatenated_model = Kintecus_conc.data; % not really concatenated
    nspecies = size(Kintecus_conc.data(1,:),2)-1;
    header = Kintecus_conc.colheaders();
end

% This program builds the model (and convolves it for the precursor
concentrations, to create time-dependent concentrations from -20 to 60
ms. There are 2 precursors so this program is called twice.
p1_data =
convolvePrecursor(concatenated_model,fitParm,p1_index,p1_conc0);
p2_data =
convolvePrecursor(concatenated_model,fitParm,p2_index,p2_conc0);
precursor_data = [p1_data p2_data(:,2)];

% This program convolves the full model
[new_output, nrows] = convolveModel(concatenated_model,fitParm);

out_file = [file_location 'conc_all.txt'];
out_precursor = [file_location 'conc_prec.txt'];

% Create or rewrite a file to store the convolved model
fid = fopen(out_file, 'w');
```

```

fprintf(fid, 'Time(ms)\t');
for i = 2:nspecies+1
    fprintf(fid, '%s\t', header{1,i});
end
fprintf(fid, '\r\n');

for i = 1:nrows-1
    for j = 1:nspecies+1
        fprintf(fid, '%f\t', new_output(i,j));
    end
    fprintf(fid, '\r\n');
end
fclose(fid);

% Create or rewrite a file to store the convolved precursors
out_fid2 = fopen(out_precursor, 'w');
fprintf(out_fid2, 'Time(ms)\t');
fprintf(out_fid2, 'Cl2\t');
fprintf(out_fid2, 'C2H6\t');
fprintf(out_fid2, '\r\n');
for precursor_row = 1:length(precursor_data(:,1))-1
    for j = 1:3
        fprintf(out_fid2, '%f\t', precursor_data(precursor_row,j));
    end
    fprintf(out_fid2, '\r\n');
end
fclose(out_fid2);
new_output = [new_output(1:299,1:2) new_output(1:299,5:18)];
precursor_data = precursor_data(1:399,:);
precursor_data(1:25,2) = p1_conc0;
precursor_data(1:25,3) = p2_conc0;
end
% end of function-----createConvolvedModelEtO2

```

2.2 runKintecusEtO2.m

```

function runKintecusEtO2(initialConc,phot)
% This program runs the Kintecus.exe program with specified initial
concentrations

photolysis = initialConc.photolysis;
Cl2_conc = initialConc.Cl2;
O2_conc = initialConc.O2;
C2H6_conc = initialConc.C2H6;
He_conc = initialConc.He;

cd('C:\Kintecus');
% Read in SPECIES.DAT and PARM.DAT files.
species_workbook = fopen('SPECIES.DAT', 'r');
species_content = textscan(species_workbook, '%s %s %s %s %s %s %s %s',
'Delimiter', '\t');
fclose(species_workbook);
[~,species_ncols] = size(species_content);
species_nrows = length(species_content{1});

```

```

if phot == 1 % runs Kintecus 61 times, changing the photolysis rate at
each step
    total_iterations = 61;
else
    total_iterations = 1;
end

for photolysis_iterations = 1:total_iterations
    % Determine new starting reagent concentrations
    photolysis_rate =
photolysis_calc(phot,photolysis,photolysis_iterations); % controls
whether a gradient is used
    disp('Photolysis rate');
    disp(photolysis_rate);
    new_Cl = photolysis_rate*Cl2_conc*2;
    new_Cl2 = Cl2_conc-(new_Cl/2);

    for yes_no = 4:species_nrows-1
        species_content{1,3}{yes_no,1} = num2str(zeros); %Sets all
concentrations to zero
        if yes_no == 5 || yes_no == 7 || yes_no == 8 || yes_no == 10 ||
yes_no == 11 || yes_no == 12 ...
            || yes_no == 13 || yes_no == 14 || yes_no == 15 ||
yes_no == 16 || yes_no == 17 ...
            || yes_no == 24 || yes_no == 25 || yes_no == 33 ||
yes_no == 42 || yes_no == 57 ...
            || yes_no == 75 %|| yes_no == 111 || yes_no == 21
            species_content{1,4}{yes_no,1} = 'Y'; %Selects products to
print
        else
            species_content{1,4}{yes_no,1} = 'No';
        end
    end
end
% Sets new concentrations. Keep 15 digits in num2str.
formatSpec = '%10.15e';
species_content{1,3}{4,1} = num2str(O2_conc,formatSpec);
species_content{1,3}{5,1} = num2str(new_Cl,formatSpec);
species_content{1,3}{6,1} = num2str(He_conc,formatSpec);
species_content{1,3}{7,1} = num2str(new_Cl2,formatSpec);
species_content{1,3}{8,1} = num2str(C2H6_conc,formatSpec);

% Rewrite the SPECIES.DAT file with new concentrations
species_workbook = fopen('SPECIES.DAT', 'r+');
for species_row = 1:species_nrows
    for species_col = 1:species_ncols
        fprintf(species_workbook, '%s\t',
species_content{1,species_col}{species_row,1});
    end
    fprintf(species_workbook, '\r\n');
end
fclose(species_workbook);

```

% Run the Kintecus program. Some initial setup is required.
Running the Kintecus program independently (through the Excel workbook) once before running the full program guarantees your settings (i.e. populates the SPECIES.DAT, MODEL.DAT, and PARM.DAT files with your specific model and settings).

```
stringKintecus = 'Kintecus.exe';
evalc('system(stringKintecus);');
% Use of 'evalc' suppresses the command line output that Kintecus
generates. This is useful because if it is not suppressed, the Matlab
Command Window is filled with Kintecus information.

if phot == 1 % using photolysis gradient
    % Save the concentration file as a new file
    destination = ['CONC' num2str(photolysis_iterations-1) '.txt'];
    copyfile('CONC.txt',destination);

    % Reports to the user the Kintecus run has ended.
    Report = rem(photolysis_iterations,61);
    if Report == 0
        fprintf('runKintecus iteration is complete.\r');
    else
    end
else % no photolysis gradient
    fprintf('Single runKintecus iteration is complete.\r');
end
end
end
cd('C:\Users\Leah\Documents\MATLAB\');
end
% end of function-----runKintecusEtO2
```

2.3 photolysis_calc.m

```
function photolysis_rate =
photolysis_calc(phot,photolysis,photolysis_iterations)
parm_workbook = fopen('PARM.DAT', 'r');
parm_content = textscan(parm_workbook, '%s %s %s %s %s',
'Delimiter','\t');
fclose(parm_workbook);
[~,parm_ncols] = size(parm_content);
parm_nrows = length(parm_content{1});

if phot == 1
    fprintf('Using a photolysis gradient.\r');
    % Determine the photolysis rate
    photolysis_rate =
((photolysis_iterations*photolysis(2,1))+photolysis(1,1))/1.0585;
    % Set the time length for the Kintecus model to run (makes program
more efficient).
    if photolysis_iterations == 1
        time_limit = 0.002;
        parm_content{1,4}{11,1} = time_limit;
        % Rewrite the PARM.DAT file with new time limit
        parm_workbook = fopen('PARM.DAT', 'r+');
        for parm_row = 1:parm_nrows
            for parm_col = 1:parm_ncols
```

```

        fprintf(parm_workbook, '%s\t',
parm_content{1,parm_col}{parm_row,1});
        end
        fprintf(parm_workbook, '\r\n');
    end
    fclose(parm_workbook);
else
    time_limit = photolysis_iterations*0.001;
    parm_content{1,4}{11,1} = time_limit;
    % Rewrite the PARM.DAT file with new time limit
    parm_workbook = fopen('PARM.DAT', 'r+');
    for parm_row = 1:parm_nrows
        for parm_col = 1:parm_ncols
            fprintf(parm_workbook, '%s\t',
parm_content{1,parm_col}{parm_row,1});
            end
            fprintf(parm_workbook, '\r\n');
        end
        fclose(parm_workbook);
    end
else % no gradient
    fprintf('No photolysis gradient used.\r');
    % Determine the photolysis rate
    photolysis_rate = photolysis(1,1);
    % Set the time length for the Kintecus model to run
    time_limit = 61*0.001;
    parm_content{1,4}{11,1} = time_limit;
    % Rewrite the PARM.DAT file with new time limit
    parm_workbook = fopen('PARM.DAT', 'r+');
    for parm_row = 1:parm_nrows
        for parm_col = 1:parm_ncols
            fprintf(parm_workbook, '%s\t',
parm_content{1,parm_col}{parm_row,1});
            end
            fprintf(parm_workbook, '\r\n');
        end
        fclose(parm_workbook);
    end
end
end
% end of function-----photolysis_calc

```

2.4 buildModel.m

```
function [concatenated_data, header, nspecies] = buildModel(filepath)
```

```
% Program is not specific to any chemical system.
```

```
% Opens the base file for the run. filepath is the location (e.g.
```

```
'C:\Kintecus\').
```

```
location = [filepath 'CONC60.txt'];
```

```
Kintecus_conc = importdata(location);
```

```
nspecies = size(Kintecus_conc.data(1,:),2)-1;
```

```
npoints_conc = size(Kintecus_conc.data(:,1),1);
```

```
header = Kintecus_conc.colheaders();
```

```

% Concatenates the data in 1 ms chunks. If the Kintecus program is
run 61 times, with 61 different photolysis rates at 0.00002 second step
sizes in the numerical simulation, then taking blocks of 50 data points
from each photolysis file results in a change in the photolysis rate
every 1 ms.
concatenated_data = zeros(npoints_conc,nspecies+1);
for conc_i = 1:60
    filename = [filepath 'CONC' num2str(conc_i) '.txt'];
    data_file = importdata(filename);
    concatenated_data((conc_i*50)-49:conc_i*50,:)...
        = data_file.data((conc_i*50)-49:conc_i*50,:);
end
% end of function-----buildModel

```

2.5 convolveModel.m

```

function [new_output, time_nrows] =
convolveModel(concatenated_model,fitParm)

% Program is not specific to any chemical system. This program
convolves the kinetics model output with the instrument response
function of the MPIMS instrument

A = fitParm.A;
t0 = fitParm.t0;
delta = fitParm.delta;
bin = fitParm.bin;

% Read data file
concatenated_model_npoints = size(concatenated_model(:,1),1);
concatenated_model_nspecies = size(concatenated_model(1,:),2)-1;

% Generate convolution function
x = -5:delta:5;
y = exp(A./((x-t0).^2))./((x-t0).^4);
remove = x <= t0;
y(remove) = 0;
y = y/sum(y);

factor = bin/delta;
time = concatenated_model(:,1);

% Convolve model concentrations with convolution function. Restrict
result to only the same length as the input concentration vector.
conv_conc =
zeros(concatenated_model_npoints,concatenated_model_nspecies);
for species_col = 1:concatenated_model_nspecies
    conv_conc(:,species_col) =
conv(concatenated_model(:,species_col+1),y,'same');
end

% Bin convolved concentration data to desired time steps to match data
rebin = zeros(round((concatenated_model_npoints-
1)/factor)+1,concatenated_model_nspecies);

```

304

```
    for rebin_i = 1:concatenated_model_nspecies
        for rebin_j = 1:factor:concatenated_model_npoints-2
            rebin(round(rebin_j/factor)+1,rebin_i) =
mean(conv_conc(rebin_j:rebin_j+factor,rebin_i));
        end
    end

% Shift x axis to account for averaging
smallBins = 1;
new_time = zeros(size(rebin,1),1);
for largeBins = 1:size(rebin,1)-1
    new_time(largeBins) = sum(time(smallBins:smallBins+factor-
1))/factor;
    smallBins = smallBins + factor;
end
new_time = new_time.*1000; % Time in ms

time_nrows = length(new_time);
convolved_model = rebin;
new_output = [new_time, convolved_model];
% end of function-----convolveModel
```

2.6 convolvePrecursor.m

```
function new_output_precursor =
convolvePrecursor(concatenated_data,fitParm,p_index,p_conc0)

% Program is not specific to any chemical system
% Program has one dependent: convolveModel
% p_index is the column number for the precursor location in the output
file
% Step size of data (in s) is found from the fitParm.delta (which is in
ms)
deltaS = fitParm.delta/1000;

time = concatenated_data(:,1);
p = concatenated_data(:,p_index);

negative_time = -0.02:deltaS:-0.00002; % in seconds
initial_p = ones(1,size(negative_time,2))*p_conc0;

full_time = [negative_time time]';
full_p = [initial_p p]';

concatenated_precursor = [full_time,full_p]';

new_output_precursor = convolveModel(concatenated_precursor,fitParm);
% end of function-----convolvePrecursor
```

3 Fitting ALS Data

Using the program just described, a fitting program can be used to vary rate constants to find the best fit of the simulated model to experimental data. The program below can fit to a

variety of situations: (1) fitting for the self-reaction branching ratio while allowing the total rate constant to float, (2) fitting for the same ratio, keeping the rate constant equal to the JPL evaluated rate, (3) fitting the ethyl peroxy radical wall loss rate, and (4) fitting for the prompt $\text{C}_2\text{H}_4 + \text{HO}_2$ formation yield from the ethyl + O_2 reaction.

3.1 fitALSEtO2.m

```
function [P,sigP,history] = fitALSEtO2(image,p_init,fitParm,typeFit)
% This program calls the createConvolvedModelEtO2 program which has 5
dependents: buildModel, convolvePrecursor, convolveModel,
runKintecusEtO2, and photolysis_calc. This program has several modes:
typeFit = 1&2) branching ratio fit, without a constraint on the total
rate constant (10.7 or 11.45 eV) or 3&4) fitting the ratio of CH3CHO to
C2H5OH (10.7 or 11.45 eV) with a constraint on the total rate or 5)
fitting the EtO2 wall loss or 6) fitting the yield of C2H4 + HO2 from
ethyl + O2

global initialConc;
dataSheet = image.dataSheet;
history.model_out = [];
history.data_out = [];

% Obtain starting concentrations and data from Excel spreadsheet
filename = fitParm.filename;
concI = 'B4:B9';
conc = xlsread(filename,dataSheet,concI);
dataI = 'Z107:CR405'; % Obtains data from t = 0.09 - 59.69 ms
data = xlsread(filename,dataSheet,dataI);
initialConc.Cl2 = conc(4,1); % B7
initialConc.O2 = conc(1,1); % B4
initialConc.C2H6 = conc(5,1); % B8
initialConc.He = conc(3,1); % B6
initialConc.photolysis = image.photolysis;

% Read in the raw data
time = data(:,1);
if typeFit == 1 || typeFit == 2 || typeFit == 3 || typeFit == 4 % Fit
the branching ratio of the self-rxn
    if typeFit == 1 % 10.7 eV, variable ktot
        CH3CHO = data(:,7); % AF
        C2H5OH = data(:,9); % AH
        history.data_out = [time CH3CHO C2H5OH];
        time = [time(26:101);time(26:101)]; % 5-20 ms
        fitData = [CH3CHO;C2H5OH];
        W = sqrt(abs(fitData));
    elseif typeFit == 2 % 11.4 eV, variable ktot
        CH3CHO = data(:,10); % AI
        C2H5OH = data(:,12); % AK
        history.data_out = [time CH3CHO C2H5OH];
        time = [time(26:101);time(26:101)]; % 5-20 ms
```

```

        fitData = [CH3CHO(26:101),C2H5OH(26:101)];
        W = sqrt(abs(fitData));
    elseif typeFit == 3 % 10.7 eV, fixed ktot 6.8e-14, fit
CH3CHO/C2H5OH
        CH3CHO = data(:,7); % AF
        C2H5OH = data(:,9); % AH
        history.data_out = [time CH3CHO C2H5OH];
        time = time(101:201);
        fitData = CH3CHO(101:201)./C2H5OH(101:201); % 20-40 ms
        W = [CH3CHO(101:201),C2H5OH(101:201)];
        W = sqrt(abs(min(W,[],2)));
    else % 11.4 eV, fixed ktot 6.8e-14 fit CH3CHO/C2H5OH
        CH3CHO = data(:,10); % AI
        C2H5OH = data(:,12); % AK
        history.data_out = [time CH3CHO C2H5OH];
        time = time(101:201);
        fitData = CH3CHO(101:201)./C2H5OH(101:201); % 20-40 ms
        W = [CH3CHO(101:201),C2H5OH(101:201)];
        W = sqrt(abs(min(W,[],2)));
    end
elseif typeFit == 5 % Fit the C2H5O2 wall loss term (10.7 eV)
    C2H5O2 = data(:,3); % AB
    history.data_out = [time C2H5O2];
    time = time(26:251); % 5-50 ms
    fitData = C2H5O2(26:251);
    W = sqrt(abs(fitData));
else % fit C2H4 prompt yield
    C2H4 = data(:,5); % AD
    history.data_out = [time C2H4];
    time = time(26:101); % 5-20 ms
    fitData = C2H4(26:101);
    W = sqrt(abs(fitData));
end

% Run the fitting routine
opts = statset('Display','iter');
[P,~,~,CovB] =
nlinfit(time,fitData,@create_model,p_init,opts,'Weights',W);
sigP = sqrt(diag(CovB));
P = P';
% end of function-----fitALSEtO2

```

3.2 create_model.m

```

function F = create_model(p_try,time)
    cd('C:\Kintecus\');
    % Open MODEL.DAT and read text
    model_workbook = fopen('MODEL.DAT','r');
    model_content = textscan(model_workbook,'%s %s %s %s %s',
'Delimiter','\t');
    fclose(model_workbook);
    [~,model_ncols] = size(model_content);
    model_nrows = length(model_content{1});

```

```

    % Change the rate constants. Keep 15 digits in num2str. nlinfit
    does not work well if it is given numbers with large exponentials.
    Therefore, nlinfit is given a value that gets multiplied by the
    exponential later.
    formatSpec = '%10.15e';
    if typeFit == 1 || typeFit == 2 % ethyl peroxy self-reaction
        p1 = p_try(1)*1e-14; % alkoxy channel
        model_content{1,1}{42,1} = num2str(p1,formatSpec);
        p2 = p_try(2)*1e-14; % acetaldehyde/ethanol channel
        model_content{1,1}{43,1} = num2str(p2,formatSpec);
    elseif typeFit == 3 || typeFit == 4
        p1 = p_try*6.8e-14; % alkoxy channel
        model_content{1,1}{42,1} = num2str(p1,formatSpec);
        p2 = (1-p_try)*6.8e-14; % acetaldehyde/ethanol channel
        model_content{1,1}{43,1} = num2str(p2,formatSpec);
    elseif typeFit == 5 % C2H5O2 wall loss
        model_content{1,1}{14,1} = num2str(p_try,formatSpec); % C2H5O2
    wall loss
    else % fit C2H4 prompt yield
        p1 = p_try*4.71803e-12; % 8 Torr
        model_content{1,1}{40,1} = num2str(p1,formatSpec);
        p2 = (1-p_try)*4.71803e-12; % 8 Torr
        model_content{1,1}{41,1} = num2str(p2,formatSpec);
    end

    % Rewrite the MODEL.DAT file with new rate constants
    model_workbook = fopen('MODEL.DAT', 'r+');
    for model_row = 1:model_nrows
        for model_col = 1:model_ncols
            fprintf(model_workbook, '%s\t',
model_content{1,model_col}{model_row,1});
        end
        fprintf(model_workbook, '\r\n');
    end
    fclose(model_workbook);

    % Run the createConvolvedModelEtO2.m file (runs Kintecus). The
    createConvolvedModel routine must be specific to the chemical system to
    run Kintecus with the proper concentrations and output variables.
    cd('C:\Users\Leah\Documents\MATLAB\');
    [new_output, ~] =
createConvolvedModelEtO2(fitParm,initialConc,'yes');
    history.model_out = [new_output(:,6) new_output(:,5)
new_output(:,3) new_output(:,4)];

    % Compute the error vector
    if typeFit == 1 || typeFit == 2
        F = [history.model_out(26:101,1);history.model_out(26:101,2)];
        figure(1);
        subplot(2,1,1);
        plot(history.data_out(:,1),history.data_out(:,2),'og');
        hold on
        plot(history.data_out(:,1),history.model_out(:,1),'-b');
    end

```

```

        str1 = ['CH_{3}CHO formation = ' num2str((p_try(1)*1e-14),5)
' cm^{3} molecule^{-1} s^{-1}'];
        title(str1);
        ylabel('CH_{3}CHO Concentration (molec/cm^{3})');
        subplot(2,1,2);
        plot(history.data_out(:,1),history.data_out(:,3),'og');
        hold on
        plot(history.data_out(:,1),history.model_out(:,2),'-b')
        str2 = ['C_{2}H_{5}OH formation = ' num2str((p_try(2)*1e-14),5)
' cm^{3} molecule^{-1} s^{-1}'];
        title(str2);
        ylabel('C_{2}H_{5}OH Concentration');
        xlabel('Time (ms)');
        elseif typeFit == 3 || typeFit == 4
            F = history.model_out(101:201,1)./history.model_out(101:201,2);
            figure(1);
            plot(time,(history.data_out(101:201,2)./history.data_out(101:201,3)),'o
g');
            hold on
            plot(history.data_out(:,1),(history.model_out(:,1)./history.model_out(:,
2)),'-b');
            str1 = ['Alkoxy yield ' num2str(p_try,3)];
            title(str1);
            ylabel('Ratio CH_{3}CHO/C_{2}H_{5}OH');
            xlabel('Time (ms)');
            elseif typeFit == 5
                F = history.model_out(26:251,3);
                figure(1);
                plot(history.data_out(:,1),history.data_out(:,2),'og');
                hold on
                plot(time,F,'-b');
                str1 = ['C_{2}H_{5}O_{2} + wall = ' num2str((p_try),5) ' s^{-
1}'];
                title(str1);
                ylabel('C_{2}H_{5}O_{2} Concentration (molec/cm^{3})');
                xlabel('Time (ms)');
            else
                F = history.model_out(26:101,4);
                figure(1);
                plot(history.data_out(:,1),history.data_out(:,2),'og');
                hold on
                plot(time,F,'-b');
                str1 = ['C_{2}H_{4} yield = ' num2str((p_try*100),5) ' %'];
                title(str1);
                ylabel('C_{2}H_{4} Concentration (molec/cm^{3})');
                xlabel('Time (ms)');
            end
        end
    end
    % end of function -----create_model
end

```